Dissertation
submitted to the
Combined Faculties for the Natural Sciences and for Mathematics
of the Ruperto-Carola University of Heidelberg, Germany
for the degree of
Doctor of Natural Sciences

Put forward by
Marian Weiss
Born in: Mannheim, Germany
Date of oral examination: 24. January 2018

Microfluidic Approaches for the Sequential Bottom-up Assembly of Droplet-based Minimal Synthetic Cells

Referees
Prof. Dr. Joachim P. Spatz
Prof. Dr. Rainer H.A. Fink

Abstract

The formation of lipid-membrane compartments is one of the distinguishing features of eukaryotic cells. Inspired by the complexity of cellular functional modules and compartments, scientists have concentrated on developing synthetic compartments for the bottom-up assembly of cellular functions. This cumulative thesis bridges the gap between the development of droplet-based microfluidic technology, and its application towards the creation of synthetic cells. Towards this end, polymer-based water-in-oil droplets and microfluidic devices were optimized to achieve stable retention of encapsulated biomolecules within the droplet-based compartments. The outcomes of this research provided crucial information for the successful reconstitution of microtubule networks, representing a minimal cytoskeleton model system. Furthermore, in an attempt to combine the properties of biological lipid membranes with the advantages of droplet-based microfluidics, a new compartment system termed *droplet-stabilized Giant Unilamellar Vesicles* (dsGUVs) was developed. Importantly, the enhanced stability of dsGUVs and the implementation of 'pico-injection' microfluidic technology enabled the sequential and precise loading of dsGUVs with biomolecules and membrane proteins without compromising their functionality. In order to expand the potential of this technology, a new microfluidic device was developed for the release of the assembled protocells into a physiological environment. Finally, Fluorescence Correlation Spectroscopy (FCS) was reconceptualized as a new analysis tool, allowing for the efficient monitoring of the high-throughput generation process of droplet-based synthetic cells in the kHz-range.

Zusammenfassung

Jede lebende Zelle besitzt eine Hülle aus einer Biomembran. Um die komplexen Eigenschaften und Funktionen von Zellbestandteilen nachzubilden, sind Wissenschaftler auf der Suche nach synthetischen Hüllen, die den Aufbau einer minimalen synthetischen Zelle aus ihren fundamentalen Bestandteilen ermöglichen sollen. Diese kumulative Arbeit verbindet die Entwicklung von tröpfchen-basierter Mikrofluidik-Technologie und deren Anwendung für den Aufbau von synthetischen Zellen. Dafür wurde zunächst die grundsätzliche Eignung mikrofluidischer Tropfen als künstliche Hülle untersucht, wobei die Stabilität der Tropfen sowie die Fähigkeit, Fluorophore und Biomoleküle langfristig einzukapseln, verbessert wurde. Diese Ergebnisse machten es möglich, die Selbstorganisation von Mikrotubuli-Netzwerken zu untersuchen, was ein minimales Modellsystem des Cytoskeletts darstellt. Um die Eigenschaften von biologischen Lipidmembranen mit den Vorteilen der tröpfchen-basierten Mikrofluidik zu kombinieren, wurde ein neuartiges Kompartiment entwickelt, das *droplet-stabilized Giant Unilamellar Vesicle* (dsGUV) genannt wurde. Es konnte gezeigt werden, dass sich nach der Herstellung der dsGUVs weitere funktionale Biomoleküle über ein mikrofluidisches ‚Piko-Injektionssystem' vollautomatisch und kontrollierbar injizieren lassen. Um das Potential dieser Technologie noch zu erweitern, wurde eine Methode entwickelt, mit der sich die aufgebauten Minimalzellen mitsamt ihrer Lipidmembran aus der stabilisierenden Polymerschicht in eine wässrige Umgebung überführen lassen. Darüber hinaus wurde die Fluoreszenz-Korrelations-Spektroskopie (FCS) als Analysemethode neu konzipiert, um eine Kontrolle der effizienten Herstellung von tröpfchen-basierten synthetischen Zellen im kHz-Bereich zu ermöglichen.

Cell and tissue, shell and bone, leaf and flower,
are so many portions of matter,
and it is in obedience to the laws of physics
that their particles have been moved, moulded and conformed.

D'Arcy Thompson, Cambridge 1917

Contents

List of Figures

List of Abbreviations

AC	Alternating Current
AFM	Atomic Force Microscopy
ADP	Adenosine Diphosphate
AMP	Adenosine Monophosphate
ATP	Adenosine Triphosphate
BSA	Bovine Serum Albumin
CAD	Computer Aided Design
CMC	Critical Micelle Concentration
CPP	Critical Packing Parameter
DC	Direct Current
DLS	Dynamic Light Scattering
DOPC	1,2-dioleoyl-sn-glycero-3-phosphocholine
DOPS	1,2-dioleoyl-sn-glycero-3-phospho-L-serine
DPPC	1,2-dipalmitoyl-snglycero-3-phosphocholine
DSPC	1,2-distearoyl-sn-glycero-3-phosphocholine
dsGUV	droplet-stabilized Giant Unilamellar Vesicle
FCS	Fluorescence Correlation Spectroscopy
FRAP	Fluorescence Recovery After Photobleaching
GDP	Guanosine-diphosphate
GTP	Guanosine-triphosphate
GUV	Giant Unilamellar Vesicle
HLB	Hydrophilic-Lipophilic Balance
MAP	Microtubule-Associated Proteins
MLV	Multilamellar Vesicles
MTOC	Microtubule-Organizing Centers
PDMS	Polydimethylsiloxane
PEG	Polyethylene Glycol
PMT	Photo-Multiplier Tube
SLB	Supported Lipid Bilayer
SUV	Small Unilamellar Vesicle

CHAPTER 1

Introduction

1.1   What is Life?

The question 'What is Life?' is one of the most fundamental and most striking questions to ask. The world around us is full of life in multifaceted forms, dimensions, complexities and developments: The length scale of living systems goes from several $10^{-7}m$ diameter (bacteria, archaea) [1] up to $10^2 m$ length of the *Sequoiadendron giganteum* (Giant Sequoia tree) [2]. Simple unicellular organisms like bacteria, archaea or protozoa can individually and independently execute all vital functions to survive. Multicellular organisms consist of specialized and interdependent cells allow for the formation of higher-ranking functional units such as tissue and organs. This enables an effective sharing of specific tasks and allows for the performance of more complex functions [3]. Life is adopted to miscellaneous and extreme environmental conditions [4, 5], for example to extreme temperatures (thermophile), to acidic (acidophile) or alkaline conditions (alkaliphile) or even to high pressure in the underground or deep down in the ocean (piezophile). And yet this is only the occurrence and facets of life as we know it on earth. Since there is no comparable system it is hard to judge whether essential features of life on Earth already include all possible aspects of life or whether they are just a specific occurrence adopted to this environment [6].

In the past philosophers and scientists from diverse research fields made different attempts to explain and define life. They developed manifold theories, which strongly influenced the way of thinking and the social relations in their times. Their attempts reach back to the beginnings of philosophical thinking: The philosopher Empedocles (ca 430 BC) developed the concept of four elementary and eternal elements, earth, water, air and fire, from which everything in the universe is made up [7]. In his theory, life can be reduced to different combinations and arrangements of the four elements and is thus merely matter (materialism). On the other hand, Aristotle (ca. 350 BC) introduced in his book *De anima* [8] the soul as the entity which allows to identify a natural body as a living thing (Hylomorphism). Different kinds of living things possess different faculties of the soul, like reproduction and growth for plants, self-motion and sensation for animals and intellect, thought and reflection for humans. Thus, the soul is an immaterial principle necessary for all living things (idealism).

Based on these ideas two controversial philosophical concepts of the definition of life were developed: **Mechanical Philosophy** [9], assuming that life is nothing but matter influenced by mechanical principles. These principles can be described by natural laws, making it theoretically possible to determine the state of a living organism at any time by knowing the exact state of the system at a given time (determinism). In this case a living organism is often compared to a machine (see Figure 1.1). In contrast to this concept, **Vitalism** explains life by an immaterial principle, some non-physical or non-natural element. All living things are characterized by a purposeful 'vital force' (*vis vitalis*) [10, 11].

Scientific models try to identify the building components of life and the universal processes, that drive a living organism. In this context, the Physicist E. Schroedinger defined life as a system being able to maintain or decrease its internal entropy [12]. This means that a living organism is able to delay its decay into the thermodynamic equilibrium for a sufficiently long time. A system that 'feeds on negative energy', does not contradict the second law of thermodynamics, since it is an open system: The creation of ordered structures within the organism is possible by the uptake of free energy from the environment and by a subsequent increase of disorder outside the system. Therefore, the definition of
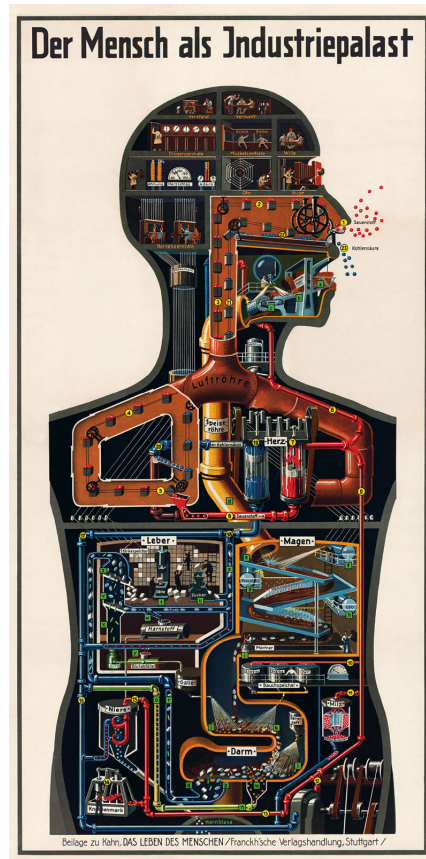
Figure 1.1 – This drawing by Fritz Kuhn from 1926 demonstrates the mechanical ideology, which also reflects the way how a living organism was considered to function. Organic functions and living procedures are compared to mechanical or industrial processes. Dr. Fritz Kahn, *Der Mensch als Industriepalast*, 1926, drawing.

life in this context is concentrated on the energy requirements of the system.

The wide range of different scientific approaches to explain life culminated in the creation of a whole new research field, *Biology* (bios-logia), the 'study of life'. Biology as an independent research field aims for the phenomenological description of living organisms on earth and analyzes their interaction with each other, with other organisms and with their environment. In order to define life, Biologists describe, dissect and investigate the different forms and characteristics of living organisms. Resulting from these findings, essential principles necessary for life as it is known on Earth have been identified. D. Koshland lists seven features of life on Earth [13] : *Program* (an organized plan, implemented by DNA), *Improvisation* (response to environment, evolution), *Compartmentalization* (to maintain the concentrations and arrangement of the interior), *Energy* (movement and metabolism), *Regeneration* (compensation for metabolism), *Adaptability* (immediate response to stimuli), and *Seclusion* (chemical control and selectivity). Other authors try to define life by the things life on earth needs and consumes: energy, liquid water, carbon and a small amount of other elements. [6]

However, there are obviously living organisms that do not fulfill these criteria, e.g. a mule, which is the offspring of a female horse and a male donkey, is unable to reproduce itself and to undergo an evolutionary development. Another example are viruses, which

are particles containing all information for reproduction and proliferation, however they do not possess an individual metabolism and need a host cell to actually replicate. On the other hand these criteria are not exclusive characteristics for life, since e.g. fire also fulfills most of them. Furthermore the features would also apply to robots or computer programs, which is at least a matter of debates. Finally, these definitions could exclude forms of possible extraterrestrial life and also possible forms of future synthetic life on earth.

Summarizing the above, it can be said that till now there is no clear, general definition of life. In order to approach this issue, scientists try nowadays to develop a fundamental theory similar to e.g. the quantum theory or the standard model, which describes how matter is constructed internally. To achieve a fundamental understanding of life, scientists want to dissect the complex varieties of life on earth into the smallest common building units. The understanding of what these building units are composed off and how they dynamically interact could lead to a fundamental understanding of life.

1.2 Fundamental Building Blocks of Life

Chemists use the periodic table of the elements to explain the composition and construction of matter. Nowadays, Biologist strive for a similar construct by identifying the elementary building blocks of living organisms. Jamey D. Marth [14] identified 68 fundamental molecular building blocks, which can be grouped into the four macromolecular units of all cells (see Figure 1.2):

- **Lipids**: hydrophobic and amphipathic molecules, 8 molecular building blocks

- **Proteins**: polymers consisting of combinations of 20 natural amino acids

- **Nucleic Acid**: DNA and RNA being produced from 8 nucleosides

- **Glycans**: polysaccharides and simple sugars, 32 molecular building blocks

Nucleic acids (DNA and RNA)

Glycans

Deoxyadenosine, deoxycytidine,
deoxyguanosine, deoxythymidine,
adenosine, cytidine, guanosine, uridine

Fucose, galactose, glucose, glucuronic acid, mannose,
N-acetylgalactosamine, *N*-acetylglucosamine, neuraminic acid, xylose,
nononic acid, octulosonic acid, arabinose, arabinofuranose,
colitose, fructose, galactofuranose, galacturonic acid,
glucolactilic acid, heptose, legionaminic acid, mannuronic acid,
N-acetylfucosamine, *N*-acetylgalacturonic acid,
N-acetylmannosamine, *N*-acetylmannosaminuronic acid,
N-acetylmuramic acid, *N*-acetylperosamine,
N-acetylquinovosamine, perosamine,
pseudaminic acid, rhamnose, talose

dA, dC, dG, dT, rA, rC, rG, rU
A, R, D, N, C, E, Q, G, H, I, L, K, M, F, P, S, T, W, Y, V
Fuc, Gal, Glc, GlcA, Man, GalNAc, GlcNAc, NeuAc, Xyl,
Kdn, Kdo, Ara, Araf, Col, Frc, Galf, GalUA, GlcLA, Hep,
Leg, ManUA, FucNAc, GalNAcUA, ManNAc, ManNAcUA,
MurNAc, PerNAc, QuiNAc, Per, Pse, Rha, Tal
Fa, Gl, Glpl, Pk, Pl, Scl, Spl, Stl

Proteins

Lipids

Alanine, arginine, aspartic acid, asparagine,
cysteine, glutamic acid, glutamine,
glycine, histidine, isoleucine, leucine, lysine,
methionine, phenylalanine, proline, serine,
threonine, tryptophan, tyrosine, valine

Fatty acyls, glycerolipids, glycerophospholipids,
polyketides, prenol lipids, saccharolipids,
sphingolipids, sterol lipids

Figure 1.2 – This sketch represents the elementary building blocks of a living cell, as identified by J. Marth [14]. DNA and RNA are composed of eight nucleosides (red color). Combinations of the twenty amino acids (green) allow for the formation of proteins. The class of glycans includes 32 saccharides, which are often attached to lipids and proteins (blue). Finally, lipids have been categorized into eight groups, as indicated in purple. Taken with Permission from J. Marth [14].

These fundamental molecular building blocks form a variety of approximately 10^5 different (macro-) molecules in a single eukariotic cell [15]. Not only the amount of these

molecules is remarkable, also the complexity and variety of their functions is astonishing. Furthermore, the composed molecules assemble again into higher functional units. This self-organization of molecules into functional units depends on the concentration of the components, the environment, the size of their confinement and much more [16]. Despite the fact that the functions of the major cellular units are known, the chemical and physical mechanisms behind the self-organization of the molecules into functional units is only partly understood.

In this thesis, the self-assembly process of selected bio-molecules was experimentally studied under defined and well-controlled conditions. The following section provides a general overview of the most important molecular building units and highlights the specific functions of bio-molecules used in the context of this thesis.

1.2.1 Lipids

Lipids are hydrophobic or amphiphilic molecules [16], having a high amount of C-H bonds (carbon - hydrogen). The simplest constructs are fatty acids, having a carboxyl group at one end and long hydrocarbon chains on the other, usually containing 16 or 18 carbon atoms. Saturated fatty acids have straight hydrocarbon chains (see Figure 1.3, octadecanoic acid), while unsaturated fatty acids contain at least one double bond between the carbon atoms, thus showing a king in their hydrocarbon chain (see Figure 1.3, oleic acid). Three fatty acids can be combined with glycerol to triglyceride, the main constituents of fat in the body. They serve mainly as energy storage and form fat droplets in an aqueous environment since they are insoluble in water. [16].

Phospholipids represent the most abundant lipid types in cellular membranes [15]. They consist of a hydrophilic head and two fatty acids forming a hydrophobic tail. In case of glycerophospholipids, the two fatty acids are connected via glycerol, however the third carbon atom binds to a phosphate group, which can bind another small polar molecule. Both the polar head group as well as the two hydrophobic tail can be varied, allowing for different combinations with different physical properties, see Figure 1.3, right column. When the connecting glycerol is replaced by serine, the resulting complex is a so-called sphingomyelin.

In contrast to phospholipids, steroids consist of four very hydrophobic hydrocarbon rings. In case of cholesterol a hydroxylic OH - group is attached to one end, making the molecule amphipathic.
Amphipathic lipids exposed to water can exist as monomers up to a specific lipid concentration. When reaching the **critical micelle concentration** (CMC) the lipids start to assemble into aggregates. In order to reduce the free energy of the system, lipids expose the hydrophilic heads to the aqueous environment and thus minimize the contact of the hydrophobic tails to water [17]. Further increase of the lipid concentration will not increase the concentration of lipid monomers, but will increase the concentration of the aggregates. The CMC depends on the physical properties of the amphipathic lipids, e.g. the length of the hydrocarbon chains [18].

Additionally, the exact arrangement of the aggregates can be described by the **critical packing parameter** CPP [16, 19]

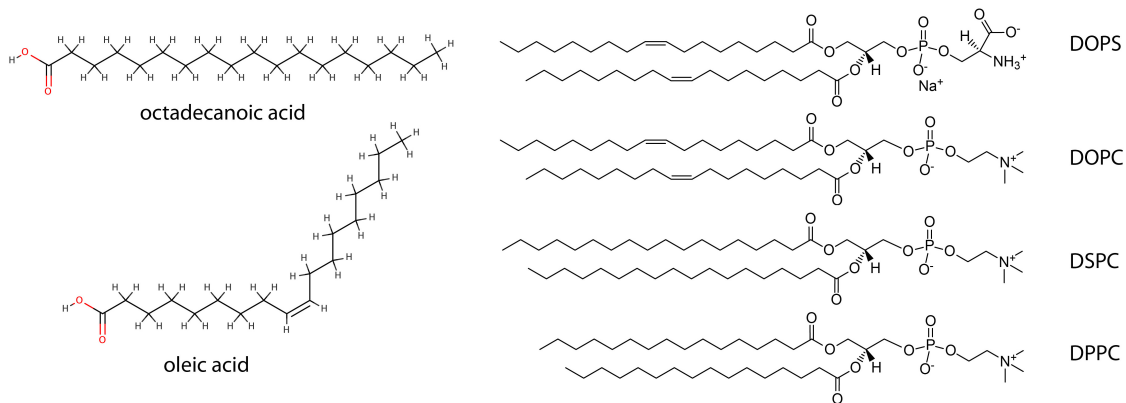$$CPP = \frac{V}{a_0 . l_c} \tag{1.1}$$

Figure 1.3 – Left side: Chemical structure of octadecanoic acid (top) and oleic acid (bottom). The double bound leads to a kink in the spatial configuration. Right side: Different phospholipids. DOPS (1,2-dioleoyl-sn-glycero-3-phospho-L-serine) and DOPC (1,2-dioleoyl-sn-glycero-3-phosphocholine) have the same hydrophobic tails and differ by their head group. DSPC (1,2-distearoyl-sn-glycero-3-phosphocholine) has the same head group as DOPC, however the hydrophobic tails consist of only saturated fatty acids. In contrast to DSPC, DPPC (1,2-dipalmitoyl-sn-glycero-3-phosphocholine) has 16 instead of 18 C-Atoms. Chemical structures are taken from https://avantilipids.com/ and were drawn with ChemDraw 15 (Perkin Elmer, USA)

with V: volume of the hydrocarbon tail, a_0: optimum surface area of the head group and l_c: critical length of the hydrocarbon chains [20, 21].

The packing parameter roughly describes the structure of the molecule and thus determines the possible geometrical arrangements. In case of only one hydrophobic tail the amphipathic lipid has a cone shape with $CPP \leq 0.5$ (see Figure 1.4, left side). Therefore the lipids tend to form circular micelles. In contrast, lipids having two hydrophobic tails such as phospholipids, form a more or less cylindrical molecule with $CPP \approx 1.0$ (see Figure 1.4, right side). Therefore, these lipids arrange into a bilayer-like structure after reaching the CMC.
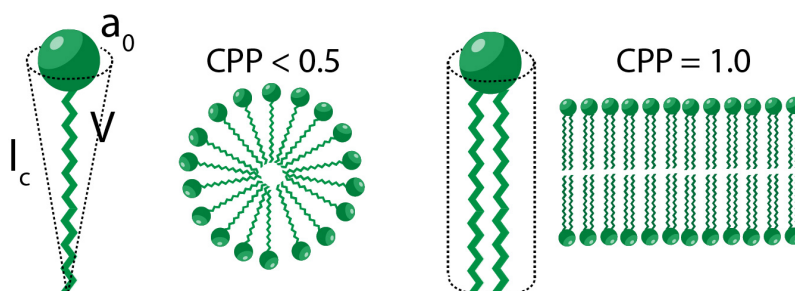
Figure 1.4 – The chemical composition and the structure of phospholipids determines the spatial expansion and orientation of lipid arrangements.

The arrangement of phospholipids into a lipid bilayer is a self-assembly process driven by need to decrease the system's free energy [22]. In an aqueous environment the lipids normally arrange into a liposome, i.e. an enclosed lipid bilayer shell. Lipid bilayers have a thickness of roughly 4 nm [16]. Due to thermal movement, single lipid monomers can rotate freely around their longitudinal axis as well as diffuse laterally within the plane of

the bilayer. The latter movement is described by the **diffusion coefficient** and can be up to several $\mu m^2/s$ at room temperature [23]. This means that lipid monomers change their position with their neighbors millions of times per second and travel several μm in the same time.

The mobility of the lipids is strongly influenced by the phase of the lipid, which depends on the **phase transition temperature** [24, 25]. At temperatures below the transition temperature, lipids are in the *ordered gel phase*, where the hydrocarbon chains are fully stretched out and thus closely packed [26]. Here, lipids show a slow lateral diffusion, leading to a higher rigidity of the lipid bilayer. For temperatures higher than the transition temperature, lipids are in the *disordered liquid phase*, showing a random orientation of the hydrocarbon chains and thus a greater mobility. The transition temperature depends on the physical properties of the lipids, e.g. longer hydrocarbon chains increase the van der Waals interactions between the lipids and thus require more energy i.e. higher temperature for the transition. Mixtures of lipids with different phase transition temperatures can lead to a phase separation, where ordered gel phases and disordered liquid phases coexist in a lipid bilayer and spatially separated patches in the respective phases are observable [27].

The presence of lipid bilayer compartments is a distinguishing feature of living cells. Every cell is confined by a lipid bilayer and this so-called *plasma membrane* acts as a physical barrier between the extracellular aqueous environment and the interior of the cell [16]. In case of eukariotic cells, lipids additionally form specific subcompartments, the organelles. The composition of the plasma membrane and the organelles is a mixture of hundreds of different types of lipids as well as numerous membrane and transmembrane proteins [16]. The compartmentalization allows for a physical separation of different molecules, ions or other cellular components, thus allowing several metabolic activities at the same time inside living systems. Furthermore, it enables the establishment of different micro-environments inside the cell, in which specific biochemical reactions and other processes take place. Finally, transmembrane proteins enable a selective permeability for molecules and ions and thus the creation of transmembrane concentration gradients. Such gradients can drive other molecules to perform specific tasks such as the synthesis of ATP (see Section 1.2.2).

All in all, the formation of lipid bilayer compartments is considered to be an essential step in the origin and the evolution of life and therefore a fundamental piece of the puzzle to the question 'What is life?'.

1.2.2   Proteins

Each protein is composed of several amino acid groups or polypeptides and thus has a distinct amino acid sequence. This specific sequence is called the **primary structure** of the protein (see Figure 1.5) [16]. Small proteins consist of something around 100 amino acids. Regarding the large number of 20 amino acids as building blocks, the total amount of different combination (20^{100}) seems to be overwhelmingly high (higher than the number of atoms known in the universe [28]). However, only a small fraction of combinations can form stable three-dimensional structures. This is because the polar groups of the amino acid sequence can form hydrogen bonds with each other, resulting in two different three-dimensional arrangements (**secondary structure**): In an *alpha-helix* hydrogen bonds are formed between two nearby separated amino acids along one individual chain, thus pulling the chain into a coil. The second structure is the *beta-sheet*, where hydrogen bonds

are formed between two individual chains, thus allowing for the linkage of many chains side-by-side (see Figure 1.5).
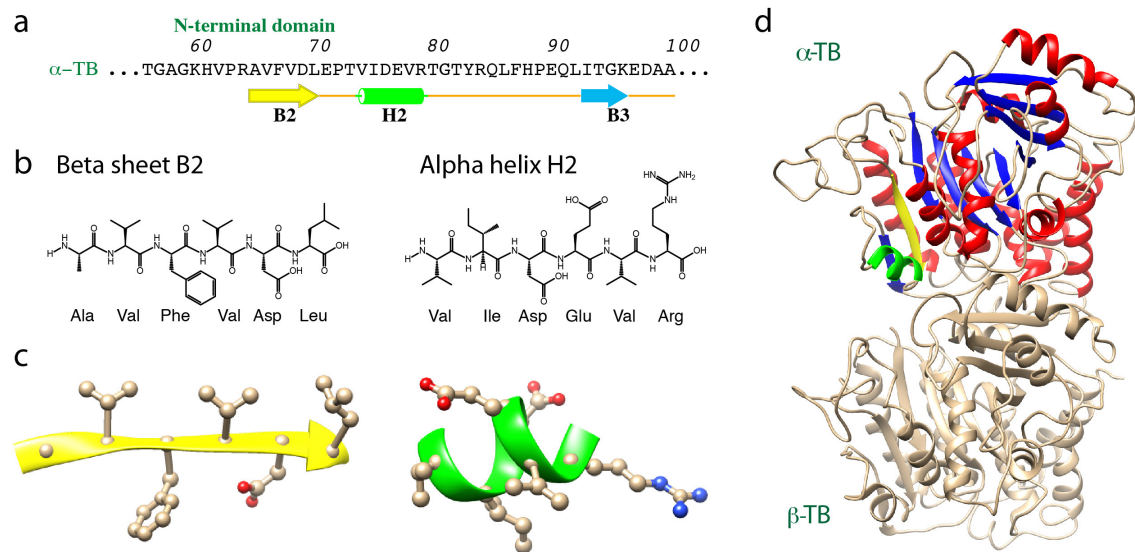

Figure 1.5 – The basic structural arrangement of the protein Tubulin (see Section 1.2.2), composed of two subunits α-TB and β-TB. a) represents an extract of the amino acid sequence (primary structure). The sequence of B2 (yellow) corresponds to a beta sheet, the sequence H2 to an alpha helix. The chemical structures of these sequences are presented in b). c) shows the corresponding three-dimensional arrangements (secondary structure). These parts are marked with the same color in the globular protein (tertiary structure), presented in d). Together with the β part, the tubulin dimer is formed (quaternary structure). Adopted with Permission from [29]

Finally the hydrophobic interactions between distinct amino acids drive the arrangement into the **tertiary structure**, which is the final folded shape of a globular protein (see Figure 1.5). In the end, this three-dimensional arrangement is already defined by chemical nature of the side groups of the primary structure. Hydrophobic interactions between different amino acids are believed to be the dominant driving force for protein folding [30]. Thus the native conformation of the three dimensional protein structure is driven by the system to minimize the free energy. Some proteins consist of more than one polypeptide chain as a base. The different tertiary structure of the single chains cluster into the **quaternary structure** and form a singe functional protein.

Due to the diverse structures, proteins are able to fulfill various functions and tasks like:

- **Transport**: proteins can transport small molecules and ions, e.g. hemoglobin can transport oxygen in the blood

- **Support**: Fibrous proteins like collagen form structural units

- **Motion**: contractile proteins can move materials within cells, e.g. actin and myosin cause muscular movement through sliding motion

- **Regulation**: Proteins can regulate intracellular processes as well as intercellular processes via hormones

- **Defense**: Foreign microbes or other invaders such as cancer cells can be recognized by globular proteins like antibodies

- **Enzyme catalysis**: Proteins can facilitate chemical reactions e.g. for metabolism

The following section introduces the proteins **Tubulin** and **ATPsynthase**, which were studied in the context of a bottom-up synthetic cell approach in this thesis.

Tubulin

Tubulins are spherical proteins existing in all eukariotic cells [29]. They can be divided into six major groups, α, β, γ, δ, ε and ζ, all of them having a molecular weight of roughly 55 kDa and consisting of around 450 amino acids [31]. α and β tubulin form a dimer (see Figure 1.5 and 1.6) by binding two molecules of Guanosine-triphosphate (GTP) [32]. Several dimers can attach to each other, thus forming a long protofilament. In turn, these protofilaments attach to each other side by side and form a stiff, hollow cylinder with a base of 13 protofilaments. This structure is called **microtubule**. Microtubules have an outer diameter of 25 nm, an inner diameter of 14 nm and a length of up to 50 μm.

The GTP molecule of the α-tubulin shifts into the inner part of the microtubule, whereas the GTP of the β-tubulin is accessible at the outside. The microtubule can grow in both directions, however the presence of the GTP molecules at the β-subunits leads to an increased growth speed. Thus, the microtubule is directional, having a fast growing plus end (β-subunits) and a slower growing minus end (α-subunits).
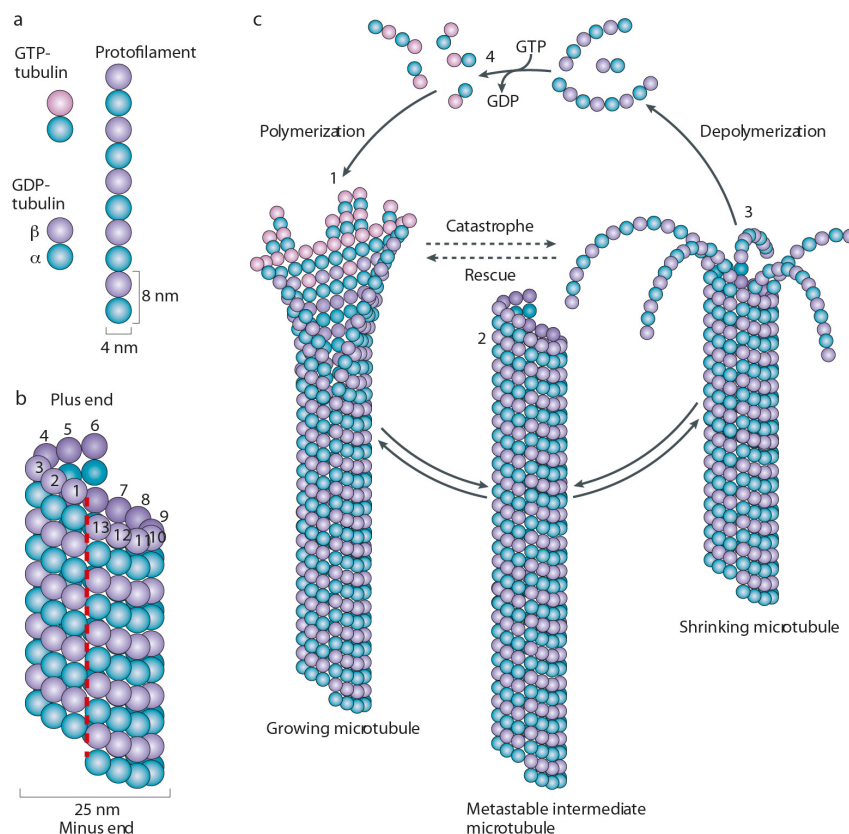
Figure 1.6 – Structural arrangement of microtubules being composed of α and β tubulin. a) shows the combination of tubulin dimers to a protofilament. These protofilaments arrange to a hollow cylinder-like structure, called microtubule, b). The stability and formation of microtubules depends on the tubulin concentration and is a highly dynamic process, as schematically shown in c). Taken with Permission from [32]

Additionally, the accessible GTP at the β-subunit can be hydrolyzed, leading to a deformed guanosine diphosphate (GDP) structure and thus resulting in a destabilization of the microtubule. This process regulates the elongation of the microtubules and is the reason for the so-called *dynamic instability* of microtubules.

The growth of microtubules depends on the concentration of free tubulin dimers. In case of an excess of free tubulin dimers the polymerization is faster than the GTP hydrolysis, leading to a *GTP-Cap* at the plus end of the microtubule. When the concentration of free tubulin dimers is reduced, polymerization is slower than hydrolysis, resulting in a loss of the GTP-Cap and thus in a fast depolymerization. This process is called catastrophe. The tubulin concentration, at which polymerization and depolymerization balance equally, is the critical concentration, which is around 20 μM [33], corresponding to half of the total tubulin concentration in a cell. Typically the half-life time of a microtubule is 5-10 min [34]. However, so-called microtubule-associated proteins MAPs regulate the polymerization and depolymerization velocity, as well as the occurrence of the catastrophes.

In eukariotic cells microtubule-organizing centers (MTOC) serve as nucleation points and organize the arrangement of microtubules [35]. The centrosome is the main MTOC, bundling the minus ends of the microtubules at its center and thus forming a star-like structure. The plus ends reach into the cellular interior and up to the cellular membrane, stabilizing the physical shape of the cell. Due to these attributes, microtubules are one of the main components of the cytoskeleton. Beside their function as backbones of the cell, the microtubules serve as guiding structures for motor proteins, which can transport organelles or vesicles to the plus end (kinesin) [36] or to the minus end (dynein) [37]. During cell migration the dynamic behavior of the microtubules plays a central roll, e.g. as regulators of G-proteins (such as RhoA and Rac1) or to trigger focal adhesion disassembly. Additionally microtubules are involved in the cellular division by inducing forces to the cell. During mitosis microtubules mechanically separate the replicated chromosomes into two new nuclei, forming a structure which is called mitotic spindle [38]. The origin of this formation remains unclear, currently two models describe the organization:

1. **Search and capture model:** Microtubules nucleate from two bipolar centrosomes, get in contact with the two chromosomes in a 'search and capture' manner and finally adopt the stabilized spindle structure [39–41].

2. **Self assembly model:** Microtubules nucleate from the two chromosomes, are moved and organized into anti-parallel bundles via motor proteins and finally adopt the mitotic spindle formation [42].

In the context of this thesis, the self-assembly of tubulin into microtubule structures in a compartment under controlled conditions was investigated.

ATP synthase

ATP synthases (also called H^+-ATPase, F-ATPase or F_0F_1-ATPase) are transmembrane proteins with a molecular mass of roughly 550 kDa [43, 44]. They synthesize the central molecule for chemical energy within the cells: Adenosine triphosphate (ATP). Many cellular functions like movement, cellular division, synthesis of proteins etc. are driven by the hydrolysis of ATP into ADP (Adenosine diphosphate) or AMP (Adenosine monophosphate). The recoupment of ATP from ADP and phosphate (P_i) plays a central roll: The human body contains on average only 250g pure ATP, whereas the total need of ATP each day is equivalent to the human body weight.

ATP synthases catalyze the reaction of ATP from ADP and P_i. According to the chemiosmotic theory, proposed by P. Mitchell 1961 [45], the electron transport chain of the cellular respiration is responsible for the pumping of protons from the matrix of the mitochondrion (in case of eukariotic cells) across the stroma, thus creating a transmembrane electrochemical gradient $\Delta\mu_{H+}$ between the two compartments. This gradient consists of two components: The difference in transmembrane proton concentration ΔpH and the difference in the transmembrane electric potential $\Delta\phi$. The resulting flux of the protons back into the mitochondrion is the driving force for the activity of ATP-synthase.
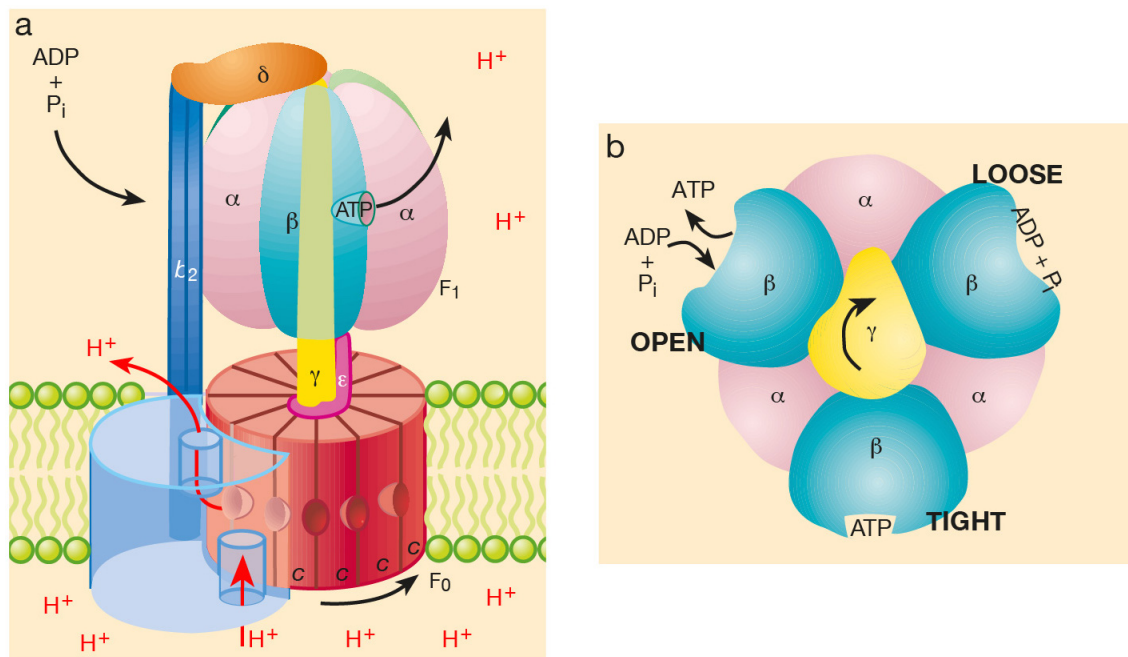

Figure 1.7 – a) schematic representation of the structural arrangement of the transmembrane protein ATPsynthase. c-, γ- and ε - parts can perform a rotation, driven by a transmembrane electrochemical gradient. The α and β units allow for the synthesis of ATP from ADP and P_i. b) illistrates the top view of the protein, demonstrating the synthesis process. Adopted with Permission from [46].

ATP-synthases consist of two main parts (see Figure 1.7). The hydrophobic F_0-part is incorporated into the cellular membrane of the mitochondrion and can be divided in three subparts: one a-part, facilitating the flow of the protons, two b-parts, stabilizing the protein and twelve c-parts, forming a rotational ring [46, 47]. The hydrophilic F_1-part consists of five subunits: three α-parts and three β-parts, forming a catalytic hexamer, one γ-part and one ε-part, connected to the c12-ring and one δ-part, connected to the b-part.

The whole complex can additionally be divided into a rotation unit (*rotor*), consisting of the c12 ring, the γ-part and the ε-part and a *stator* (other parts).

The flow of the protons through the contact area of the part a and the c12-ring forces the latter into a continuous rotation. Since the γ-part and the ε-part are connected to the c12-ring, they follow the rotation. However, the γ-part is asymmetric and extended up into the $\alpha\beta$-hexamer. Thus, the continuous rotation of the c12-part is converted into a step-wise rotation of 120°. As a result, the conformation of the $\alpha\beta$ part changes cyclically, allowing for the synthesis of ATP.

Every active binding side of the three β parts passes sequentially through three different phases (see Figure 1.7): During the *Loose-binding-phase* (L), the conformation of the β-part has a high affinity to bind ADP and P_i; in the *Tight-phase* (T) the conformation of the β-part changes, shielding ADP and P_i from water and thus allowing the synthesis to ATP; finally, in the *Open-phase* (O) the conformation of the β-part changes again, opening the active binding side for a release of the synthesized ATP.

The generation of ATP plays a critical role in providing energy for a living organism. Therefore, in this thesis, the possible implementation of an ATP-generating unit for a synthetic cell was investigated.

1.3 Synthetic Biology

The previous chapter gave an insight into the fundamental building units, which are required to form complex biological systems. However the original question 'What is Life?' still remains unanswered. Moreover, there are several scientific questions that derive from the original one: How do fundamental building units interact and form a living system? What is the minimum amount of fundamental building units to form a living system? Where is the difference between a non-living assembly of fundamental building units and a living cell? How is the organization of the fundamental building units controlled, both spatially and temporally? Or, in short: What are the minimum requirements for a functional assembly of fundamental building units to form a living system? In the last few years a new interdisciplinary research field arose to answer these questions: **synthetic biology**.

This new field aims to not only observe and describe biological systems but to mimic them synthetically and even to construct them in new ways. A major motivation is the application of engineering principles to biological systems [48]. The famous words of the Physicist Richard Feynman became the new guiding principle of this research field:

'What I cannot create I do not understand'

The underlying hope is that synthetic biological systems might allow the study of self-organization processes of molecular building units and the pattern and shape formation under defined conditions. Following this motif, two methodological approaches in synthetic biology can be distinguished: *Top-Down* and *Bottom-Up* approaches [49].

1.3.1 Top-Down vs Bottom-Up approach

The top-down approach emanates from an existing living organism. As described in Section 1.2, even 'simple' organisms such as unicellular bacteria are composed of a multitude of different molecules, which have to be organized and conducted in defined ways to perform specific tasks. Researcher following the top-down approach try to simplify and reduce the living organism step by step until only a minimal system remains, which however is still able to perform fundamental tasks (see Figure 1.8). As an example, Venter et al. presented a synthetic bacterium called *Mycoplasma mycoides JCVI-syn3.0*, a minimal living system that needs only 473 genes (532kbp) to survive [50]. Remarkably, still 149 of the genes being essential to survive cannot be assigned to a specific biological task. Such a reduced system can provide information about the fundamental building blocks and their functional interactions. Additionally a reduced cell can serve as a base or platform to build and construct new synthetic cells, being able to perform predefined metabolic tasks. These cells can be genetically transformed to serve as molecular factories producing specific materials and chemical products. As an example, Jay Keasling et al. [51, 52] showed, that the bacterium *Escherichia coli* can be genetically modified to produce the malaria medication *Artemisinin*.

In contrast, the bottom-up approach emanates from fundamental building blocks such as genes, proteins or even small functional units. They can be either isolated from living systems or produced synthetically. In an engineering-like manner these building blocks can be arranged to fulfill specific tasks, therewith mimicking a living organism (see Figure 1.8).

Towards this goal, engineering principles have to be applied to biological systems [54]. The first one is the definition and classification of unique, well-defined and functional building units or modules. They can be genes, proteins or even large macromolecular
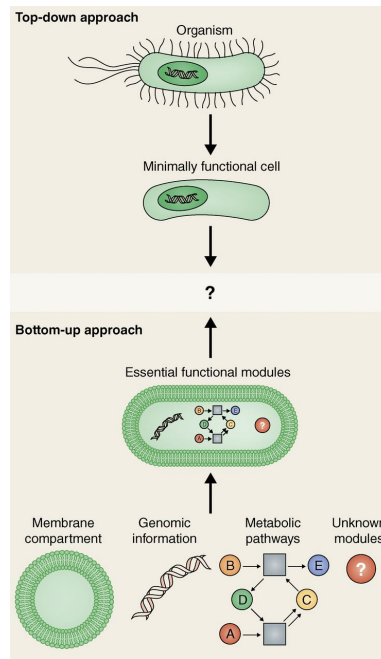
Figure 1.8 – This sketch demonstrates the working principles of the different approaches in Synthetic Biology. The Top-down approach emerges form a living organism such as bacteria. The controlled deactivation of different units leads to a minimal functional cell, might providing information about the essential components to survive and their working principles. On the other hand, the Bottom-up approach emerges from isolated cellular components. The combination of these components might lead to functional modules. Taken from [53], ⓒSchwille, P., 2015. Originally published in JCB. https://doi.org/10.1083/jcb.201506125.

arrangements. In a second step these modules have to be characterized thoughtfully and their functions have to be described. Ideally, mathematical models and simulations provide insight in their functions, how they could be manipulated and how they behave in different environments. Thirdly the modules should be standardized in a way they can be used for broad applications, i.e. independent of their 'natural' environment. This might allow for a general construction and combination of several modules and also a possible substitution of the modules. Finally, the mentioned procedures might enable the combination of these modules in order to form functional cellular units, being able to perform specific tasks. A combination of different functional cellular units can ultimately lead to a complex synthetic cell, being able to perform specific tasks and thus to mimic a living cell.

For such an assembly, an appropriate compartment plays a crucial roll. Compartments allow for the accumulation of molecular components and, additionally, serve to create physical barriers to establish chemical and potential gradients, which are necessary for metabolism and energy production.

In my research , I used the bottom-up approach to study the behavior and self-assembly of different proteins (see Section 1.2.2) in defined and controlled compartments. The following section will introduce the most common model systems for synthetic compartments.

1.3.2 Model Systems and Compartments for Synthetic Biology

Supported Lipid Bilayer

Supported lipid bilayer (SLB) are planar lipid structures supported by a hydrophilic substrate such as glass or silica [55, 56]. The most common method to produce SLB is the fusion of liposomes (see Section 1.2.1) with the supporting substrate [57]. The fusion process involves initially an adhesion of the liposomes to the substrate followed by a rupture and fusion of the lipids. These processes depend on van der Waals and electrostatic interactions and thus on the physical properties of the lipids, the supporting surface and the aqueous environment. Negatively charged lipids rupture and fuse best for low pH and high ionic strength, i.e. a minimum of roughly 5 mM of bivalent cations such as Mg^{2+} or Ca^{2+} [58, 59]. After rupturing the liposomes fuse and form disconnected patches, which can then merge to form a full coverage, depending on a sufficient high lipid concentration [60].
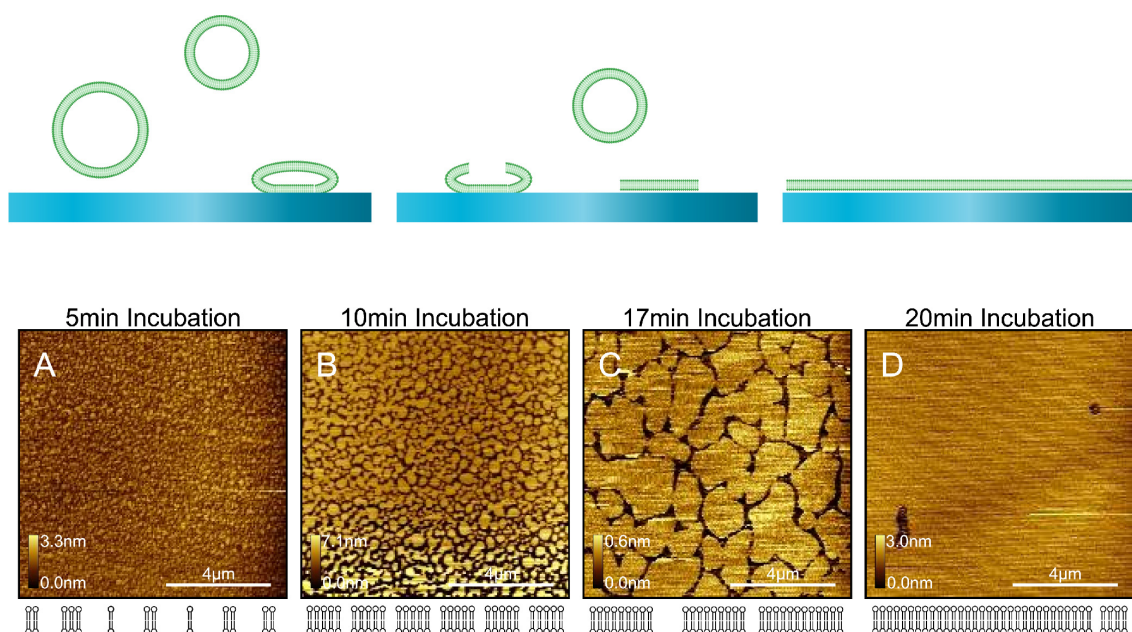

| 5min Incubation | 10min Incubation | 17min Incubation | 20min Incubation |

Figure 1.9 – Top panel represents schematically the formation process of Supported Lipid Bilayer (SLB). Liposomes adhere to the substrate and rupture, thus forming lipid bilayer patches. These patches can fuse and form a continuous lipid bilayer, supported by the substrate. Lower panel shows time-lapse AFM measurements of the lipid bilayer formation process and the fusion of patches over time. Adapted from Attwood et al.[60] licensed under CC BY 3.0

SLB have the advantages of a high stability due to the supporting substrate and a accessibility to optical and analytic tools, such as Atomic Force Microscopy (AFM), quartz crystal microbalance with dissipation monitoring (QCM-D) or total internal reflection fluorescence microscopy (TIRF) [57, 61]. This allows for the characterization and analysis of the lipid bilayer formation process. Additionally, the mobility of lipids can be investigated using fluorescence recovery after photobleaching (FRAP) measurements. Furthermore, transmembrane proteins can be incorporated into the lipid bilayer and their activity and functionality can be studied *in vitro* [62, 63].

However, the use of SLBs as a model system has certain limitations: Both lipids and incorporated transmembrane proteins can be subject to perturbations of the substrate, since

they are separated only by a thin gap of water of around 10 Å [64]. Additionally, one side of the lipid bilayer is not accessible for experiments due to the supporting substrate and thus it is also difficult to create a transmembrane gradient. Finally, a SLB model system is not a confined compartment and thus not suitable to mimic a living cell [65].

To summarize, SLB are a good tool to analyze specific molecular building blocks *in vitro*, especially lipids and transmembrane proteins. However, to assemble the molecular building units in a synthetic bottom-up approach, a suitable compartment is crucial (see Section 1.3.1). Synthetic *in vitro* compartments should fulfill the following criteria:

- The size of the compartment should mimic the dimensions of a natural cell

- The formation, composition as well as the physical and chemical properties of the compartment should be controllable

- The compartment should be stable enough to allow for the encapsulation of biomolecules under physiological conditions

- The compartment should be manipulatable, i.e. they should enable the loading with molecules or functional units

Currently there are three major types of compartments in synthetic biology [65, 66], which are introduced in the following section and which are schematically shown in Figure 1.10.
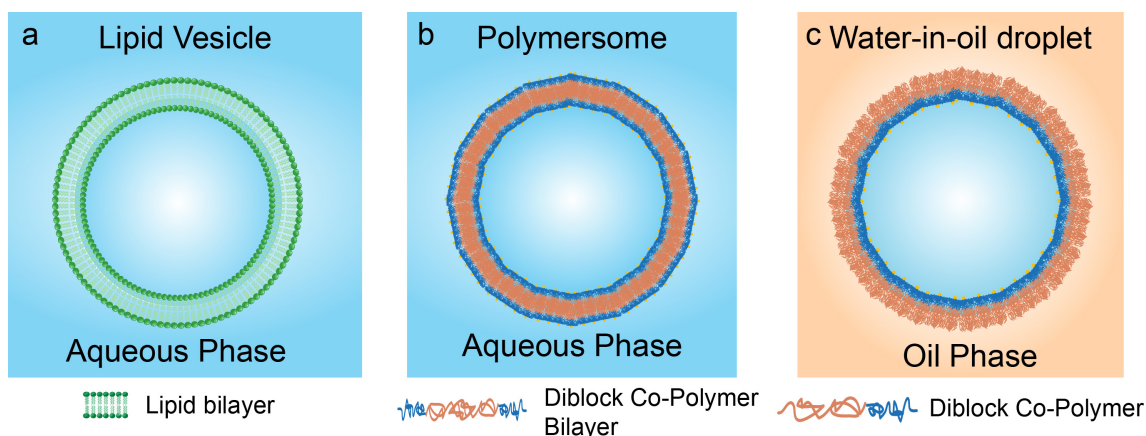

Figure 1.10 – Schematic representation of the most commonly used compartments in bottom-up synthetic biology. a) Giant Unilamellar Vesicle (GUVs) consist of naturally occurring lipids, such as phospholipids, which arrange into an enclosed lipid bilayer compartment. b) Polymersomes consist of synthetic amphiphilic block copolymers. In an aqueous environment, the copolymers arrange in a bilayer-like structure. c) Copolymers are also used to stabilize water-in-oil droplets, where the encapsulated aqueous interior is surrounded by an oil phase.

Lipid Vesicles

Lipid vesicles are three-dimensional water-in-water lipid bilayer structures. Depending on their production technique, they can be unilamellar (a single bilayer) or multilamellar (several bilayer) [67]. When a film of dried lipids is exposed to water, *multilamellar vesicles* (MLV) are formed spontaneously. These vesicles can be transformed into unilamellar

vesicles of an uniform diameter using techniques such as sonication or extrusion through a membrane [68]. The resulting vesicles can be categorized by their size: vesicles smaller than 100 nm are called *small unilamellar vesicles* (SUVs), vesicles with a diameter between 100 nm and a few micrometer are called *large unilamellar vesicles* (LUVs) [66].

Giant unilamellar vesicles (GUVs) are vesicles with a diameter of several tens of micrometers. Due to their cell-sized dimensions they are the most common compartments for many synthetic biology applications [69, 70]. Several techniques to form GUVs have been developed, like spontaneous swelling [71, 72], electroformation [73, 74], emulsion methods [75] or microfluidic methods [76–78].

However, GUVs as model systems for synthetic compartments have disadvantages mainly due to their mechanical and chemical instabilities. Furthermore, the controlled injection of additional bio-molecules into assembled GUVs represents a challenge, since precise and efficient technology is still missing [59, 79, 80]. Additionally, the most common formation methods result in a polydisperse size distribution of the GUVs, making reproducible experiments impossible.

Polymersomes

Polymersomes are water-in-water constructs composed of synthetic amphiphilic block copolymers [81, 82]. In an aqueous phase, the hydrophobic parts of diblock copolymers face eachother in order to minimize energy, thus forming a bilayer-like structure. The formation techniques of polymersomes are similar to lipid vesicles. The most commonly used techniques nowadays are electroformation, gel hydration and microfluidic-based double emulsion techniques [83]. In contrast to lipid vesicles, polymersomes exhibit a higher stability, a tunable rigidity and a longer lifetime. Due to the controllable synthetic components of the polymers the properties of polymersomes such as thickness and permeability can be adjusted to specific needs. Additionally, it is possible to engineer polymersomes having transmembrane channels or allowing the incooperation of transmembrane proteins [84, 85]. However, a controlled encapsulation of biomolecules and an additional manipulation of polymersomes is still a challenging task.

Water-in-oil Droplets

In contrast to polymersomes, water-in-oil droplets are cell-sized aqueous compartments surrounded by a continuous oil phase. In order to prevent fusion with neighboring droplets, they are stabilized by synthetic amphiphilic block copolymers [86]. The most common way to produce droplets is by microfluidic-based techniques, allowing for a very controllable production and manipulation at high-throughput rates [87] (see Section 1.4.2). Droplets can provide stable containers for the assembly of biomolecules [88, 89]. Additionally, the hydrophilic parts of the stabilizing amphiphilic block copolymers, which face into the droplets interior, can be modified for specific biological applications [90]. Several microfluidic techniques can be used to handle, proceed and manipulate the compartments and their content (see Section 1.4.4). Moreover, microfluidics allows for the sequential loading of the created droplets with biomolecules by means of pico-injection technology [91]. However, droplets fail to mimic the biophysical properties of cellular lipid membranes due to the stabilizing synthetic amphiphilic block copolymers and the surrounding continuous oil phase.

In this work, the use of microfluidic water-in-oil droplets as compartments for the bottom-up assembly of minimal synthetic cells was investigated. Therefore, the next section provides theoretical background and an overview of microfluidic techniques and applications.

1.4 Microfluidics

Microfluidics is a research field that investigates both the behavior of fluids in small constraints ranging typically from 0.1 to 100 μm as well as their controlled handling and manipulation [92, 93]. The development of soft lithography methods allowed for the fabrication of micrometer scaled structures, neccesary for the microfluidic channel formation. The arrangement of such microchannels allows a guidance, mixing, separation or other manipulations of the fluids in an automated high-throughput manner [94]. The major advantages of down-scaling the size and volume of the fluids are a reduced amount of necessary reactants, faster processing times and a parallelization of processes. The ultimate goal is the integration of various lab processes into one single microfluidic device, so-called *lab-on-chip* technology [95].

However, since the physics of microfluidics happens on much smaller scales than our direct, daily experience, the behavior of fluids is different and has to be considered for designing devices and planning experiments on a micrometer scale. The next section covers the properties of fluids in these regimes.

1.4.1 Fluid Dynamics of Microfluidic Systems

Laminar flow vs. turbulent flow

The flow dynamics of viscous fluids under the influence of friction depends on their velocity and on their physical constraints. For low velocities, stream lines do not mix and the viscous forces are dominant. This flow regime is called **laminar flow**. For high velocities **turbulent flow** dominates, characterized by chaotic vortices and eddies. The methodology to differentiate between these flow regimes was first developed by G. Stokes 1851 [96], but popularized by O. Reynolds in 1883 [97]. Following the theory the Reynolds-Number Re is defined as:

$$\text{Re} = \frac{\text{inertial forces}}{\text{viscous forces}} = \frac{F_i}{F_v} \tag{1.2}$$

Applying dimension analysis leads to: $F_i = ma = (\rho L^3)(\frac{U}{t})$ and $F_v = \mu \frac{U}{L} A$. Thus, the Reynolds-Number can be written as:

$$\text{Re} = \frac{(\rho L^3)(\frac{U}{t})}{\mu \frac{U}{L} A} = \frac{\rho U L}{\mu} \tag{1.3}$$

where U is the mean velocity of the liquid, L the characteristic linear dimension, t the time, μ the dynamic viscosity and ρ the density of the fluid.

The Reynolds number is not an intrinsic property of the fluid, but a combination of fluid properties (density and dynamic viscosity) as well as geometric properties of the system and the flow velocity. The characteristic linear dimension depends on the geometry of the system. In case of flow in a pipe, equation 1.3 transfers to:

$$\text{Re} = \frac{\rho U D_H}{\mu} \tag{1.4}$$

with D_H being the hydraulic diameter. In case of a circular pipe, D_H equals the inner diameter of the pipe. For this geometric configuration, the transition between the two regimes occurs for Re ≈ 2400, however there is a wide transition range.

For many biological system on micrometer scale such as e.g. blood circulation, the flow takes place in laminar regime. The same is true for all microfluidic devices. As an example the Reynolds number is calculated for the flow of water (at 20°C) in a microfluidic device, assuming a circular pipe with a diameter of 30 μm and the corresponding cross section $A = \pi r^2 = 707 \mu m^2$ at a volumetric flow rate of $U_V = 500 \mu L/h$. This leads to a mean velocity of $U = U_V/A = \frac{500 \cdot 10^{-9} m^3}{3600 s}/(707 \mu m^2) = 0.20 m/s$. With $\rho = 1000 kg/m^3$ and $\mu = 1.002 mPas = 1.002 \cdot 10^{-3} kg/(ms)$ it follows:

$$\text{Re} = \frac{\rho U D_H}{\mu} = \frac{1000 kg/m^3 \cdot 0.20 m/s \cdot 30 \cdot 10^{-6} m}{1.002 \cdot 10^{-3} kg/(ms)} \approx 5.9 \tag{1.5}$$

The result indicates that in microfluidic devices water behaves as a viscous fluid. This means that the fluid flows in parallel layers (or laminae) without a lateral mixing. However, mixing due to diffusion between the layers does exist. But the time scale of diffusive mixing is much lower than that of turbulent mixing.

Flow profile

The Navier-Stokes equation for an incompressible fluid describes the relevant forces on a water parcel and is given by:

$$\frac{\partial \mathbf{u}}{\partial t} + (\mathbf{u} \cdot \nabla) \mathbf{u} - \frac{\mu}{\rho} \nabla^2 \mathbf{u} = -\nabla w + \mathbf{g} \tag{1.6}$$

The first term describes the temporal variation of the flow velocity $\mathbf{u}$, the second term the mean convection, the third term the friction, with μ: viscosity and ρ: density of the liquid, the forth term the internal force, whereas $\nabla w \equiv \nabla(p/\rho_0) = (1/\rho_0)\nabla p$, and the last term the external force.

In microfluidic devices the solution of the Navier-Stokes equation can be derived for a fully developed and stationary flow: $\partial u_z/\partial z = 0$ and $\partial \mathbf{u}/\partial t = 0$. In case of flow through a circular pipe, three-dimensional cylindrical coordinates can be applied. For this confinement no radial flows or swirls can occur, thus $u_r = u_\theta = 0$. Furthermore, the flow is axisymmetric. With these specifications equation 1.6 simplifies to:

$$\nabla w = \frac{\mu}{\rho} \nabla^2 \mathbf{u} \iff \frac{1}{r} \frac{\partial}{\partial r} \left(r \frac{\partial u_z}{\partial r} \right) = \frac{1}{\mu} \frac{\partial p}{\partial z} \tag{1.7}$$

In the circular pipe, boundary conditions require the velocity of the fluid at the inner pipe wall to be zero: $u_z = 0$ at $r = a$ with a: radius of the pipe. This leads to the following solution, also called Hagen-Poiseuille law:

$$u(r) = \frac{1}{4\mu} \left(a^2 - r^2 \right) \frac{\partial p}{\partial z} \tag{1.8}$$

The pressure gradient $\frac{\partial p}{\partial z}$ along the pipe is roughly constant for most microfluidic flows. The flow field describes a parabolic velocity profile along the flow direction. This means that the velocity is maximal in the middle of the pipe and decays to zero at the boarders, i.e. the walls of the pipe. In microfluidics it is common to use the volumetric flow rate Q:

$$Q = 2\pi \int_0^a u(r) r dr = \frac{\pi a^4}{8\mu} \frac{\partial p}{\partial z} \tag{1.9}$$

It is worth mentioning here that the volumetric flow rate and the pressure change is proportional to the fourth power of the radius, leading to an enormous increase in pressure

for small changes in the channel diameter at the same flow rates.

To conclude this section, microfluidic devices allow to scale down lab processes and to reduce the amount of reactants. However the parabolic velocity profile can lead to an axial dispersion of the reactants in the liquid (see Equation 1.8) and the laminar flow prohibits rapid mixing of fluids (see Equation 1.5), thus limiting the use of microfluidic devices for several lab-on-chip applications. To overcome these problems, microfluidic water-in-oil droplets have become popular.

1.4.2 Droplet-based Microfluidics

The concept to use water-in-oil droplets as compartments for chemical and biological applications dates back to 1954, when Lederberg encapsulated cells in individual water droplets [98]. However, the use of droplet compartments was limited due to the wide size distribution resulting from the production methods. Variances in size lead to variability in reaction conditions and concentrations and thus to an uncontrolled behavior.

The use of microfluidic devices to produce water-in-oil droplets allows to exploit the maximum potential of droplets as compartments. Microfluidic devices allow the controlled production of uniform, monodispers droplets (< 1% in diameter) at rates up to the MHz range [99, 100]. The possibility to manipulate and analyze the droplets in an automated way opens the door for many applications. It also allows to overcome the problems addressed in the last paragraph, since each droplet can be considered as an individual controllable reaction chamber and microfluidic channel designs enable processing steps like a fast mixing of the reagents (see Figure 1.12)) [101, 102]. Therefore it is no surprise, that droplet-based microfluidics has arrived in many disciplines such as biology, chemistry, material science, physics and other fields.

In this thesis the use of polymer-stabilized, microfluidic water-in-oil droplets as compartments for a bottom-up assembly of synthetic cells was investigated. The following section gives a background on the physics behind droplet formation and manipulation in microfluidic devices.

Generation of Droplets using Microfluidic Devices

The production of microfluidic droplets requires two immiscible phases: one phase being the carrier phase, often referred to **continuous phase** and another phase inside the droplets, so-called **dispersed phase**. In order to create water-in-oil droplets, oil is used as the continuous phase and mixed with a dispersed aqueous phase [103]. According to Equation 1.3 the micrometer-dimensions of microfluidic devices lead to laminar flows. Thus, in order to break the co-stream of the two immiscible phases and to form droplets, different geometries were designed to generate droplets. Most designs allow a passive production of droplets, where the flow field of the two phases deforms their interface, thus forming a droplet that eventually pinches off due to free surface instability [103]. Today the most commonly used designs are the T-junction (cross-flowing streams [104]) and the cross-junction (flow focusing [87]), depicted in Figure 1.11.
The formation process depends on an individual control of the flows of the two immiscible liquids. The flow can either be gas pressure driven, where the imposed pressure is controlled by a regulatory unit or driven by constant volumetric flow rates imposed by syringe pumps. A general physical model for the formation process of droplets is still subject to investigations and so far only partially understood [103]. This is mainly due to
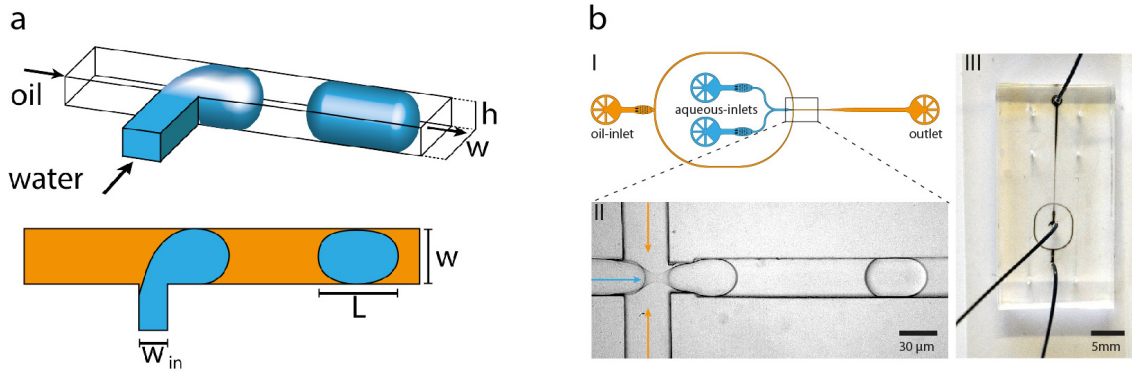
Figure 1.11 – a) shows the production of microfluidic water-in-oil droplets using a T-junction. Aqueous phase is shown in blue, the continuous oil phase in orange. b) shows a microfluidic production device, using flow-focusing geometry. A sketch of the whole device is shown in I, in which the oil channels are colored in orange and the aqueous channels in blue. The extract II shows the production unit, where the aqueous phase is ripped of by the crossing oil phase. Part III shows a photograph of the whole device. Adopted from [105].

the manifold geometric designs to produce droplets but also to different break up modes of the droplets. In total, five fundamental modes for droplet generation have been identified, as summarized by Zhu 2017 [103]. The three major modes are *squeezing mode*, with monodisperse droplets larger than the channel dimension, *dripping mode*, with monodisperse droplets smaller than the channel dimension and *jetting mode*, with polydisperse droplets.

The physical differentiation between these modes requires to identify the forces involved in the formation process. During droplet production, generally four forces are involved: inertial force (force due to the momentum of the liquid, $(\rho v)v$), viscous force, gravity and capillary force. In order to compare the influence of the forces, they can be unified in the form of stress, the force per unit area. A volume of fluid with the velocity u_s in a microfluidic device with the characteristic length L is then exposed to the following stresses: inertial stress $f_i \sim \rho u^2$, viscous stress $f_v \sim \eta u/L$, gravity stress $f_g \sim \rho g L$ and capillary pressure $f_\gamma \sim \gamma/L$, with ρ: density of the fluid, η: dynamic shear viscosity, g: gravitational acceleration, γ: interfacial tension.

From these considerations, dimensionless numbers can be defined to characterize the fluid. The Reynolds number Re can be used to define the laminar or turbulent regime and is given as the ratio of inertial and viscous force (see Section 1.4.1).

During the droplet formation process the interfacial tension plays the crucial roll. Therefore the ratio of f_γ to the other three forces is considered to be most important one for the description of droplet production. The capillary number Ca is defined as:

$$Ca = f_v/f_\gamma = \frac{\eta u}{\gamma} \tag{1.10}$$

The ratio of f_i to f_γ is defined as Weber number We:

$$We = f_i/f_\gamma = \frac{\rho u^2 L}{\gamma} \tag{1.11}$$

Finally, the Bond number Bo is:

$$Bo = f_g/f_\gamma = \frac{\rho g L}{\gamma} \tag{1.12}$$

In microfluidic devices, the length scale L is small, therefore both f_v and f_γ are enhanced, whereas f_i is not influenced by L and f_g is even reciprocally. Thus, the capillary number has the most impact in describing and characterizing droplet generation. These dimensionless numbers allow for a characterization of the droplet production modes, as described by Zhu 2017 [103]:

Squeezing $\qquad Ca < 10^{-2}$
Dripping $\quad 10^{-2} < Ca < 1$ and $We < 1$
Jetting $\qquad Ca + We > 1$

Therefore, mainly changes in the capillary number of the continuous or dispersed phase lead to transitions between the different modes and thus to modifications of the droplet size. As an example (see [106] and [104]), the droplet diameter D in dripping mode for a flow focusing device can be estimated by balancing the capillary pressure and the viscous stress:

$$\frac{\gamma}{D} = \frac{\eta u}{L} \iff \frac{D}{L} = \frac{\gamma}{\eta u} = Ca^{-1} \tag{1.13}$$

whereas in this case the characteristic length corresponds to the diameter of the nozzle. Therefore, in dripping mode with $Ca < O(1)$, the produced droplets are larger than the diameter of the nozzle but smaller than the diameter of the channel.

To conclude, the size of the droplets depends on the flow rates, the densities, the viscosity and the interfacial tension of the dispersed and the continuous phase as well as the microfluidic device geometry. The diameter of the droplets can be adapted to a range from 1 to 200 μm, corresponding to volumes from femtoliters to nanoliters. The lower limit is mainly defined by the current limitations in soft lithography methods, necessary to produce microfluidic devices.

1.4.3 Surfactants

So far, the introduced methods for microfluidic droplet production would lead to the fusion of droplets as soon as they come in contact with each other, driven by the aim to minimize the surface energy. Therefore, to prevent droplet coalescence, so-called **'surfactants'** are used to stabilize the droplets. The word 'surfactant' is the short form of 'surface active agent' and describes a class of amphiphilic molecules. These molecules consist mostly of two groups with attractions for different phases, such as water and oil in the case of microfluidic droplets. In this case surfactants have a hydrophilic part ('head') attached to one or two hydrophobic groups ('tail'). Due to these properties, the surfactants are driven towards the interface of the two immiscible phases, i.e. to the periphery of the droplets. When surfactants accumulate at the interface, the surface tension between the phases is decreased and thus the surface free energy is reduced, as given by the Gibbs adsorption isotherm for dilute solutions [86]:

$$\Gamma = -\frac{c}{RT}\frac{d\gamma}{dc} \tag{1.14}$$

With Γ: Surface concentration, T: temperature, R: gas constant and c: surfactant bulk concentration. Additionally, the interface becomes more rigid after the adsorption of

surfactants. Therefore, the addition of surfactants provides the energy to stabilize the droplets in a metastable state. The coalescence of droplets is then hindered by the steric repulsion of the surfactants.

In order to use microfluidic water-in-oil droplets as compartments for a bottom-up assembly of synthetic cells, the whole emulsification system, i.e. the combination of aqueous phase, oil phase and surfactants, must be bio-compatible. This means on the one hand that the droplets should form a stable and sealed container, where molecular exchange both between droplets and between the continuous phase is minimized. On the other hand, the water-oil-interface should be inert to the content inside the droplets, i.e. the attraction or adsorption of proteins to the interface should be hindered. In order to address the second point, a variety of different head groups have been tested. Most commonly, surfactants with a hydrophilic group composed of polyethylene glycol (PEG) are used [89]. PEG molecules form a passivation layer at the droplets' inner interface and therefore minimize unspecific interactions of proteins or other molecules. Additionally, the PEG groups can be chemically modified leading to anchoring points at the droplets inner periphery and a functionalization of the interface [90].

The hydrophobic tail can be adopted to the chemical composition of the surrounding oil. Many biological applications are performed in droplets surrounded by fluorinated oils. These types of oil show a good bio-compatibility and most organic compounds, i.e. the composition of biological structures, are insoluble in fluorinated oil. Therefore, surfactants with (per)fluorinated carbon chains are the preferred choice. Additionally it could be shown that fluoro-based surfactants are more efficient in stabilizing droplets compared to e.g. hydrocarbon based surfactants, even for the same chain length and the same head group. However, the stability of the droplets depends not only on the chemical composition of the surfactants, but also on the physical properties. In order to assess the stability, the hydrophilic-lipophilic balance (HLB) can be considered:

$$HLB = 20 \frac{H_W}{H_W + L_W} \tag{1.15}$$

where H_w and L_W are the molecular weights of the hydrophilic and the hydrophobic part, respectively. Therefore, HLB = 0 represents a pure hydrophobic and HLB = 20 a pure hydrophilic molecule. A HLB value between 1 and 10 for the surfactants allows for the stable production of water-in-oil droplets.
Furthermore, surfactants can be synthesized as Triblock- or Diblock copolymer surfactants, having two or one hydrophobic chains, respectively. All these properties can influence the stability of the droplets.

One crucial requirement for the compartments in a bottom-up synthetic cell approach is the ability to encapsulate and retain bio-molecules, buffers, ions etc. Therefore the first publication in this thesis comprised a thorough investigation of the retention ability of diverse molecules in microfluidic droplets, stabilized by different surfactant types and compositions.

1.4.4 Microfluidic Devices for Droplet Manipulation and Analysis

Microfluidic devices allow not only for the production of monodisperse droplets at high productions rates in the kHz range, but also their manipulation and analysis in multiple ways. The following section provides an overview of the most commonly used microfluidic methods and techniques used in this work.

One major advantage for the production of water-in-oil droplets using a microfluidic device is not only their uniform size but also their periodic flow within the channels. The single droplets are separated from each other by an equal oil spacing, thus allowing for automated operations on the droplets (see Figure 1.12, a).
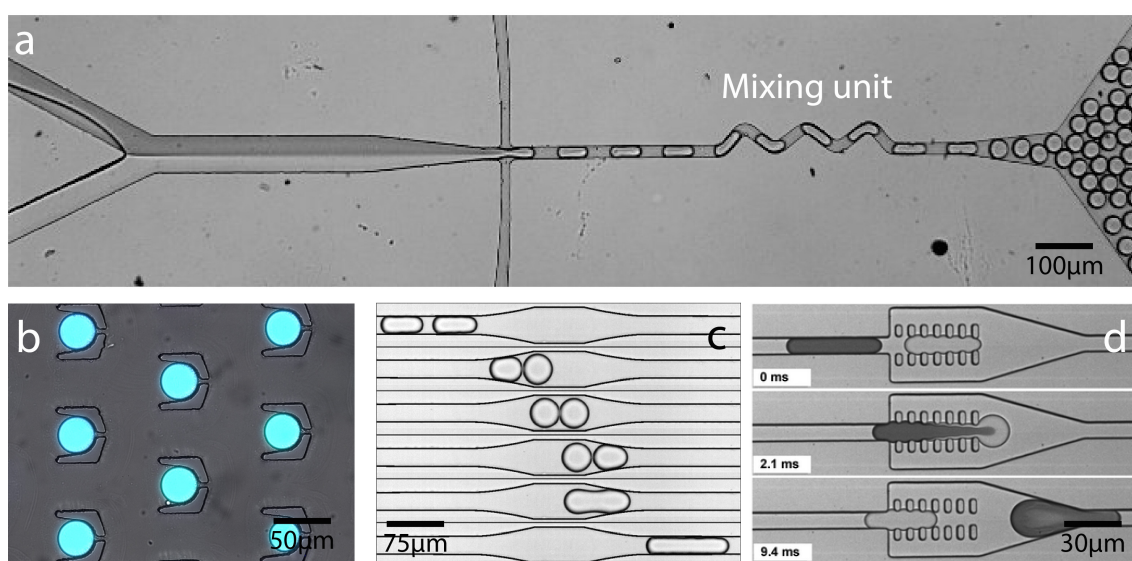

Figure 1.12 – a) In this device, droplets are produced with two aqueous-phase inlet channels. The upper phase is visualized by black inc. The highly-periodical flow of the droplets after production can be observed. The subsequent zigzag-mixing unit allows for a fast mixing of the droplet's content [107]. b) Combined fluorescence and brightfield image of a trapping structures for long term observation of microfluidic droplets [108]. Different approaches to merge droplets are shown in c) and d). The common principle is to slow down one droplet, thus enabling the subsequent droplet to come into close contact and to merge. Droplets can be decelerated by enlarged channels (c) or pillar structures (d).
Figure c) taken with Permission from [109], Figure d) taken with Permission from [110].

Mixing

Droplets flowing in a microfluidic device are often in contact with the channel walls and are therefore subject to friction boundary conditions. This induces a circular flow pattern inside the droplets, being symmetric identical to an axis parallel to the movement velocity of the droplet [101]. Therefore, the content in the two circulating halves of a flowing droplet is spatially separated. In many biological applications, two different aqueous phases e.g. with different chemical reactants are used and merged only shortly before the production of the dropelts. In order to mix them rapidly, special channel designs are necessary. One way to perform fast mixing is the use of zigzag structures [102, 107],

which break the symmetry of the flow profile inside the droplet and thus allow for a fast mixing of the reagents (see Figure 1.12 a).

Droplet Storage

For some applications time lapse visualization and analysis of the droplets' content has to be performed. Towards this end, microfluidic trapping or storage structure are necessary. One example for a droplet trapping structure is shown in Figure 1.12, b). The traps have a small opening, allowing the oil to pass through the structure when no droplets are trapped [108]. However, when the array is flushed with droplets, the trapping structures are filled with these droplets. A trapped droplet blocks the opening, therefore the resulting steam-lines of the continuous oil phase move around the trap so that no other droplets can enter. In this configuration, droplets can be stored for long-term observations and are available for analytically methods such as microscopic investigations.

Droplet Fusion/Merging

One main requirement for the performance of biological or chemical reactions inside water-in-oil droplets is the ability to add reactants to the system, i.e. to merge and mix different liquids. One possibility is the fusion of two individual droplets into one single droplet. The use of surfactants (see Section 1.4.3) actually hinders the fusion of droplets. However, for low surfactant concentrations, droplets fuse when they are in close contact to each other. In this case, droplet coalescence can be achieved using optimized channel geometry to slow down the droplets. In that case, the subsequent droplet can come into close contact with the leading droplet and finally merge. Several channel designs allow for the deceleration of droplets such as narrowed channels, which increase the fluid resistance [111], enlarged channels, where the continuous phase can flow around the droplet [109] (see Figure 1.12, c), pillar structures [110] (see Figure 1.12, d) or even pockets, where the droplet is physically entrapped by narrowing channel walls [112].

For higher surfactant concentrations coalescence of the droplets can be induced by electrical fields. In this case an inhomogeneous or homogeneous electrical field in the range of 1-100 kV/m is applied across two droplets being in close contact [113, 114]. The induced dipoles of the droplets align, thus creating an attractive Coulomb force between them, which can overcome the energy barrier of the steric repulsion of the surfactants (see 1.4.3) and finally lead to the fusion of the droplets.

The major limitations of the droplet fusion methods for the controlled addition of components are the necessary alternating alignment of droplets with different contents and their controlled combination. Furthermore the added volume equals almost the volume of the original droplet and cannot be adequately controlled. In order to overcome these limitations, the 'Pico-Injection' technology was developed.

Pico-Injection

The pico-injection technology allows for a sequential addition of reactants into the droplets in a controlled and automated fashion. The concept was first developed and demonstrated by Abate et al. [91]. Preformed droplets are reintroduced into a microfluidic device, separated by an orthogonal oil channel and thus aligned to an uniform, periodic and adjustable droplet - oil - pattern. The oil spacing between the droplets hinders the uncontrolled fusion of subsequent droplets. In a next step, droplets reach the injection unit, where a pressurized injection channel with a narrowing tip is attached orthogonal to
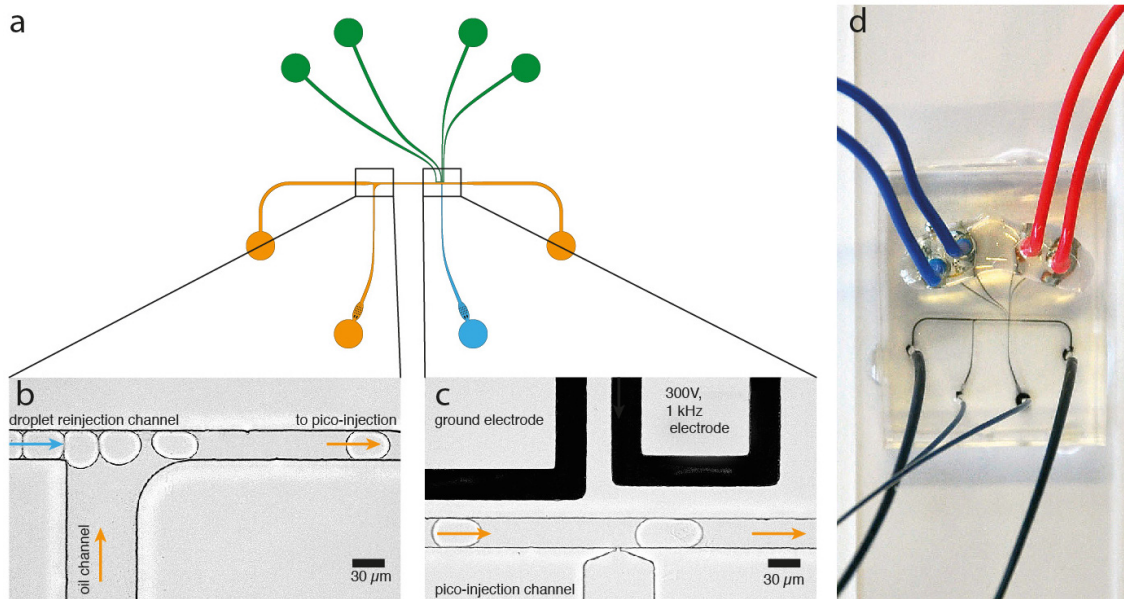
Figure 1.13 – This figure shows the microfluidic pico-injection unit. a) shows an overview of the device, where oil channels are indicated by an orange color, aqueous channels by a blue one and electrodes by a green one. b) shows the droplet separation unit, allowing to separate the reintroduced droplets to equivalent distances. In the injection unit c), microelectrodes apply an electrical field to the droplets, leading to electroporation of the surfactant layer. This allows for the injection of liquids through the attached injection channel. d) shows a photograph of the actual device. Adopted from [105]

the main channel. Since the connection between the injection channel and the main channel is only a small slit, a high pressure difference is created, which can be approximated by the Laplace pressure:

$$P_{in} - P_{out} = 2\gamma/r \tag{1.16}$$

With P_{in}: pressure of the injection fluid, P_{out}: pressure in the main flow channel, γ: surface tension of water and oil and r: radius of the curvature of the interface at the slit.

In this configuration nothing will be injected into the droplets, even for a high pressure on the injection channel. This is due to the surface tension of the remaining oil film between the interior of the droplets and the injection fluid and the small radius of the curvature. However, optimized micro-electrodes, usually attached to the opposing sides of the injection channel, are used to generate electrical fields, which rupture the surfactant layer at the water-oil-water interface (see Section 1.4.4 and Figure 1.13, c). This enables the injection fluid to stream into the droplet. After the droplet has passed the injection unit, surfactants reassemble and the droplet is sealed again. It is worth to emphasize that this is a fully automated technique operating at several hundreds of droplets per second, where only the pressures of the droplet-inlet channel, the spacing oil channel and the injection channel have to be adjusted to control the injected volume. Depending on the specific need, the injection volume can be adjusted from 0.1 pL to several tenth of pL.

Additionally, several injection units can be placed in a row, thus allowing for serial and combinatorial injections. In the latter case ground electrodes in between the injection

units shield the electrical field of the neighboring electrodes, thus enabling an independent combination of the injections.

The controllable injection of fluids, reactants, biomolecules or even cells into the droplets opens the door for many applications. The ability of pico-injection technology for a bottom-up synthetic cell approaches was a major investigation in this thesis.

1.5 Research Objectives of the Thesis

The major goal of my research was to progress and to further develop methods and technology for bottom-up synthetic cell approaches with the ultimate goal to investigate and better understand fundamental processes of life. More concrete, I aimed for the development of a model system with reduced complexity in order to experimentally study the formation and self-organization of microtubule networks as well as to create an synthetic ATP-generating module. Towards this end, I used microfluidic water-in-oil droplets as compartments, taking advantage of the highly-controllable and adjustable production methods as well as the variety of manipulation and analysis tools. The underlying methodological principles were introduced in Section 1.4. Since the results achieved in this context were published in several publications, the present thesis is written in cumulative form. The following section provides an overview of the results presented in the corresponding publications:

In a first step, the use of microfluidic water-in-oil droplets as compartments for biological applications was investigated. Towards this end, the stability of droplets for different surfactant types and concentrations was analyzed, as well as the ability of the droplets to encapsulate and retain selected fluorophores and bio-molecules. The results are crucial for the selection of proper and adjusted fluorescent dyes in order to label and to visualize bio-molecules in future synthetic cell applications and are represented in Publication 1:
Key Factors for Stable Retention of Fluorophores and Labeled Biomolecules in Droplet-Based Microfluidics [115].

In a second step, the use of microfluidic water-in-oil droplets as compartments for microtubule polymerization under confined and controlled conditions was investigated. Different strategies to initiate the polymerization of tubulin were compared and the resulting microtubule networks and arrangements were analyzed. These results are summarized in Appendix A. Based on these results, the influence of additional motor proteins on the microtubule self-organization in microfluidic droplets was investigated and the achieved results were published in Publication 2:
Spherical Network Contraction Forms Microtubule Asters in Confinement.

So far however, the investigation of microfluidic water-in-oil droplets as compartments for synthetic cell applications had one major drawback: The inability to mimic the cellular bio-membrane with regard to both the continuous oil phase, surrounding the droplets' aqueous interior as well as the polymeric surfactants at the interface between oil and aqueous phase. To overcome this problem, a fundamental new approach was investigated.
The basic idea behind the newly-developed system was to use the microfluidic droplets only as stabilizing compartments and to set up the synthetic cell inside the droplets, including a lipid bilayer and thus a bio-membrane. Towards this goal, different possibilities to form an enclosed lipid bilayer system at the inner periphery inside water-in-oil droplets were investigated. It turned out, that the encapsulation of vesicles under specific ionic conditions enabled the formation of the desired structures, which were termed: *droplet-stabilized Giant Unilamellar Vesicles* (dsGUVs). A thorough and comprehensive analysis of the system allowed for an understanding of the formation process and the conclusion, that the structure is indeed an enclosed, unilamellar lipid bilayer showing full mobility of the lipids and incorporated transmembrane proteins (see also Appendix A.2). Furthermore it was demonstrated, that the lipids are fully available for functionalization and that microfluidic tools such as pico-injection technology in particular can be

applied to the system.

In order to demonstrate the capabilities of the developed system to serve as a compartment for synthetic cell applications, microtubule polymerization was performed inside dsGUVs. It was shown, that the interactions of tubulin with the surfactant layer were reduced in the presence of a shielding lipid bilayer. Furthermore, the functional reconstitution of the transmembrane protein ATPase into the dsGUVs was achieved, allowing for the creation of a minimal, ATP-generating system. Finally, to exploit the maximum potential of the newly developed system, different approaches were investigated to release the assembled synthetic cells from the stabilizing droplet shell into a continuous aqueous phase and thus into a physiologically relevant environment (see Appendix A.3). One approach included the design and the construction of a novel microfluidic device, allowing to include the release process into future lab-on-chip applications. These findings are represented in Publication 3:

Sequential Bottom-up Assembly of Mechanically Stabilized Synthetic Cells by Microfluidics [116].

The analysis of the formation process of the dsGUV system included the use of an optical microscope setup with a defined, confocal fluorescent detection-volume. This procedure enabled the detection of fluorescently labeled lipids, which were encapsulated into microfluidic droplets. Due to the fast (MHz) sampling rates of the setup, the lipid-bilayer formation process could be analyzed for flowing droplets in a microfluidic device (see Appendix A.4). Based on these results, the idea arose to analyze periodically passing droplets by Fluorescence Correlation Spectroscopy (FCS), allowing to correlate the content of thousands of microfluidic droplets. The developed method represents a suitable tool to monitor the flow of microfluidic droplets and thus to analyze and control the production of of several thousand droplet-based synthetic cells per second. These findings were published in Publication 4:

Reconceptualizing fluorescence correlation spectroscopy for monitoring and analyzing periodically passing objects [117].

CHAPTER 2

Publications

General information on publications

This thesis is written in cumulative form, i.e in the form of a series of publications. Following the requirements of the Faculty for Physics and Astronomy of the Heidelberg University, I am the principle author of two of the submitted publications (Publication 1 and Publication 3), as confirmed by all participating authors and the co-author of two additional publications (Publication 2 and Publication 4). All four publications are contributions in international, peer-reviewed journals and are published online (Publication 1, Publication 3 and Publication 4) or accepted (Publication 2) to the date of submission of this thesis. The publications have not been used in other dissertations. Permissions to reprint the publications are given in Appendix B. The author contributions to the respective publications are given on the following page.

Publication 1:
'Key Factors for Stable Retention of Fluorophores and Labeled Biomolecules in Droplet-Based Microfluidics'
Jan-Willi Janiesch, Marian Weiss, Gerri Kannenberg, Jonathon Hannabuss, Thomas Surrey, Ilia Platzman, and Joachim P. Spatz
Analytical Chemistry 2015 87 (4), 2063-2067
DOI: 10.1021/ac504736e
Reprinted with Permission from [115]. Copyright 2015 American Chemical Society.

Publication 2:
'Spherical Network Contraction Forms Microtubule Asters in Confinement'
Michael Juniper, Marian Weiss, Ilia Platzman, Joachim P. Spatz, and Thomas Surrey
Accepted for publication, 26th of October 2017.
Reproduced with permission from the Royal Society of Chemistry.

Publication 3:
'Sequential Bottom-up Assembly of Mechanically Stabilized Synthetic Cells by Microfluidics'
Marian Weiss, Johannes Patrick Frohnmayer, Lucia Theresa Benk, Barbara Haller, Jan-Willi Janiesch, Thomas Heitkamp, Michael Börsch, Rafael B. Lira, Rumiana Dimova, Reinhard Lipowsky, Eberhard Bodenschatz, Jean-Christophe Baret, Tanja Vidakovic-Koch, Kai Sundmacher, Ilia Platzman, and Joachim P. Spatz
Nature Materials, Published online: 16 October 2017
doi:10.1038/nmat5005
Reprinted with Permission from [116].

Publication 4:
'Reconceptualizing Fluorescence Correlation Spectroscopy for Monitoring and Analyzing Periodically Passing Objects'
Eli Zamir, Christoph Frey, Marian Weiss, Silvia Antona, Johannes P. Frohnmayer, Jan-Willi Janiesch, Ilia Platzman, and Joachim P. Spatz
Analytical Chemistry Article ASAP
DOI: 10.1021/acs.analchem.7b03108
Reprinted with Permission from [117]. Copyright 2017 American Chemical Society.

Author contributions to the respective publications

Publication 1:

Key Factors for Stable Retention of Fluorophores and Labeled Biomolecules in Droplet-Based Microfluidics

The idea behind the retention analysis of different fluorophores originated from observations made by Jan-Willi Janiesch. In close cooperation with him, I performed and analyzed the droplet stability experiments as well as the retention experiments. I developed the analysis method for the categorization of the fluorophore retention and performed the droplet stability analysis. I identified and applied the method to estimate the hydrophilicity of the fluorophores by calculating the LogD value. Furthermore I performed the experiments with fluorescently labeled tubulin and antibodies and wrote the manuscript. Synthesis and analysis (FTIR measurements and interfacial tension measurements) of the different surfactants were performed by Jan-Willi Janiesch and Gerri Kannenberg. Labeled tubulin was provided by Jonathon Hannabuss and Thomas Surrey. Ilia Platzman and Joachim P. Spatz designed, supervised and managed the experiments and wrote the manuscript.

Publication 2:

Spherical Network Contraction Forms Microtubule Asters in Confinement

The investigation of microtubule self-organization in microfluidic droplets was performed in cooperation with Thomas Surrey and Michael Juniper. In this context, I performed preliminary experiments, demonstrating a successful polymerization of tubulin inside microfluidic droplets as summarized in Appendix A.1. These results paved the road towards the results achieved by Michael Juniper in Publication 2. For this publication I produced the microfluidic droplet production device, installed and assisted with the droplet-based microfluidics, evaluated the droplet size distribution and wrote parts of the manuscript. Michael Juniper performed and analyzed the tubulin polymerization experiments, Thomas Surrey designed the study and wrote the manuscript. Ilia Platzman and Joachim P. Spatz assisted with the polymer stabilized droplet microfluidics and designed, supervised and managed the experiments.

Publication 3:

Sequential Bottom-up Assembly of Mechanically Stabilized Synthetic Cells by Microfluidics

In this publication, I realized experimentally the general concept of dsGUVs by microfluidic technology and identified and analyzed the mechanism of the dsGUV formation process. In close cooperation with Johannes Frohnmayer, I developed and performed analysis strategies for dsGUV characterization - this includes FRAP measurements, intensity analysis and the establishment of pico-injection technology and its application

towards a sequential loading of dsGUVs. Furthermore, I wrote the manuscript, investigated phase-separated dsGUVs (see Appendix A.2), assessed the functionality of dsGUVs by his-tagged GFP, performed the assembly of microtubules inside dsGUVs and performed the reconstitution of ATPsynthase inside dsGUVs. For the latter, I developed different strategies to create and monitor a pH gradient to drive the synthesis of ATP and developed and demonstrated different strategies to measure the produced ATP. Additionally, I demonstrated the successful bulk release approach (see also Appendix A.3) and designed and tested the microfluidic release device. For the latter, the application to release GUVs from dsGUV was performed by Johannes Frohnmayer. He also reconstituted functional integrin in liposomes and dsGUV and performed the release of integrin-containing GUVs into a water phase. Lucia Benk optimized the release of GUVs from oil to water phase, in particular the release of integrin functionalized GUVs, performed adhesion experiments of integrin functionalized GUVs to different matrices, and wrote parts of the manuscript. Barbara Haller performed the experiments of dsGUVs with F-actin and its release from oil to water phase and performed Raman spectroscopy analysis. Jan-Willi Janiesch performed the experiments of dsGUVs with F-actin and synthesized polymer-based surfactants. Thomas Heitkamp and Michael Börsch prepared the labeled FoF1-ATP synthase. Rafael B. Lira, Rumiana Dimova and Reinhard Lipowsky discussed lipid bilayer formation using droplets. Eberhard Bodenschatz and Jean-Christophe Baret helped install the pico-injection technology. Tanja Vidakovic-Koch and Kai Sundmacher supported the reconstitution of FoF1-ATP synthase. Ilia Platzman designed and supervised the experiments, and wrote the manuscript. Joachim P. Spatz invented the concept of synthetic cell formation by sequential bottom-up assembly in droplet-stabilized compartments, designed, supervised and managed the experiments, and wrote the manuscript.

Publication 4:

Reconceptualizing Fluorescence Correlation Spectroscopy for Monitoring and Analyzing Periodically Passing Objects

Based on the results achieved in Appendix A.4 and together with Eli Zamir, I developed the general concept of applying FCS to droplet-based microfluidic and performed first experiments with fluorescently labeled droplets. Furthermore, I measured the autofluorescence of the carrier oil phase and wrote parts of the manuscript. Christoph Frey performed other droplet-based experiments and measured the droplet production rate with a high-speed camera. Eli Zamir analyzed and interpreted the data, performed the simulations and wrote the manuscript. Silvia Antona performed the experiments with encapsulated cells. Johannes P. Frohnmayer designed the microfluidic production device. Jan-Willi Janiesch synthesized the surfactants. Ilia Platzman and Joachim P. Spatz designed, supervised and managed the experiments and wrote the manuscript.

Publication 1

2.1 Key Factors for Stable Retention of Fluorophores and Labeled Biomolecules in Droplet-Based Microfluidics

Janiesch, J.-W., Weiss, M., Kannenberg, G., Hannabuss, J.,
Surrey, T., Platzman, I., and Spatz, J.P.

Key Factors for Stable Retention of Fluorophores and Labeled Biomolecules in Droplet-Based Microfluidics

Jan-Willi Janiesch,[§,||,‡] Marian Weiss,[§,||,‡] Gerri Kannenberg,[§,||] Jonathon Hannabuss,[¶] Thomas Surrey,[¶] Ilia Platzman,*[,§,||] and Joachim P. Spatz*[,§,||]

[§]Department of New Materials and Biosystems, Max Planck Institute for Intelligent Systems, Heisenbergstr. 3, 70569 Stuttgart, Germany

[||]Department of Biophysical Chemistry, University of Heidelberg, 69120 Heidelberg, Germany

[¶]London Research Institute, Cancer Research U.K., 44 Lincoln's Inn Fields, London WC2A 3LY, United Kingdom

Ⓢ *Supporting Information*

ABSTRACT: Water-in-oil emulsion droplets created in droplet-based microfluidic devices have been tested and used recently as well-defined picoliter-sized 3D compartments for various biochemical and biomedical applications. In many of these applications, fluorescence measurements are applied to reveal the protein content, spatial distribution, and dynamics in the droplets. However, emulsion droplets do not always provide entirely sealed compartments, and partitioning of dyes or labeled molecules to the oil phase is frequently observed. Therefore, stable molecular retention in the droplets represents a challenge, and many physical and chemical key factors of microfluidic system components have to be considered. In this study, we investigated the retention of 12 commonly used water-soluble dyes in droplets having six different aqueous phase conditions. We demonstrate that the physicochemical properties of the dyes have a major influence on the retention level. In particular, hydrophilicity has a strong influence on retention, with highly hydrophilic dyes (LogD < −7) showing stable, buffer/medium independent retention. In the case of less hydrophilic dyes, we showed that retention can be improved by adjusting the surfactants physical properties, such as geometry, length, and concentration. Furthermore, we analyzed the retention stability of labeled biomolecules such as antibodies, streptavidin, and tubulin proteins and showed that stable retention can be strongly dependent on dye and surfactants selection.
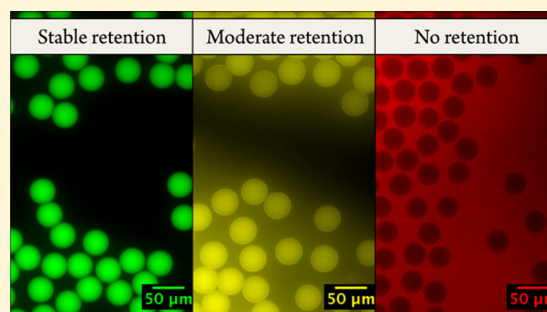
Over the past decade, water-in-oil emulsion droplets created in droplet-based microfluidic devices have become widely used as a screening tool for biological and chemical applications.[1,2] Using flexibly designed microfluidic devices, the formation speed and diameter size of monodisperse droplets can be controlled during their creation: the first may be varied from a slow drip to over 1 MHz,[3] and the latter is variable upward of 2 μm (diameter difference <1%).[4] The soft and dynamic nature of these biocompatible droplets, their ultrafast generation, and the well-controlled environment add up to a system that combines the necessary functions of microcompartments for various biochemical and biomedical applications, including high-throughput cellular investigations,[5−8] polymerase chain reaction-assays (PCR),[9−11] and *in vitro* protein expression analyses.[12−14]

In most of these applications, fluorescence measurements are applied to reveal the content of droplets and to gauge success and efficiency. For example, fluorescently labeled proteins were used to characterize their localization within the droplets for amyloidosis investigation,[15] protein crystallization,[16] and immunological[5] and digital PCR applications.[17] Moreover, a high-throughput fluorescence-activated droplet sorting technol-

ogy was developed to monitor and sort droplets according to their fluorescence signal.[18]

Emulsion droplets do not always provide entirely sealed microcompartments, and the release of dyes or fluorescently labeled proteins is observed.[19] Diffusion-driven[20,21] and micellar-induced[22,23] mechanisms have been proposed to describe the molecular transport to the oil phase. To minimize the transport due to diffusion and to reduce the solubility of biomolecules and fluorophores in the oil phase to a minimum, fluorinated oil became the most prominent choice in droplet-based microfluidics.[24] However, the proper conditions for reduction of the micellar-induced transport are not as clear as in the case of diffusion. Molecular retention depends strongly on the surfactant's concentration: lower surfactant concentration reduces the creation of reverse micelles but also affects droplet stability. An addition of biomolecules leading to the formation of a passivation (protection) layer at the inner periphery of the droplets can improve molecular retention.[25] However, it will

prevent the interactions between biomolecules, the biomolecules, and the droplet periphery, as required in certain studies. Therefore, surfactant concentration and its type as well as the aqueous phase conditions have to be chosen carefully in order to avoid molecular partitioning into the oil phase.

Here, we describe a detailed study of the retention of 12 water-soluble dyes, which are extensively used in biochemical and biomedical droplet-based microfluidic applications. We also describe the influence of concentration, geometry, and molecular weight of commonly used fluorinated surfactants on the molecular stability within the droplets. Moreover, the influence of the four most commonly used buffers and of two cell culture media is presented. We demonstrate that with the right choice of fluorophores and optimized surfactant physicochemical properties the partitioning to the oil phase can be minimized or avoided. Additionally, we analyzed the encapsulation stability of labeled biomolecules such as antibodies, streptavidin, and tubulin proteins and showed that stable encapsulation can be strongly dependent on dye and surfactant selection. These findings are important and can help one choose the appropriate key factors for the stable retention of fluorescently labeled biomolecules in the droplets.

Synthesis of PFPE−PEG−PFPE (5600g/mol, (TRI2500)), PFPE−PEG−PFPE (15400g/mol, (TRI7000)), PFPE−PEG (7750g/mol, (DI7000)), and PFPE−PEG−gold (DI-Au) surfactants followed the procedure reported earlier[5] (see Supporting Information, Section 1). Fourier transform infrared (FT-IR) spectroscopy was used to confirm the success of the surfactant synthesis and to assess the purity of the product (see Supporting Information, Section 1.1). Following synthesis, the surfactants were dissolved in fluorinated oil (FC-40, Acros Organics, Germany) at different concentrations, ranging from 0.5 to 50 mM. Interfacial tension measurements between the aqueous and the oil phase were performed to obtain the CMC values of 0.01 and 0.05 mM for TRI2500 and TRI7000 surfactants, respectively (see Supporting Information, Section 1.4). Twelve different dyes were dissolved in two culture media (DMEM and RPMI 1604) and four different buffers (PBS, PIPES, HEPES, and TRIS) at a concentration of 5 μM and used as aqueous phase to create droplets in a microfluidic device (see Supporting Information, Section 2). Hydrophilicity of fluorophores with a hydrolyzed active group was analyzed using the calculated distribution coefficient, LogD, which is a measure of the expected ratio of the sum of concentrations of all forms of the fluorophore (ionized plus unionized) in water and in a nonpolar solvent (octanol) (see Supporting Information, Section 2). Negative LogD values correspond to hydrophilic fluorophores and positive values to hydrophobic ones. A droplet-based microfluidic device made of PDMS was used to create the droplets, and an analysis chamber was used to monitor the droplets content (see Supporting Information, Section 3). Time-lapse analysis of the droplets content was performed using brightfield and fluorescence microscopy (see Supporting Information, Section 4). Fluorescence intensities I_0, I_{t0}, and I_{t24} correspond to the emission values obtained in an aqueous phase inside the microfluidic channels (fluorophore solution prior to droplets creation), 1 min and 24 h after droplets insertion into the analysis chamber, respectively. Retention of fluorophores was categorized according to
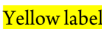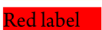
$I_0 \approx I_{t0} \approx I_{t24}$ → Stable retention   Green label

$I_0 \approx I_{t0} > I_{t24}$ → Moderate retention   Yellow label

$I_0 \gg I_{t0}$ → No retention   Red label

Figure 1 shows a retention summary of 12 fluorophores in the droplets produced with TRI2500 (10 mM) surfactants. Note: Similar results were observed with and without addition of 3 μM gold-linked surfactants. These gold-linked surfactants were used in our previous studies to provide anchoring points for bioactive molecules in biomedical applications.[5,26,27]

Figure 1. Fluorophores retention in the droplets (diameter (D) = 40 μm) having different buffer/medium conditions. TRI2500 (10 mM) surfactants were used to generate droplets for this experiment.

As expected, stable retention in all buffers and media was observed with highly hydrophilic (LogD < −7) Alexa 488, Alexa 647, and ATTO 488 dyes. However, less hydrophilic fluorophores with distribution coefficients of around −4 presented buffer/medium-dependent retention. In the case of Alexa 532 and ATTO 532 fluorophores, high pH values reduced the protonation state of secondary amines and, therefore, moderate retention was observed. In the case of hydrophobic dyes (LogD > 0), no retention was observed with the exception of RPMI medium, where moderate retention was detected. Surprisingly, stable retention was not observed in any of the slightly hydrophilic dyes (−1 < LogD < 0). Furthermore, no retention was observed with ATTO 495 dye (LogD = −0.81). This behavior can be attributed to the relatively small molecular weight and planar structure of the ATTO 495 dye and, therefore, to a small energetic barrier to be transported through the surfactant layer.[28] In the case of ATTO 565 and 655 dyes, moderate retention was observed only in 50% of the buffer/medium choices. In an attempt to improve retention, we investigated the influence of the physical properties of the surfactants (i.e., molecular weight and geometry) on the stability of the fluorophores within the droplets.

Figure 2 shows a retention summary of the 12 fluorophores in the droplets produced with TRI2500, TRI7000, and DI7000 (10 mM) surfactants. Detailed analysis revealed that DI7000 is the best among the tested surfactants for stable fluorophore encapsulation. However, emulsions formed with this surfactant consisted of droplets that were highly polydisperse in size. Stable retention in the droplets produced with surfactants having diblock geometry can be attributed to the denser PEG brush layer due to a reduced steric effect as in comparison to triblock geometry. However, for emulsion stability, it is desirable to have a dense PFPE layer on the outside droplet interface. The most efficient layer against coalescence can be provided by surfactants that contain two PFPE-tails (i.e., triblock geometry).[29] Since droplet-based microfluidic applications require monodisperse droplets, further experiments were performed with TRI2500 and TRI7000 surfactants. As shown in Figure 2, improved retention for some of the fluorophores was achieved in the droplets produced with longer surfactants.

This observation is straightforward since dyes have to pass a higher energetic barrier due to a thicker surfactant layer.[28]

Figure 2 table — Fluorophore [LogD] (columns): Alexa 488 M [-9.47], Alexa 532 M [-4.43], Alexa 647 M [-7.75], ATTO 488 SE [-7.60], ATTO 495 SE [-0.81], ATTO 520 SE [+0.59], ATTO 532 SE [-4.49], ATTO 565 SE [-0.18], ATTO 590 SE [+1.56], ATTO 633 SE [n.a.], ATTO 647N SE [+4.47], ATTO 655 SE [-0.61].

Surfactant (rows): TRIS [7.7]: TRI 2500, TRI 7000, DI 7000; PIPES [6.8]: TRI 2500, TRI 7000, DI 7000; RPMI [7.9]: TRI 2500, TRI 7000, DI 7000.

Figure 2. Fluorophores retention in the droplets ($D = 40\ \mu m$) as a function of buffer/medium selection and surfactant physical properties. The droplets were generated using three different surfactants (TRI2500, TRI7000, and DI7000 (10 mM)).

To further optimize the retention of fluorophores within the droplets, we investigated the optimal range of surfactant concentrations required for stable monodisperse droplets creation. The measurements were performed immediately after droplet formation using a high-speed camera (see Supporting Information, Section 5).

In agreement with previous studies,[30] surfactant concentrations below 1 mM result in the droplets coalescence immediately after creation. On the other hand, high surfactant concentrations ($C > 10$ mM) lead to creation of small droplets ($D < 5\ \mu m$), which can be easily observed with optical microscopy during the droplets creation (see Supporting Information, Section 5) and during the flow in microchannels where droplets experience high shear rates. On the basis of these results and considering that molecular retention is dependent on surfactants concentration, we investigated the retention of the fluorophores in the droplets produced with 2.5 and 10 mM surfactants concentration in the oil phase. It is worth mentioning here that the diameter size of monodisperse droplets ($150 > D > 25\ \mu m$) and their formation speeds ($30 > f > 0.5$ kHz) have no effect on fluorophores retention (see Supporting Information, Section 6).

Figure 3 shows the retention summary of 12 fluorophores encapsulated in droplets made of 2.5 and 10 mM TRI7000 and TRI2500 surfactants. In both cases, lower surfactant concentration leads to improved fluorophores retention. However, this effect was pronounced mainly in TRIS buffer and RPMI medium. The decrease of free surfactants in the oil phase reduces the formation of carriers for the solubilized fluorophores such as reverse micelles and small droplets. This behavior is in agreement with previous observations in which a decrease of the fluorescence intensity of fluorescein inside the droplets was measured due to increased surfactant concentration.[25]

We showed that the retention of most of the dyes can be controlled efficiently by proper selection of the surfactant's physical properties such as concentration, geometry, and molecular weight. However, it is also important to show if the fluorophore and surfactant selection will influence the retention of labeled biomolecules within the droplets. Toward this end, we investigated the influence of fluorophores and surfactants on the retention of highly hydrophilic biomolecules

Figure 3 table — Buffer: TRIS, PIPES, RPMI. Surfactant: TRI 2500, TRI 7000 (under each buffer). Surf.Conc. [mM]: 2.5, 10 (for each surfactant). Fluorophore (rows): Alexa 488, Alexa 532, Alexa 647, ATTO 488, ATTO 495, ATTO 520, ATTO 532, ATTO 565, ATTO 590, ATTO 633, ATTO 647N, ATTO 655.

Figure 3. Fluorophores retention in the droplets ($D = 40\ \mu m$) as a function of surfactant length and concentration. Fluorophores were dissolved in TRIS, PIPES buffers, and RPMI medium. The oil phase contained 2.5 or 10 mM of triblock surfactants.

such as antibodies and streptavidin and compared it to less hydrophilic biomolecules such as tubulin.

For the retention experiments, TRIS buffer was used to dissolve labeled streptavidin proteins and antibodies (see Supporting Information, Section 2) to a final concentration of 0.2 μM. In the case of labeled tubulin, we used the PIPES buffer (the most common buffer used for tubulin experiments) for microtubule creation (1 μM) in a bulk condition and used it as aqueous phase to create droplets (see Supporting Information, Section 2.4).

Microtubule retention was found to be strongly dependent on the hydrophilicity of the selected dye and on the surfactant physical properties. Stable retention of ATTO 633-labeled microtubules was observed in the droplets created with TRI7000 surfactants. In the case of droplets made of TRI2500 surfactants, the release of ATTO 633-labeled microtubules into the oil phase was observed immediately after the droplets creation (see Supporting Information, Video S7 (ac504736e_si_008.avi)), whereas stable retention was observed with microtubules labeled with highly hydrophilic ATTO 488 (Figure 4). In contrast to experiments with labeled

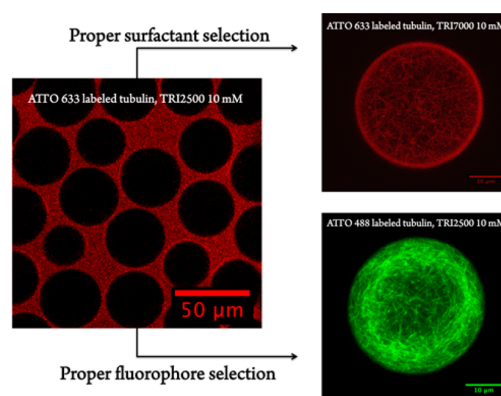**Figure 4.** Retention of labeled microtubules in the droplets strongly depends on the degree of hydrophilicity of the dye and surfactant selection. ATTO 633- and ATTO 488-labeled microtubules were polymerized in PIPES buffer and used as an aqueous phase for droplets creation. The oil phase contained 10 mM TRI7000 and TRI2500 surfactants. Note: Similar results were observed with and without addition of gold-linked surfactants.

microtubules, independent of the hydrophilicity of the dye and surfactant selection, stable retention for a period of 14 days was observed for all differently labeled antibodies and streptavidin proteins.

High hydrophilicity of antibodies and of streptavidin proteins is a major reason for their dye independent stable retention within the droplets. Even the most hydrophobic ATTO 647N dye (LogD = +4.47), which showed no retention in the droplets in a pure state, had no influence on the retention of sheep antimouse antibodies or streptavidin. In contrast to antibodies, tubulin is a less hydrophilic biomolecule and has even been considered as an "amphipotential" protein, i.e., a protein that can exist in both aqueous and lipid phases (like membrane proteins). This was concluded from a significant fraction of tubulin (up to 8%) having distributed into the detergent rich phase in some experiments.[31] Therefore, in the case of tubulin or other less hydrophilic proteins, the proper dye for labeling has to be selected very carefully.

CONCLUSION

In many biochemical and biomedical droplet-based microfluidic applications, stable retention of fluorophores and labeled biomolecules is pivotal for their successful implementation. In this letter, we describe the physical and chemical key factors of fluorescent dyes, surfactants, and buffer conditions that have to be considered for improved retention of labeled molecules and fluorophores within the emulsion droplets. For the retention investigation, we dissolved 12 commercially available ATTO and Alexa dyes in four different buffers (TRIS, HEPES, PIPES, and PBS) and two cell-culture mediums (RPMI and DMEM) and used them as an aqueous phase for droplet creation. We showed that retention is strongly dependent on the physicochemical properties of the dyes. In particular, the hydrophilicity level of the dye has been found to be a key factor influencing the retention within the droplets. We demonstrated that highly hydrophilic dyes (i.e., LogD < −7) showed stable retention within the droplets, independent of buffer/medium type. In the case of less hydrophilic dyes, we showed that stable retention can be achieved by optimization of the surfactant physical properties, such as geometry, molecular weight, and concentration. Furthermore, we analyzed the encapsulation stability of labeled biomolecules such as antibodies, streptavidin, and microtubules. In the case of "amphipotential" proteins, such as tubulin, we showed that stable encapsulation can be strongly dependent on dye and surfactant selection.

ASSOCIATED CONTENT

⊙ Supporting Information

Additional information as noted in text. This material is available free of charge via the Internet at http://pubs.acs.org

AUTHOR INFORMATION

Corresponding Authors

*E-mail: plazman@is.mpg.de.
*E-mail: spatz@is.mpg.de.

Author Contributions

‡J.-W.J. and M.W. contributed equally to the work.

Notes

The authors declare no competing financial interest.

REFERENCES

(1) Whitesides, G. M. *Lab Chip* **2012**, *13*, 11.
(2) Lagus, T. P.; Edd, J. F. *J. Phys. D: Appl. Phys.* **2013**, *46*, 114005.
(3) Shim, J. U.; Ranasinghe, R. T.; Smith, C. A.; Ibrahim, S. M.; Hollfelder, F.; Huck, W. T. S.; Klenerman, D.; Abell, C. *ACS Nano* **2013**, *7*, 5955.
(4) Thorsen, T.; Roberts, R. W.; Arnold, F. H.; Quake, S. R. *Phys. Rev. Lett.* **2001**, *86*, 4163.
(5) Platzman, I.; Janiesch, J.-W.; Spatz, J. P. *J. Am. Chem. Soc.* **2013**, *135*, 3339.
(6) Huebner, A.; Srisa-Art, M.; Holt, D.; Abell, C.; Hollfelder, F.; deMello, A. J.; Edel, J. B. *Chem. Commun.* **2007**, 1218.
(7) Shim, J. U.; Olguin, L. F.; Whyte, G.; Scott, D.; Babtie, A.; Abell, C.; Huck, W. T. S.; Hollfelder, F. *J. Am. Chem. Soc.* **2009**, *131*, 15251.
(8) Hofmann, T. W.; Anselmann, S. H.; Janiesch, J. W.; Rademacher, A.; Bohm, C. H. J. *Lab Chip* **2012**, *12*, 916.
(9) Williams, R.; Peisajovich, S. G.; Miller, O. J.; Magdassi, S.; Tawfik, D. S.; Griffiths, A. D. *Nat. Methods* **2006**, *3*, 545.
(10) Tewhey, R.; Warner, J. B.; Nakano, M.; Libby, B.; Medkova, M.; David, P. H.; Kotsopoulos, S. K.; Samuels, M. L.; Hutchison, J. B.; Larson, J. W.; Topol, E. J.; Weiner, M. P.; Harismendy, O.; Olson, J.; Link, D. R.; Frazer, K. A. *Nat. Biotechnol.* **2009**, *27*, 1025.
(11) Kiss, M. M.; Ortoleva-Donnelly, L.; Beer, N. R.; Warner, J.; Bailey, C. G.; Colston, B. W.; Rothberg, J. M.; Link, D. R.; Leamon, J. H. *Anal. Chem.* **2008**, *80*, 8975.
(12) Mazutis, L.; Baret, J. C.; Griffiths, A. D. *Lab Chip* **2009**, *9*, 2665.
(13) Courtois, F.; Olguin, L. F.; Whyte, G.; Bratton, D.; Huck, W. T.; Abell, C.; Hollfelder, F. *ChemBioChem* **2008**, *9*, 439.
(14) Dittrich, P. S.; Jahnz, M.; Schwille, P. *ChemBioChem* **2005**, *6*, 811.
(15) Meier, M.; Kennedy-Darling, J.; Choi, S. H.; Norstrom, E. M.; Sisodia, S. S.; Ismagilov, R. F. *Angew. Chem., Int. Ed.* **2009**, *48*, 1487.
(16) Kreutz, J. E.; Li, L.; Roach, L. S.; Hatakeyama, T.; Ismagilov, R. F. *J. Am. Chem. Soc.* **2009**, *131*, 6042.
(17) Pekin, D.; Skhiri, Y.; Baret, J. C.; Le Corre, D.; Mazutis, L.; Salem, C. B.; Millot, F.; El Harrak, A.; Hutchison, J. B.; Larson, J. W.; Link, D. R.; Laurent-Puig, P.; Griffiths, A. D.; Taly, V. *Lab Chip* **2011**, *11*, 2156.
(18) Baret, J. C.; Miller, O. J.; Taly, V.; Ryckelynck, M.; El-Harrak, A.; Frenz, L.; Rick, C.; Samuels, M. L.; Hutchison, J. B.; Agresti, J. J.; Link, D. R.; Weitz, D. A.; Griffiths, A. D. *Lab Chip* **2009**, *9*, 1850.
(19) Mary, P.; Studer, V.; Tabeling, P. *Anal. Chem.* **2008**, *80*, 2680.
(20) Hai, M.; Magdassi, S. *J. Controlled Release* **2004**, *96*, 393.
(21) Pays, K.; Giermanska-Kahn, J.; Pouligny, B.; Bibette, J.; Leal-Calderon, F. *J. Controlled Release* **2002**, *79*, 193.
(22) Cheng, J.; Chen, J. F.; Zhao, M.; Luo, Q.; Wen, L. X.; Papadopoulos, K. D. *J. Colloid Interface Sci.* **2007**, *305*, 175.
(23) Skhiri, Y.; Gruner, P.; Semin, B.; Brosseau, Q.; Pekin, D.; Mazutis, L.; Goust, V.; Kleinschmidt, F.; El Harrak, A.; Hutchison, J. B.; Mayot, E.; Bartolo, J. F.; Griffiths, A. D.; Taly, V.; Baret, J. C. *Soft Matter* **2012**, *8*, 10618.
(24) Studer, A. *Science* **1997**, *275*, 823.
(25) Courtois, F.; Olguin, L. F.; Whyte, G.; Theberge, A. B.; Huck, W. T. S.; Hollfelder, F.; Abell, C. *Anal. Chem.* **2009**, *81*, 3008.

(26) Platzman, I.; Gadomska, K. M.; Janiesch, J.-W.; Louban, I.; Cavalcanti-Adam, E. A.; Spatz, J. P. In *Methods in Cell Biology*; Piel, M., Théry, M., Eds.; Academic Press: New York, 2014; Vol. *119*, p 237.

(27) Platzman, I.; Janiesch, J. W.; Matic, J.; Spatz, J. P. *Isr. J. Chem.* **2013**, *53*, 655.

(28) Ahn, Y. N.; Gupta, A.; Chauhan, A.; Kopelevich, D. I. *Langmuir* **2011**, *27*, 2420.

(29) Holtze, C.; Rowat, A. C.; Agresti, J. J.; Hutchison, J. B.; Angile, F. E.; Schmitz, C. H. J.; Köster, S.; Duan, H.; Humphry, K. J.; Scanga, R. A.; Johnson, J. S.; Pisignano, D.; Weitz, D. A. *Lab Chip* **2008**, *8*, 1632.

(30) Baret, J. C.; Kleinschmidt, F.; El Harrak, A.; Griffiths, A. D. *Langmuir* **2009**, *25*, 6088.

(31) Wolff, J. *Biochim. Biophys. Acta, Biomembr.* **2009**, *1788*, 1415.

Key Factors for Stable Retention of Fluorophores and Labeled Biomolecules in Droplet-Based Microfluidics

Jan-Willi Janiesch,[§,‡] Marian Weiss,[§,‡] Gerri Kannenberg,[§] Jonathon Hannabuss,[†] Thomas Surrey,[†] Ilia Platzman[§,*] and Joachim P. Spatz[§,*]

[§]Department of New Materials and Biosystems, Max Planck Institute for Intelligent Systems, Heisenbergstr. 3, 70569 Stuttgart and Department of Biophysical Chemistry, University of Heidelberg, 69120 Heidelberg, Germany

[¥]London Research Institute, Cancer Research UK, 44 Lincoln's Inn Fields, London WC2A 3LY, UK

[*]Corresponding authors: plazman@is.mpg.de and spatz@is.mpg.de

TABLE OF CONTENTS

1. Surfactants Synthesis and Analysis

The used surfactants PFPE(2500)-PEG(600)-PFPE(2500) triblock-copolymer (5600 g/mol, TRI2500) and Gold-PEG(436)-PFPE(7000) were synthesized according to protocols reported earlier.[1]

1.1. Perfluorpolypropylene-Polyethylene Glycol Monoethyl Ether Diblock-Copolymer 7000 (DI7000)

The synthesis of the perfluorpolypropylene-7000-polyethylene-750 glycol monoethyl ether diblock-copolymer (in the following referred to as DI7000) followed the procedure reported earlier[1] but with several modifications as shown in Figure 1S. The synthesis was carried out under argon atmosphere in dry THF (Acros Organics, Germany) as solvent in a heated Schlenk flask. PEG-OMe (750 mg, 1 mmol, molecular weight 750 g/mol, Fluka, Germany) was dissolved in 70mL dry THF and cooled to -78°C with isopropanol/dry ice. N-butyl lithium (0.4 mL of a 2.5 M solution in hexane, 1 mmol, Sigma-Aldrich, Germany) was added dropwise over a period of 45 minutes at -78°C to the PEG-OMe solution and stirred for additional 30 min at -78°C. While continuously stirred, the reaction was thawed slowly to room temperature and stirred for another 30 minutes. PFPE-carboxylic acid (7.0 g, 1 mmol, molecular weight 7000 g/mol, DuPont, Netherlands) was added dropwise over a period of 30 minutes and stirred for another 2 hours. After the reaction was finished, the THF solvent with unreacted PEG-OMe was removed by separatory funnel. Two washing steps with dry THF were used to remove unreacted PEG-OMe. The product was dissolved in methanol (Carl Roth GmbH, Karlsruhe, Germany) to separate it from unreacted PFPE7000-carboxylic acid and thereby transferred to a clean flask. Methanol was removed with a rotary evaporator at 40 °C and the product was dried on the vacuum line.
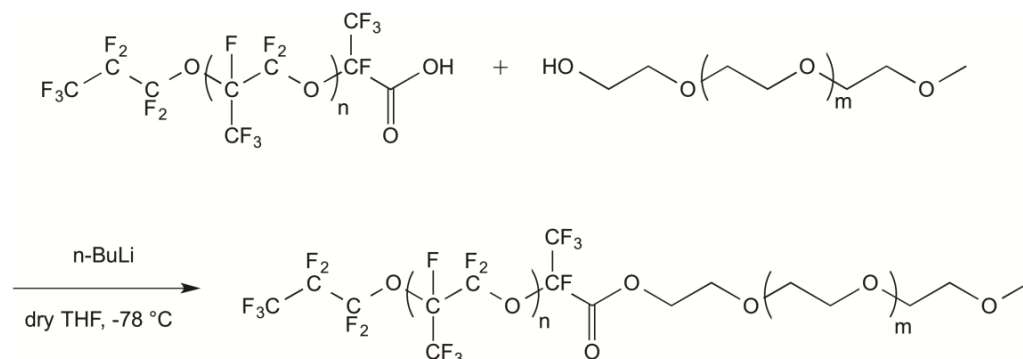
Figure 1S. Synthesis of PFPE(7000)-PEG(750) diblock-copolymer surfactants.

1.2. Perfluorpolypropylene–Polyethylene glycol-Perfluorpolypropylene Triblock-Copolymer PFPE(7000)- PEG(1400)-PFPE(7000) (TRI7000)

The synthesis of PFPE-PEG-PFPE triblock-copolymer followed the procedure reported earlier[1] but with several modifications as shown in Figure 2S. The synthesis was carried out under argon atmosphere in dry THF solvent (99.8%, Carl Roth, Germany) in a heated Schlenk-flask. PEG (1400 mg, 1 mmol, molecular weight 1400 g/mol, Sigma-Aldrich, Germany) was solved in 90 ml dry THF and cooled to -78 °C. N-butyl lithium (1.25 ml of a 1.6 M solution in hexane, 2 mmol, Sigma-Aldrich, Germany) was added dropwise over a period of 60 min at -78 °C to the PEG solution and stirred for additional 30 min at -78 °C. Under continuous stirring the reaction was slowly heated to room temperature followed by an additional 30 min stirring. PFPE-carboxylic acid (Krytox FSH, 14 g, 2 mmol, molecular weight 7000g/mol, DuPont, Netherlands) was added dropwise over a period of 30 min and

stirred for another 2 hours. After the reaction was finished, the THF solvent with unreacted PEG was removed by separatory funnel. Two washing steps with dry THF were used to purify the crude product from the unreacted PEG. The product was dissolved in methanol (99.8 %, Carl Roth GmbH, Germany) to separate it from unreacted PFPE(7000)-carboxylic acid. The PFPE-PEG-PFPE product, soluble in methanol, was transferred to a clean flask and dried with a rotary evaporator at 40°C. Following the rotary evaporator the product was additionally dried on the vacuum line, the desired PFPE-PEG-PFPE surfactant was obtained (12.18 g, 87 %). The purity of the product was analysed by IR measurements (see following section).

Figure 2S. Synthesis of PFPE(7000)-PEG(1400)-PFPE(7000) triblock-copolymer surfactants.

1.3. FTIR Spectroscopy

IR measurements were performed to confirm the success of the surfactant synthesis and evaluate the purity. The measurements were conducted on a Nicolet Nexus 870 Fourier transform infrared spectrophotometer (Thermo Electron GmbH, Dreieich, Germany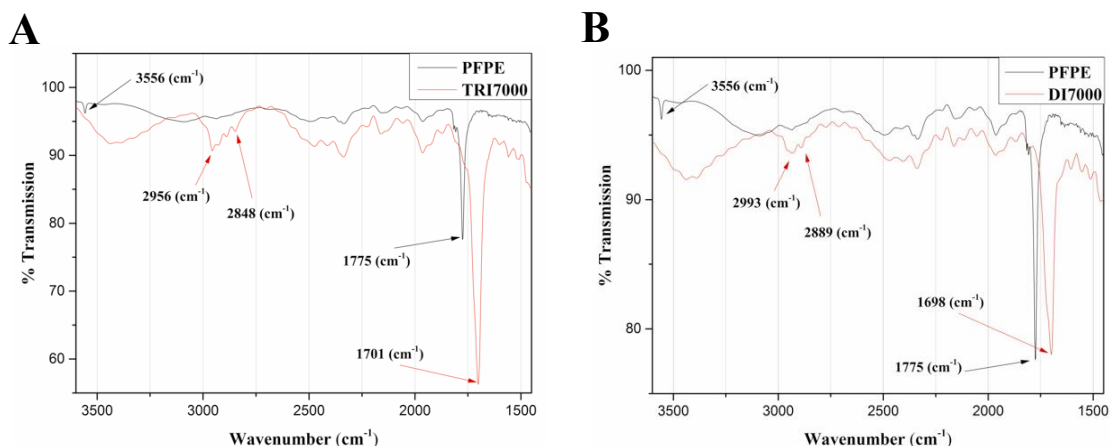) using a demountable pathlength cell for liquid FTIR (Thermo Scientific, USA) with KBr glasses and FC-40 perflourinated oil as solvent.

Figure 3S (A) shows the representative FTIR spectra of the PFPE(7000)-carboxylic acid reactant and the triblock surfactant product PFPE(7000)-PEG(1400)-PFPE(7000) (TRI7000). This figure presents five major bands at 1701, 1775, 2848, 2956 and 3556 cm^{-1}. The band at 1701 cm^{-1} is attributed to the ester (C=O) stretching mode. The band at 1775 cm^{-1} is attributed to a stretching mode of the (C=O) bond of the PFPE-carboxylic acid which is strongly blueshifted (by ~ 50 cm^{-1}) due to the electronegative fluor atoms in alpha position to the carboxylic group.[2] The same blueshift of the carboxylic (C=O) band was observed previously in the studies measuring the FTIR spectrum of the trifluoroacetic acid.[3,4] The bands at 2848 and 2956 cm^{-1} are assigned to symmetric and asymmetric stretching modes of the PEG (C-H) groups of the PFPE-PEG-PFPE product.[2] The band at 3556 cm^{-1} is assigned to the asymmetric stretching (OH) vibrations.[5]

Figure 3S (B) shows representative FTIR spectra of the DI7000 and PFPE(7000)-carboxylic acid. This figure presents major bands at 1698, 1775, 2889, 2993 and 3556 cm^{-1}. The band at 1698 cm^{-1} represents a stretching mode of the ester ν(C=O). The broad band at 2889 and 2993 cm^{-1} represents the symmetric and asymmetric stretching of PEG ν_a(CH). The band at 3556 cm^{-1} is assigned to the asymmetric stretching (OH) vibrations.[5]

Figure 3S. FTIR spectra of the reactants and the products of the surfactant synthesis. FC-40 perflourinated oil was used as a background solvent to obtain the spectra. (A) Comparison between the PFPE(7000)-carboxylic acid (20 mM) as a reactant and the PFPE(7000)-PEG(1400)-PFPE(7000) triblock product (20 mM) as described in section 1. (B) Comparison between PFPE(7000)-carboxylic acid as a reactant (20 mM) and the PFPE(7000)-PEG-OMe(750) diblock product (20 mM) as described in section 1.

1.4. Interfacial Tension Measurement via Pendant Drop

The interfacial tension (IFT) measurements between the aqueous and the oil phase were performed using pendant drop shape analysis technique (OCAH 230, DataPhysics Instruments GmbH, Germany). Experiments were performed using a 0.8 mm flat-tipped needle were oil-surfactant solutions with different concentrations were extruded into a cuvette filled with deionised water and photographed. The Interfacial tension values were extracted by the OCAH 230 software using droplet radius, pressure and droplet form for the calculation. The critical micelle concentration (CMC) values of 0.01 and 0.05 mM for TRI2500 and TRI7000 surfactants, respectively were evaluated using a standard fit curve.[6]

2. Fluorophores, Buffers, Cell Culture Media and Biomolecules

2.1. Fluorophores

ATTO 488 N-Hydroxysuccinimidyl ester (SE), ATTO 495 SE, ATTO 520 SE, ATTO 532 SE, ATTO 565 SE, ATTO 590 SE, ATTO 647N SE and ATTO 655 SE were purchased from ATTO-TEC GmbH (Siegen, Germany). ATTO 532 SE, ATTO 565 SE, ATTO 590 SE and ATTO 647N SE were used to label sheep anti-mouse antibodies according to the protocol described in the section 2.3. Alexa Fluor® 488 C5 Maleimide (M), Alexa Fluor® 532 C5 M, Alexa Fluor® 647 SE, Alexa Fluor® 488 goat anti-mouse IgG and Alexa Fluor® 647 goat anti-mouse IgG were purchased from Thermo Fisher Scientific (Schwerte, Germany). ATTO 647N-labeled streptavidin was purchased from Sigma–Aldrich, Germany.

Pure fluorophores were dissolved in anhydrous DMSO at a concentration of 1 mM, stored at -20°C and further diluted with each of buffers and culture mediums (see the following section) to a final concentration of 5 μM and used as aqueous phase for droplet creation. To work with labeled antibodies the stock solutions (see section 2.3) were diluted with TRIS buffer to final concentrations of 200 nM.

Hydrophilicity of fluorophores was analyzed using the distribution coefficient, LogD, which is a measure of the expected ratio of the sum of concentrations of all forms of the fluorophore (ionized plus un-ionized) in water and in a non-polar solvent (octanol). Negative LogD values correspond to hydrophilic fluorophores, positive values to hydrophobic ones.

Calculations for the fluorophores with a hydrolyzed SE and M reactive groups at pH 7.4 were performed by MarvinSketch version 14.10.20.0 (Chem Axon, Cambridge, MA), using the dye structures (Figure 4S). Three different calculation methods were used (VG, KLOP, PHYS) and weighted equally. Tautomerization and resonance were considered and electrolyte concentrations were adapted to:

LogD (PBS): 141 mM Cl^-,   141 mM Na^+ & K^+,   pH7.4
LogD (TRIS): 156 mM Cl^-,   150 mM Na^+ & K^+,   pH7.7

Table 1S Calculated LogD values and photophysical characteristics of the fluorophores used in this study.

Fluorophore	LogD (PBS)	LogD (TRIS)	λ_{abs} [nm]	λ_{fl} [nm]	MW [g/mol]	η_{fl}
Alexa 488 M	-9,47	-9,61	494	517	721	0.92
Alexa 532 M	-4,43	-4,54	530	555	813	0.61
Alexa 647 M	-7,75	-7,75	651	671	1250	0.33
ATTO 488 SE	-7,60	-7,60	501	523	981	0.80
ATTO 495 SE	-0,81	-0,71	495	527	549	0.20
ATTO 520 SE	0.59	0.45	516	538	564	0.90
ATTO 532 SE	-4.49	-5.30	532	553	1081	0.90
ATTO 565 SE	-0,18	-0,18	563	592	708	0.90
ATTO 590 SE	+1,56	+1,56	594	624	788	0.80
ATTO 633 SE	n.a	n.a.	629	657	749	0.64
ATTO 647N SE	+4,47	+4,47	644	669	843	0.65
ATTO 655 SE	-0.61	-1.46	663	684	887	0.30

λ_{abs}:   maximum absorption wavelength
λ_{fl}:   maximum emission wavelength
MW: Molecular weight
η_{fl}:   Quantum yield: ratio of photons emitted and photons absorbed

ATTO 488 SE   ATTO 495 SE   ATTO 520 SE

ATTO 532 SE   ATTO 565 SE   ATTO 590 SE

ATTO 647N SE   ATTO 655 SE

Alexa 488 Maleimide   Alexa 532 Maleimide
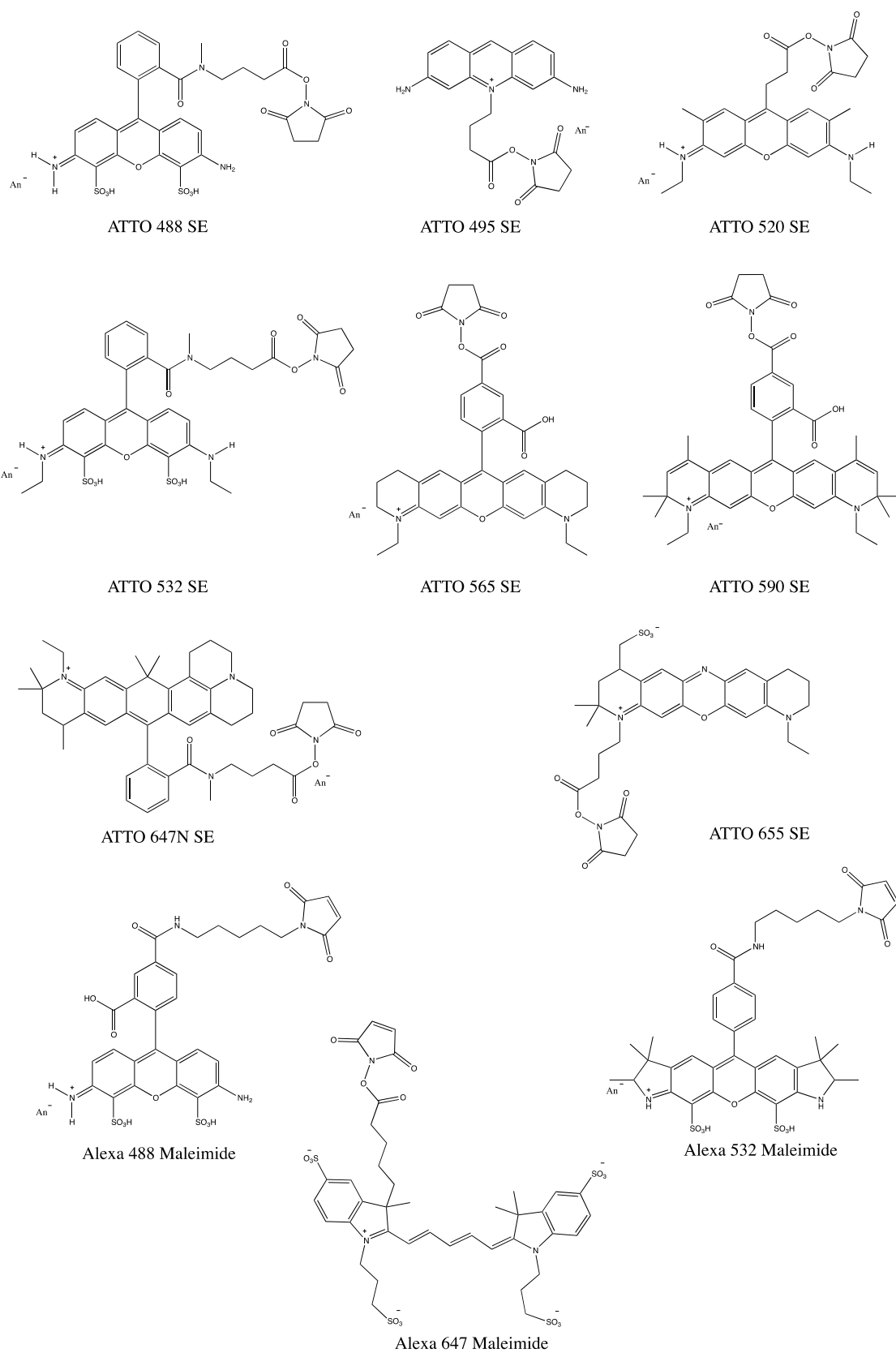
Alexa 647 Maleimide

Figure 4S. Structures of selected Alexa Fluor® and ATTO dyes used in this study.

2.2. Buffers and Cell Culture Media

All buffers were prepared with ultra-pure (R ≥ 18 MΩ/cm, Millipore) water and stored at 4°C. Following buffers were used: 1) PBS pH 7.4 was prepared using PBS tablets (Sigma – Aldrich, Germany); 2) TRIS buffer consisted of 50 mM TRIS, 150 mM NaCl, 2 mM $MgCl_2$, 1 mM $MnCl_2$, pH 7,4; 3) 30 mM HEPES pH 7,4; 4) PIPES buffer consisted of 20 mM PIPES, 7.25 mM $MgCl_2$, 1 mM EGTA, 3 mM GTP, 1 mM 2-mercaptoethanol, 50 mM KCl, 1 μM paclitaxel, 31 mM glucose, 1 mg/ml glucose oxidase and 0.5 mg/ml catalase, 0.25 mg/ml beta-casein, pH 6.8.

The pH values were adjusted using HCl and KOH solutions. Two cell culture media were used: 1) DMEM (Life technologies, USA) containing 4,5 g/l D-glucose, 1 mM L-glutamine, and 1% (v/v) penicillin/streptomycin (Gibco, Darmstadt, Germany); and 2) RPMI 1640 supplemented with 2 mM L-glutamine, 10% FBS (Invitrogen, Darmstadt, Germany) and 1% (v/v) penicillin/streptomycin (Gibco, Darmstadt, Germany).

2.3. Antibody and Tubulin Labeling

Labeling of anti-mouse antibodies with ATTO NHS dyes followed the protocols from ATTOtec with some modifications. The fluorophores were dissolved in DMF in a concentration of 10 mg/ml and used in a 15- to 20-fold molar excess. The AffiniPure Sheep anti-mouse (c = 2,4 mg/ml, IgG, Dianova (515-005-003)) was mixed with 10% (v/v) of 1 M $NaHCO_3$ (pH 8,3 – 9,0) and stirred at RT. The fluorophore was added dropwise under constant stirring, the solution was protected from light and stirred for one hour at RT. The crude product was purified by gel filtration with a Sephadex G25 (PD-10) gel filter (GE Healthcare GmbH, Solingen, Germany), equilibrated with 30 ml PBS pH 6.5. Following purification step, antibody-dye fractions of 500μl were collected and the protein content was determined with a Bradford Assay. The degree of labeling of 6 was determined by UV/VIS (Lambda 25 UV/VIS Spectrometer, PerkinElmer Precisely, USA). The labeled antibodies were stored at -20 °C.

Tubulin was purified from pig brain as described.[7] It was then labeled using ATTO 633-SE (Sigma) and ATTO 488-SE (Life Technologies) as described.[8] Tubulin concentrations were measured using UV spectroscopy (λ = 280 nm; ε = 115000 $M^{-1}cm^{-1}$); they are expressed as tubulin heterodimer concentrations. The labelling ratio was determined by UV spectroscopy, using the appropriate extinction coefficients at 280 nm and at the absorbance maximum for the dyes. Labeling ratios of ATTO 633 and ATTO 488 labeled tubulin were 0.75 and 0.65 dye molecules per tubulin dimer respectively.

2.4. Microtubule Polymerization

Microtubules were polymerised by incubating 14.5 μM tubulin (10% labeled) in PIPES buffer (buffer 4 above) at 37 °C for 20 minutes. Then they were used for droplet formation.

3. Microfluidic Device, Droplet Creation and Analysis

Droplet-based microfluidic devices, made of PDMS (Sylgard 184, Dow Corning, Michigan, USA) were prepared by photo- and soft-lithography methods[9] as previously described.[1,10] Water-in-oil emulsion droplets with an average diameter of 40 μm were created at a stable rate of 3 kHz by adjusting the flow rates of aqueous and oil phase to 240 μL/h and 320 μL/h, respectively. Surfactants (TRI2500, TRI7000 and DI7000) were dissolved in fluorinated oil (FC-40, Acros Organics, Germany) at different concentrations, ranging from 0.5 to 50 mM. In some experiments, the surfactants were mixed with 3μM gold-linked surfactants prior to droplets production. Figure 5S (A and B) shows an example for a microfluidic device and the flow focusing junction in which droplets are created. Blue and red colours indicate water and oil inlets and channels, respectively. The flow rates were controlled with precision syringe pumps (Aladdin-1000, World Precision Instruments, USA) connected to the inlets of the microfluidic device via polyethylene tubes (inner diameter 0.3 mm, Portex Fine Bore, Smiths

Medical Instruments Ltd., USA). Droplets were collected with a pipette tip at the outlet of the microfluidic device and transferred immediately to an analysis chamber[10] (Figure 5S C and D) for further analysis and characterization. To create the chamber two stripes of double face sticky tape (thickness ≈ 80 μm, Tesa, Germany) were glued on the longer sides of a 24 x 60 mm coverslip (Carl Roth, Germany), droplets were added in between the stripes and a 24 x 24 mm glass (Carl Roth, Germany) was glued on top. The chamber was filled completely with FC-40 oil containing the same surfactant concentration as used for droplet creation. To avoid evaporations the open sides of the chamber were closed by two-component glue (Twinsil, Picodent GmbH, Germany). Droplets stored in these chambers remained stable for more than two weeks.
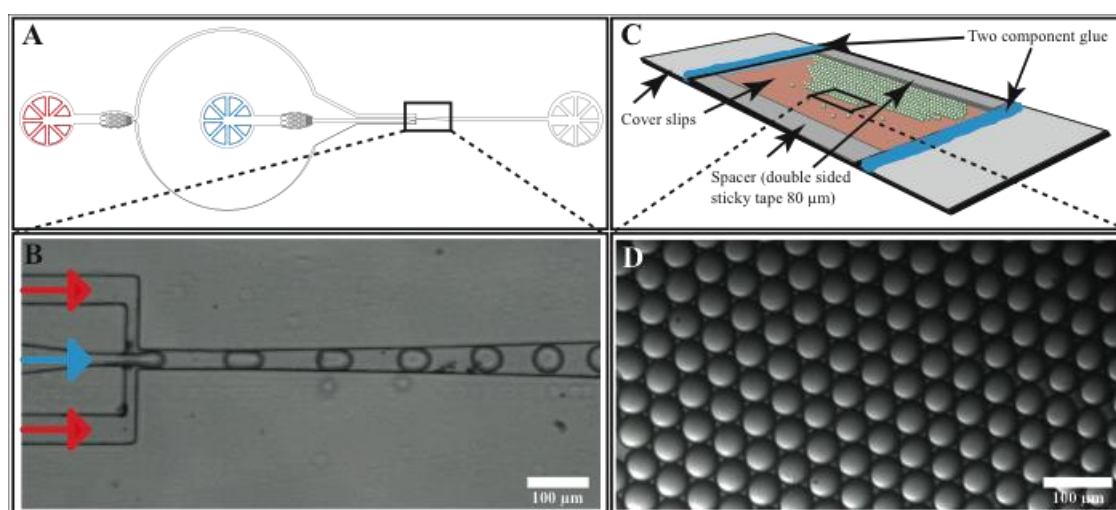

Figure 5S. (A) Representation of the droplet-based microfluidic device. Red and blue colourings indicate the oil and the aqueous inlets, respectively. (B) Shows the flow-focusing junction with 20 μm wide nozzle, where oil (red) and aqueous (blue) phases meet and the droplets are generated. (C) Schematic representation of an analysis chamber in which the droplets are stored for further analysis and characterization. (D) Representative phase contrast image of 40 μm diameter droplets in an analysis chamber.

4. Fluorescence Microscopy

All experiments were performed on an upright Leica DM6000B epifluorescence microscope (Leica Microsystems, Wetzlar, Germany) at 25°C. The droplets in an analysis chamber were excited via a 20x air objective (HC PLAN APO 20x/0.7; Leica Microsystems, Wetzlar, Germany). The field of sample excitation was limited using a rectangular aperture in the optical pathway. Brightfield and fluorescence images were taken every 15 sec for a period of 10 minutes and additionally 24 hours after droplets insertion with the image acquisition LAS AF software (Leica Microsystems, Wetzlar, Germany) with 1392 x 1040 pixels (1 pix = 0.46 μm) resolution. Analysis of fluorescence images was done using Fiji (ImageJ 2.0.0-rc-14, Rasband, W.S., ImageJ, U. S. National Institutes of Health, Bethesda, Maryland, USA, http://imagej.nih.gov/ij/, 1997-2014) program (Figure 6S).

To calibrate the emission intensity, fluorescence images of the aqueous phase (fluorophore solution) inside the microfluidic channels were taken. Illumination times were adjusted within the range of 10 to 50 ms to obtain the same fluorescence intensity value I_0 for each buffer-dye-combination. These illumination times were used to analyse the droplets within the analysis chamber. Fluorescence intensities I_{t0} and I_{t24} correspond to the values obtained immediately and 24 hours after droplets insertion, respectively. Fluorophore retention was categorized according to the following criteria: (see also Figure 6S):

$I_0 \approx I_{t0} \approx I_{t24}$ →   Stable fluorophore retention

$I_0 \approx I_{t0} > I_{t24}$ →   Moderate retention (slow release over 24h)

$I_0 \gg I_{t0}$ →   No retention (immediate release)
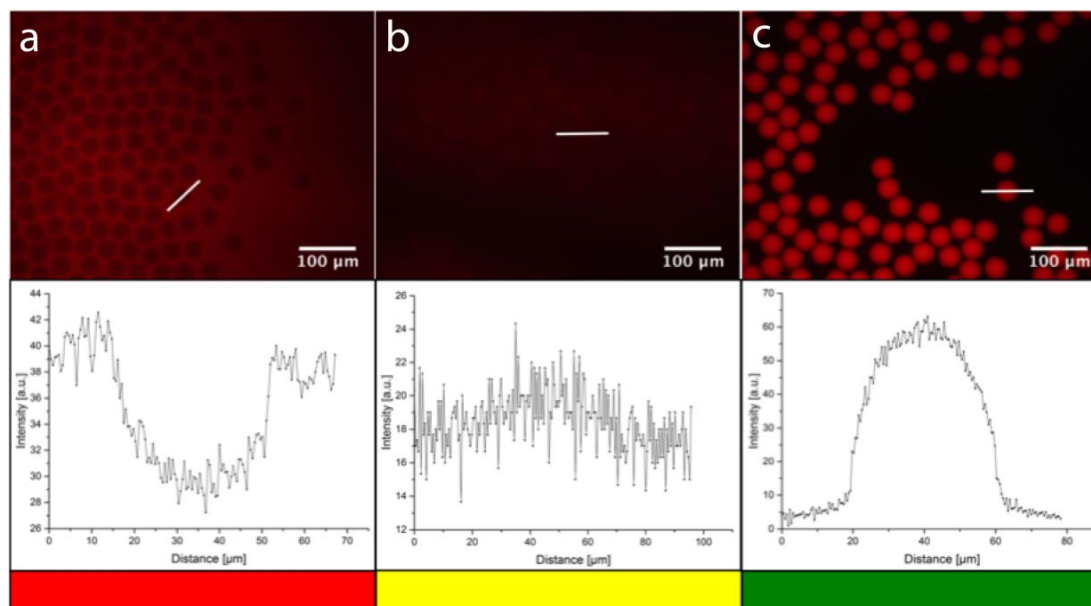
green labeling

yellow labeling

red labeling

Figure 6S. Microfluidic droplets produced with 10 mM TRI7000. Droplets containing ATTO 633 in TRIS (A), ATTO 655 in RPMI (B) and Alexa 488 in TRIS (C) were analyzed immediately after production (Intensity I_{t0}). Upper panel: Selected fluorescence images demonstrating different fluorescence retention in droplets. Middle panel: Intensity profiles of cross-sections marked in upper panel. Lower panel: Red, yellow and green blocks illustrate the color marking used in all tables.

5. Droplets Stability

To optimize the conditions for monodisperse droplets creation we investigated the optimal range of TRI2500 and TRI7000 surfactants concentrations. Videos of droplets, created in a microfluidic device, were recorded with a Phantom V7.2 camera at 10000 fps (Videos ac504736e_si_002.avi, ac504736e_si_003.avi, ac504736e_si_004.avi, ac504736e_si_005.avi, ac504736e_si_006.avi and ac504736e_si_007.avi). Representative images of droplets created using different surfactant conditions are shown in Figure 7S.
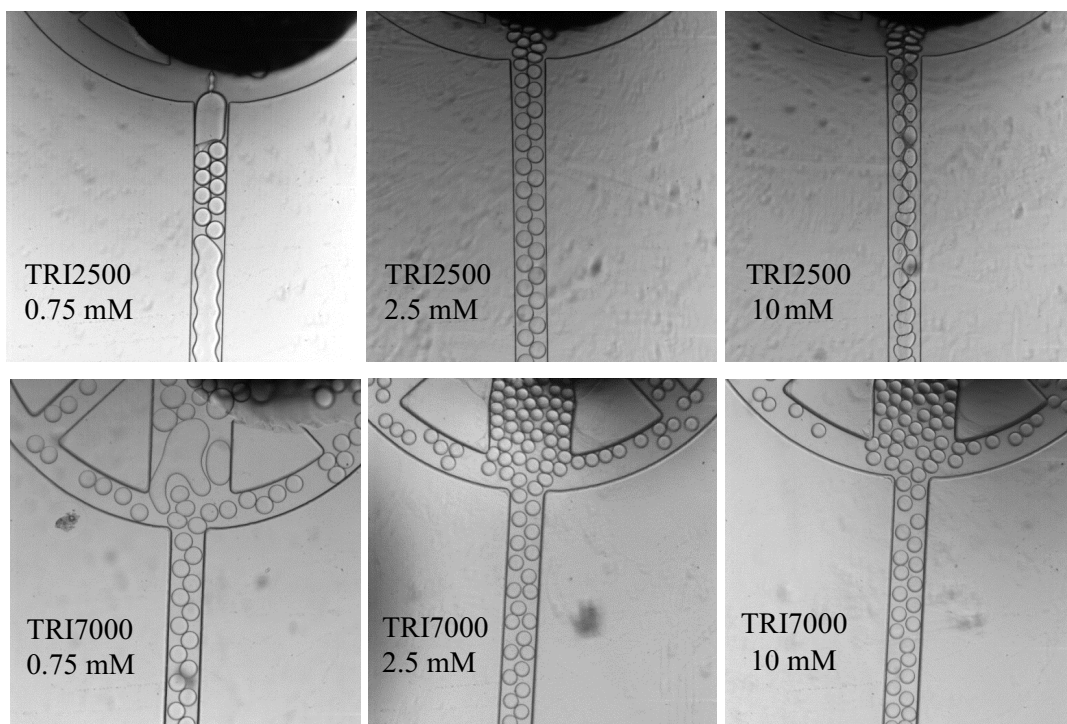
Figure 7S. Representative brightfield images of water-in oil droplets immediately after production. At low surfactant concentration (C < 1mM) coalescence of droplets is observed (left panel). At high surfactant concentration creation of small droplets occurs (right panel). Monodisperse and stable droplets are produced in a stable regime as it can be seen in the middle panel.

6. Effect of Droplet Sizes and Droplets Formation Speed on Retention Stability

To assess if the moderately encapsulated fluorophores could be lost to the oil before a stable layer of the surfactant is formed we investigated the retention stability of the moderately encapsulated fluorophores at different formation speeds (0.5, 3, and 30 kHz). NOTE: in droplet-based microfluidic studies the common rates of droplets creation are between 1 to 30 kHz. As can be observed in Figure 8S moderate retention was not affected by different rates of droplets formation.
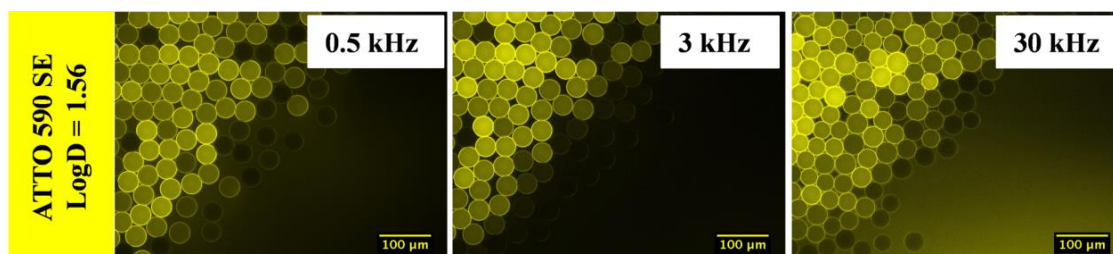

Figure 8S. Moderate retention of ATTO 590 SE fluorophores in the droplets does not depends on different rates of droplets formation. ATTO 590 SE fluorophores were dissolved in TRIS buffer and used as an aqueous phase for droplets creation. The oil phase contained 2.5 mM of TRI7000 surfactants.

Moreover, we checked whether different droplet sizes (Diameter = 25, 40 and 150 μm) affect the retention stability of fluorophores (Figure 9S). NOTE: in the droplet-based microfluidics the most commonly used droplets are in the range of 10 to 100 μm in diameter. As can be observed in Figure S9 the droplet dimensions at the selected range do not affect the encapsulation stability.
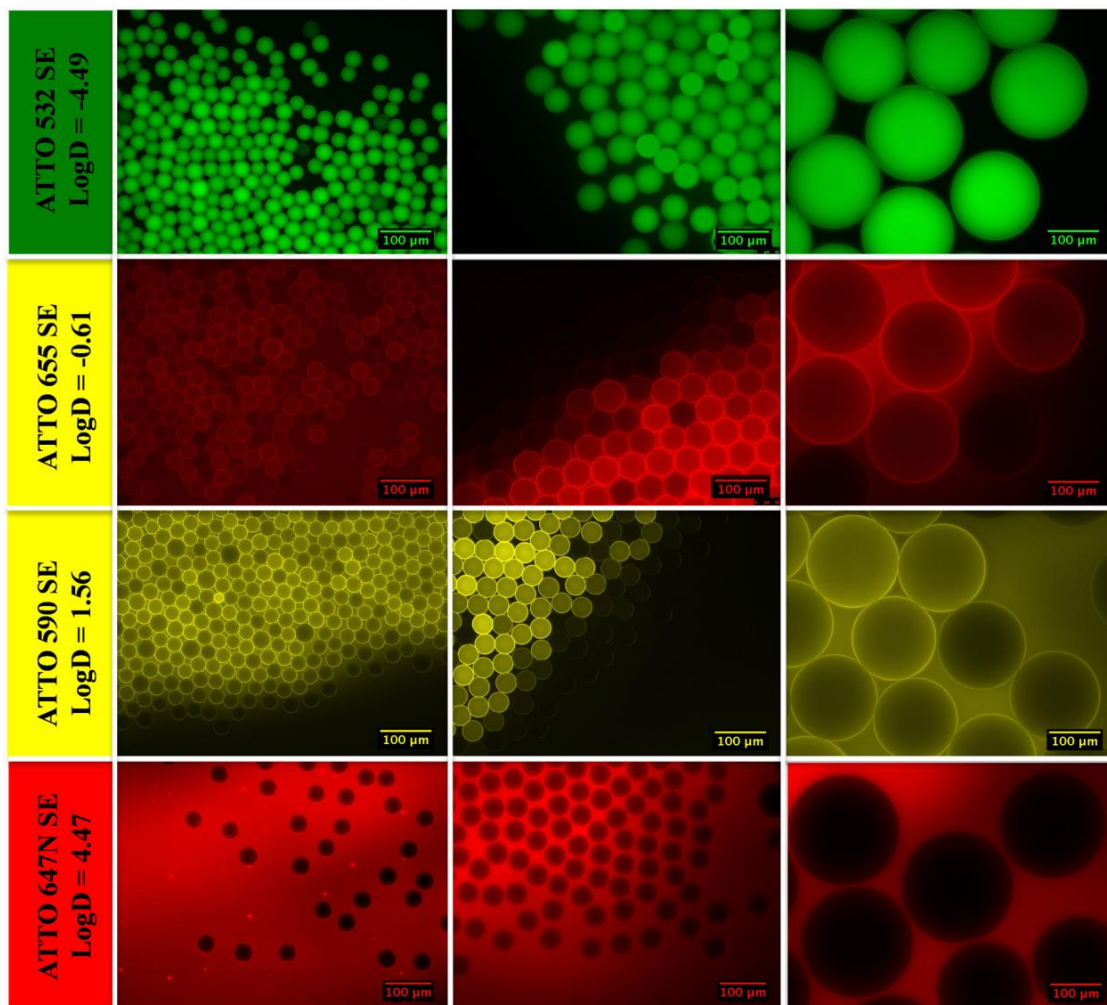

Figure 9S. Retention of fluorophores in the droplets does not depends on the droplets dimensions. ATTO 532 SE, ATTO 655 SE, ATTO 590 SE and ATTO 647N SE fluorophores were dissolved in TRIS buffer and used as an aqueous phase for droplets creation. The oil phase contained 2.5 mM of TRI7000 surfactants.

References

(1)   Platzman, I.; Janiesch, J.-W.; Spatz, J. P. *Journal of the American Chemical Society* **2013**, *135*, 3339.
(2)   Hesse, M.; Meier, H.; Zeeh, B.; Thieme: Stuttgart, 2002.
(3)   Wierzejewska-Hant, M.; Mielke, Z.; Ratajczak, H. *Spectrochimica Acta* **1987**, *43*, 675.
(4)   Redington, R. L.; Lin, K. C. *Spectrochimica Acta* **1971**, *27*, 2445.
(5)   Redington, R. L. *The Journal of Chemical Physics* **1971**, *54*, 4111.

(6)   Holt, D. J.; Payne, R. J.; Chow, W. Y.; Abell, C. *J. Colloid Interface Sci.* **2010**, *350*, 205.

(7)   Castoldi, M.; Popov, A. V. *Protein Expr. Purif.* **2003**, *32*, 83.

(8)   Hyman, A.; Drechsel, D.; Kellogg, D.; Salser, S.; Sawin, K.; Steffen, P.; Wordeman, L.; Mitchison, T.-. *Methods Enzymol* **1991**, *196*, 478.

(9)   Duffy, D. C.; McDonald, J. C.; Schueller, O. J. A.; Whitesides, G. M.; Baroud, G. M.; Delville, J. P.; Gallaire, F.; Wunenburger, R. *Anal. Chem.* **1998**, *70*, 4974.

(10) Hofmann, T. W.; Anselmann, S. H.; Janiesch, J. W.; Rademacher, A.; Bohm, C. H. J. *Lab on a Chip* **2012**, *12*, 916.

Publication 2

2.2   Spherical Network Contraction Forms Microtubule Asters in Confinement

Juniper, M., Weiss, M., Platzman, I., Spatz, J.P., and Surrey, T.

PAPER

Spherical network contraction forms microtubule asters in confinement†

Michael Juniper,[a] Marian Weiss,[b] Ilia Platzman,[b] Joachim P. Spatz[b] and Thomas Surrey (ORCID) *[a]

Microtubules and motor proteins form active filament networks that are critical for a variety of functions in living cells. Network topology and dynamics are the result of a self-organisation process that takes place within the boundaries of the cell. Previous biochemical *in vitro* studies with biomimetic systems consisting of purified motors and microtubules have demonstrated that confinement has an important effect on the outcome of the self-organisation process. However, the pathway of motor/microtubule self-organisation under confinement and its effects on network morphology are still poorly understood. Here, we have investigated how minus-end directed microtubule cross-linking kinesins organise microtubules inside polymer-stabilised microfluidic droplets of well-controlled size. We find that confinement can impose a novel pathway of microtubule aster formation proceeding *via* the constriction of an initially spherical motor/microtubule network. This mechanism illustrates the close relationship between confinement, network contraction, and aster formation. The spherical constriction pathway robustly produces single, well-centred asters with remarkable reproducibility across thousands of droplets. These results show that the additional constraint of well-defined confinement can improve the robustness of active network self-organisation, providing insight into the design principles of self-organizing active networks in micro-scale confinement.

[a] The Francis Crick Institute, 1 Midland Road, London, NW1 1AT, UK.
E-mail: thomas.surrey@crick.ac.uk
[b] Department of Cellular Biophysics, Max Planck Institute for Medical Research, Heidelberg & Department of Biophysical Chemistry, University of Heidelberg, Jahnstraße 29, D-69120 Heidelberg, Germany

† Electronic supplementary information (ESI) available: Movie 1: Microtubule vortex formation in surfactant stabilised droplets. Conditions as in Fig. 2a: 0.9% surfactant in oil, 200 nM mCherry-kinesin-14 and 40 μM Alexa647-tubulin in the droplet. Temperature was 34 °C, Microtubules are shown in red, motor protein in green. Movie 2: Distorted microtubule aster formation in surfactant stabilised droplets. Conditions as in Fig. 2b: 0.9% surfactant in oil, 400 nM mCherry-kinesin-14 and 40 μM Alexa647-tubulin in the droplet. Temperature was 34 °C, Microtubules are shown in red, motor protein in green. Movie 3: Centred microtubule aster formation in surfactant stabilised droplets. Conditions as in Fig. 2c: 1.8% surfactant in oil, 200 nM mCherry-kinesin-14 and 40 μM Alexa647-tubulin in the droplet. Temperature was 34 °C, Microtubules are shown in red, motor protein in green. Movie 4: Movie illustrating the process of averaged kymograph generation. The movie shows 360 individual kymographs of aster formation along droplet diameters separated by 1°. Conditions as in Fig. 2c and Movie 3. Movie 5: Repeatability of aster formation by the network constriction mechanism. Three time sequences are shown: first, aster formation at 30 °C; second, microtubule depolymerisation and aster disappearance after cooling to 4 °C; third, aster reformation after reheating to 30 °C. Surfactant and protein concentrations as in Fig. 2c and Movie 3. Microtubules are shown in red, motor protein in green. See DOI: 10.1039/c7sm01718a

Introduction

The internal structure of living cells depends on the organisation of the cytoskeleton within the cell boundary. Microtubules are dynamic tubular polymers of the cytoskeleton that interact with a multitude of associated proteins. Among these are several types of molecular motor that can form active cross-links between microtubules to create a dynamic network, which critically contributes to the overall organisation of the cytoskeleton.[1–5] Depending on the cellular state, the microtubule cytoskeleton can re-organise into remarkably different architectures with different biological functions.[6,7] In the interphase, the microtubule cytoskeleton is important for providing a polar scaffold for intracellular cargo transport, and during cell division it is essential for mitotic spindle assembly and chromosome segregation.[1,2,6,7] The molecular mechanisms determining the dynamic organisation of the complex microtubule network within the boundary of a eukaryotic cell are however only poorly understood.

Biomimetic systems of purified cytoskeletal components provide reduced complexity relative to their living counterparts. This offers the opportunity to gain insight into the mechanisms underlying the basic behaviour of active cytoskeletal networks,[3,8] as well as addressing more fundamental questions about the design principles of active matter systems. In

previous work, *in vitro* experiments with microtubules and motors led to the formation of large contracting networks or multiple microtubule asters or vortices,[9–12] or, in the additional presence of depletion forces, to the generation of active gels or nematic liquid crystals consisting of extensile microtubule bundles.[13–15] Related observations were also made for microtubules organised by motors in more complex cell extracts.[16,17] The role of physical confinement on self-organising motor/ microtubule systems is less studied, despite the importance of this constraint for the organisation of the cytoskeleton within cells, but some studies exist.

Pioneering work visualised individual dynamic microtubules growing from purified tubulin in small unilamellar vesicles.[18,19] Later, microtubule asters nucleated from purified centrosomes (microtubule nucleating organelles) were studied in micro-fabricated chambers, investigating the conditions for the centering of aster in these chambers.[20–22] Recently centrosome-nucleated asters were also encapsulated in lipid-monolayered droplets in oil.[23] In the absence of centrosomes, and in the presence of motor proteins and a depletion force by a non-adsorbing polymer, active nematics were observed at the inner surface of large unilamellar liposomes formed by short stabilised microtubules that were cross-linked and slid relative to each other by molecular motors.[24] Self-organisation of microtubules and motors was also studied in the absence of depletion forces in micro-fabricated chambers[10] and in lipid monolayer droplets surrounded by oil that ranged in size from typically 5 to 50 μm in diameter.[25] In these experiments, microtubules nucleated and grew within their confined space, followed by motor protein cross-linking, sliding and organisation. In micro-chambers, initially forming microtubule asters transformed into vortices as more and/or longer microtubules grew.[10] In the much smaller droplets most microtubules organised into bent bundles at the droplet boundary, whereas in droplets larger than about 40 μm the motors were able to cluster microtubule ends into a single focal point, leading to the formation of a microtubule aster.[25] The dependence of aster formation on droplet size was explained by considering that an aster with a distinct typical microtubule length will only fit into droplets where the induced microtubule bending is not too strong.[10,25] This is in agreement with a study performed using cell extract.[26] In previous work with purified motors and microtubules in droplets surrounded by oil, the droplet size was not controlled and only some droplets were large enough to allow aster formation having prevented a detailed study of the pathway of aster self-organisation under confinement.[25]

Here, we extend this previous work by producing relatively large droplets of uniform size using microfluidic droplet formation. Using polymer surfactants instead of phospholipids allowed for improved tubulin activity compared to previous experiments.[25,27] We find that the mechanism of aster formation is determined by both the biochemistry of the encapsulated solution and the chemistry of the droplet boundary. Under optimal conditions, single asters form robustly in thousands of droplets. We observe a novel pathway of aster

formation based on the contraction of a spherical network which arises due to the imposed confinement.

Materials and methods

Protein biochemistry

Pig brain tubulin was purified and labelled with Alexa647-*N*-hydroxy succinimidylester (Sigma) using standard procedures,[28,29] flash frozen in aliquots and stored in liquid nitrogen. mCherry-labelled *Xenopus laevis* kinesin-14 XCTK2[30] was prepared as described previously,[25] flash frozen in aliquots and stored in liquid nitrogen.

Droplet-based microfluidics

Microfluidic devices for droplet production using a flow focusing geometry[31] were designed using QCADpro (RibbonSoft, Switzerland). The corresponding photomasks were printed on chrome-coated soda lime glass (JD-Photodata, UK). The photolithography process was performed as described before:[32,33] a negative photoresist (SU-8-3025, MicroChem, USA) was spin-coated onto silicon wafers at 2500 rpm, resulting in uniform coating of 30 μm thickness. Wafers were then transferred to a hot plate for soft bake at 65 °C for five minutes, then ramped slowly to 95 °C and held for 15 minutes. Following this, the photoresist and the corresponding photomask were exposed for 7.5 seconds to UV light in a mask aligner (MJB4, SÜSS MicroTec, Germany). For the post exposure bake, the wafers were placed for 1 minute on a hot plate at 65 °C and 5 minutes at 95 °C. The remaining resist was removed with mr-DEV 600 developer (MicroChemicals, Germany). The final hard bake was carried out in an oven at 150 °C for 15 minutes.

Soft lithography was performed as described before:[34,35] briefly, PDMS (polydimethylsiloxane, Sylgard 184, Dow Corning, USA) was prepared by mixing the polymerization catalyst with the cross-linking oligomer in a 1 : 9 (w/w) ratio. The mixed elastomer was degassed using vacuum, poured over the silicon wafer and cured at 65 °C for 2 hours. After curing, the flexible PDMS mold was cut off and peeled off the wafer. The injection and outlet holes with a diameter of 0.75 mm were punched using a biopsy puncher (World Precision Instruments, USA). The device was cleaned with ethanol and activated together with a 24 × 60 mm coverslip (#1, Carl Roth, Germany) in an oxygen plasma (PVA TePla 100, PVA TePla, Germany) at 0.45 mbar, 200 W for 20 s. After activation, the PDMS device was pressed on the coverslip and heated for 2 hours at 65 °C. In order to make the device hydrophobic, Sigmacote (Sigma-Aldrich, Germany) was flushed through the micro channels of the device.

Internal droplet solution

The droplet solution was prepared by mixing on ice: 20 μl SOB2x buffer (40 mM K-PIPES pH 6.8, 100 mM KCl, 67 mM glucose, 10 mM ATP, 3 mM GTP, 4.5 mM MgCl$_2$, 2 mM EGTA, 2 mM 2-mercaptoethanol, 0.5 mg ml^{-1} β-casein), 1 μl antioxidant mix (20 mg ml^{-1} glucose oxidase, 10 mg ml^{-1} catalase in BRB80

(80 mM PIPES pH 6.8, 1 mM MgCl$_2$, 1 mM EGTA), pre-centrifuged at 21 000g for 15 min), 9.76 μl tubulin mix (10.75 mg ml^{-1} unlabelled tubulin, 5.57 mg ml^{-1} Alexa647-labelled tubulin (25% labelling ratio) in BRB80), 4 μl of motor mix (1 volume 1 mg ml^{-1} mCherry-kinesin-14 mixed with 4 volumes motor buffer (25 mM HEPES pH 7.2 250 mM KCl, 2 mM MgCl$_2$, 1 mM 2-mercaptoethanol)), and 5.24 μl water (total volume 40 μl). The final mix was centrifuged at 17 000g for 5 min and kept on ice until used (as internal phase) to make droplets. Final protein concentrations were 40 μM tubulin dimer (final Alexa647 labelling ratio ∼9%) and 200 nM mCherry-kinesin-14 (monomer concentration). For experiments with 400 nM motor protein, motor mix consisted of 2 volumes mCherry-kinesin-14 and 3 volumes motor buffer.

Droplet production

For the surfactant/oil mixture, first, a 10% w/w stock solution of RAN-008 fluorosurfactant (according to the manufacturer, a non-ionic PFPE–PEG–PEPE triblock copolymer surfactant, RAN Biotechnologies, USA) in HFE7500 (3M, USA) perfluorinated oil was prepared. Then an 18% or 9% v/v dilution of this stock solution in HFE7500 was made to generate a 1.8% or 0.9% mixture of surfactant in oil, respectively. This mixture was briefly vortexed before being used as the external phase in droplet making. Droplets of about 145 μm diameter in the x/y plane were produced in a cold room at 4 °C using the microfluidic droplet maker and Aladdin AL-1000 (World Precision Instruments, USA) precision syringe pumps with flow rates of 320 μl h^{-1} for the external oil phase and 280 μl h^{-1} for the internal (aqueous) protein-containing solution. Droplets were collected in 10 μl pipette tips in an Eppendorf tube and kept on ice.

Fluorescence microscopy

To prepare flow chambers for microscopy, 25 × 75 mm glass slides and 22 mm × 22 mm glass cover slips (no. 1.5) were sonicated in 20% ethanol, rinsed with MilliQ water, sonicated in MilliQ water, dried and coated with Aquapel, which is a fluorophilic and hydrophobic chemical which bonds covalently to glass. A flow chamber of ∼15 μl volume was constructed from a slide and coverslip using TESA double sided tape, placed on a metal block on ice and filled with ice cold HFE7500. Droplets were then drawn in using a tissue, followed by sealing the chamber with clear nail varnish. Microtubule polymerisation was started by transferring the flow chamber to a temperature controlled box heated to 30–34 °C around a 3i Marianas spinning disk confocal fluorescence microscope. It is based on a Zeiss Axio Observer Z1 and is equipped with a 20×/ NA 0.8 plan apo objective, a Yokogawa CSU-X1 spinning disk system and a Hamamatsu Orcaflash 4.0 CMOS camera controlled by 3i SlideBook 6 software. Movies of the central droplet plane parallel to the glass surface were recorded for 45 min at two frames per min with 100 ms and 200 ms exposure times for the 640 nm and 561 nm laser respectively.

For experiments where microtubules were depolymerised and repolymerised by temperature shifts (Fig. 5), depolymerisation was induced by placing onto the flow chamber a North-bridge cooler connected to a liquid circulating pump (Lauda Eco RE 415) containing ∼5% ethanol in water at 2 °C. This shifted the temperature in the flow chamber to 4 °C within ∼2 min. Removing the cooler allowed the temperature in the chamber to increase back to 30 °C within ∼6 min. For these experiments, movies were recorded during the cooling phase for 15 min at 12 frames per minute.

Three-dimensional images were created by making images at multiple confocal planes separated by 1 μm, which were then reconstructed in ImageJ to produce slices through the xz and yz planes.

Kymograph analysis

Merged colour time series and kymographs were produced using Fiji. To produce averaged diameter kymographs, a line across the diameter of a droplet was drawn, and the 'Radial Reslice' tool was used to generate a stack of 360 kymographs for each diameter line rotated by 1 degree increments around the droplet centre. 'Z project' averaged these kymographs into one
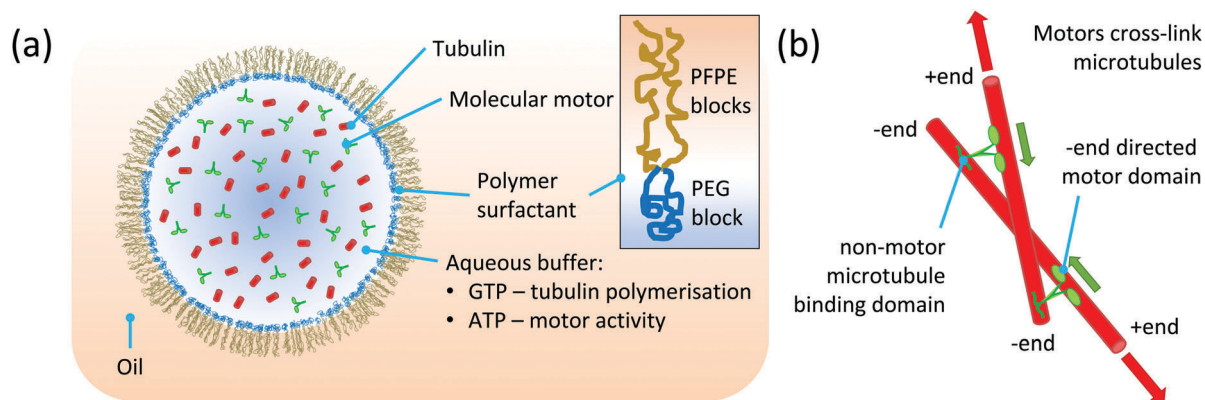

Fig. 1 Schematic of confined active self-organising motor/microtubule system. (a) Schematic of a tri-block copolymer-stabilised protein containing droplet. Encapsulated are tubulin, the motor kinesin-14, GTP (for microtubule polymerisation) and ATP (for motor activity). (b) Schematic view of kinesin-14 cross-linking motor activity. Motor walks towards the minus ends of microtubules as it hydrolyses ATP, and transports other microtubules by binding to them in a non-ATP dependent manner.

image. Network constriction speed was manually extracted from the initially approximately linear phase of constriction in the five kymographs shown in Fig. 4c.
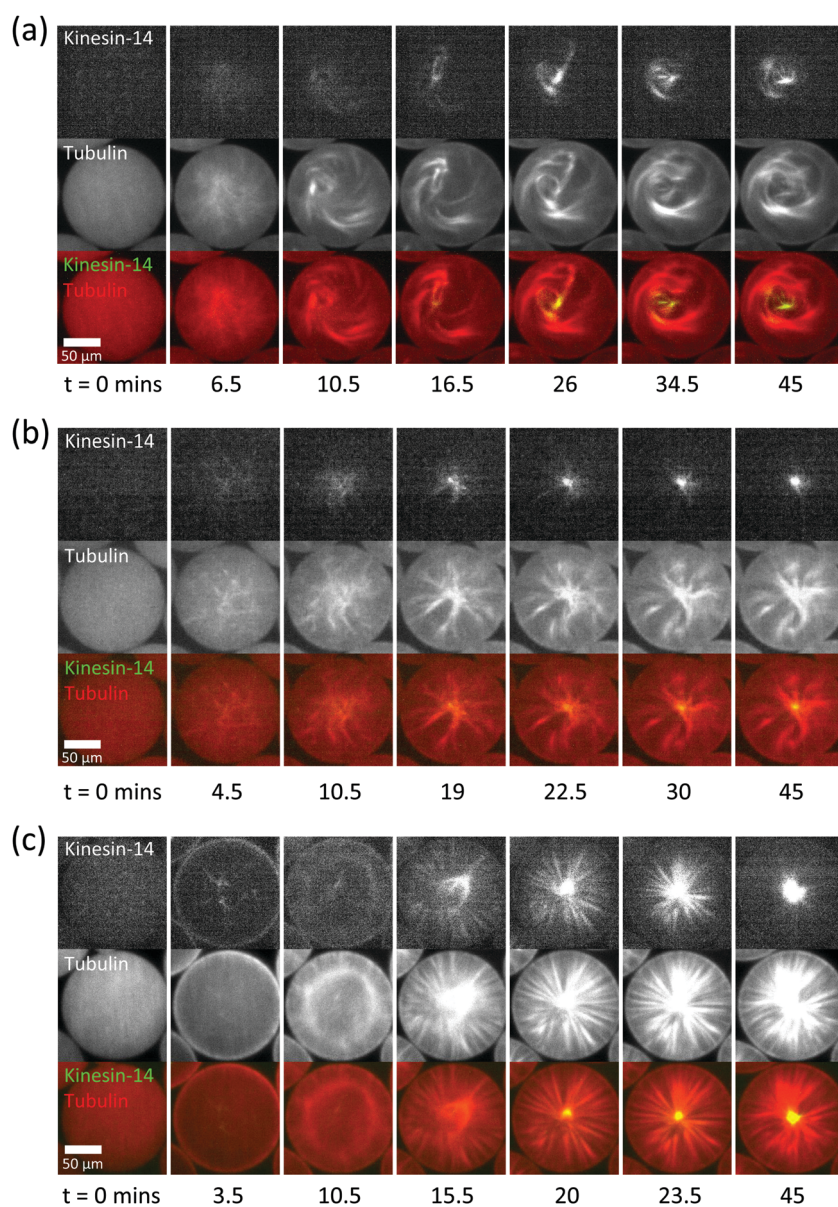
Droplet size

The droplet size distribution was analyzed using Fiji's Analyze Particle plugin. Recorded fluorescence images of the droplets produced in the presence of 1.8% surfactant were converted into binary images with optimized thresholds. The particle analyzer was applied to this image and identified the Area A of the single droplets, from which the diameter in the x/y plane was calculated. A total amount of 343 droplets was detected, resulting in a mean diameter of 145.3 μm a standard derivation

of 5.7 μm. The corresponding coefficient of variation is 4%, in good agreement with previous studies.[36,37]

Results and discussion

To study how confinement can influence the mechanism of self-organisation of motors and microtubules, we further developed a recent realisation of an *in vitro* self-organisation assay in which purified motors and tubulin were encapsulated in phospholipid-based droplets surrounded by mineral oil.[25] In the new experimental set-up, we used droplet-based microfluidics to reproducibly generate monodisperse droplets with about 145 μm diameter (Methods), a size expected to be

Fig. 2 Microtubule structures in surfactant-stabilised droplets produced using microfluidic droplet generator. (a–c) Confocal fluorescence microscopy time series of self-organising motors (green in merge) and dynamic microtubules (red in merge) at different surfactant and mCherry-kinesin-14 concentrations: (a) 0.9% surfactant in oil, 200 nM motor; (b) 0.9% surfactant in oil, 400 nM motor; (c) 1.8% surfactant in oil, 200 nM motor. The Alexa647-tubulin concentration was always 40 μM. Microtubule polymerisation was started by shifting the temperature to 34 °C. See also Movies 1–3 (ESI†).

considerably larger than typical microtubule lengths under our *in vitro* conditions and therefore optimal for our study here.[25] We furthermore changed the chemistry of the droplet-surrounding solution. We replaced mineral oil by perfluorinated oil, and phospholipids by a non-ionic PFPE–PEG-based copolymer surfactant (Methods) that provides a polyethylene glycol (PEG) layer on the inner surface of the droplet (Fig. 1a). Such PEG layers are often used to minimise interactions of proteins with surfaces in microscopy or microfluidics experiments.[38–41] The modified chemistry at the droplet boundary allowed us to omit microtubule stabilising agents (taxol, glycerol) from the encapsulated solution that were previously required to stimulate efficient microtubule nucleation in droplets[25,42] (Methods). Omitting these stabilising agents is expected to allow microtubules to remain dynamic throughout the experiment.

Using our modified method of droplet generation, we encapsulated purified mCherry-tagged *Xenopus laevis* kinesin-14 (XCTK2[30]) and Alexa647-labelled tubulin, together with GTP and ATP (Methods). Nucleation of microtubules was started by a temperature shift from 0 to 34 °C ($t = 0$ min) allowing then the minus end-directed kinesin-14[9,43,44] to cross-link and slide the growing microtubules relative to each other[9,45] (Fig. 1b). This can lead to large-scale organisation of a dynamically interconnected network, as observed previously for this motor in the absence and presence of confinement.[9,25] At a surfactant concentration of 0.9% in the oil surrounding the droplets and at 200 nM kinesin-14 inside the droplet we

observed, using confocal time-lapse fluorescence microscopy, the development of a dynamic vortex-like organisation of microtubules with the motor distributing along the microtubules, eventually becoming enriched towards the centre of the vortex (Fig. 2a and Movie 1, ESI†). This type of organisation is reminiscent of previous vortices observed when microtubules were organised by plus end directed motors, either in micro-fabricated chambers similar in diameter to our droplets[10] or in the absence of confinement at low motor concentrations where motors are thought to reach microtubule ends less efficiently.[11]

To investigate whether vortex formation in our droplets has geometrical or biochemical origins, we doubled the kinesin-14 concentration to 400 nM and observed now a self-organisation process more resembling aster formation with a more concentrated motor accumulation in the centre of the aster (Fig. 2b). However, many microtubules appeared bent, suggestive of a potential geometrical effect on the aster structure. This might indicate that microtubules are very long, or that cross-linked microtubule bundles are too long to fit into the droplet. Individual microtubules are expected to be longer at lower nucleation rates because the free tubulin concentration decreases more slowly when fewer microtubules are growing, and parallel microtubule bundles are also expected to be longer at lower motor activities, because microtubule end-to-end sliding may be less efficient.

Next, we used a surfactant concentration of 1.8%, double the value used above, in an attempt to increase the efficiency of

Fig. 3 Robust formation of centred microtubule asters in surfactant-stabilised droplets. Conditions as in Fig. 2c: 1.8% surfactant, 200 nM mCherry-kinesin-14 (green), 40 µM Alexa647-tubulin (red), 34 °C. (a) Confocal microscopy image of the central plane of individual isolated microtubule asters formed inside several droplets. (b) Slices through a z-stack generated from confocal images, showing the three-dimensional nature of the aster structure. (c) Montage of 95 images showing a region of the microscope slide 7.4 × 2.7 mm, and containing approximately 1400 droplets. Whole slide contains approximately 10 000 droplets.
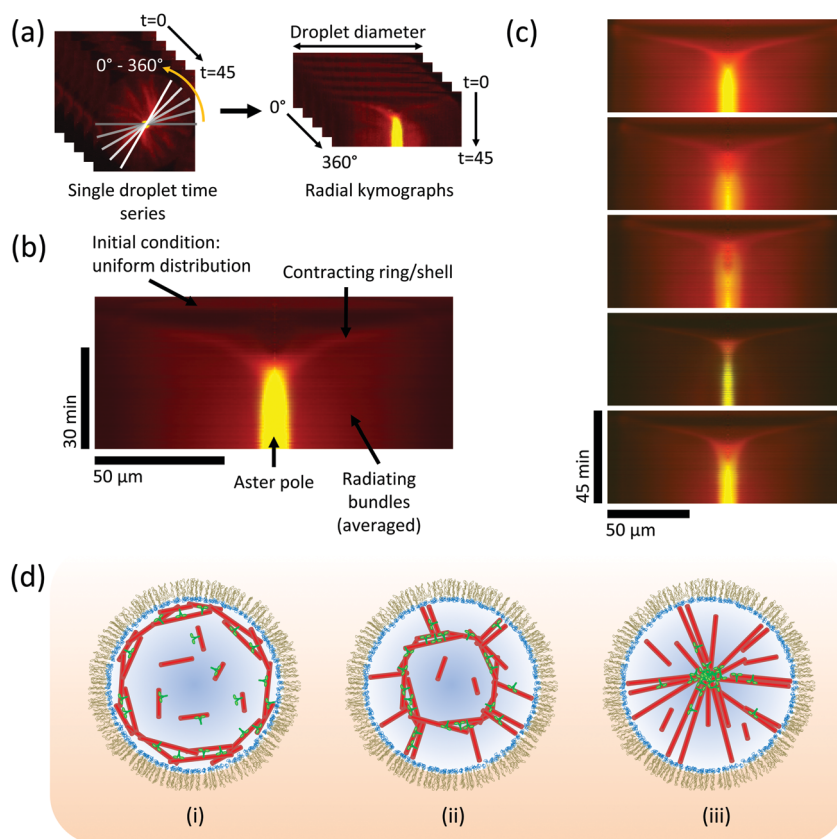
Fig. 4 Kinetics of aster formation *via* contraction of a spherical network. (a) Illustration of the procedure for generating a radially averaged kymograph (space–time plot) from a time-lapse movie, to reveal how the average density of motors and microtubules measured along the droplet diameter develops over time. 360 kymographs are produced at 1° intervals, and averaged together (Methods and Movie 4, ESI†). (b) Typical averaged kymograph, showing the main features of the pathway of aster formation by a constriction mechanism. Kinesin-14 in green, tubulin in red. *t* = 0 is at the top of the image. (c) Selection of five kymographs from different droplets at the same conditions (as in Fig. 2c and 3), showing that the essential features of the mechanism are retained. Colour code as in (b). (d) Schematic model: (i) microtubules nucleate preferentially at the boundary; (ii) molecular motors cross-link microtubules and slide them, causing contraction of the ring/shell; (iii) microtubule minus-ends sorted into a pole, stabilised by cross-linking motors.

microtubule nucleation. With a kinesin-14 motor concentration of 200 nM, we now observed relatively fast microtubule nucleation locally at the droplet boundary (Fig. 2c, 3.5 min), possibly induced a by PEG density dependent protein adsorption effect.[46] This was followed by the appearance of an apparently structureless microtubule/motor ring, indicative of a microtubule/motor shell in three dimensions. Remarkably, rather than remaining stuck to the boundary, this shell contracted, thereby dramatically reorganising the microtubules. Eventually an aster formed with microtubule minus ends focused into a single pole where the vast majority of motors strongly accumulated, while the microtubules radiated outward towards the droplet boundary as rather straight bundles (Fig. 2c). This mechanism of aster formation by contraction of a spherical network shell differs markedly from motor-driven microtubule aster formation pathways observed earlier[9–11,25] and appears to be a direct consequence of confinement in combination with the more efficient microtubule nucleation at the droplet boundary under our conditions. This mechanism of aster formation also demonstrates that pole formation is a special case of three-dimensional network contraction.

Aster formation was remarkably robust. In the vast majority of observed cases, a single aster formed in each droplet, having its focal point well centred with respect to the droplet boundary, both in the *x*/*y* plane (Fig. 3a) and the *z* direction (Fig. 3b). Thousands of droplets, almost all of them with well centred self-organised microtubule asters could be reproducibly observed on a single slide (Fig. 3c), indicating a very strong preference for this configuration of our biochemical system when under confinement. This suggests that a well-controlled size of confinement can impose constraints on self-organising motor/microtubule systems to promote robustness of organisation, as is also required for the cytoskeleton in living cells.

To elucidate the characteristic features of the network constriction mechanism, we produced kymographs (space-time plots) showing the temporal development of motor and microtubule densities measured along the droplet diameter (Fig. 4a, Movie 4 and Methods, ESI†). Evidently, an initially uniform distribution leads within a few minutes to local microtubule nucleation at the boundary, followed by network constriction towards the droplet centre (Fig. 4b). Constriction slows down over time as the density of the spherical network increases, finally leading to a pole with strong motor accumulation (Fig. 4b), indicative of efficient polarity sorting of the now
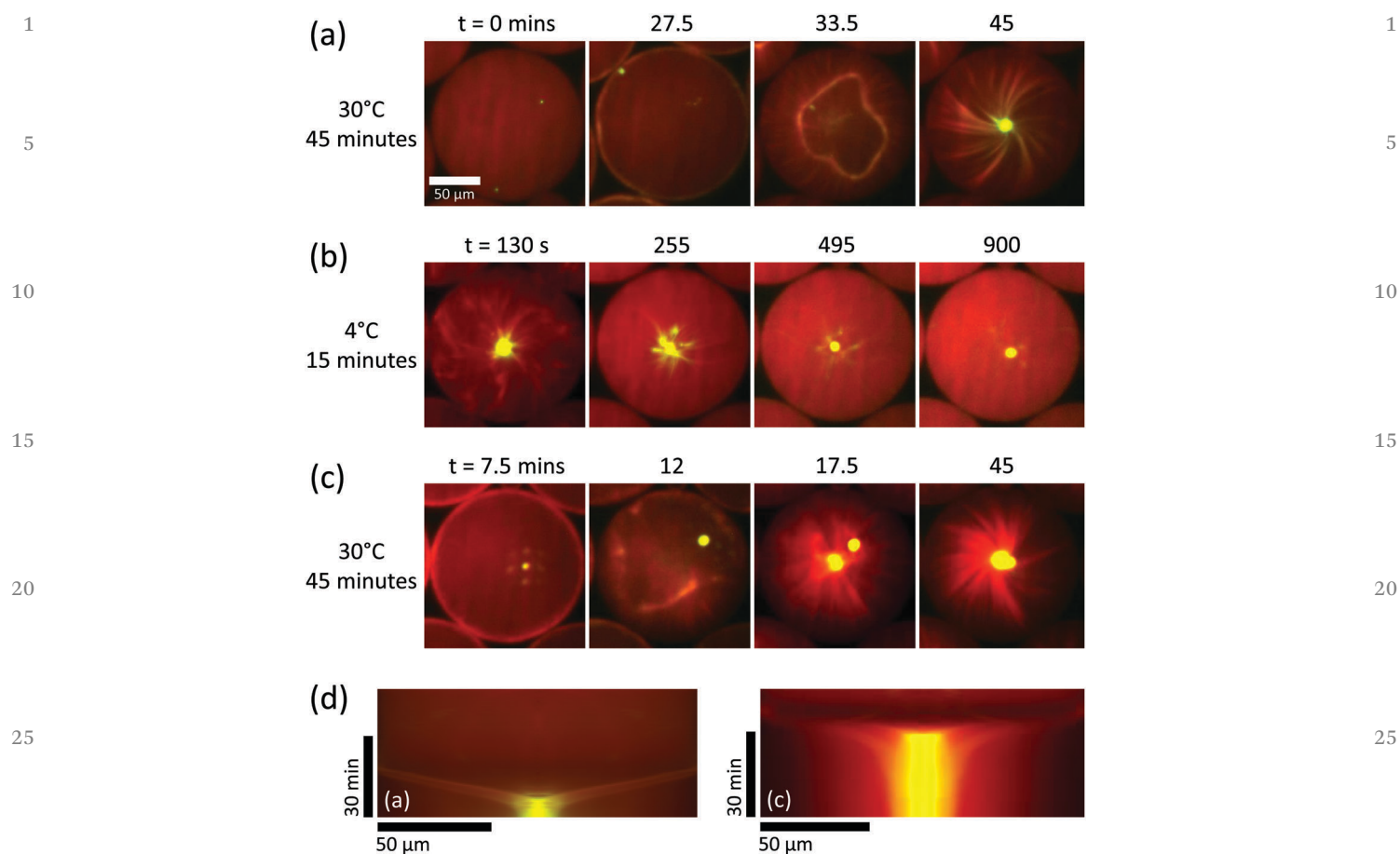
Fig. 5 Repeatability of aster formation *via* the constriction mechanism. Surfactant and protein concentrations as in Fig. 2c–4. (a) Aster forms *via* network contraction at 30 °C. (b) Depolymerisation of microtubules at 4 °C causes microtubule depolymerisation, leaving only a small aggregated remnant of the aster pole which diffuses away from the droplet centre. Same slide, different droplet to (a). (c) When heated again to 30 °C, an aster rapidly forms again *via* a contracting shell, and the original pole remnant joins the new pole. Same droplet as (b). (d) Averaged kymographs relating to panels (a) and (c), which show characteristic contracting rings. Note the different time intervals between the images shown in (b). See Movie 5 (ESI†).

radiating microtubules. These characteristic features of the pathway are remarkably reproducible, as kymographs showing self-organisation in an arbitrary selection of five droplets show (Fig. 4c). These kymographs revealed that initially constriction caused the diameter of the network to shrink with 188 ± 20 nm, which is considerably faster than the typical kinesin-14 speed of ~ 20 nm s^{-1},[9] demonstrating that multiple local contraction events are coupled leading to fast collective network constriction. Taken together, these observations demonstrate a novel and robust mechanism of motor-dependent microtubule aster formation (Fig. 4d).

Finally, we investigated whether the constriction mechanism was a consequence of the process of droplet formation or an inherent property of the encapsulated biochemical system. To address this question, we asked whether aster formation *via* the shell contraction mechanism can be repeated after aster disassembly. We first allowed asters to form in droplets at 30 °C, showing again aster formation by network constriction (Fig. 5a and Movie 5 – part 1, ESI†). We then induced microtubules to depolymerise by cold treatment (Methods), causing the asters to disappear, leaving only a

small remnant of the aster centre where the protein concentration was highest, while most tubulin and motors redistributed throughout the droplet (Fig. 5b and Movie 5 – part 2, ESI†). Reheating the flow chamber initiated microtubule polymerisation again, and a second round of aster formation began, again by the constriction mechanism (Fig. 5c and Movie 5 – part 3, ESI†). This conclusion was confirmed by a 'funnel'-shaped congression of high motor and microtubule densities in the kymographs, indicative of spherical network constriction and pole formation (Fig. 5d, left and right, respectively). These observations demonstrate the dynamic steady state nature of the self-organised aster, in contrast to a static structure formed by an irreversible process. This demonstrates also that the biochemical conditions here allow the preservation of enzyme activities for well over an hour in our droplet system. Moreover, the repeatability of aster formation demonstrates that the constriction mechanism is an intrinsic property of the system characterised by its (bio)chemical composition and its geometrical properties, in contrast to a history-dependent process retaining some memory from droplet formation.

Conclusions

We have developed a new and robust experimental system for motor/microtubule self-organisation in surfactant-stabilised droplets of well-defined size. The experimental system preserved protein activities well, allowing efficient nucleation of dynamic microtubules in the absence of artificial microtubule stabilisers. Choosing a large droplet diameter of about 145 μm allowed us to study the conditions of reproducible microtubule aster formation in thousands of almost identical droplets. The pathway of self-organisation depended on both the motor concentration, as expected,[9–11] as well as on the chemical properties of the boundary. Under optimal conditions, single asters formed robustly *via* spherical network constriction, a mechanism that was notably different from previous aster formations in unconfined geometries.[9–11] The constriction pathway illustrates the close relationship between active network contraction and aster formation. It is particularly interesting to note the continuous topological transition whereby a spherical network of randomly oriented filaments is reorganised by constriction to form a point from which polarity-sorted bundles radiate.

Compared to previous biochemical self-organisation experiments with purified motors and microtubules without confinement[9–11] or within droplets of uncontrolled size,[25] the pathway of aster formation was highly reproducible and the size of the asters was uniform. The radial symmetry of asters filling the entire droplet volume led to reliable concentration of the vast majority of microtubule minus ends and minus-end-directed motors in the droplet centre, demonstrating the ability of the system to find its centre with high fidelity. The additional constraint of imposing confinement of well-controlled size confers robustness to the outcome of self-organisation, which may well be of relevance for the self-organising cytoskeleton in living cells.

It is also interesting to see that microtubules and cross-linking kinesins can form a constricting network that resembles to a certain extent the contraction of the cytokinetic ring consisting of actin filaments and myosin motors that assembles at the cell boundary to separate the two daughter cells during cell division.[47,48] The outcome of constriction is different in these cases due to differences in the properties of the filaments and motors, with the cytokinetic ring collapsing without a topological change to form a compact midbody, whereas the microtubules in our experiments undergo a topological transition to form a large aster of bundles tethered to a well-defined central pole. Despite the different final structures described, the use of symmetrical boundary conditions to determine the eventual organisation of a dynamic system can be seen as a fundamental design principle for micro-scale active matter self-assembly.

Author contributions

M. J. performed all experiments and data analysis. M. W. made the droplet-based microfluidic devices. M. J. and T. S. designed the study. M. J. and T. S. wrote the manuscript with input from M. W. I. P. and J. S. assisted with the polymer stabilized droplet microfluidics. All authors contributed to discussions and to editing the manuscript.

Conflicts of interest

Q3

Acknowledgements

References

1 K. J. Helmke, R. Heald and J. D. Wilbur, *Int. Rev. Cell Mol. Biol.*, 2013, **306**, 83–125.
2 T. M. Kapoor, *Biology*, 2017, **6**. Q4
3 D. Needleman and Z. Dogic, *Nat. Rev. Mater.*, 2017, **2**, 1–14.
4 E. J. Peterman and J. M. Scholey, *Curr. Biol.*, 2009, **19**, R1089–R1094.
5 E. Karsenti, F. Nedelec and T. Surrey, *Nat. Cell Biol.*, 2006, **8**, 1204–1211.
6 T. J. Keating and G. G. Borisy, *Biol. Cell.*, 1999, **91**, 321–329.
7 A. D. Sanchez and J. L. Feldman, *Curr. Opin. Cell Biol.*, 2017, **44**, 93–101.
8 M. Dogterom and T. Surrey, *Curr. Opin. Cell Biol.*, 2013, **25**, 23–29.
9 C. Hentrich and T. Surrey, *J. Cell Biol.*, 2010, **189**, 465–480.
10 F. J. Nedelec, T. Surrey, A. C. Maggs and S. Leibler, *Nature*, 1997, **389**, 305–308.
11 T. Surrey, F. Nedelec, S. Leibler and E. Karsenti, *Science*, 2001, **292**, 1167–1171.
12 T. Torisawa, D. Taniguchi, S. Ishihara and K. Oiwa, *Biophys. J.*, 2016, **111**, 373–385.
13 G. Henkin, S. J. DeCamp, D. T. Chen, T. Sanchez and Z. Dogic, *Philos. Trans. R. Soc., A*, 2014, **372**. Q5
14 T. Sanchez, D. T. Chen, S. J. DeCamp, M. Heymann and Z. Dogic, *Nature*, 2012, **491**, 431–434.
15 T. Sanchez, D. Welch, D. Nicastro and Z. Dogic, *Science*, 2011, **333**, 456–459.
16 P. J. Foster, S. Furthauer, M. J. Shelley and D. J. Needleman, *eLife*, 2015, **4**.

17 K. Suzuki, M. Miyazaki, J. Takagi, T. Itabashi and S. Ishiwata, *Proc. Natl. Acad. Sci. U. S. A.*, 2017, **114**, 2922–2927.

18 M. Elbaum, D. Kuchnir Fygenson and A. Libchaber, *Phys. Rev. Lett.*, 1996, **76**, 4078–4081.

19 D. K. Fygenson, J. F. Marko and A. Libchaber, *Phys. Rev. Lett.*, 1997, **79**, 4497–4500.

20 M. Cosentino Lagomarsino, C. Tanase, J. W. Vos, A. M. Emons, B. M. Mulder and M. Dogterom, *Biophys. J.*, 2007, **92**, 1046–1057.

21 C. Faivre-Moskalenko and M. Dogterom, *Proc. Natl. Acad. Sci. U. S. A.*, 2002, **99**, 16788–16793.

22 L. Laan, N. Pavin, J. Husson, G. Romet-Lemonne, M. van Duijn, M. P. Lopez, R. D. Vale, F. Julicher, S. L. Reck-Peterson and M. Dogterom, *Cell*, 2012, **148**, 502–514.

23 M. Vleugel, S. Roth, C. F. Groenendijk and M. Dogterom, *J. Visualized Exp.*, 2016, DOI: 10.3791/54278.

24 F. C. Keber, E. Loiseau, T. Sanchez, S. J. DeCamp, L. Giomi, M. J. Bowick, M. C. Marchetti, Z. Dogic and A. R. Bausch, *Science*, 2014, **345**, 1135–1139.

25 H. Baumann and T. Surrey, *J. Biol. Chem.*, 2014, **289**, 22524–22535.

26 M. Pinot, F. Chesnel, J. Z. Kubiak, I. Arnal, F. J. Nedelec and Z. Gueroui, *Curr. Biol.*, 2009, **6**, 6.

27 I. Platzman, J. W. Janiesch and J. P. Spatz, *J. Am. Chem. Soc.*, 2013, **135**, 3339–3342.

28 M. Castoldi and A. V. Popov, *Protein Expression Purif.*, 2003, **32**, 83–88.

29 A. Hyman, D. Drechsel, D. Kellogg, S. Salser, K. Sawin, P. Steffen, L. Wordeman and T. Mitchison, *Methods Enzymol.*, 1991, **196**, 478–485.

30 C. E. Walczak, S. Verma and T. J. Mitchison, *J. Cell Biol.*, 1997, **136**, 859–870.

31 P. B. Umbanhowar, V. Prasad and D. A. Weitz, *Langmuir*, 2000, **16**, 347–351.

32 B. Bohl, R. Steger, R. Zengerle and P. Koltay, *J. Micromech. Microeng.*, 2005, **15**, 1125–1130.

33 D. Qin, Y. N. Xia and G. M. Whitesides, *Adv. Mater.*, 1996, **8**, 917–&.

34 D. C. Duffy, J. C. McDonald, O. J. A. Schueller and G. M. Whitesides, *Anal. Chem.*, 1998, **70**, 4974–4984.

35 G. M. Whitesides, E. Ostuni, S. Takayama, X. Y. Jiang and D. E. Ingber, *Annu. Rev. Biomed. Eng.*, 2001, **3**, 335–373.

36 S. Takeuchi, P. Garstecki, D. B. Weibel and G. M. Whitesides, *Adv. Mater.*, 2005, **17**, 1067–+.

37 P. A. Zhu and L. Q. Wang, *Lab Chip*, 2017, **17**, 34–75.

38 P. Bieling, I. A. Telley, C. Hentrich, J. Piehler and T. Surrey, *Methods Cell Biol.*, 2010, **95**, 555–580.

39 R. Roy, S. Hohng and T. Ha, *Nat. Methods*, 2008, **5**, 507–516.

40 S. Tyagi, V. VanDelinder, N. Banterle, G. Fuertes, S. Milles, M. Agez and E. A. Lemke, *Nat. Methods*, 2014, **11**, 297–300.

41 J. W. Janiesch, M. Weiss, G. Kannenberg, J. Hannabuss, T. Surrey, I. Platzman and J. P. Spatz, *Anal. Chem.*, 2015, **87**, 2063–2067.

42 H. Baumann and T. Surrey, *Methods Cell Biol.*, 2015, **128**, 39–55.

43 H. B. McDonald, R. J. Stewart and L. S. Goldstein, *Cell*, 1990, **63**, 1159–1165.

44 R. A. Walker, E. D. Salmon and S. A. Endow, *Nature*, 1990, **347**, 780–782.

45 G. Fink, L. Hajdo, K. J. Skowronek, C. Reuther, A. A. Kasprzak and S. Diez, *Nat. Cell Biol.*, 2009, **11**, 717–723.

46 P. Katira, A. Agarwal and H. Hess, *Adv. Mater.*, 2009, **21**, 1599–+.

47 B. Mierzwa and D. W. Gerlich, *Dev. Cell*, 2014, **31**, 525–538.

48 T. D. Pollard, *Biophys. J.*, 2014, **107**, 2499–2507.

Publication 3

2.3 Sequential Bottom-up Assembly of Mechanically Stabilized Synthetic Cells by Microfluidics

Weiss, M., Frohnmayer, P.J., Benk, L.T., Haller, B., Janiesch, J.-W., Heitkamp, T., Boersch, M., Lira, R.B., Dimova, R., Lipowsky, R., Bodenschatz, E., Baret, J.-C., Koch-Vidakovic, T., Sundmacher, K., Platzman, I., and Spatz, J.P.

Sequential bottom-up assembly of mechanically stabilized synthetic cells by microfluidics

Marian Weiss[1,2][†], Johannes Patrick Frohnmayer[1,2][†], Lucia Theresa Benk[1,2][†], Barbara Haller[1,2], Jan-Willi Janiesch[1,2], Thomas Heitkamp[3], Michael Börsch[3], Rafael B. Lira[4], Rumiana Dimova[4], Reinhard Lipowsky[4], Eberhard Bodenschatz[5], Jean-Christophe Baret[6,7], Tanja Vidakovic-Koch[8], Kai Sundmacher[8,9], Ilia Platzman[1,2]★ and Joachim P. Spatz[1,2]★

Compartments for the spatially and temporally controlled assembly of biological processes are essential towards cellular life. Synthetic mimics of cellular compartments based on lipid-based protocells lack the mechanical and chemical stability to allow their manipulation into a complex and fully functional synthetic cell. Here, we present a high-throughput microfluidic method to generate stable, defined sized liposomes termed 'droplet-stabilized giant unilamellar vesicles (dsGUVs)'. The enhanced stability of dsGUVs enables the sequential loading of these compartments with biomolecules, namely purified transmembrane and cytoskeleton proteins by microfluidic pico-injection technology. This constitutes an experimental demonstration of a successful bottom-up assembly of a compartment with contents that would not self-assemble to full functionality when simply mixed together. Following assembly, the stabilizing oil phase and droplet shells are removed to release functional self-supporting protocells to an aqueous phase, enabling them to interact with physiologically relevant matrices.

The formation of lipid membrane-based compartments is one of the distinguishing features of eukaryotic cells. Compartments provide physical and chemical barriers that prevent the uncontrolled diffusion of molecular components to and from the surrounding environment, thereby allowing independent and self-contained metabolic, signalling, or synthesizing activities[1–4]. Moreover, biological membranes allow for chemically selective intra- and intercellular material transport and signal transduction by various transmembrane proteins, such as ion channels and receptors[5,6]. In the context of synthetic biology, protocells are synthetic, biomolecule-containing, lipid-based compartments. These compartments can either be small, large or giant unilamellar vesicles (SUVs, LUVs or GUVs)[7,8]. The chemical and mechanical instabilities of phospholipids under high ionic strength conditions, especially multivalent cations, and their sensitivity to pH changes are considered to be the main challenges in utilizing protocells for synthetic biology[9–11]. In addition, inserting molecules into protocells represents a particular challenge given their impermeability and mechanical instability[12].

Polymersomes made from amphiphilic block copolymers constitute alternative compartments to protocells. They enclose and are surrounded by an aqueous solution[13]. Some polymersomes can be engineered with transmembrane proteins or synthetic channel molecules that enable certain chemicals to pass the polymer membrane[14,15]. They are both chemically and mechanically more stable than protocells and are adjustable to certain environments and functionalities[13]. In contrast to GUVs, where the manipulation of chemical and physical properties bears limitations, the thickness, bending and stretching moduli of the polymeric membrane is tuned by changing the block-copolymer molecular properties. However, the encapsulation of biomolecules and further manipulation of traditional water-in-water polymersomes still represent challenges. The uncontrolled permeability of the polymersomes[16,17] and a lack of technologies which allow for the precise and efficient delivery of different biological components are the main drawbacks.

In contrast to polymersomes, copolymer-stabilized water-in-oil droplet compartments can be manipulated at high throughput using automated microfluidic technologies[18,19]. The biophysical properties of droplet-based compartments, their ultra-fast generation (up to 1 MHz), and the high degree to which this micro-environment is controllable add up to a system that combines the necessary requirements of various synthetic biology applications[20–22]. Moreover, it was shown that the continuous oil phase and its additives play an important role not only in the stable separation of the droplets and in preserving the bio-content[23] but also in the combinatorial delivery of biological materials exclusively into the droplets by means of microfluidic pico-injection technology[24]. However, much like in the case of polymersomes, the ability of the droplets to serve as optimal cell-like compartments is mainly hindered by their inability to imitate the biophysical properties of cellular lipid membranes[17,25].

[1]Department of Cellular Biophysics, Max Planck Institute for Medical Research, Jahnstraße 29, 69120 Heidelberg, Germany. [2]Department of Biophysical Chemistry, University of Heidelberg, Im Neuenheimer Feld 253, 69120 Heidelberg, Germany. [3]Single-Molecule Microscopy Group, Jena University Hospital, Friedrich Schiller University Jena, 07743 Jena, Germany. [4]Theory & Bio-Systems, Max Planck Institute of Colloids and Interfaces, 14424 Potsdam, Germany. [5]Laboratory for Fluid Dynamics, Pattern Formation and Biocomplexity, Max Planck Institute for Dynamics and Self-Organization, 37077 Göttingen, Germany. [6]Droplets, Membranes and Interfaces, Max Planck Institute for Dynamics and Self-Organization, 37077 Göttingen, Germany. [7]Soft Micro Systems, CNRS, Univ. Bordeaux, CRPP, UPR 8641, 115 Avenue Schweitzer, 33600 Pessac, France. [8]Process System Engineering, Max Planck Institute for Dynamics of Complex Technical Systems, 39106 Magdeburg, Germany. [9]Otto-von-Guericke University Magdeburg, Process Systems Engineering, Universitätsplatz 2, 39106 Magdeburg, Germany. [†]These authors contributed equally to this work. *e-mail: ilia.platzman@mpimf-heidelberg.mpg.de; joachim.spatz@mpimf-heidelberg.mpg.de
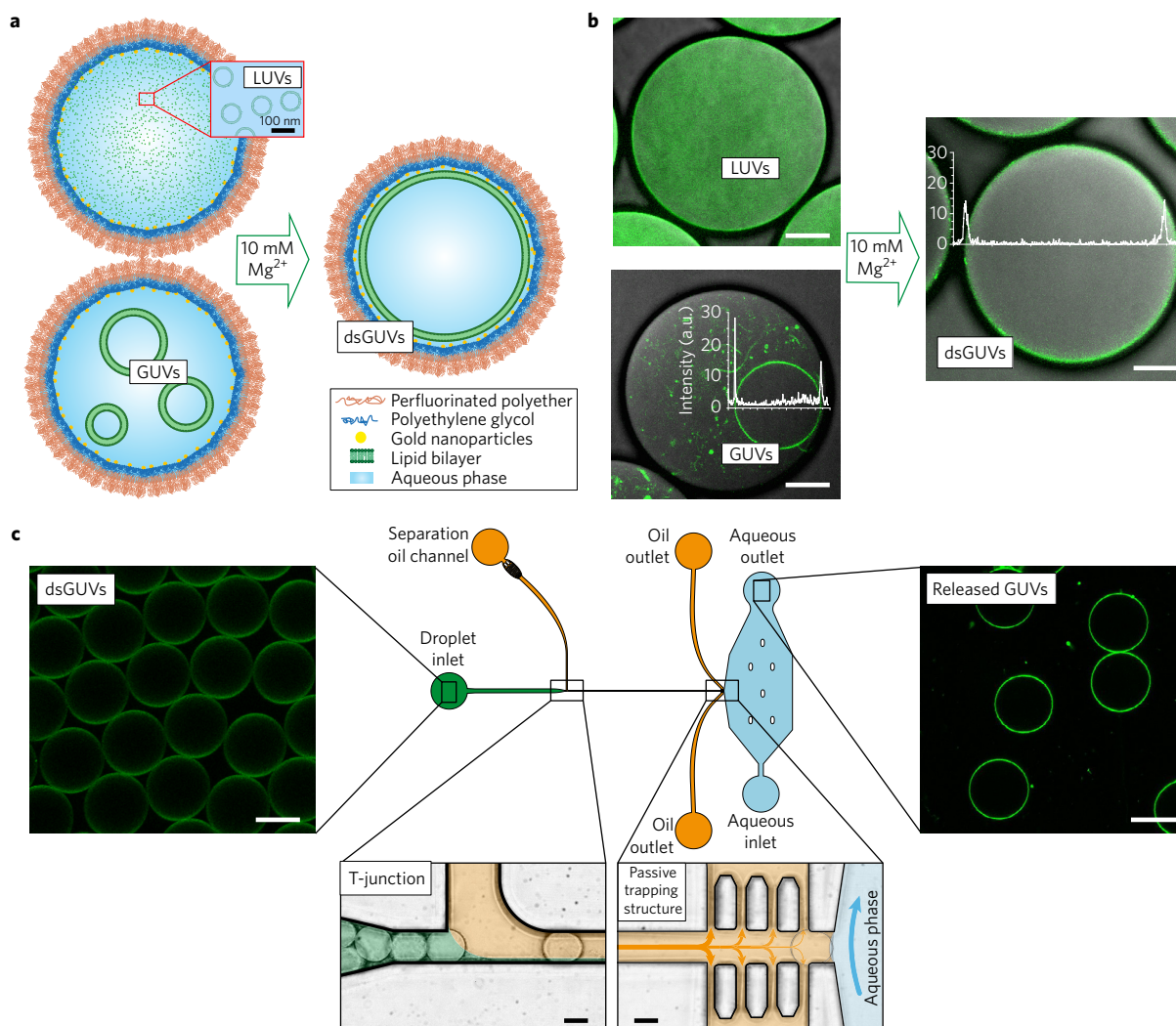
Figure 1 | Formation and analysis of droplet-stabilized GUVs. a, Lipid vesicles, either LUVs or GUVs, were encapsulated in water-in-oil copolymer-stabilized droplets by means of microfluidics. To transform the encapsulated vesicles into a supported lipid bilayer at the copolymer-stabilized droplets' inner interface, 10 mM Mg^{2+} was applied during droplet production or by means of pico-injection. **b**, Representative combined images of green fluorescence from lipids (ATTO 488-labelled DOPE) and bright-field microscopy of the encapsulated LUVs and GUVs, and of the dsGUVs. The latter two images show superimposed the fluorescence intensity profile. Scale bar, 10 μm. **c**, The microfluidic device designed to release the assembled lipid compartments from the surrounding stabilizing polymer droplets into the aqueous phase. The left image shows the fluorescence images of the monodisperse dsGUVs in the oil phase prior to release. After injection, droplets are separated from each other at a T-junction where a tributary oil flow containing 20 vol% destabilizing surfactants merges with the droplet flow. Passive trapping structures within the microfluidic channel enable the draining of the continuous oil phase into adjacent oil outlets and decelerate the droplets before they enter the aqueous phase. A comparison of dsGUVs and released lipid compartments shows that they are comparable in size. Scale bars, 20 μm.

In this study, we present an approach that merges lipid vesicles and copolymer-stabilized droplets to generate mechanically and chemically stable cell-like compartments, which we have called droplet-stabilized GUVs (dsGUVs). These compartments can be sequentially loaded with biomolecules by means of pico-injection technology and offer a well-defined micro-environment for a real step-by-step bottom-up assembly of intracellular modules with desired features. Moreover, the model systems were released from the oil phase and stabilizing droplets after assembly, thus paving the way towards interactions of these synthetic cells with physiologically relevant environments such as extracellular matrices, cells or signalling proteins.

Formation of dsGUVs and their analysis

Droplet-based microfluidics allows for high-throughput generation of monodisperse droplets, thus enabling the precise estimation of the lipid concentration required for the formation of a continuous lipid bilayer at the droplets' inner interface of the polymer shell (Supplementary Note 1 and Supplementary Fig. 1). The determined optimal amount (800 μM) of various lipid compositions in the form of LUVs or GUVs was dissolved in Milli-Q water and encapsulated into copolymer-stabilized droplets of 40 μm diameter (Supplementary Methods). The lipid-containing droplets are shown in Fig. 1a,b. To transform the encapsulated vesicles into a continuous supported lipid bilayer at the droplets' inner interface, a solution with optimized $MgCl_2$ concentration of 10 mM was introduced during droplet production or by means of pico-injection (Supplementary Methods). In the case of droplets containing LUVs, the formation of the continuous lipid bilayer was detected within a few seconds. The formation of a dsGUV out of the GUVs was considerably slower (in the range of 30 min) due to the slow diffusion of the GUVs towards the droplets' interface (Supplementary Note 2 and Supplementary Movie 1). Mg^{2+} ions are considered to be the most efficient mediators of lipid vesicle

Table 1 | Lipid diffusion coefficients obtained by FRAP measurements.

Lipid composition	D (μm² s⁻¹)	Lipid-based compartment
DOPC:DOPE:DOPS(8:1:1), 1% ATTO488-DOPE	3.52 ± 0.26	GUV formed by electroformation and encapsulated into droplet
Egg PC:Egg PG (1:1), 1% ATTO488-DOPE	3.96 ± 0.51	GUV formed by electroformation and encapsulated into droplet
DOPC, 1% RhB-DOPE	4.42 ± 0.65	GUV formed by electroformation and encapsulated into droplet
DOPC:DOPE:DOPS(8:1:1), 1% ATTO488-DOPE	3.31 ± 0.77	dsGUV
Egg PC:Egg PG (1:1), 1% ATTO488-DOPE	2.88 ± 0.06	dsGUV
DOPC, 1% RhB-DOPE	4.11 ± 0.59	dsGUV
DOPC:Chol:DOPS(8:1:1), 1% ATTO488-DOPE	4.03 ± 0.56	dsGUV
DOPC:Chol:DOPS(8:1:1), 1% ATTO488-DOPE	4.24 ± 0.94	Released lipid compartment
DOPC:Chol:DOPS(8:1:1), 1% ATTO488-DOPE	4.43 ± 1.23	GUV formed by electroformation

rupture, because they promote adhesion to a supporting surface[10,26]. It is worth mentioning that neither the addition of Ca^{2+} (10 mM) nor lower concentrations of Mg^{2+} (1 mM) as tested using the same lipid concentration could obtain comprehensive vesicle fusion to the droplets' inner surface (Supplementary Fig. 2).

To assess the formation process and the dynamics of the assembled dsGUV lipid bilayer, fluorescence intensity analyses, fluorescence recovery after photobleaching (FRAP) measurements, and the release of GUVs from the stabilizing droplet shell were performed. The insets in Fig. 1b show representative fluorescence intensity profiles of the encapsulated GUVs and the dsGUVs (both with identical lipid compositions), evaluated with a laser scanning confocal microscope using the same acquisition conditions (Methods). A fit to the profile revealed similar integrated intensity values of 42 ± 8 and 44 ± 4 (arbitrary intensity units) for dsGUVs and encapsulated GUVs, respectively. These findings may indicate a similar lipid density for dsGUVs and GUVs.

FRAP measurements (Table 1) revealed slightly lower lipid mobility in dsGUVs compared to encapsulated free-standing GUVs (Supplementary Methods and Supplementary Note 3). This can be attributed to the fact that the supported lipid membrane is subject to perturbations from the inner interface of the copolymer-stabilized droplet. Previous reports found a similar or an even lower diffusion coefficient for planar supported lipid membranes in comparison to free-standing GUVs[27,28].

Importantly, a microfluidic release device was developed to transfer the assembled lipid compartments into a physiologically relevant, aqueous phase (Fig. 1c, Methods). The release of the assembled lipid compartments (Methods) from the stabilizing polymer droplets into the aqueous phase is shown in Fig. 1c. As can be observed from the fluorescence images, the diameter of the released GUVs (26.2 ± 1.2 μm) in the aqueous phase is slightly smaller compared to that of the dsGUV prior to release (28.3 ± 0.6 μm). A slight shrinkage of the released GUVs can be explained by the change of the osmotic balance. FRAP measurements performed on the released GUVs and on those formed by traditional electroformation (consisting of the same lipid composition) revealed similar lipid mobility (Table 1).

Biofunctionalization of dsGUVs

To test the ability of the dsGUVs to serve as anchoring points for the immobilization of (His-tag) proteins, a lipid solution consisting of 9:1 DOPC:DGS-NTA(Ni) (220 μM) and (His6)-GFP was encapsulated into copolymer-stabilized droplet shells (Methods). The analysis of the fluorescence images of the (His6)-GFP inside the dsGUVs revealed the localization of the fluorescence signal at the periphery of the dsGUV—in other words, the same place at which the anchor DGS-NTA(Ni^{2+}) lipids are situated (Supplementary Fig. 3a). In contrast, a homogeneously distributed fluorescence signal was observed inside non-functionalized dsGUVs (Supplementary Fig. 3b).

FRAP measurements were performed to assess the kinetics of diffusion within the GFP-linked copolymer-stabilized droplets[21] and the GFP-linked dsGUVs (Supplementary Fig. 3c). Data analysis revealed diffusion coefficients of 1.22 ± 0.03 and 0.20 ± 0.05 μm² s⁻¹ for proteins linked to the lipid bilayer or to the polymer membrane, respectively.

Sequential assembly of sub-cellular units into the dsGUVs

To construct cellular modules by means of bottom-up assembly, an automated microfluidic approach was adapted to allow for the sequential loading of various sub-cellular functional units into the dsGUVs. Towards this end, we incorporated transmembrane proteins (integrin and ATP synthase) and cytoskeletal proteins (G-actin and tubulin) into the dsGUVs (Fig. 2).

Following the formation of the dsGUVs, we used a pico-injection system[24] to inject and to fuse transmembrane protein-containing proteoliposomes, that is, liposomes containing TAMRA-labelled $\alpha_{IIb}\beta_3$ integrin or Alexa 488-labelled F_oF_1-ATP synthase (Methods), with the dsGUVs composed of 8:1:1 DOPC:DOPE:DOPS. Lipid labelling was obtained by adding either 1% ATTO 488-labelled DOPE or 1% Rhodamine B (RhB)-labelled DOPE. The co-localization of the integrin or the F_oF_1-ATP synthase with the lipid fluorescence signals is shown in Fig. 3a, indicating the successful fusion of the proteoliposomes with the dsGUVs. As a control, we injected F_oF_1-ATP synthase into copolymer-stabilized droplets without any dsGUVs, and mixed these droplets with dsGUVs containing F_oF_1-ATP synthase. It should be noted that only within the dsGUV was the F_oF_1-ATP synthase fused with the periphery. In the case of droplets without dsGUVs, F_oF_1-ATP synthases were distributed homogeneously within the entire droplet. Similar results were obtained for integrin. This clearly indicates that transmembrane proteins such as F_oF_1-ATP synthase or integrin need the formation of a dsGUV to fuse with the lipid bilayer on the droplet periphery.

FRAP measurements of transmembrane proteins reconstituted into dsGUVs revealed diffusion coefficients of 1.20 ± 0.7 and 0.70 ± 0.1 μm² s⁻¹ for F_oF_1-ATP synthase and integrin, respectively. This value is in good agreement with previously published studies on integrin $\alpha_{IIb}\beta_3$ mobility in planar supported lipid bilayers and in cellular membranes[29–31]. Moreover, to test the functionality of the reconstituted integrin, RGD peptides anchored to gold-linked surfactants[21,32] (Methods) were used to provide binding sites for integrin adhesion (Fig. 3b). In this case, the diffusion coefficient of integrin dropped to 0.13 ± 0.03 μm² s⁻¹, consistent with the mobility of the copolymer surfactant layer that stabilizes the droplet. Successful binding between the integrin and the RGD on the droplet interface indicates the functional incorporation of integrin into the lipid bilayer of the dsGUVs. It also reveals that at least some of the integrin proteins are oriented correctly, with their extracellular parts pointing towards the inner interface of the copolymer-stabilized droplet. It should be mentioned that the establishment of a methodology for integrating membrane proteins into lipid bilayers
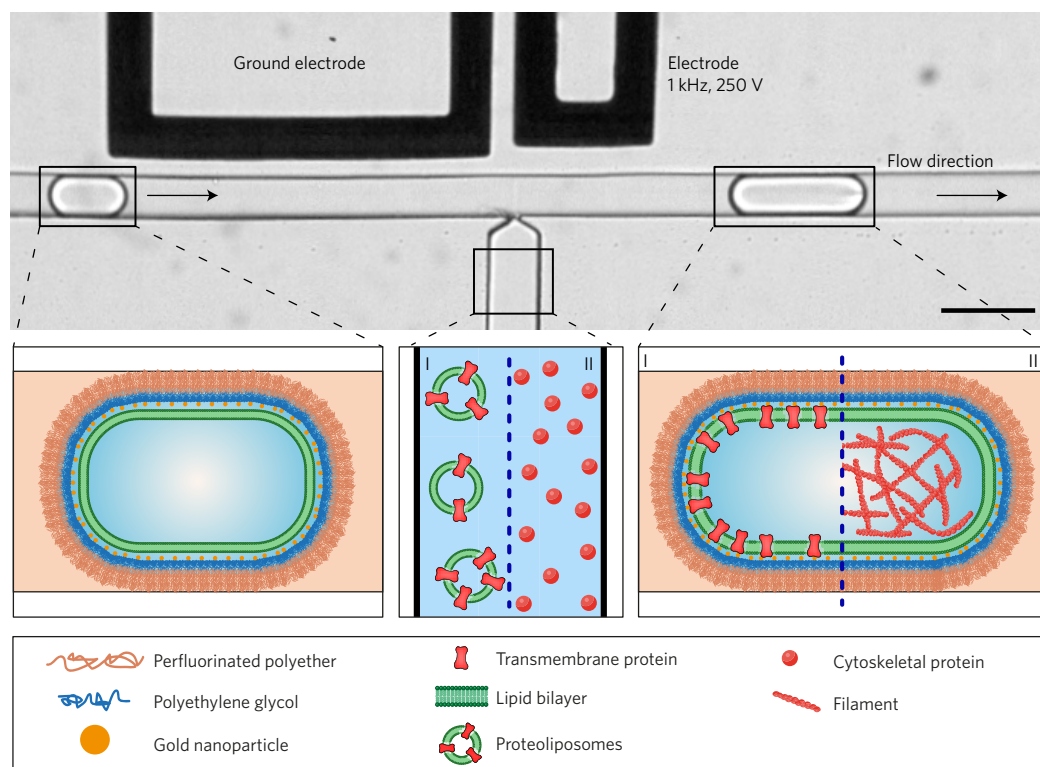
Figure 2 | Sequential bottom-up assembly of dsGUV cell-like compartments. Schematic representation of the process for incorporating transmembrane and cytoskeletal proteins into dsGUVs by means of high-throughput droplet-based pico-injection technology. Scale bar, 50 μm.

with a specific orientation is not in the scope of this work, but is an important task for future studies.

For the activity assessment of the reconstituted F_oF_1-ATP synthase in dsGUVs, an acidic FC-40 oil was added to the oil phase. This addition resulted in the establishment of a transmembrane pH gradient (ΔpH) as a driving force for ATP synthesis inside the droplets (Methods and Fig. 3c). Following 2 min incubation time, the aqueous content of the dsGUVs was released and the synthesized ATP concentration was determined by means of bioluminescence luciferase in a plate reader (Methods). A total amount of 5 nM ATP was measured in the released solution (Fig. 3c and Methods), which indicates the functional reconstitution of the F_oF_1-ATP synthases in the dsGUVs. It also reveals that at least some of the F_oF_1-ATP synthases are oriented correctly—that is, the F_1 portion is pointing towards the inside of the dsGUV. The low concentration of synthesized ATP can be attributed to the lack of a sufficient transmembrane electric potential gradient[33]. Moreover, the time delay between generating the proton motive force for ATP synthesis and the determination of the produced ATP was long so that enzyme-catalysed and pH-dependent ATP hydrolysis could reduce the amount of the remaining ATP. The drop of ATP over time as measured in the plate reader is attributed to the kinetic instability of ATP (Fig. 3c).

The same pico-injection approach was applied to obtain a bottom-up reconstitution of the actin cytoskeleton or microtubules within the dsGUVs (Methods). Towards this end, we proceeded by the following two-step process: the formation of dsGUVs (90% DOPC, 9% DOPS and 1% RhB-DOPE) in the presence of an actin or tubulin polymerization buffer; the pico-injection of G-actin (10 μM final concentration, including 1% Alexa 488-labelled G-actin) or tubulin (10 μM final concentration, including 10% ATTO 488-labelled tubulin) solution into the dsGUVs. Moreover, we compared this pico-injection approach to the premixed (one-step) approach, in which G-actin or tubulin proteins were mixed with LUVs prior to droplet formation (Methods).

The successful reconstitution of the actin filaments and microtubules within the dsGUVs could be obtained by sequential pico-injection only (Fig. 3d, middle panel). When using the one-step premixed approach, vesicle fusion to the droplets' inner surface was suppressed. In the case of microtubules none, and in the case of F-actin only partial fusion, was observed (Fig. 3d, top panel). The inability to form dsGUVs in the presence of microtubules is related to the fact that LUVs are subject to perturbations stemming from the amphiphilic nature of tubulin[34]. The sequential pico-injection approach enables the prior formation of stable dsGUVs with appropriate ionic conditions followed by the injection of proteins without perturbing the lipid bilayer of the dsGUVs.

Release of GUVs into physiological environments

To pave the way towards investigations of protocell interactions with physiological environments, we developed both a bulk and a microfluidic method to release assembled GUVs with or without proteins from the oil phase and stabilizing droplet shell to the water phase (Methods). By dissolving distinctive fluorophores in the oil phase as well as the enclosed and continuous aqueous phase, we could validate that the lipid membrane remains fully intact and impervious during the release process and that no oil residue could be detected in the water phase or the released GUVs (Supplementary Fig. 6). Moreover, to assess the purity of the GUVs, Raman spectra were collected on released GUVs (Supplementary Methods and Supplementary Fig. 7). As can be observed, no oil/surfactants were detected in the Raman spectra of the released GUVs. Additionally, by means of fluctuation analysis we calculated the bending rigidity values ($21.5 \pm 3.4 k_B T$) of released GUVs (Supplementary Methods). This value lies in the range of typical values reported for the bending rigidity of PC membranes[35], suggesting that the bilayers are clean of impurities. Moreover, these values correlate strongly with the bending rigidity values ($25.3 \pm 3.0 k_B T$) of the GUVs, consisting of the same lipid composition and formed by a standard electroformation method (Supplementary Methods).
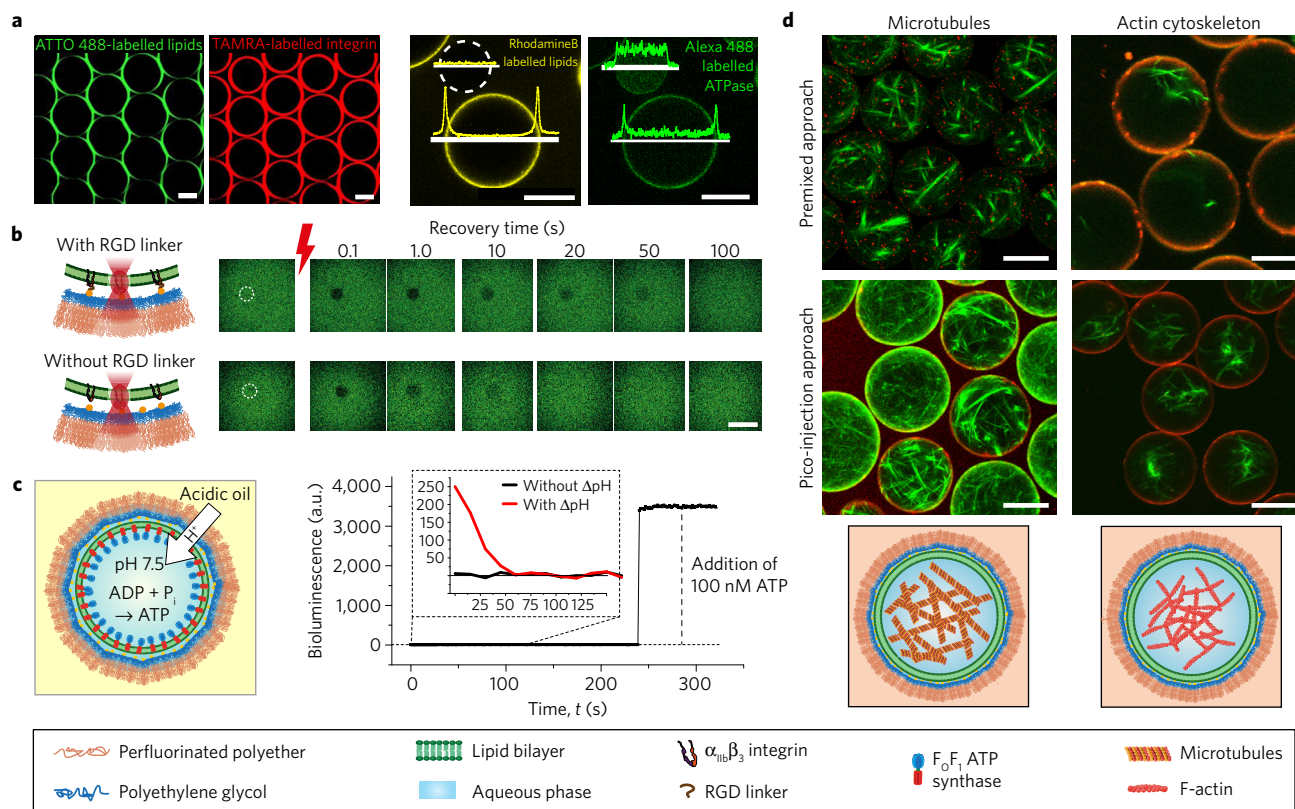
Figure 3 | Incorporation of transmembrane and cytoskeletal proteins into the dsGUV compartments by pico-injection technology. a, The left and right pair of images show representative fluorescence images of the same areas of observation after pico-injection of integrin-containing liposomes (ATTO 488-labelled DOPE lipids in green and TAMRA-labelled $\alpha_{IIb}\beta_3$ integrin in red) and of F_oF_1-ATP synthase-containing liposomes into the dsGUVs (RhB-labelled DOPE lipids in yellow and Alexa 488-labelled F_oF_1-ATP synthase in green), respectively. Superimposed on the right pair of images is the fluorescence intensity profile. Lipids and F_oF_1-ATP synthases clearly co-localize in dsGUVs. Without an inner dsGUV (white dashed circle), the signal from the Alexa 488-labelled F_oF_1-ATP synthase is equally distributed within the droplet. Scale bars, 20 µm. **b**, Schematic illustration and representative results of FRAP measurement of labelled integrin with (top row) and without (bottom row) immobilization to the gold-linked surfactants via RGD peptides. The focus area of the light source is encircled in the pre-bleach frame and the timeline on top indicates when follow-up images were taken. Scale bar, 10 µm. **c**, Schematic illustration of F_oF_1-ATP synthase-reconstituted dsGUVs and of the transmembrane pH gradient—the driving force of ATP synthesis—as achieved by the addition of acidic FC-40 oil. The right graph shows the bioluminescence intensity response to the ATP content as a function of time. The insert shows the representative bioluminescence intensity curves obtained from the aqueous content of dsGUVs activated (red) by a pH gradient and dsGUVs without a pH gradient (black). The bioluminescence curve was calibrated by the addition of 100 nM ATP solution. **d**, Representative fluorescence images of microtubules (10% ATTO 488-labelled tubulin, left panel) or the actin cytoskeleton (1% Alexa 488-labelled actin, right panel) in droplets containing RhB-labelled DOPE lipids, as obtained by either the premixed (top) or the pico-injection approach (bottom). Scale bar, 20 µm.

To demonstrate the interactions of the released protocells with physiological environments, Fig. 4 shows optical micrographs of integrin $\alpha_{IIb}\beta_3$- or F-actin-containing dsGUVs and their corresponding protocells in the aqueous phase after release. To validate the functionality of the reconstituted integrin $\alpha_{IIb}\beta_3$, the spreading behaviour of the released integrin $\alpha_{IIb}\beta_3$-functionalized GUVs is investigated. While these integrin $\alpha_{IIb}\beta_3$-protocells do not spread on BSA-coated interfaces, they spread well on fibrinogen but less on fibronectin or collagen matrices as is expected from the platelet adhesion receptor integrin $\alpha_{IIb}\beta_3$ (Fig. 4b and Supplementary Methods and Supplementary Fig. 8; refs 32,36). The differential adhesion on the various matrices further demonstrates that the protein reconstitution and release process does not affect the biological functionality of the synthetic cells.

In conclusion, the developed technology overcomes fundamental limitations associated with the formation and manipulation of currently existing protocells or polymersomes for the design of complex synthetic cells. Recently developed microfluidic methods showed remarkable success with the high-throughput formation of monodisperse GUVs[37–39]. Moreover, a control over the GUV lipid composition and its asymmetry was achieved by microfluidic

methods such as layer-by-layer lipids assembly[40], pulse-jet[41] and droplet shooting[42]. Despite the progress made in recent years in designing protocells, the major drawback of all of these methods is a lack of ability to sufficiently manipulate the protocell content sequentially. The assembly of a cell-like compartment with distinct functionality requires the combination of different proteins, molecules and buffer conditions that are incompatible when applied to the same spatial confinement all at once. The formation of dsGUVs enables the generation of mechanically and chemically stable compartments which can be loaded sequentially with different proteins and molecules using pico-injection technology. This sequential procedure allows for a combination of molecules and organized molecular structures that would not occur spontaneously. These system properties lay the groundwork for realizing a real bottom-up assembly of rather complex combinations and functions in synthetic compartments. Importantly, the ability to release functional protocells from the stabilizing droplets into water phase paves the way towards investigations of interactions of synthetic cells with physiologically relevant environments such as given by extracellular matrices, cells, viruses or signalling molecules. Finally, it is worthwhile mentioning that the formation of synthetic cells by this technology is a
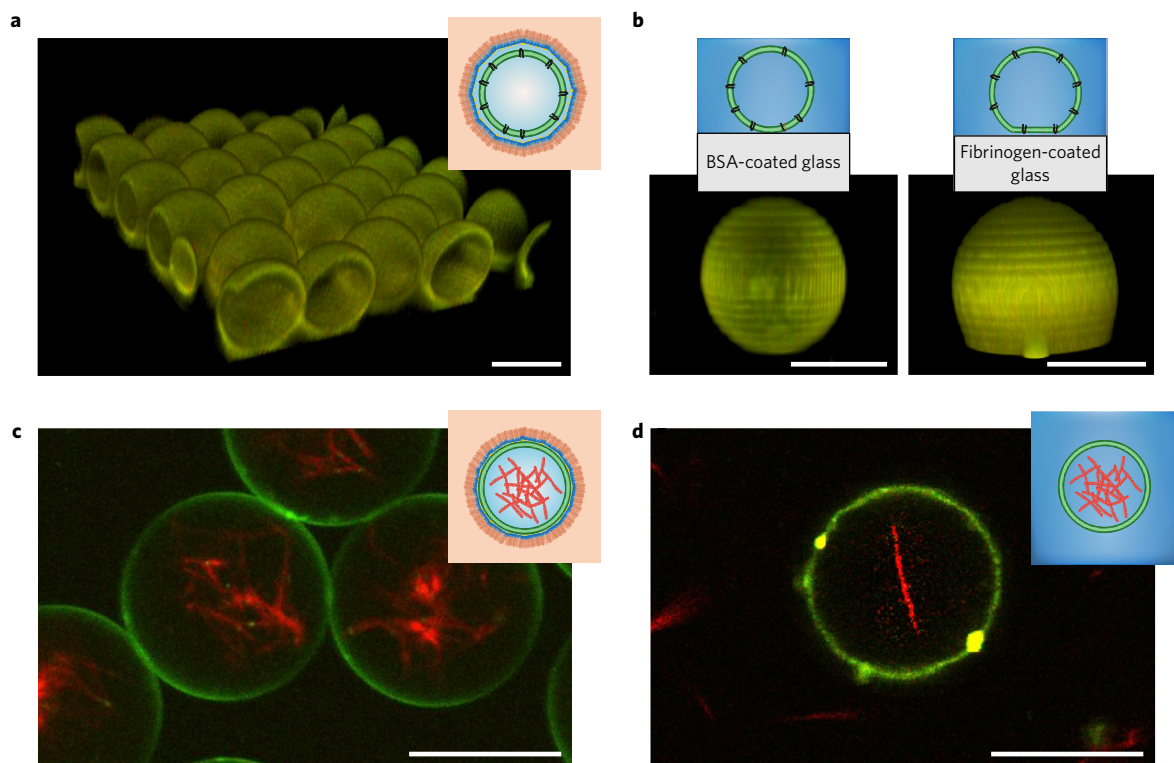
Figure 4 | Release of actin- and integrin-reconstituted GUVs. a,b, Representative 3D reconstitution of confocal images of dsGUVs with reconstituted integrin (**a**) and released lipid compartments with reconstituted integrin in contact with BSA- (left image) and fibrinogen-coated (right image) glass surfaces (**b**). The merged fluorescence signals include both ATTO 488-labelled DOPE lipids and TAMRA-labelled $\alpha_{IIb}\beta_3$ integrin. **c,d**, Representative fluorescence images of the actin cytoskeleton-containing dsGUVs (**c**) and of the released actin cytoskeleton-containing lipid compartments (**d**). The fluorescence signals correspond to Alexa 488-labelled actin (red) and RhB-labelled DOPE lipids (green). Scale bar, 20 μm.

high-throughput method enabling the generation of up to 10^3 functional compartments per second. As a result, it generates a vast number of synthetic cells of unique and precise composition, which can be applied for follow-up scientific and technological applications.

Methods

Methods, including statements of data availability and any associated accession codes and references, are available in the online version of this paper.

References

1. Szostak, J. W., Bartel, D. P. & Luisi, P. L. Synthesizing life. *Nature* **409**, 387–390 (2001).
2. Tawfik, D. S. & Griffiths, A. D. Man-made cell-like compartments for molecular evolution. *Nat. Biotechnol.* **16**, 652–656 (1998).
3. Diekmann, Y. & Pereira-Leal, J. B. Evolution of intracellular compartmentalization. *Biochem. J.* **449**, 319–331 (2013).
4. Agapakis, C. M., Boyle, P. M. & Silver, P. A. Natural strategies for the spatial optimization of metabolism in synthetic biology. *Nat. Chem. Biol.* **8**, 527–535 (2012).
5. Yoshida, M., Muneyuki, E. & Hisabori, T. ATP synthase—A marvellous rotary engine of the cell. *Nat. Rev. Mol. Cell Biol.* **2**, 669–677 (2001).
6. Geiger, B., Spatz, J. P. & Bershadsky, A. D. Environmental sensing through focal adhesions. *Nat. Rev. Mol. Cell Biol.* **10**, 21–33 (2009).
7. Nomura, S. M. *et al*. Gene expression within cell-sized lipid vesicles. *Chembiochem* **4**, 1172–1175 (2003).
8. Merkle, D., Kahya, N. & Schwille, P. Reconstitution and anchoring of cytoskeleton inside giant unilamellar vesicles. *Chembiochem* **9**, 2673–2681 (2008).
9. Hardy, G. J., Nayak, R. & Zauscher, S. Model cell membranes: techniques to form complex biomimetic supported lipid bilayers via vesicle fusion. *Curr. Opin. Colloid Interface Sci.* **18**, 448–458 (2013).

10. Seantier, B. & Kasemo, B. Influence of mono- and divalent ions on the formation of supported phospholipid bilayers via vesicle adsorption. *Langmuir* **25**, 5767–5772 (2009).
11. Shigematsu, T., Koshiyama, K. & Wada, S. Effects of stretching speed on mechanical rupture of phospholipid/cholesterol bilayers: molecular dynamics simulation. *Sci. Rep.* **5**, 15369 (2015).
12. Jorgensen, I. L., Kemmer, G. C. & Pomorski, T. G. Membrane protein reconstitution into giant unilamellar vesicles: a review on current techniques. *Eur. Biophys. J.* **46**, 103–119 (2016).
13. Discher, B. M. *et al*. Polymersomes: tough vesicles made from diblock copolymers. *Science* **284**, 1143–1146 (1999).
14. Palivan, C. G. *et al*. Bioinspired polymer vesicles and membranes for biological and medical applications. *Chem. Soc. Rev.* **45**, 377–411 (2016).
15. Onaca, O., Nallani, M., Ihle, S., Schenk, A. & Schwaneberg, U. Functionalized nanocompartments (Synthosomes): limitations and prospective applications in industrial biotechnology. *Biotechnol. J.* **1**, 795–805 (2006).
16. Picker, A., Nuss, H., Guenoun, P. & Chevallard, C. Polymer vesicles as microreactors for bioinspired calcium carbonate precipitation. *Langmuir* **27**, 3213–3218 (2011).
17. Lee, J. C. M., Santore, M., Bates, F. S. & Discher, D. E. From membranes to melts, rouse to reptation: diffusion in polymersome versus lipid bilayers. *Macromolecules* **35**, 323–326 (2002).
18. Duncombe, T. A., Tentori, A. M. & Herr, A. E. Microfluidics: reframing biological enquiry. *Nat. Rev. Mol. Cell Biol.* **16**, 554–567 (2015).
19. Martino, C. & deMello, A. J. Droplet-based microfluidics for artificial cell generation: a brief review. *Interface Focus* **6**, 20160011 (2016).
20. Schaerli, Y. *et al*. Continuous-flow polymerase chain reaction of single-copy DNA in microfluidic microdroplets. *Anal. Chem.* **81**, 302–306 (2009).
21. Platzman, I., Janiesch, J.-W. & Spatz, J. P. Synthesis of nanostructured and biofunctionalized water-in-oil droplets as tools for homing T cells. *J. Am. Chem. Soc.* **135**, 3339–3342 (2013).
22. Huebner, A. *et al*. Quantitative detection of protein expression in single cells using droplet microfluidics. *Chem. Commun.* **12**, 1218–1220 (2007).
23. Janiesch, J. W. *et al*. Key factors for stable retention of fluorophores and labeled biomolecules in droplet-based microfluidics. *Anal. Chem.* **87**, 2063–2067 (2015).

24. Abate, A. R., Hung, T., Mary, P., Agresti, J. J. & Weitz, D. A. High-throughput injection with microfluidics using picoinjectors. *Proc. Natl Acad. Sci. USA* **107,** 19163–19166 (2010).
25. Itel, F. *et al*. Molecular organization and dynamics in polymersome membranes: a lateral diffusion study. *Macromolecules* **47,** 7588–7596 (2014).
26. Bhatia, T., Husen, P., Ipsen, J. H., Bagatolli, L. A. & Simonsen, A. C. Fluid domain patterns in free-standing membranes captured on a solid support. *Biochim. Biophys. Acta Biomembr.* **1838,** 2503–2510 (2014).
27. Machan, R. & Hof, M. Lipid diffusion in planar membranes investigated by fluorescence correlation spectroscopy. *Biochim. Biophys. Acta* **1798,** 1377–1391 (2010).
28. Przybylo, M. *et al*. Lipid diffusion in giant unilamellar vesicles is more than 2 times faster than in supported phospholipid bilayers under identical conditions. *Langmuir* **22,** 9096–9099 (2006).
29. Goennenwein, S., Tanaka, M., Hu, B., Moroder, L. & Sackmann, E. Functional incorporation of integrins into solid supported membranes on ultrathin films of cellulose: impact on adhesion. *Biophys. J.* **85,** 646–655 (2003).
30. Erb, E. M., Tangemann, K., Bohrmann, B., Muller, B. & Engel, J. Integrin alpha IIb beta 3 reconstituted into lipid bilayers is nonclustered in its activated state but clusters after fibrinogen binding. *Biochemistry* **36,** 7395–7402 (1997).
31. Edel, J. B., Wu, M., Baird, B. & Craighead, H. G. High spatial resolution observation of single-molecule dynamics in living cell membranes. *Biophys. J.* **88,** L43–L45 (2005).
32. Frohnmayer, J. P. *et al*. Minimal synthetic cells to study integrin-mediated adhesion. *Angew. Chem. Int. Ed.* **54,** 12472–12478 (2015).
33. Fischer, S. & Graber, P. Comparison of Delta pH- and Delta phi-driven ATP synthesis catalyzed by the H+-ATPases from *Escherichia coli* or chloroplasts reconstituted into liposomes. *FEBS Lett.* **457,** 327–332 (1999).
34. Wolff, J. Plasma membrane tubulin. *Biochim. Biophys. Acta Biomembr.* **1788,** 1415–1433 (2009).
35. Dimova, R. Recent developments in the field of bending rigidity measurements on membranes. *Adv. Colloid Interface Sci.* **208,** 225–234 (2014).
36. Streicher, P. *et al*. Integrin reconstituted in GUVs: a biomimetic system to study initial steps of cell spreading. *Biochim. Biophys. Acta Biomembr.* **1788,** 2291–2300 (2009).
37. Karamdad, K., Law, R. V., Seddon, J. M., Brooks, N. J. & Ces, O. Preparation and mechanical characterisation of giant unilamellar vesicles by a microfluidic method. *Lab Chip* **15,** 557–562 (2015).
38. Matosevic, S. & Paegel, B. M. Stepwise synthesis of giant unilamellar vesicles on a microfluidic assembly line. *J. Am. Chem. Soc.* **133,** 2798–2800 (2011).
39. Deng, N.-N., Yelleswarapu, M. & Huck, W. T. S. Monodisperse uni- and multicompartment liposomes. *J. Am. Chem. Soc.* **138,** 7584–7591 (2016).
40. Matosevic, S. & Paegel, B. M. Layer-by-layer cell membrane assembly. *Nat. Chem.* **5,** 958–963 (2013).
41. Kamiya, K., Kawano, R., Osaki, T., Akiyoshi, K. & Takeuchi, S. Cell-sized asymmetric lipid vesicles facilitate the investigation of asymmetric membranes. *Nat. Chem.* **8,** 881–889 (2016).
42. Morita, M. *et al*. Droplet-shooting and size-filtration (DSSF) method for synthesis of cell-sized liposomes with controlled lipid compositions. *ChemBioChem* **16,** 2029–2035 (2015).

Additional information

Supplementary information is available in the online version of the paper. Reprints and permissions information is available online at www.nature.com/reprints. Publisher's note: Springer Nature remains neutral with regard to jurisdictional claims in published maps and institutional affiliations. Correspondence and requests for materials should be addressed to I.P. or J.P.S.

Competing financial interests

The authors declare no competing financial interests.

Methods

Fluorescence intensity analysis. To compare the lipid membrane fluorescence intensity of encapsulated GUVs to that of dsGUVs with the same lipid composition (1:1 Egg PC:Egg PG, including 0.5% ATTO488-DOPE), the droplets were evaluated back-to-back, preserving identical settings with a Leica SP5 confocal microscope (Supplementary Methods). More than twenty intensity profiles were extracted for each droplet type using Fiji/ImageJ. Fluorescence analysis of the encapsulated GUVs revealed a reduction in the amplitude and a broadening of the fluorescence intensity profile peak in proximity to the copolymer-stabilized droplet interface (Fig. 1b). This is due to refraction and diffraction at the water–oil phase barrier. To compare the fluorescence intensities, a Gaussian function with a background correction was fitted to the intensity profile peaks using a nonlinear least-squares fit (Matlab 2015 SP1).

Microfluidic release device. A high-throughput microfluidic device was developed to release assembled lipid compartments from the stabilizing polymer droplet shells into the aqueous phase (Fig. 1c). All flows inside the device were controlled by a microfluidic flow control system (MFCS-EZ, Fluigent). To minimize shear forces, the height of the channels was designed to exceed the droplet diameter, and the pressure in the inlet channels was adjusted to a maximum of 20 mbar with minor corrections for individual devices and experimental conditions. The dsGUVs were injected into the inlet channel of the release device and isolated at the T-junction where a tributary oil flow containing 20 vol% perfluoro-1-octanol destabilizing surfactants (Sigma-Aldrich) joins. The total flow was adjusted to allow efficient time for the destabilizing surfactants to replace and displace stabilizing surfactants prior to reaching the release unit. In this unit, the dsGUVs encounter the aqueous phase in a wide perpendicular channel. To minimize the mechanical impact on the droplets at the oil/water junction, the droplets were decelerated using passive trapping structures within the microfluidic channels (that is, rows of pillars separated by distances smaller than the representative droplet dimensions), which we designed for this purpose (Supplementary Movie 2)[43].

To avoid oil penetrating into the aqueous channel whenever there were no droplets in the trapping structures, the aqueous flow was adjusted to achieve a zero-pressure gradient at the oil/water junction. As a result, the oil flows into the adjacent oil outlet channels without droplets blocking the slits. Whenever a droplet enters, it blocks the first slits on both sides, thereby increasing the pressure. As the droplet flows along the passive trapping structures, it passes pairs of slits, opening these up for oil flow to the oil outlet channels. With each pair of slits that opens up, the channel cross section for the oil flow to the adjacent oil channels increases, subsequently decreasing the pressure that is pushing the droplet along the channel. The droplet decelerates as it approaches the oil–water interface. Upon contact with the aqueous phase, the residual surfactant layer peels off the droplet's polymer shell, which flows to the oil outlet channel. This releases the droplet's aqueous content (including the lipid compartments) into the aqueous phase with the appropriate ionic conditions.

Lipid composition for release. The release efficiency of GUVs was found to be dependent on the lipid composition. A few general key factors for the stability of lipid bilayers have been identified. First, for better stability of self-supporting released GUVs 10–20 mol% cholesterol were included (C8667, Sigma-Aldrich) for the release experiments. The lipid composition used for the results presented in Fig. 1c, consisted of a molar ratio of 4:4:2 of DOPC, POPC and cholesterol, respectively and included 0.5% Atto488-DOPE for observation. Second, in the case of negatively charged GUVs, release efficiency was affected when lipid compositions exceeded a net concentration of 10 mol% of negatively charged lipids. Therefore, the optimized lipid composition for the release experiments of negatively charged GUVs consisted of a molar ratio of 1:8:1 of DOPG, DOPC and cholesterol, respectively.

RGD-peptide immobilization to the gold-linked surfactants. To provide integrin adhesion sites inside the gold-nanostructured droplets, a two-step method to immobilize SN528 RGD peptides[32] (kindly provided by Kessler's group from TU Munich) on gold nanoparticles via its thiol linker was followed[21]. The freeze-dried Au-PEG(436 g mol^{-1})-PFPE(7,000 g mol^{-1}) diblock-copolymer surfactant was dissolved in 100 μl fluorinated FC-40 oil. Next, the aqueous RGD-peptide solution (50 μM, 100 μl) was added and everything was stirred for 1 h. To remove the unbound RGD peptides, the crude product solution was centrifuged. The supernatant solution was removed and the precipitant was freeze-dried for 24 h to completely remove the remaining water. Finally, the product was dissolved in 1 ml of FC-40 oil and filtered with a hydrophobic filter (PTFE 0.2 μm) to remove traces of unreacted peptide.

GFP immobilization. (His6)-GFP was a gift from S. Gardia, Addgene, plasmid #29663. The protein was expressed in *Escherichia coli* using standard protocols and purified by Ni-NTA chromatography. The linkage of (His6)-GFP to gold-linked surfactants via Ni-NTA-thiol was performed as previously described[21], with the

exception that purified Milli-Q water (Millipore filtered) was used as the aqueous phase instead of PBS buffer. To link (His6)-GFP to the lipid bilayer, the following procedure was applied. NiCl$_2$ (9 μl, 100 mM, Fluka) was mixed with a water solution of DGS-NTA lipids (300 μl, 1 mM) and stirred for 20 min. LUVs produced from 9:1 DOPC:DGS-NTA(Ni) (220 μM) were encapsulated into copolymer-stabilized droplet shells (100 μm diameter). Following encapsulation, a water solution containing (His6)-GFP (10 μM) and MgCl$_2$ (10 mM) was pico-injected into the droplets to form GFP-linked dsGUVs.

Integrin purification labelling and reconstitution. Integrin $\alpha_{IIb}\beta_3$ was purified from outdated human blood platelets (Katharinenhospital Stuttgart) using TBS and Triton X-100 according to a previously reported protocol[32]. Affinity chromatography over Concanavalin A and Heparin columns was followed by gel filtration over a Superdex 200 Prep Grade column (GE Healthcare). The biological activity of the purified integrin was analysed by an enzyme-linked immunosorbent assay (ELISA) using AB1967 anti-integrin α_{IIb} antibodies (Merck Millipore). Following purification, integrin was stored at $-80\,°C$ in TRIS storage buffer, consisting of 20 mM TRIS/HCl pH 7.4, 150 mM NaCl, 1 mM CaCl$_2$, 1 mM MgCl$_2$, 0.1% (w/v) Triton X-100, 0.02% (w/v) NaN$_3$ and 2 mg ml^{-1} Aprotinin. Integrin $\alpha_{IIb}\beta_3$ was labelled with 5-(and-6)-carboxytetramethylrhodamine, succinimidyl ester, #C1171 TAMRA (Life Technologies) according to a previously published protocol[44]. A dye/protein ratio of 1.0 to 1.2 was measured by molecular dye extinction ($\varepsilon_{555} = 80,000$ mol^{-1}cm^{-1}). Functionality was measured with an ELISA binding assay.

Integrin reconstitution into the liposomes followed a previously published protocol[30]. In brief, 50 mol% of Egg PC and Egg PG were dried under a gentle stream of nitrogen and then placed under vacuum conditions overnight. Dried lipids were dissolved in 1 ml of TRIS buffer, consisting of 20 mM TRIS/HCl, pH 7.4, 50 mM NaCl, 0.5 mM CaCl$_2$ and 0.1% (w/v) Triton X-100, and integrin was added to a final 1:1,000 integrin–lipid ratio and incubated in the solution at 37 °C for 2 h. Triton X-100 was removed in two subsequent washing steps of 3.5 h each using 50 mg ml^{-1} BT Bio-Beads SM-2 (#152-8920, BIO-RAD). The size distribution of the liposomes and integrin-reconstituted proteoliposomes was measured by dynamic light scattering (DLS) in a Malvern Zetasizer (Nano ZS). Pico-injection technology was used to inject the integrin liposomes into the dsGUVs, which contained integrin activation buffer (20 mM TRIS/HCl, pH 7.4, 50 mM NaCl, 0.5 mM CaCl$_2$, 1 mM MnCl$_2$ and 1 mM MgCl$_2$). Theoretical estimation of the number of integrin proteins that might be reconstituted into dsGUVs is presented in Supplementary Note 4.

For the release of integrin-reconstituted GUVs from the stabilizing droplet shells, integrin was reconstituted into liposomes consisting of 100% EggPC. These proteoliposomes were mixed at a ratio of 1:9 with liposomes containing 4:3:2 DOPC:POPC:cholesterol including 1% ATTO 488-labelled DOPE and used for dsGUV formation.

F$_o$F$_1$-ATP synthase purification, labelling, reconstitution and activity assessment. The purification of F$_o$F$_1$-ATP synthase from *E. coli* and subsequent cysteine labelling at the C terminus of subunit *a* with Alexa 488 maleimide were performed according to the protocols described in Zimmermann *et al.*[45] and Heitkamp and colleagues[46]. Labelled (or unlabelled) F$_o$F$_1$-ATP synthase was reconstituted into preformed liposomes (∼120 nm diameter) as described in Fischer and Gräber[33] and stored at $-80\,°C$ in tricine buffer, consisting of 20 mM tricine–NaOH (pH 8.0), 20 mM succinic acid, 0.6 mM KCl, 50 mM NaCl and 2.5 mM MgCl$_2$. Pico-injection technology was used to inject the F$_o$F$_1$-ATP synthase liposomes into the dsGUVs, which contained F$_o$F$_1$-ATP activity buffer, consisting of 20 mM tricine–NaOH (pH 7.5), 20 mM succinic acid, 10 mM MgCl$_2$, 5 mM NaH$_2$PO$_4$ and 50 μM ultra-pure ADP (Cell Technology).

For the activity assessment of the reconstituted F$_o$F$_1$-ATP synthase in dsGUVs the ATP synthase has to be energized by a transmembrane pH gradient established between the F$_o$F$_1$-ATP synthase-containing dsGUVs and the surrounding oil. To generate a pH gradient (ΔpH $\approx$ 3), 1μl of trifluoroacetic acid (TFA, 99%, Sigma-Aldrich) was dissolved in 1 ml FC-40 oil[47] and an oil exchange was performed. Following the application of the acidic oil, the change in the droplets' internal pH through proton diffusion was analysed by pyranine intensity detection (Supplementary Movie 3 and Supplementary Fig. 10)[48].

Following the reconstitution of the F$_o$F$_1$-ATP synthases in dsGUVs, 100 μl oil/dsGUVs solution was transferred to a 500 μl Eppendorf tube and 20 μl of acidic FC-40 oil was added by pipetting. The Eppendorf tube was carefully tilted and slowly rotated for 2 min. Then, 5 μl of perfluoro-1-octanol 20 vol% destabilizing surfactants (Sigma-Aldrich) was added to release the content of the droplets. To analyse the ATP content, 5 μl of the released aqueous solution was transferred to a well on a non-transparent 96-well plate with a flat bottom, containing 180 μl tricine buffer and 20 μl of 10-fold concentrated luciferase reagent (ATP Bioluminescence Kit CLS II, Sigma-Aldrich). A plate reader (Infinite M200, Tecan) was used to detect the bioluminescence intensity corresponding to the synthesized ATP in the aqueous solution. As a control, the same amount of aqueous solution was released

from the F_oF_1-ATP synthase-containing dsGUVs that were not energized by a transmembrane pH gradient and analysed. To assess the amount of synthesized ATP, a bioluminescence calibration curve was produced by the addition of 100 nM ATP solution.

Actin polymerization within dsGUVs. Actin was purchased from Cytoskeleton. Actin was stored in TRIS storage buffer, consisting of 2.0 mM TRIS/HCl pH 8, 0.2 mM CaCl$_2$, 0.2 mM ATP, 0.005% NaN$_3$ and 0.2 mM DTT, at −80 °C. Human recombinant fascin was purchased from Novubio (Bio-Techne), aliquoted and stored at −80 °C. 1% of Alexa 488-labelled actin (Life Technologies) was added to the non-labelled actin in all experiments to detect actin filament formation. To polymerize actin inside the dsGUVs, two methods were tested:

Premixed approach: Lipid and G-actin solutions were introduced via a microfluidic aqueous two-phase system (Supplementary Fig. 4C). To avoid polymerization prior to droplet formation, one aqueous phase contained 10 μM actin (1% Alexa 488-labelled actin) in storage buffer and the other aqueous phase contained the polymerization buffer (2.0 mM TRIS/HCl pH 8, 20 mM MgCl$_2$, 0.2 mM CaCl$_2$, 0.5 mM ATP, 0.005% NaN$_3$ and 0.2 mM DTT), 0.5 μM fascin and LUV solution consisting of 90% DOPC, 9% DOPS and 1% RhB-DOPE. The two aqueous phases were mixed during droplet generation at a flow-focusing junction (Supplementary Fig. 4).

Pico-injection approach: Two experimental steps were required for stable F-actin creation in dsGUVs. The first step entailed the creation of dsGUVs (90% DOPC, 9% DOPS and 1% RhB-DOPE) that contain actin polymerization buffer. The second step was the pico-injection of storage buffer containing G-actin (10 μM final concentration) and fascin (0.5 μM final concentration) into these droplets.

For the release of F-actin-containing GUVs a lipid composition of DOPC:cholesterol:DOPG (76 mol% DOPC, 20 mol% cholesterol, 3 mol% DOPG including 1 mol% RhB-labelled DOPE) was used when creating the dsGUVs.

Microtubule formation within dsGUVs. Tubulin (kindly provided by Surrey's group, the Francis Crick Institute) was purified from pig brain according to previously described protocols[49]. It was then labelled with ATTO 488-SE (Life Technologies) as described earlier[50]. Tubulin concentrations were measured using UV spectroscopy ($\varepsilon_{280} = 115,000 \text{ M}^{-1}\text{cm}^{-1}$). The labelling ratio of ATTO 488-labelled tubulin was 0.65 dye molecules per tubulin dimer. Labelled and unlabelled tubulin were stored at −80 °C in PIPES storage buffer (20 mM PIPES pH 6.8, 7.25 mM MgCl$_2$, 1 mM EGTA, 1 mM 2-mercaptoethanol, 50 mM KCl, 31 mM glucose, 1 mg ml^{-1} glucose oxidase and 0.5 mg ml^{-1} catalase and 0.25 mg ml^{-1} beta-casein). To form microtubule networks inside the dsGUVs, two methods were tested:

Premixed approach: Tubulin 14.5 μM (10% labelled with ATTO 488-SE) dissolved in polymerization buffer (20 mM PIPES pH 6.8, 7.25 mM MgCl$_2$, 1 mM EGTA, 3 mM GTP, 1 mM 2-mercaptoethanol, 50 mM KCl, 31 mM glucose, 1 mg ml^{-1} glucose oxidase and 0.5 mg ml^{-1} catalase, 0.25 mg ml^{-1} beta-casein) was mixed with the LUV solution (90% DOPC, 9% DOPS and 1% RhB-DOPE) and introduced into the microfluidic device via an aqueous channel. To avoid tubulin polymerization prior to droplet formation, droplets were produced at 4 °C. After droplet production, tubulin polymerization was triggered by transferring the droplets to a 37 °C observation chamber.

Pico-injection approach: Two experimental steps were required for producing stable microtubules in dsGUVs. The first step entailed the creation of dsGUVs (90% DOPC, 9% DOPS and 1% RhB-DOPE) that contain tubulin polymerization buffer. The second step was the pico-injection of the storage buffer containing tubulin (14.5 μM) into these droplets to get a 10 μM final concentration.

Bulk release approach. For the successful release of integrin $\alpha_{IIb}\beta_3$- or F-actin-containing GUVs (Fig. 4a,b, respectively), the lipid compositions of the dsGUVs were optimized in each case. More details are given in the corresponding methods.

Following the formation of protein-containing dsGUVs, 100 μl oil/dsGUV-containing solution was transferred into a 2 ml Eppendorf tube containing 1 ml FC-40 oil/surfactant solution (identical to the FC-40 oil/surfactant solution used for dsGUV production). Next, 100 μl of the appropriate buffer (actin polymerization buffer or integrin activation buffer) was pipetted on to the droplet emulsion. To destabilize the polymer shell of the droplets, 100 μl of 20 vol% perfluoro-1-octanol destabilizing surfactants (Sigma-Aldrich) dissolved in FC-40 oil was added. The Eppendorf tube was carefully tilted and slowly rotated until the emulsion was broken. The released GUVs were studied in an observation chamber made of BSA-coated glass slides and cover slips. The observation chambers were prepared by incubating the glass with 10 mg ml^{-1} BSA in PBS for 2 h at room temperature, followed by two 5 min washing steps—one with PBS and one with water.

Code availability. Matlab 2015 SP1 codes used for FRAP and intensity analyses are available in the Supplementary Notes 5 and 6, respectively.

Data availability. Data supporting the findings of this study are available within the article and its Supplementary Information files and from the corresponding authors on reasonable request.

References

43. Niu, X., Gulati, S., Edel, J. B. & deMello, A. J. Pillar-induced droplet merging in microfluidic circuits. *Lab Chip* **8,** 1837–1841 (2008).
44. Eberhard, C. *Online-Ressource* (Heidelberg Univ., 2012).
45. Zimmermann, B., Diez, M., Zarrabi, N., Graber, P. & Borsch, M. Movements of the epsilon-subunit during catalysis and activation in single membrane-bound H+-ATP synthase. *EMBO J.* **24,** 2053–2063 (2005).
46. Heitkamp, T., Deckers-Hebestreit, G. & Borsch, M. in *Single Molecule Spectroscopy and Superresolution Imaging IX* Vol. 9714 (eds Enderlein, J., Gregor, I., Gryczynski, Z. K., Erdmann, R. & Koberling, F.) (Spie-Int Soc Optical Engineering, 2016).
47. Mashaghi, S. & van Oijen, A. M. External control of reactions in microdroplets. *Sci. Rep.* **5,** 11837 (2015).
48. Gan, B. S., Krump, E., Shrode, L. D. & Grinstein, S. Loading pyranine via purinergic receptors or hypotonic stress for measurement of cytosolic pH by imaging. *Am. J. Physiol.* **275,** C1158–C1166 (1998).
49. Castoldi, M. & Popov, A. V. Purification of brain tubulin through two cycles of polymerization-depolymerization in a high-molarity buffer. *Protein Expr. Purif.* **32,** 83–88 (2003).
50. Hyman, A. *et al.* Preparation of modified tubulins. *Methods Enzymol.* **196,** 478–485 (1991).

In the format provided by the authors and unedited.

Sequential bottom-up assembly of mechanically stabilized synthetic cells by microfluidics

Marian Weiss,[1,2‡] Johannes Patrick Frohnmayer,[1,2‡] Lucia Theresa Benk,[1,2‡] Barbara Haller,[1,2] Jan-Willi Janiesch,[1,2] Thomas Heitkamp,[3] Michael Börsch,[3] Rafael B. Lira,[4] Rumiana Dimova,[4] Reinhard Lipowsky,[4] Eberhard Bodenschatz,[5] Jean-Christophe Baret,[6,7] Tanja Vidakovic-Koch,[8] Kai Sundmacher,[8,9] Ilia Platzman,[1,2*] and Joachim P. Spatz [1,2*]

[1]*Department of Cellular Biophysics, Max Planck Institute for Medical Research, Jahnstraße 29, 69120 Heidelberg, Germany*

[2] *Department of Biophysical Chemistry, University of Heidelberg, Im Neuenheimer Feld 253, 69120 Heidelberg, Germany*

[3] *Single-Molecule Microscopy Group, Jena University Hospital, Friedrich Schiller University Jena, 07743 Jena, Germany*

[4]*Theory & Bio-Systems, Max Planck Institute of Colloids and Interfaces, 14424 Potsdam, Germany*

[5]*Laboratory for Fluid Dynamics, Pattern Formation and Biocomplexity, Max Planck Institute for Dynamics and Self-Organization, 37077 Göttingen, Germany*

[6]*Droplets, Membranes and Interfaces, Max Planck Institute for Dynamics and Self-Organization, 37077 Göttingen, Germany*

[7]*Soft Micro Systems, CNRS, Univ. Bordeaux, CRPP, UPR 8641, 115 Avenue Schweitzer, 33600 Pessac, France*

[8]*Process System Engineering, Max Planck Institute for Dynamics of Complex Technical Systems, 39106 Magdeburg, Germany*

[9]*Otto-von-Guericke University Magdeburg, Process Systems Engineering, Universitätsplatz 2, 39106 Magdeburg, Germany*

Corresponding authors:
ilia.platzman@mpimf-heidelberg.mpg.de and joachim.spatz@mpimf-heidelberg.mpg.de

Supplementary Text

Supplementary Movie Legends

Supplementary Movie 1

The formation of a dsGUV out of the encapsulated GUVs.
Representative time-lapse fluorescence microscopy of the process showing the transformation of the encapsulated GUVs (ATTO 488-labeled DOPE) into a continuous supported lipid bilayer at the droplet inner interface. To transform the encapsulated GUVs into a supported lipid bilayer at the copolymer-stabilized droplet inner interface, 10 mM Mg^{2+} was applied during droplet production or by means of pico-injection.

Supplementary Movie 2

Microfluidic release device.

The video shows the dsGUVs encounter the aqueous phase in a wide perpendicular channel. To minimize the mechanical impact on the dsGUVs at the oil/water junction, the droplets were decelerated using passive trapping structures within the microfluidic channels (i.e., rows of pillars separated by distances smaller than the representative droplets dimensions), which we designed for the efficient release of GUVs.

Supplementary Movie 3

Pyranine as a pH sensor inside microfluidic droplets.

The video shows water-in-oil droplets immobilized in a microfluidic trapping device. The pH-sensitive fluorophore pyranine (concentration: 50μM) in ATP activity buffer was encapsulated into the droplets. To change the pH inside the droplets via the oil phase, acidic oil (containing 1μL of trifluoroacetic acid per 1 ml FC40 oil) and basic oil (containing 1μL of propyl amine per 1 ml FC40 oil) were alternately flushed through the device. As a result, the pH inside the droplets changed accordingly from acidic to basic and vice versa. The encapsulated fluorophore pyranine was simultaneously excited at 405nm and 458nm wavelength and the corresponding emission signal was recorded. Dominant 405nm detection signal indicated by blue color corresponds to basic pH, dominant 458nm detection signal indicated by green color corresponds to acidic pH.

Supplementary Methods

Preparation of large unilamellar vesicles (LUVs) and free-standing giant unilamellar vesicles (GUVs).
Lipids used in this study: 1,2-dioleoyl-sn-glycero-3-phosphocholine (DOPC), 1,2-dioleoyl-sn-glycero-3-phosphoethanolamine (DOPE), 1,2-dioleoyl-sn-glycero-3-phospho-L-serine (DOPS), 1,2-dioleoyl-sn-glycero-3-[(N-(5-amino-1-carboxypentyl)iminodiacetic acid) succinyl] (DGS-NTA), 1,2-dioleoyl-sn-glycero-3-phosphoethanolamine-N-(lissamine rhodamine B sulfonyl) (RhB DOPE), 1-palmitoyl-2-hydroxy-sn-glycero-3-phosphate (Phosphatidic acid), L-α-phosphatidylcholine (Egg PC), L-α-phosphatidylglycerol (Egg PG) were purchased from Avanti (Avanti Polar Lipids, USA) and used without further purification. ATTO 488 1,2-dioleoyl-sn-glycero-3-phosphoethanolamine was purchased from ATTO TEC (Siegen, Germany);
To obtain the formation of dsGUVs, solutions of LUVs or GUVs, consisting of different lipid compositions, were generated according to previously reported protocols.[1, 2] In brief, lipids were dissolved in pure chloroform, mixed at desired composition and concentration and dried

under a gentle stream of nitrogen. To remove traces of the solvent, lipids were kept under vacuum in desiccator for roughly 1 h. Dried lipids were then resuspended by addition of the desired buffer, followed by one hour of vortexing. LUV size was homogenized by extruding the solution 7 times through a polycarbonate filter (Whatman, Germany) with a pore size of 50 nm using an extruder (Avanti Polar Lipids, USA). The mean LUV diameter distribution was determined to be 100 ±10 nm using DLS. Solutions containing LUVs were stored at 4°C for not longer than 48 h or used immediately after production.

GUVs consisting of DOPC:DOPE:DOPS 8:1:1, including 1% ATTO 488-labeled DOPE were formed using the electroformation protocols as described previously.[2] In brief, lipid mixtures at the desired concentration (from 1 to 5 mM) were dissolved in pure chloroform and spread onto two indium tin oxide (ITO) coated glasses (Sigma-Aldrich, Germany). Following chloroform evaporation, the electroformation cell was assembled. Towards this end, the two ITO coated glasses were faced to each other with the conductive sides. To avoid direct contact two Teflon spacers (1 mm) were used. Copper tape (3M, USA) was used to connect the conducting sides with a signal generator (RS Components, Germany). Subsequently, the chamber was filled with Milli-Q water (Millipore filtered) and sealed with two-component glue (Twinsil Picodent GmbH, Germany). An alternating electrical potential of 10 Hz at 1 V amplitude was applied for 2 h to form GUVs. Finally the GUVs were collected using a syringe. Following vesicles production, the solutions were used immediately for encapsulation into microfluidic water-in-oil copolymer-stabilized droplets.

Block copolymer surfactant synthesis. Three types of block-copolymer surfactants were synthesized according to protocols reported earlier [3, 4] and used to produce droplets: Two triblock-copolymers PFPE(7000 g/mol)-PEG(1400 g/mol)-PFPE(7000 g/mol) (TRI7000) and PFPE(2500 g/mol)-PEG(600 g/mol)-PFPE(2500 g/mol) (TRI2500) and a gold-linked diblock-copolymer surfactant Au-PEG(436 g/mol)-PFPE(7000 g/mol). Following synthesis, triblock surfactants were mixed separately with gold-linked surfactants and dissolved in FC-40 fluorinated oil (3M, USA) to the final concentrations of 2.5 mM and 3 μM for triblock and gold-linked surfactants, respectively. NOTE: The two types of triblock copolymer surfactants (i.e. TRI7000 and TRI2500) mixed with gold-linked surfactants were tested and compared in all experiments. If not stated otherwise, the same results were observed.

Droplet-based microfluidics. Droplet-based microfluidic devices made of PDMS (Sylgard 184, Dow Corning, USA) were prepared by photo- and soft-lithography methods[5, 6] as described previously.[3] To control the droplet diameter during their creation, two different nozzle designs at the flow-focusing junction were implemented (Supplementary Figures 4 A and B). Syringe pumps PUMP 11 ELITE (Harvard apparatus, USA) were used to control flow rates of 120 μL/h for the aqueous phase and 160 μL/h for the oil phase as required for stable droplet creation (diameter d = 40 μm) at the rate of 1 kHz. In case of big droplets (d = 100 μm) the flow rates were adjusted to 650 and 850 μL/h for aqueous and oil phases, respectively to achieve a stable droplet creation at a rate of 1 kHz.

Due to the variety of required cellular components in the droplets the microfluidic device was integrated with small and compact electrodes to apply an electric potential. Electrical fields allow destabilization (poration) of surfactants and lipid bilayers towards controlled injection (pico-injection) of different cellular components into the droplets. The design of the droplet-based pico-injection unit was adapted from Abate et al.[7] Droplets were introduced into the device using a MFCS-EZ flow control system (Fluigent, France). The spacing between the droplets was controlled through addition of oil via the second oil channel (Supplementary Figure 4F). Following separation step, isolated droplets passed an alternating electrical field (frequency 1kHz, potential 250 V) generated by HM 8150 signal generator (HAMEG, Germany) and amplified by 623B-H-CE amplifier (TREK, USA) and two electrodes made of

Indalloy 19 (51% indium, 32.5% bismuth, 16.5% tin, GPS Technologies, Germany). This process destabilizes the droplet copolymer shell and lipid bilayer and allows introduction of bio-reagents via a pressurized injection channel (Supplementary Figure 4G). The injection volume can be ranged between 1 to 100 pl, dependent on the applied pressure.

For analysis, droplets were collected and transferred to the observation chamber (Supplementary Figure 5). The chamber was made of two single or sandwiched stripes of double face sticky tapes (Tesa, Germany. Thickness ≈ 80 µm or 160 µm for analysis of small and large droplets, respectively) as spacers, glued between two cover slips (Carl Roth, Germany). Finally, the chamber was filled with surfactant-containing oil and closed by two-component glue (Twinsil, Picodent GmbH, Germany).

Glass coatings for integrin-reconstituted GUVs adhesion experiments. To validate the biological functionality of the reconstituted integrin after the process of release, the adhesion of the integrin-reconstituted GUVs to fibrinogen-, fibronectin-, collagen-, and BSA-coated glass surfaces was examined and compared (Supplementary Figure 8). Therefore, dsGUVs with reconstituted $\alpha_{IIb}\beta_3$ integrin were formed and released as described in (Online Methods). For adhesion experiments integrin activation buffer (20 mM TRIS/HCl, pH 7.4, 50 mM NaCl, 0.5 mM $CaCl_2$, 1 mM $MnCl_2$ and 1 mM $MgCl_2$) was used inside and outside the GUVs. Following release the integrin-reconstituted GUVs were transferred to an observation chamber (Supplementary Figure 5) containing fibrinogen-, fibronectin-, collagen-, or BSA-coated glass slides. The adhesion was analyzed after 8 h incubation at 4°C to allow the integrin to interact with the different coatings. For these experiments fibronectin isolated from human plasma[8] was dissolved in PBS, collagen Type I (calf skin, Sigma-Aldrich, Germany) was dissolved in 0.1 M acetic acid and fibrinogen (human plasma, Merck Millipore, Germany) was first dissolved in 8.5% NaCl and for the incubation transferred to PBS.

For coating the glass surface of the observation chamber, pretreated glass slides (O_2 plasma, 200 W, 30 s) were incubated with 0.1 mg/ml protein solution (8.5 µg/cm²) over night at 4°C (fibrinogen and collagen) or 1.5 h at room temperature (fibronectin). For the BSA coating the glasses were incubated with 10 mg/ml BSA in PBS for 2 h at room temperature, followed by a washing step with PBS and water for each 5 min. After incubation, the glass slides were air dried over night at 4°C. The coverslips for the observation chamber were passivated with BSA.

Microscopy. All experiments were performed on a Leica SP5 confocal microscope (Leica Microsystems, Germany) equipped with an argon and a white light laser. The measurements were conducted at 25°C and in case of microtubule analysis at 37°C. Droplets, sealed in an analysis chamber, were observed via a 63x oil objective (HCX PL APO 63x/1.40-0.60; Leica Microsystems GmbH, Germany). Fluorophores were exited at 488, 550 and 555 nm and the detection windows were set at 498-540 and 560-620 nm and 565-625 nm in case of ATTO 488, Rhodamine B and TAMRA-labeling, respectively. The pinhole for data acquisition was set to 1 Airy unit, which corresponds to an Airy disk diameter of 96 µm and 0.9 µm thickness of the optical slice.

FRAP measurements. Due to the density differences between the aqueous droplets and the surrounding oil (1.0×10^3 vs. 1.9×10^3 kgm⁻³), the droplets ascend towards the upper slide of the observation chamber (Supplementary Figure 5). In this position, the droplets were scanned in z-direction until the bottom slice of the droplet was identified. The base of the droplet was chosen as a focal plane for FRAP measurements in order to exclude any influence from the cover slip at the chamber ceiling. A circular spot with a diameter of 5 µm was selected as the bleaching area. It should be noted that in case of FRAP measurements performed inside the droplets or on their periphery the actual bleaching area was measured and corrected for each measurement due to distortion of the optical path as a reason of diffraction/refraction at the

oil/water interface. Time course of each FRAP experiment included 10 pre-bleaching images, 2 to 10 bleach cycles to eliminate the fluorescent signal and 50 to 200 post-bleaching images to record the fluorescence recovery. The bleaching time was adjusted to each fluorophore and laser used in the experiments, the acquisition frequency of post-bleaching images was adapted to the total recovery time. The average diffusion coefficient for each experiment and its standard error were calculated from at least 20 measurements. The analysis followed the protocols proposed by Axelrod et al.[9] and Soumpasis[10] as described in Supplementary Note 3.

Raman spectroscopy. For Raman spectra collection released GUVs or dsGUVs were injected into the observation chamber (Supplementary Figure 5). GUVs or dsGUVs, sealed in an analysis chamber, were observed via a 100x oil objective (NA 1.2, Zeiss, Germany) using a confocal Raman microscope (Alpha300RA, WITec GmbH, Germany). To collect Raman scattered light, the same objective was used for focusing a 532 nm laser (20 mW, spot size 350 nm) onto single GUVs or dsGUVs. The acquisition time was fixed to 2.14 seconds with five accumulations for each collection window. At the end of spectra collection the location of the observed subject was investigated and, in case the location was preserved the collected data was saved. The representative Raman spectra of the dsGUVs and of the released GUVs can be observed in Supplementary Figure 7.

Fluctuation analysis. Fluctuation analysis was performed following the protocol described earlier.[11] The GUVs were placed in a chamber made of two cover slips and a 2 mm-thick ring made of Teflon, and observed under phase contrast. The data was acquired at room temperature ~23°C. The acquisition of five thousands of snapshots was done by high-resolution camera (pco.edge, PCO AG, Kelheim, Germany). More than 10 vesicles per type of sample were examined.

The bending rigidity of vesicles released from droplets was measured and compared to that of vesicles prepared following the method of electrofromation[12, 13] or gel-assisted swelling.[14] The membrane composition was DOPC:POPC:Chol (4:4:2) in mole ratios and small amount of the ATTO 488 labeled DOPE was also added at concentration of 1 mol% of total lipid. The buffer composition used for fluctuation analysis of the released GUVs was adjusted to be similar to integrin activation buffer within the GUVs (20 mM TRIS/HCl, pH 7.4, 50 mM NaCl, 0.5 mM $CaCl_2$, 1 mM $MnCl_2$ and 1 mM $MgCl_2$). The bending rigidity of the released vesicles was measured to be $21.5 \pm 3.4\,k_BT$ (standard deviation). This value lies in the range of typical values reported for the bending rigidity of PC membranes,[15] suggesting that the bilayers are clean of impurities. The methods of electroformation and gel-assisted swelling did not yield suitable vesicles (the vesicles were small and with defects or multilamellar) when grown in the buffer used for the preparation of dsGUVs. Therefore, we electroformed vesicles with the same membrane composition but in solution of 1 mM $MgCl_2$. The bending rigidity values for these membranes were found to be $25.3 \pm 3.0\,k_BT$ ideally corresponding to the data for released vesicles.

Supplementary Notes

Supplementary Note1. Calculation of minimal lipid concentration required to form a continuous lipid bilayer inside droplets - dsGUV:

The following lipid concentration calculation is done for droplets with 75 μm radius. The volume $V_{droplet}$ and the surface area $A_{droplet}$ of a spherical droplet is given by

$$V_{droplet} = \frac{4}{3}\pi r^3 = 1.8 \times 10^6 \; \mu m^3 = 1.8 \; nL$$

and

$$A_{droplet} = 4\pi r^2 = 7.1 \times 10^{10} \; nm^2.$$

Assumption: Average area occupied by a single phospholipid in a lipid membrane equals[16]

$$A_{headgroup} = 0.7 \; nm^2.$$

The amount of lipids per droplet needed to form a complete lipid bilayer is therefore:

$$N_{lipids} = 2 * A_{droplet} / A_{headgroup} = 2.3 \times 10^{11}.$$

Thus, the lipid concentration required to form a lipid bilayer inside droplets is

$$c = \frac{N_{lipids}}{V_{droplet} * N_A} = \frac{6}{r \cdot N_A \cdot A_{headgroup}} = 190 \; \mu M.$$

The concentration for droplets with different radii used in this study is c(r=50 μm) = 285 μM and c(r=20 μm) = 712 μM.

For the experiments an excess of ≈15% in lipid concentration was used for the following two reasons: 1) to compensate for possible lipids loss during the production; and 2) to compensate for volume increase due to pico-injection.

To validate experimentally the relevance of theoretically estimated lipid concentration, we systematically varied the amount of fluorescently-labeled lipids injected into monodisperse droplets and recorded their fluorescence intensity at the droplet interface. In case of minor lipid amount which would not cover the complete inner surface of the droplet we did not see the assembly of smaller GUVs than the size of the droplet itself. Instead we observed fusion of available lipids at the inner wall of the droplet. A plot of the measured data is shown in Supplementary Figure 1. Considering the diameter of 120μm of the droplets used in this experiment, a calculated concentration of 237 μM lipids is required for full bilayer coverage. As can be observed in Supplementary Figure 1, the intensity values are increasing approximately linear up to the theoretical estimated concentration. At elevated concentration the intensity reaches a plateau. It should be noted that at higher concentrations the excess lipids form aggregates of liposomes at the droplet interface. Inhomogeneous aggregation of liposomes on the droplet's periphery affecting precise estimation of the intensity. Therefore, higher deviation in the recorded intensity at 500μM is attributed to this effect.

Supplementary Note 2. Calculation of vesicle diffusion in microfluidic droplets

Assuming 3D Brownian motion, the mean square displacement $\langle r^2(t) \rangle$ of a particle in solution is

$$\langle r^2(t) \rangle = 6D \langle t \rangle.$$

The mean time $\langle t \rangle$ needed for the particle to travel the distance $\sqrt{\langle r^2(t) \rangle}$ is therefore

$$\langle t \rangle = \frac{\langle r^2(t) \rangle}{6D}.$$

The diffusion coefficient D of a spherical particle with radius R in a solution with viscosity η for a given temperature T is

$$D = \frac{k_B T}{6\pi\eta R}.$$

Therefore, the average time for a vesicle with radius R needed to diffuse from the center of the droplet to the periphery $\left(\sqrt{\langle r^2(t) \rangle} = 20 \ \mu m \right)$ is

$$\langle t \rangle = \frac{\langle r^2(t) \rangle}{6} \frac{6\pi\eta R}{k_B T}.$$

Assuming an aqueous solution with $\eta = 0.1 \ Pa \cdot s$ and a temperature $T = 25°C$, the average time for all vesicle to diffuse from the centrum to the periphery of the droplet with diameter 40 μm is

$$\langle t(R = 50 \ nm) \rangle \approx 15 \ s$$

and

$$\langle t(R = 5 \ \mu m) \rangle \approx 25 \ min.$$

Supplementary Note 3. Evaluation of FRAP data
The analysis followed a protocol proposed by Axelrod et al.[9] and Soumpasis.[10] To correct the background noise I_{bg}, the detector signal was measured in the oil phase using the same settings as for the FRAP measurements. I_{bg} was subsequently subtracted from all the measured intensity values. Average intensity values of the bleaching spot, $I(t)$, and as a reference of the whole droplet base, $T(t)$, were extracted from the recorded images. $I(t)$ and $T(t)$ were normalized by the averages of the prebleaching values, I_{pb} and T_{pb}. To correct for photofading the intensities of the bleached spot were multiplied with the reciprocal, normalized intensities of the droplet base, $T(t)$. Thus the normalized and corrected intensities, I_{nor}, were calculated as

$$I_{nor} = \frac{I(t) - I_{bg}}{I_{pb} - I_{bg}} \frac{T_{pb} - I_{bg}}{T(t) - I_{bg}}.$$

A nonlinear least-square fit was then applied using MATLAB R2015a SP1 (Mathworks, USA) to fit an exponential function $f(t)$,

$$f(t) = a\big(1 - exp(\lambda \cdot t)\big),$$

to the normalized intensities, I_{nor}. The resulting values of the coefficient λ were then used to calculate the half-recovery time $\tau_{1/2}$ for each bleaching experiment,

$$\tau_{1/2} = \frac{-\log(0.5)}{\lambda}.$$

The diffusion coefficient, D, is related to the half-recovery time $\tau_{1/2}$ via the square radius of the bleaching spot, assuming Gaussian bleaching profile,

$$D = 0.32 \frac{r^2}{\tau_{1/2}}.$$

The average diffusion coefficient for each experiment and its standard error were calculated from at least 20 measurements (Supplementary Figure 9).

Supplementary Note 4. Calculation of number of integrin proteins that might be reconstituted in dsGUVs.

Droplet surface area:
$$S(r = 20\mu m) = 5026 \ \mu m^2$$
$$S(r = 50\mu m) = 31416 \ \mu m^2$$
Area of a lipid in a membrane (from literature)
$$A_{lip} \approx 0.7 nm^2$$
Cross-section of the transmembrane domain of integrin (two α helices).[17]
$$A_{int} = 2nm^2$$

Integrin/Lipid Ratio	Surface area of lipid bilayer with one reconstituted integrin.	N_{int} $(r = 20\mu m)$	N_{int} $(r = 50\mu m)$
1:1000	$\frac{1000 * 0.7nm^2}{2} + 2nm = 352nm^2$	$1.43 * 10^7$	$8.92 * 10^7$
1:10,000	$\frac{10,000 * 0.7nm^2}{2} + 2nm = 3502nm^2$	$1.44 * 10^6$	$8.97 * 10^6$

Supplementary Note 5. Matlab code for FRAP analysis

```
%%%%%%%%%%%%%%%%%%%%%%%%%%%%%%%%%%%%%
%% FRAP evaluation
% version 5 20161010
% Matlab-script for the evaluation of FRAP data. This script is designed to to evaluate '.csv' files exported
% using the Leica Microscopy Software. For correct evaluation the files should contain
% three columns, first the intensity values form the bleaching spot, second a reference spot
% and a thrid a larger area containing the bleaching spot. The data sets can differ in time steps and total
% number of datapoints. The script will output the computed diffusion coefficient for each dataset as well
% the average diffusion coefficient and it's corresponding standard error. Optionally the script will draw
% graphs of each evaluation step.

%Program timer
%tic

%%%%%%%%%%%%%%%%%%%%%%%%%%%%%%%%%%%%%%
%% A set of parameters that control the evaluation of the results
% Plotting switch. If value is true all intermediary results are plotted into
% pdf files. This slows down script drastically
plotall = true ;
% Radius of the bleached spot in µm. Important for the evaluation of the
% diffusion coefficient
w = 2.5;
% For good results its important, to correct the collected data points for background.
bg=0;
% The calculation is on standard done according to protocols published by Axelrod et al. (1976) and Soumpasis (1983).
% Alternatively a model proposed by Kang et al. (2012) can be used, correcting for diffusion during the bleaching.
% To derive the prefactor the script 'Frap radius evaluation.m' can be used.
pf=0.32;

%%%%%%%%%%%%%%%%%%%%%%%%%%%%%%%%%%%%%%
%% Main body of code
%%%%%%%%%%%%%%%%%%%%%%%%%%%%%%%%%%%%%%

%%%%%%%%%%%%%%%%%%%%%%%%%%%%%%%%%%%%%%
```

```matlab
%% Importing the data and removing rows with empty cells
files = dir('*.csv');
for i=1:length(files)
    data=importdata(files(i).name);
    J=all(~isnan(data.data),2);
    A{i}=data.data(J,:);
    clear data J
end

%%%%%%%%%%%%%%%%%%%%%%%%%%%%%%%%%%%
%% Plotting of raw data
if plotall == true
for i=1:length(files)
    figure('vis', 'off');
    plot1=plot(A{i}(:,1),A{i}(:,2:4),'LineStyle','none');
    set(plot1(1),'Marker','o','DisplayName','ROI1');
    set(plot1(2),'Marker','.','DisplayName','ROI2');
    set(plot1(3),'Marker','x','DisplayName','ROI3');
    xlabel('time [s]');
    ylabel('intensity');
    title(files(i).name)
    print(sprintf('raw%02d',i) ,'-dpdf')
end
end

%%%%%%%%%%%%%%%%%%%%%%%%%%%%%%%%%%%
%% Data correction and normalization
% Each dataset is corrected for background, normalized by the prebleaching value
% and corrected for photofading in this step
for i=1:length(files)
    B{i}=zeros(length(A{i}),2);
    %% Mean intensity of focus point before bleach
    Ipre=mean(A{i}(1:10,2));
    %% Mean intensity of the total cell before bleach
    Tpre=mean(A{i}(1:10,4));
    %% Calculating normalized values (without background substration)
    B{i}(:,1)=A{i}(:,1);
    B{i}(:,2)=(A{i}(:,2)-bg)./(Ipre-bg) * (Tpre-bg) ./ (A{i}(:,4)-bg);
end

clear i j A Ipre Tpre bg

%%%%%%%%%%%%%%%%%%%%%%%%%%%%%%%%%%%
%% Plotting normalized graphs
if plotall == true
for i=1:length(files)
    figure('vis', 'off');
    plot(B{i}(:,1),B{i}(:,2),'Marker','o','LineStyle','none','DisplayName','B(:,1.6)');
    xlabel('time [s]');
    ylabel('intensity');
    title(files(i).name)
    print(sprintf('normalized%02d',i) ,'-dpdf')
end
clear i
end

%%%%%%%%%%%%%%%%%%%%%%%%%%%%%%%%%%%
%% Initialization of the fitting model
% As fitting function an exponential recovery curve is chosen. A robust, non-linear least square has proven to
% show good results. The fit outputs information about the fit quality to allow debugging.
    fo = fitoptions('method','NonlinearLeastSquares','Lower',[0 0],'Upper',[1 Inf],...
'Robust','Bisquare');
    st = [1 1]; %starting point
    set(fo,'Startpoint',st);
    ft = fittype('a*(1-exp(-t*b))',...
            'dependent',{'y'},'independent',{'t'},...
            'coefficients',{'a','b'});

%%%%%%%%%%%%%%%%%%%%%%%%%%%%%%%%%%%
%% The normalized data is fitted to the previously initialized fitting model. The results are directly plotted.
C=zeros(2,length(files));
for i=1:length(files)
    [cf,gof] = fit(B{i}(11:length(B{i}),1)-B{i}(11,1),B{i}(11:length(B{i}),2)-B{i}(11,2),ft,fo);
    C(:,i) =  transpose(coeffvalues(cf));
    if plotall == true
        figure('vis', 'off')
        hold on
        ylim([-0.05 0.2])
        plot(B{i}(:,1)-B{i}(11,1),B{i}(:,2)-B{i}(11,2),'Marker','o','LineStyle','none','DisplayName','B(:,1.6)');
        plot(cf);
        xlabel('time [sec]','FontSize',20)
        ylabel('normalized fluorescence Intensity','FontSize',20)
        title(files(i).name)
        print(sprintf('fitted%02d',i) ,'-dpdf')
    end
    clear cf gof
end

clear i st fo ft plotall B

%%%%%%%%%%%%%%%%%%%%%%%%%%%%%%%%%%%
```

```
%% Calculation of diffusion coefficients
% The values are computed from the fitting results and the size of the bleaching spot. They are
% first calculated for each dataset seperately and then the average and standard error is computed.
% The calculation is on standard done according to protocols published by Axelrod et al. (1976) and
Soumpasis (1983).
% Alternatively a model proposed by Kang et al. (2012) can be used, correcting for diffusion during
the bleaching
tauh=-log(0.5)./C(2,:);
C(3,:) = pf*w^2./tauh;
D = [mean(C(3,:)), std(C(3,:))/sqrt(length(C(3,:)))];

%%%%%%%%%%%%%%%%%%%%%%%%%%%%%%%%%%%%
%% Saving the results
save coefficients.txt C -ASCII
fid = fopen('diffusion_coefficient.txt', 'w');
fprintf(fid, 'diffusion_coefficient std_error [ÂµM^2/s]\n');
fprintf(fid, '%f    %f',D);
close

clear files w fid tauh pf

%toc
```

Supplementary Note 6. Matlab code for fluorescence intensity analysis

```
%%%%%%%%%%%%%%%%%%%%%%%%%%%%%%%%%%%%
%% Droplet intensity profile evaluation script
% version 4 20161205
% As there is refraction and defraction on the water oil interface of the droplets,
% it is difficult to compare the fluorescence intensity of GUV and dsGUV. This script
% tries to solve this problem by fitting and integrating the fluorescence
% intensity profile. This script is designed to to evaluate '.csv' files exported
% using the Leica Microscopy Software

%%%%%%%%%%%%%%%%%%%%%%%%%%%%%%%%%%%%
%% A set of parameters that control the evaluation of the results
% Plotting switch. If value is true all intermediary results are plotted into
% pdf files. This slows down script drastically
plotall = true;


%%%%%%%%%%%%%%%%%%%%%%%%%%%%%%%%%%%%
%% Main body of code
%%%%%%%%%%%%%%%%%%%%%%%%%%%%%%%%%%%%

%%%%%%%%%%%%%%%%%%%%%%%%%%%%%%%%%%%%
%% Importing the data and removing rows with empty cells
files = dir('*.csv');
for i=1:length(files)
    data=importdata(files(i).name);
    J=all(~isnan(data.data),2);
    A{i}=data.data(J,:);
    clear data J
end

%%%%%%%%%%%%%%%%%%%%%%%%%%%%%%%%%%%%
%% Plotting of raw data
if plotall == true
  for i=1:length(files)
    figure('vis', 'off');
    hold on
    plot1=plot(A{i}(:,3),A{i}(:,4));
    set(plot1(1),'Marker','o','DisplayName','ROI1');
    xlabel('position [Âµm]');
    ylabel('intensity');
    title(files(i).name,'FontSize',24)
    print(sprintf('raw%02d',i) ,'-dpdf')
  end
end

%%%%%%%%%%%%%%%%%%%%%%%%%%%%%%%%%%%%
%% Fitting of Gaussian functions to the peaks
% The data is split in two arrays around each peak and fitted with Gaussian functions
B=zeros(length(files)*2,2);

%%%%%%%%%%%%%%%%%%%%%%%%%%%%%%%%%%%%
%% Finding good starting points
% Searches for the position and values of two intensity peaks of a droplet crossection.
for i=1:length(files)
    j=round(length(A{i})/2);
    [m1 p1]=max(A{i}(1:j,4));
    [m2 p2]=max(A{i}(j:length(A{i}),4));
    B(i*2-1,1)=m1;
    B(i*2,1)=m2;
%%%%%%%%%%%%%%%%%%%%%%%%%%%%%%%%%%%%
%% Fitting a Gaussian function to the data via a nonlinear least square to the 'left' peak
% The fit uses the previously derived values as starting points
    fo = fitoptions('method','NonlinearLeastSquares','Lower',[0 0 0 2],'Upper',[100 A{i}(j,3) 1e-4
3], 'Robust','Bisquare');
    st = [m1 A{i}(p1,3) 1e-6 2.2]; %starting point
    set(fo,'Startpoint',st);
```

```matlab
        ft = fittype('a1*exp(-((x-b1)/c1)^2) +c3',...
                'dependent',{'y'},'independent',{'x'},'coefficients',{'a1','b1','c1','c3'});
        x=A{i}(1:j,3);
        y=A{i}(1:j,4);
        f1=fit(x,y,ft,fo);
        c=coeffvalues(f1);
        B(i*2-1,2)=c(1)*c(3)*pi^.5;
        clear c
%%%%%%%%%%%%%%%%%%%%%%%%%%%%%%%%%%%%%%%
%% Fitting a Gaussian function to the data via a nonlinear least square to the 'right' peak
% The fit uses the previously derived values as starting points
        fo = fitoptions('method','NonlinearLeastSquares','Lower',[0 A{i}(j,3) 1e-10 2],'Upper',[100
A{i}(length(A{i}),3) 1e-4 3], 'Robust','Bisquare');
        st = [m2 A{i}(p2+j,3) 1e-6 2.2];
        set(fo,'Startpoint',st);
        x=A{i}(j:length(A{i}),3);
        y=A{i}(j:length(A{i}),4);
        f2=fit(x,y,ft,fo);
        c=coeffvalues(f2);
        B(i*2,2)=c(1)*c(3)*pi^.5;
        clear c
%%%%%%%%%%%%%%%%%%%%%%%%%%%%%%%%%%%%%%%
%% Plotting of data with fitting results
        if plotall == true
            figure('vis', 'off');
            hold on
            plot(A{i}(:,3),A{i}(:,4));
            plot(f1);
            plot(f2);
            xlabel('position [µm]','FontSize',20)
            ylabel('Intensity','FontSize',20)
            title(files(i).name,'FontSize',24)
            print(sprintf('fitted%02d',i) ,'-dpdf')
        end
    clear x y j m1 m2 p1 p2 fo ft f1 f2 i st c
end
%%%%%%%%%%%%%%%%%%%%%%%%%%%%%%%%%%%%%%%
%% Calculation of maximal intesity values and integrated intensity
% The columns contain in order: the mean maximal values, the corresponding standard error,
% the integrated intensity, and the corresponding standard error.
C(1,1)=mean(B(:,1));
C(1,2)=std(B(:,1))%/sqrt(length(files));
C(1,3)=mean(B(:,2))*10^6;
C(1,4)=std(B(:,2))*10^6%/sqrt(length(files));

%%%%%%%%%%%%%%%%%%%%%%%%%%%%%%%%%%%%%%%
%% Saving the results
fid = fopen('intensitiy_values.txt', 'w');
fprintf(fid, 'max intensity [au] std error [au] integrated intensity [au*µm]  std error
[au*µm]\n %f  %f  %f  %f',C);
close

clear plotall files ans plot1 fid
```
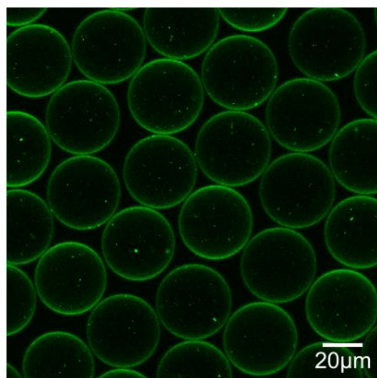
Supplementary Figures
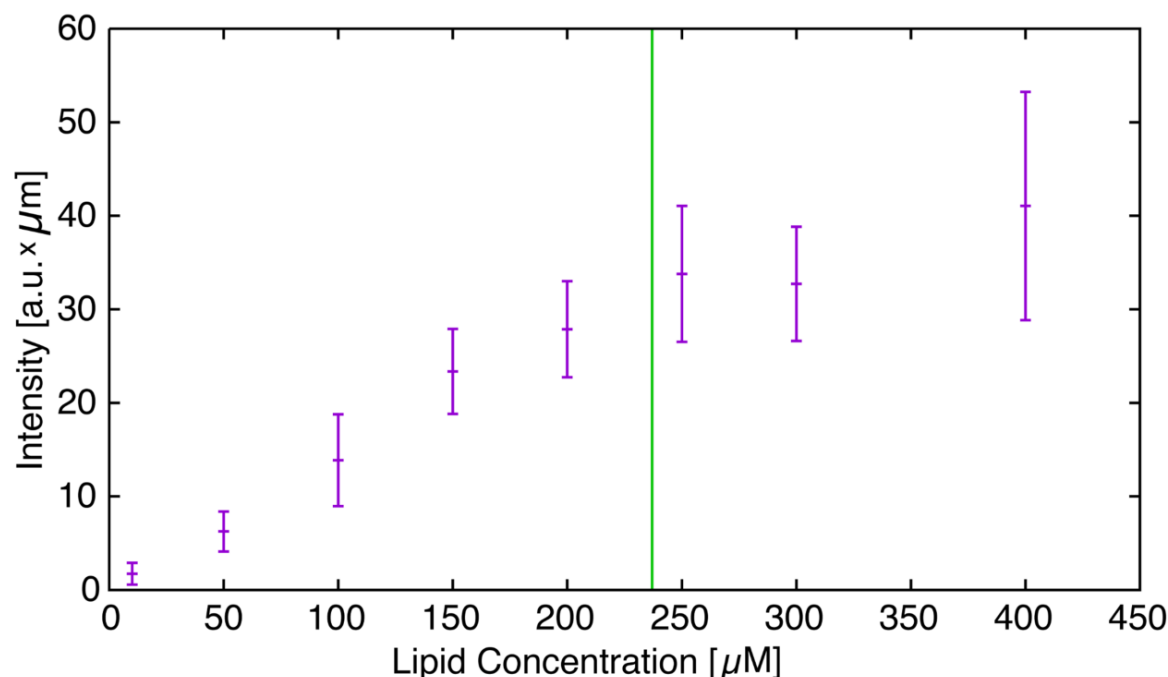
Supplementary Figure 1
Fluorescence intensity of the lipids at the droplets interface as a function of encapsulated lipid concentration.

To validate experimentally the relevance of theoretically estimated lipid concentration (237 μM, Supplementary Note 1), we systematically varied the amount of fluorescently-labeled lipids (egg PC:egg PG, 9:1, including 0. 5 % ATTO 488-labelled DOPE) encapsulated into 120 μm diameter monodisperse droplets and recorded their fluorescence intensity at the droplet interface. In case of lipid concentration lower than 237 μM no smaller GUVs than the size of the droplet itself were observed. Instead fusion of available lipids at the inner wall of the droplet was detected. As can be observed, the lipid fluorescence intensity values are increasing approximately linear up to the theoretical estimated concentration. At higher lipid concentration the intensity reaches a plateau. It should be noted that at higher concentrations the excess lipids form aggregates of liposomes at the droplet interface. Inhomogeneous aggregation of liposomes on the droplet's periphery affecting precise estimation of the intensity. Therefore, higher deviation in the recorded intensity at 400μM lipid concentration is attributed to this effect. The mean integrated intensity values and their standard deviation, indicated by the error bars, were derived from intensity profiles taken from twenty individual droplets, each intersecting the membrane twice rectangularly.

Supplementary Figure 2
Partial vesicle fusion due to 10 mM Ca^{2+} ions addition.

Representative fluorescence image of lipid distribution (DOPC:DOPE:DOPS 8:1:1, including 1% ATTO 488-labeled DOPE) within microfluidic water-in-oil droplets, containing 10 mM Ca^{2+} ions ($CaCl_2$), measured 1 h after creation.
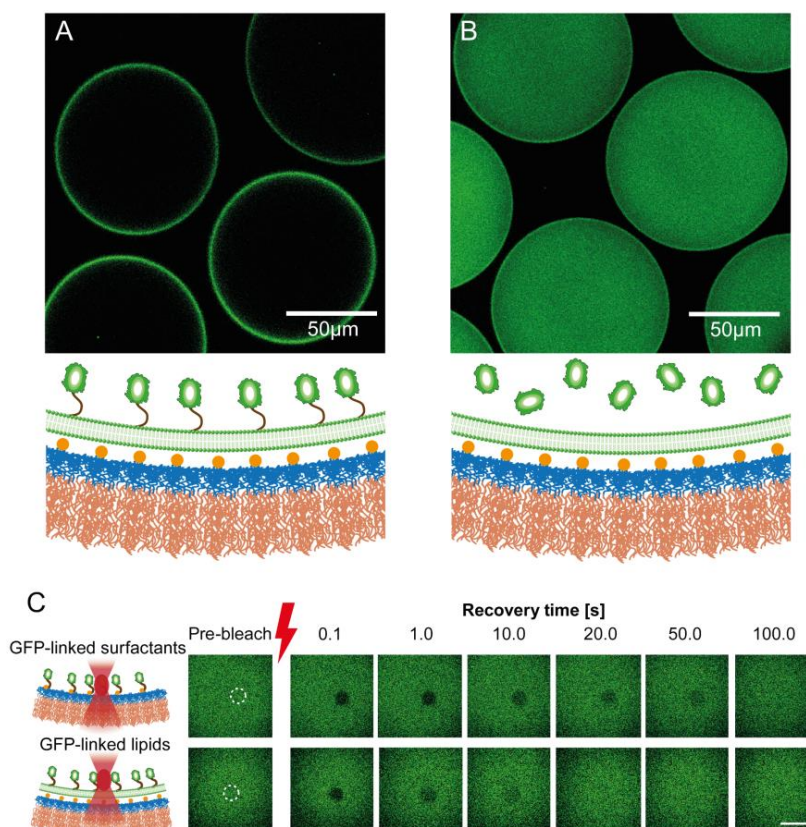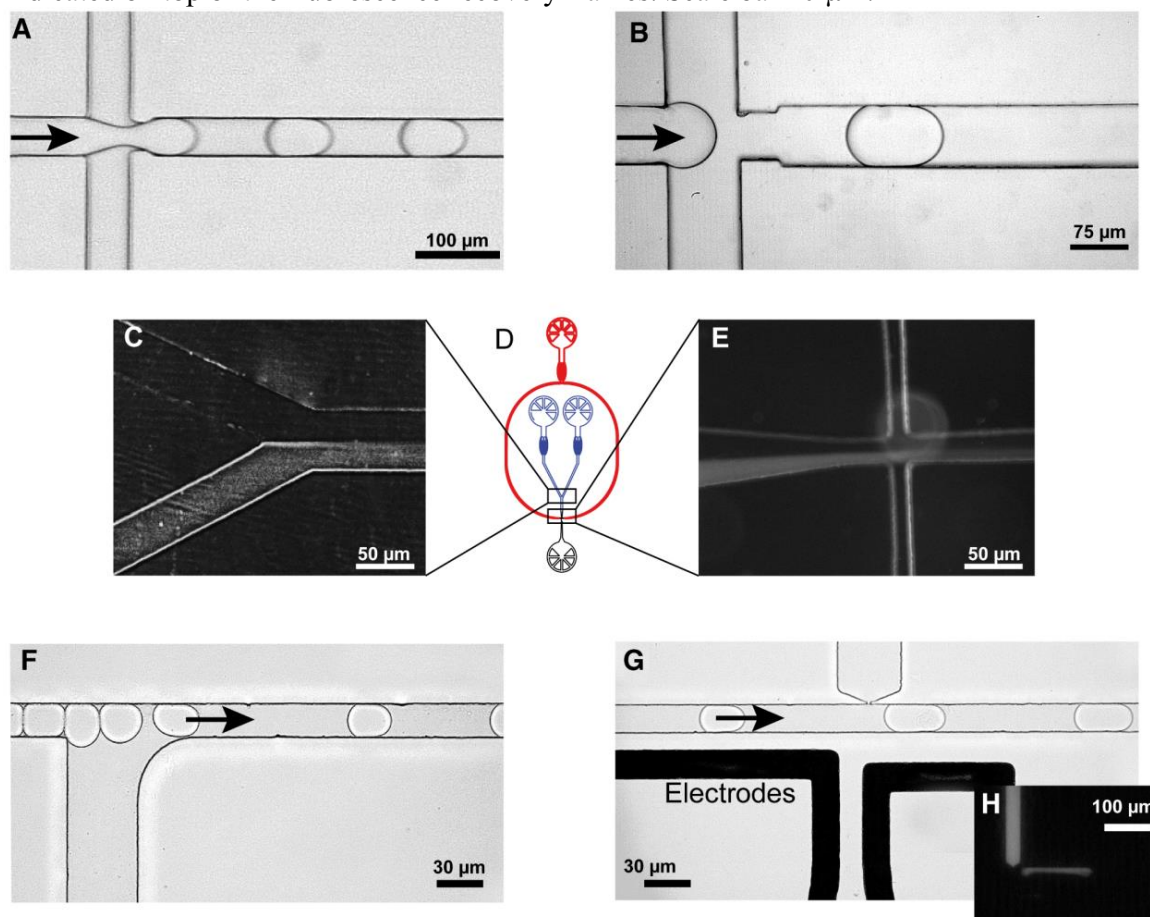

Supplementary Figure 3
Biofunctionalization of dsGUVs via DGS-NTA(Ni)lipids.

In order to test the functionalization of dsGUVs, (His6)-GFP was pico-injected into droplets. (A) For droplets containing DOPC:DGS-NTA(Ni), 9:1 (220 μM), (His6)-GFP was linked to the dsGUVs at the droplets periphery. (B) An equally distributed fluorescence signal was observed when no anchoring points were present (here: dsGUVs consisting of DOPC lipids only). (C) Representative FRAP experiments on the mobility of (His6)-GFP immobilized to the

copolymer-stabilized droplet interface (upper trace) or the dsGUV (lower trace). The bleached area is encircled in the pre-bleach frame and the recovery time (seconds after bleaching) is indicated on top of the fluorescence recovery frames. Scale bar 10 μm.

Supplementary Figure 4
Droplet-based microfluidic functional units.

Presentation of different droplet-based microfluidic operating units used in this research. (A) and (B) show representative images of the flow-focusing junctions for droplets production with a diameter of 40 and 100 μm, respectively. (D) shows a microfluidic droplet production device with two aqueous inlet channels (blue) and one oil channel (red). This device was implemented in actin-related experiments in order to avoid actin polymerization prior to droplet formation. Inset (C) and (E) show representative fluorescence images of the two phases for actin polymerization within the droplets. Bright phases represent the actin solution containing Alexa 488-labeled G-actin. The second phase contains all necessary bio-molecules for polymerization and bundling of actin. The solutions have a contact time in the millisecond range before getting encapsulated. Images (F) and (G) represent the pico-injection device for controlled introduction of different cellular components into droplets. (F) The spacing between the droplets carrying different biologically-active molecules is controlled through addition of oil via the second oil channel. (G) An alternating electric potential (1 kHz and 250 V) reduces the stability (poration) of the surfactants-lipid layer at the droplet interface for an aqueous injection of reagents from a pico-injection channel (injection volume can be ranged between 2 to 100 pl, dependent on the applied pressure). The injection process can be visualized by injection of ATTO 488-labeled F_0F_1-ATP synthase (H), using fluorescence microscopy.
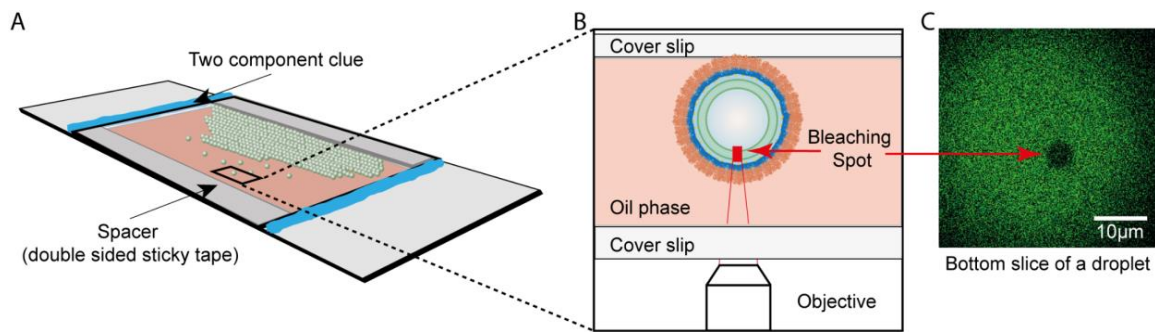
Supplementary Figure 5
Observation chamber and analysis setup.

(A) Shows the design of an observation chamber for droplet analysis. (B) Magnified cross-section representation of the analysis chamber. Due to the density differences, droplets rise to the top of the chamber. Confocal microscopy was used to scan the droplet in order to find the bottom plane. The lowest slice of the droplet was chosen as a focal plane for FRAP measurements in order to exclude any influence of stiff objects like in the case of the coverslip and the upper parts of the droplet. (C) Example of a FRAP experiment performed on dsGUV containing GFP-linked DGS lipids. The image shows a circular bleached spot with a 5 μm diameter.
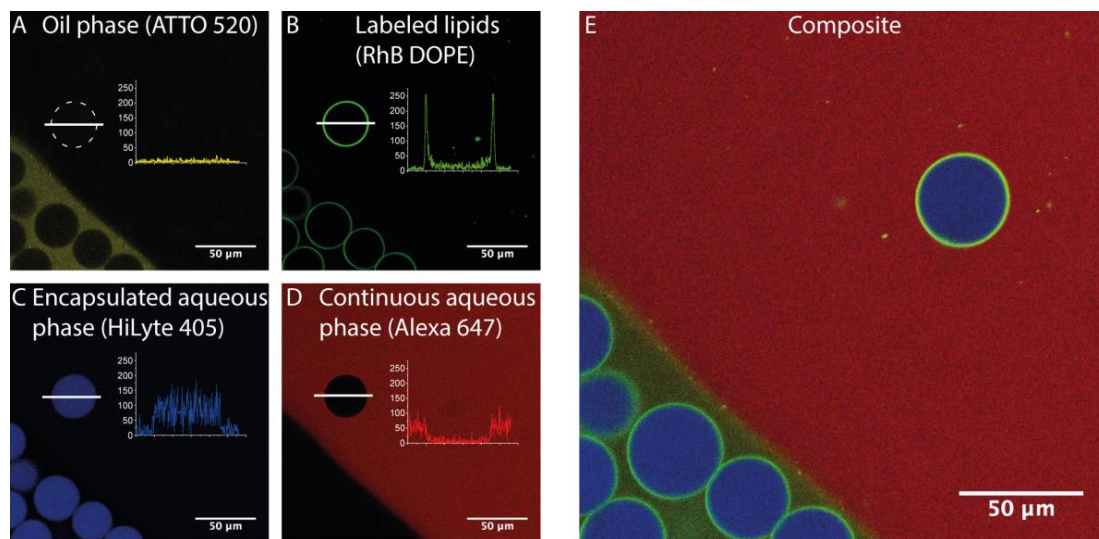
Supplementary Figure 6
Release of dsGUVs, preservation of content and checking for oil residues.

To evaluate if the lipid bilayer stayed intact during the release process the (A) oil phase (ATTO 520, yellow), the (B) lipid bilayer (RhB DOPE, green), the (C) encapsulated (HyLite 405, blue) and (D) continuous water phase (Alexa 647, red) were labeled with distinctive fluorophores. (E) A composite image of all channels. On the bottom left of each frame is the continuous oil phase containing multiple dsGUV encapsulating aqueous medium. The remainder of the frame is filled with a continuous aqueous phase containing a single released GUV. (A-D) The insets display a line profile intersecting the released GUV along the indicated white line for the respective fluorophore. (A) In the oil channel, no traces of remaining oil can be detected on the released GUV. (B) The fluorescent signal of the RhB DOPE is stronger compared to the dsGUV.

This is likely due to reduced diffraction and refraction. (C) and (D) show that no mixing between the aqueous phases was detected.
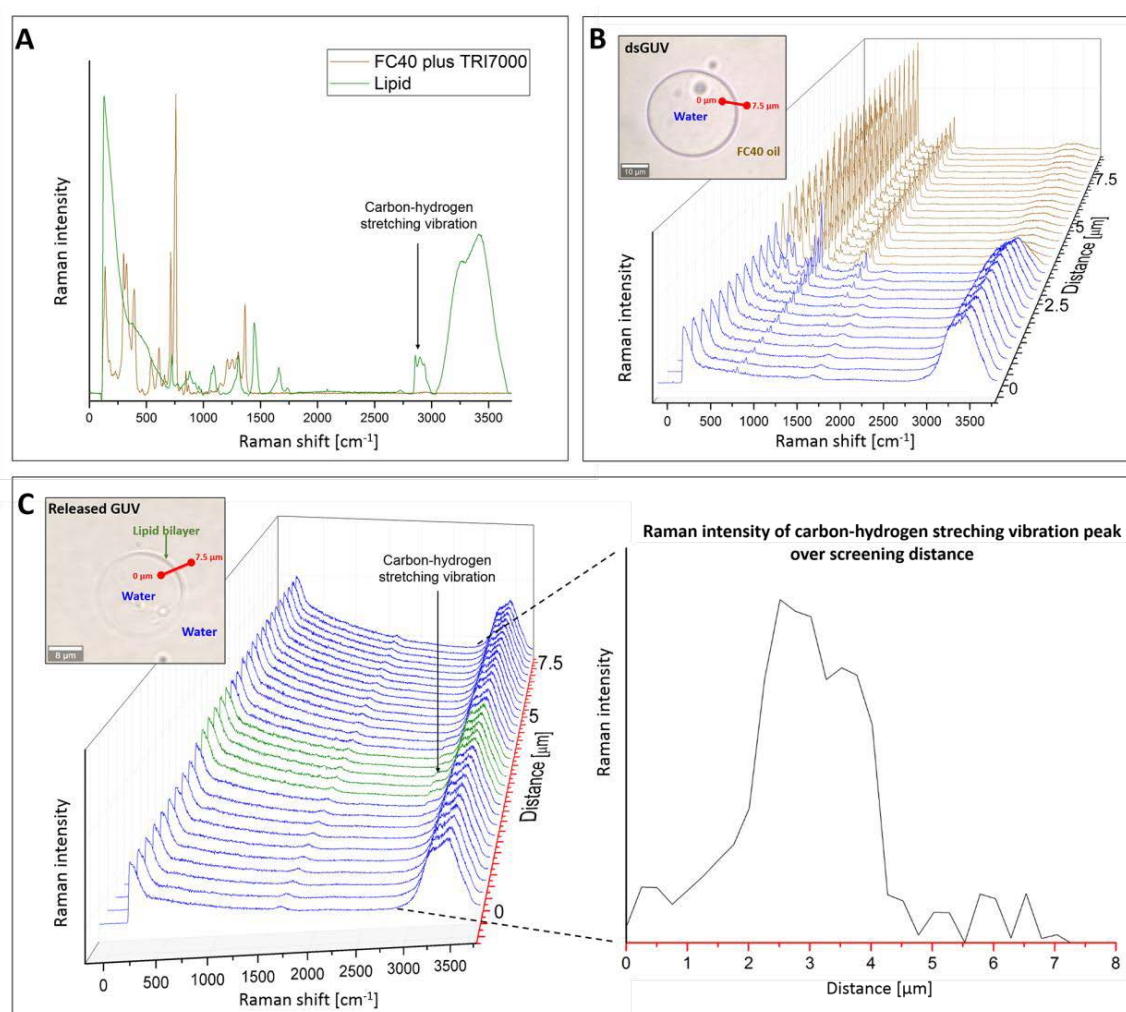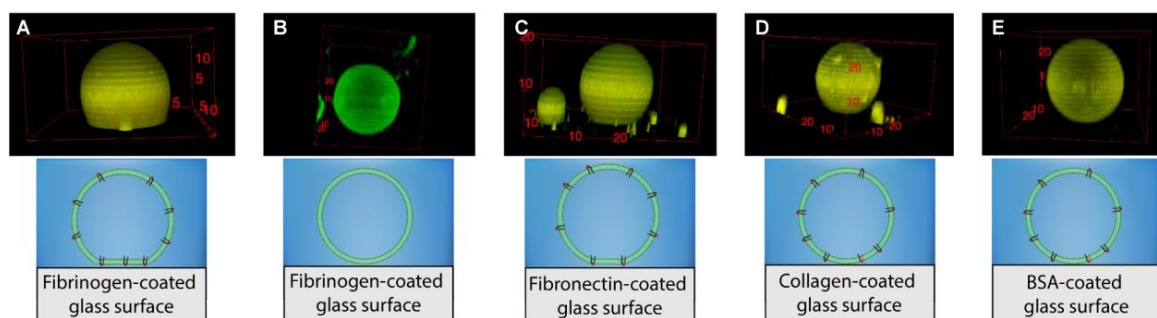

Supplementary Figure 7

Raman spectra of dsGUVs and the released GUVs.

Raman microscope was used to perform Raman spectroscopy on released GUVs to provide a method for the detection of oil/surfactant residues in the released GUVs. (A) Comparison of Raman spectra collected from the solution of surfactants in FC40 oil (brown) and from the SUVs (green), consisting of 4:4:2 of DOPC, POPC and cholesterol, respectively. Carbon-hydrogen stretching vibration of lipid tails indicated by arrow between 2800 and 3000 cm^{-1}.[18] The obtained FC40 oil spectrum in this study present similar peaks as published before.[19] (B) Representative Raman spectra collected through the water oil interphase of the single dsGUV as indicated by the red line in the insert bright-field image. In sake of clarity of presentation the spectra collected from the oil and water phases were brown and blue colored, respectively. (C) Representative Raman spectra collected through the water-lipid interphase of the released GUV as indicated by the red line in the insert bright-field image. In sake of clarity of presentation the spectra collected from the water phases and the lipid bilayer were blue and green colored, respectively. Importantly, no characteristic peaks of the FC40 oil/surfactant were detected

within the collected spectra. Raman intensity of the carbon-hydrogen stretching vibration of lipid tails (indicated by arrow) was plotted over the screening distance.

Supplementary Figure 8
Release of integrin-reconstituted GUVs and their functionality assessment.

Representative 3D reconstitution of confocal images of recovered integrin-reconstituted GUVs and their interactions with (A) fibrinogen- (C) fibronectin- (D) collagen- and (E) BSA-coated glass surfaces. The integrin-reconstituted GUVs show strong or moderate adhesion to fibrinogen- or fibronectin-coated glass surfaces, respectively. In comparison, only very weak to no interaction was detected for collagen or BSA-coated surfaces. The merged fluorescence signals consist of ATTO 488-labeled DOPE lipids and TAMRA-labeled $\alpha_{IIb}\beta_3$ integrin. (B) Shows the control experiment in which due to the absence of reconstituted integrin no interaction between the GUV and the fibrinogen-coated glass surface was observed.
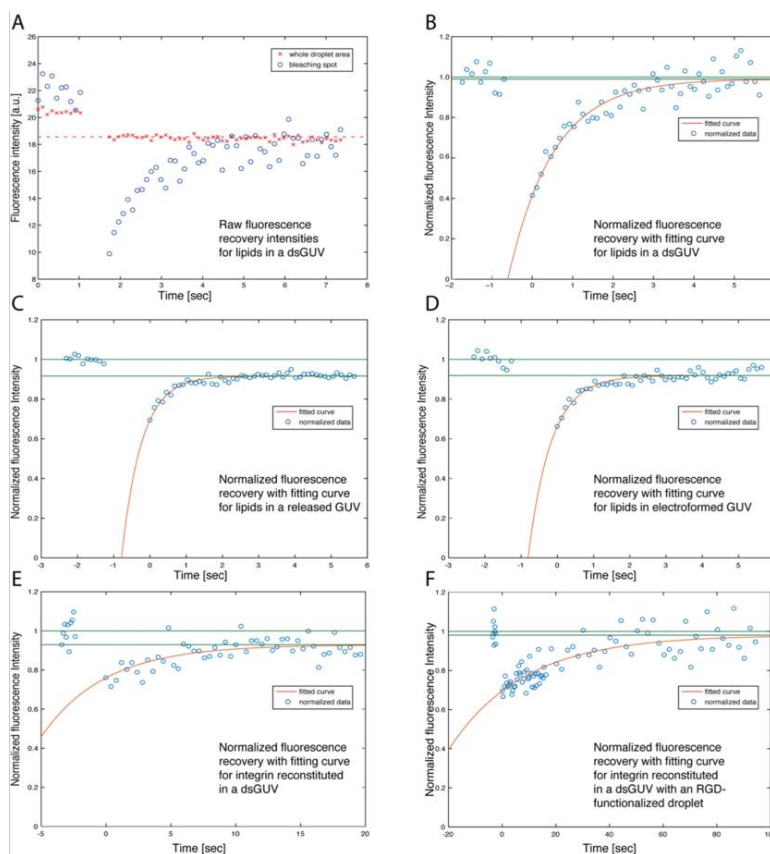
Supplementary Figure 9

Representative recovery curves.

(A) Shows representative raw data acquired for a FRAP measurement on a dsGUV. The data consists of the average intensity values of the bleaching spot and of the whole droplet area in focus. A horizontal dotted line was added as a guide for the eye to indicate photo-fading. Before analysis, all data points were corrected for background. Furthermore, data points were normalized by the average pre-bleaching value and the inverse of the average intensity of the whole droplet in focus was multiplied to the values of the bleaching spot, to correct for photo-fading. The resulting normalized intensity values of the fitting points and fitting curve are presented for the same dsGUV (B). Representative normalized fluorescence recovery curves obtained from the measurements performed on released and produced by electroformation GUVs are presented (C) and (D), respectively. In the FRAP measurements as presented in A-D the same lipid composition containing 0.5 % ATTO 488-labeled DOPE was used as fluorescent marker. (E) and (F) show represented normalized fluorescence recovery curves obtained from the measurements performed on reconstituted TAMRA-labeled integrin proteins in dsGUVs with and without interaction with RGD peptides on the surfactant layer, respectively.
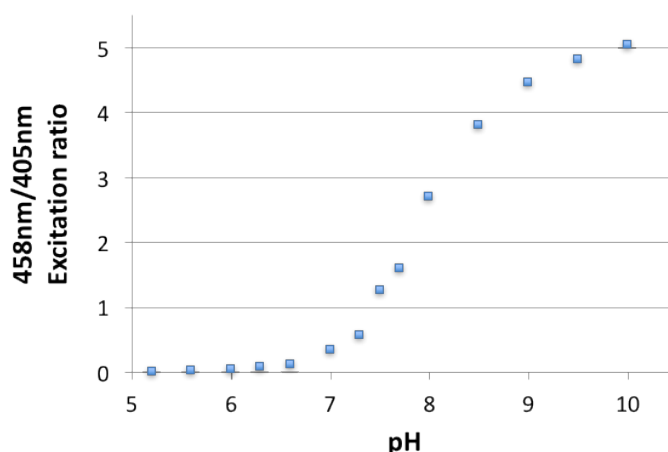
Supplementary Figure 10
Pyranine as a pH sensor within the dsGUVs.

Pyranine was used as a sensor to monitor changes of the dsGUV internal pH. To calibrate the system, dsGUVs were produced with a given pH ranging from 5 to 10 with 1μM pyranine in the aqueous solution. These dsGUVs were then excited at 405 nm and 458 nm wavelength. The figure shows the variation of the fluorescence intensity ratios as a function of a given pH.

Supplementary References

1. Johnson, J.M., Ha, T., Chu, S. & Boxer, S.G. Early Steps of Supported Bilayer Formation Probed by Single Vesicle Fluorescence Assays. *Biophys. J.* **83**, 3371-3379 (2002).
2. Herold, C., Chwastek, G., Schwille, P. & Petrov, E.P. Efficient Electroformation of Supergiant Unilamellar Vesicles Containing Cationic Lipids on ITO-Coated Electrodes. *Langmuir* **28**, 5518-5521 (2012).

3. Platzman, I., Janiesch, J.-W. & Spatz, J.P. Synthesis of Nanostructured and Biofunctionalized Water-in-Oil Droplets as Tools for Homing T Cells. *J. Am. Chem. Soc.* **135**, 3339-3342 (2013).

4. Janiesch, J.W. et al. Key factors for stable retention of fluorophores and labeled biomolecules in droplet-based microfluidics. *Anal Chem* **87**, 2063-2067 (2015).

5. Gu, H., Duits, M.H.G. & Mugele, F. Droplets Formation and Merging in Two-Phase Flow Microfluidics. *International Journal of Molecular Sciences* **12**, 2572-2597 (2011).

6. Xia, Y. & Whitesides, G.M. SOFT LITHOGRAPHY. *Annual Review of Materials Science* **28**, 153-184 (1998).

7. Abate, A.R., Hung, T., Mary, P., Agresti, J.J. & Weitz, D.A. High-throughput injection with microfluidics using picoinjectors. *Proc. Natl. Acad. Sci. U. S. A.* **107**, 19163-19166 (2010).

8. Frohnmayer, J.P. et al. Minimal Synthetic Cells to Study Integrin-Mediated Adhesion. *Angew. Chem.-Int. Edit.* **54**, 12472-12478 (2015).

9. Axelrod, D., Koppel, D.E., Schlessinger, J., Elson, E. & Webb, W.W. MOBILITY MEASUREMENT BY ANALYSIS OF FLUORESCENCE PHOTOBLEACHING RECOVERY KINETICS. *Biophys. J.* **16**, 1055-1069 (1976).

10. Soumpasis, D.M. THEORETICAL-ANALYSIS OF FLUORESCENCE PHOTOBLEACHING RECOVERY EXPERIMENTS. *Biophys. J.* **41**, 95-97 (1983).

11. Gracia, R.S., Bezlyepkina, N., Knorr, R.L., Lipowsky, R. & Dimova, R. Effect of cholesterol on the rigidity of saturated and unsaturated membranes: fluctuation and electrodeformation analysis of giant vesicles. *Soft Matter* **6**, 1472-1482 (2010).

12. Angelova, M.I. & Dimitrov, D.S. Liposome electroformation. *Faraday Discussions of the Chemical Society* **81**, 303-311 (1986).

13. Pott, T., Bouvrais, H. & Meleard, P. Giant unilamellar vesicle formation under physiologically relevant conditions. *Chemistry and Physics of Lipids* **154**, 115-119 (2008).

14. Weinberger, A. et al. Gel-Assisted Formation of Giant Unilamellar Vesicles. *Biophys. J.* **105**, 154-164 (2013).

15. Dimova, R. Recent developments in the field of bending rigidity measurements on membranes. *Adv. Colloid Interface Sci.* **208**, 225-234 (2014).

16. Nagle, J.F. & Tristram-Nagle, S. Structure of lipid bilayers. *Biochim. Biophys. Acta-Rev. Biomembr.* **1469**, 159-195 (2000).

17. Shattil, S.J., Kim, C. & Ginsberg, M.H. The final steps of integrin activation: the end game. *Nat. Rev. Mol. Cell Biol.* **11**, 288-300 (2010).

18. Cherney, D.P., Conboy, J.C. & Harris, J.M. Optical-trapping Raman microscopy detection of single unilamellar lipid vesicles. *Analytical Chemistry* **75**, 6621-6628 (2003).

19. Kim, H.S. et al. Raman spectroscopy compatible PDMS droplet microfluidic culture and analysis platform towards on-chip lipidomics. *Analyst* **142**, 1054-1060 (2017).

Publication 4

2.4 Reconceptualizing Fluorescence Correlation Spectroscopy for Monitoring and Analyzing Periodically Passing Objects

Zamir, E., Frey, C., Weiss, M., Antona, S., Frohnmayer, P.J.,
Janiesch, J.-W., Platzman, I., and Spatz, J.P.

Reconceptualizing Fluorescence Correlation Spectroscopy for Monitoring and Analyzing Periodically Passing Objects

Eli Zamir,*,† Christoph Frey,† Marian Weiss, Silvia Antona, Johannes P. Frohnmayer, Jan-Willi Janiesch, Ilia Platzman, and Joachim P. Spatz*

Department of Cellular Biophysics, Max Planck Institute for Medical Research, Jahnstraße 29, D-69120 Heidelberg, Germany
Department of Biophysical Chemistry, University of Heidelberg, Im Neuenheimer Feld 253, D-69120 Heidelberg, Germany

S *Supporting Information*

ABSTRACT: Fluorescence correlation spectroscopy (FCS) is a sensitive technique commonly applied for studying the dynamics of nanoscale-labeled objects in solution. Current analysis of FCS data is largely based on the assumption that the labeled objects are stochastically displaced due to Brownian motion. However, this assumption is often invalid for microscale objects, since the motion of these objects is dominated by Stokes drag and settling or rising effects, rather than stochastic Brownian motion. To utilize the power of FCS for systems with nonstochastic displacements of objects, the collection and analysis of FCS data have to be reconceptualized. Here, we extended the applicability of FCS for the detection and analysis of periodically passing objects. Toward this end, we implemented droplet-based microfluidics, in which monodispersed droplets containing fluorescent marker are flowing equally spaced within microchannels. We show by simulations and experiments that FCS can sensitively quantify the flow-rates, variability, and content of rapidly passing droplets. This information can be derived at high temporal resolution, based on the intensity fluctuations generated by only 5−10 passing droplets. Moreover, by utilizing the periodicity of the flowing droplets for noise reduction by averaging, FCS can monitor accurately the droplets flow even if their fluorescence intensity is negligible. Hence, extending FCS for periodically passing objects converts it into a powerful analytical tool for high-throughput droplet-based microfluidics. Moreover, based on the principles described here, FCS can be straightforwardly applied for a variety of systems in which the passing of objects is periodic rather than stochastic.
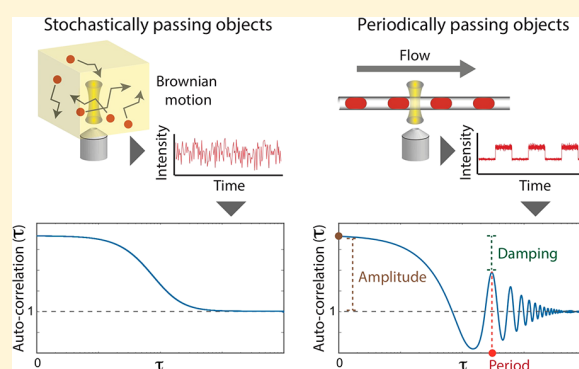
Fluorescence correlation spectroscopy (FCS) derives information from the temporal fluctuations of fluorescence intensity.[1−5] By sensitive high-rate sampling, typically >10 MHz, FCS records the intensity fluctuations generated by labeled particles passing through an observed confocal volume within the sample. The fundamental analysis of FCS data is the autocorrelation function $G(\tau)$—calculated as the correlation of the recorded intensity trace with a delayed copy of itself as a function of the delay, τ.[1] FCS is commonly applied for studying nanoscale objects (e.g., small molecules,[6] proteins,[1] quantum dots,[7] and liposomes[8]) passing the observed volume stochastically due to diffusion and flow.[1,5,9] Accordingly, the interpretations of $G(\tau)$ relies largely on the assumption that the labeled particles are been stochastically displaced due to Brownian motion.[10] Such stochasticity implies that the number of particles present in the confocal volume at the different time points distributes in a Poisson manner. Since for a Poisson distribution the variance is equal to the mean, the concentration of the labeled particles can be inferred from the amplitude of the autocorrelation. Additionally, the stochastic particles displacement implies that $G(\tau)$ decays as a function of τ, gradually approaching a baseline corresponding to zero correlation. The decay of $G(\tau)$ reflects the gradual and independent entry and exit of labeled particles in the observed volume. Accordingly, from this decay, the mobility mechanism of the particles and its parameters, such as diffusion and flow speeds, can be inferred. However, while these implications are based on the stochastic displacements of nanoscale objects in solution, a large variety of fluid dynamic processes involve motion of microscale objects. For microscale objects, Brownian motion is much less prominent, while nonstochastic displacement mechanisms dominated by Stokes drag in a laminar flow and gravity are more prevailing. Moreover, acoustic waves and electromagnetic fields can affect the displacements of microscale objects nonstochastically and arrange them in spatial patterns. To extend the applicability of FCS for such nonstochastic systems, its analysis has to be reconceptualized.

One type of nonstochastic displacements is a constant flow of equally spaced objects. Such a flow mode is typical in droplet-based microfluidics. This technology generates via

A

microchannels picoliter-scale monodisperse emulsion droplets at rates ranging from a slow drip to over 1 MHz.[11−15] The detection of droplets and their content is based mainly on fluorescence, due to the relatively high sampling rate and sensitivity of photodetectors. Conventionally, this detection relies on identifying the single droplets along the trace by segmentation using intensity threshold and/or other object-recognition criteria.[16−19] This makes the monitoring of droplets dependent on assumptions, manual tuning of parameters, and dedicated segmentation algorithms. Additionally, accurate segmentation of droplet depends on having a sufficient fluorescence signal of each droplet in comparison to the background fluorescence in the gaps between the droplets. Therefore, despite the progress made in recent years, sensitive and rapid monitoring tools are needed to further facilitate high-throughput applications of droplet-based microfluidics.[20,21]

In this work, we extended the applicability of FCS for the study of periodically passing objects. We demonstrate that this extension converts FCS into a powerful detection method for droplet-based microfluidics, enabling us to monitor rapidly and sensitively the flow and content of passing droplets.

■ MATERIALS AND METHODS

Production of Microfluidic Devices. The microfluidic devices (Figure S1) were designed with QCAD-pro (Ribbon-Soft, Switzerland). Photomasks were printed on chrome-coated soda lime glass (JD-Photodata, U.K.). For the photolithography process, a negative photoresist (SU8−3025, MicroChem, U.S.A.) was spin-coated (Laurell Technologies Corp., U.S.A.) onto silicon wafers at 2500 rpm in order to get a uniform coating of 30 μm thickness. Wafers were then placed on a hot plate for a 5 min soft bake at 65 °C, then ramped slowly to 95 °C and held for 15 min. Following this, the photoresist was exposed for 7.5 s to UV light through the corresponding photomask using a mask aligner (MJB4, SÜSS MicroTec, Germany). For the post-exposure bake, the wafers were placed for 1 min on a hot plate at 65 °C and 5 min at 95 °C. The remaining resist was removed with mr-DEV 600 developer (MicroChemicals, Germany). The hard bake was carried out in an oven at 150 °C for 15 min. Soft lithography was performed as previously described.[22,23] Briefly, polydimethylsiloxane (PDMS; Sylgard 184, Dow Corning, U.S.A.) was prepared by mixing the oligomer with the polymerization catalyst in a 9:1 (w/w) ratio. The mixed, degassed elastomer was poured over the silicon wafer and cured at 65 °C for 2 h in the oven. After curing, the flexible PDMS mold was peeled off the wafer and injection holes with a diameter of 0.75 mm were punched (Biopsy Punch, World Precision Instruments, U.S.A.). The device was cleaned with ethanol and activated together with a 24 × 60 mm coverslip (#1, Carl Roth, Germany) in an oxygen plasma (PVA TePla 100, PVA TePla, Germany; 0.45 mbar, 200 W, 20 s).[24] After activation, the PDMS device was pressed on the coverslip and heated for at least 2 h at 65 °C. Sigmacote (Sigma-Aldrich, Germany) was applied to the microchannels of the device in order to make their surfaces hydrophobic.

Surfactant Synthesis. Following a previously published protocol,[25,26] the synthesis of the PFPE (7000 g/mol)-PEG (1400 g/mol)-PFPE (7000 g/mol) triblock copolymer was carried out under argon atmosphere in dry THF solvent (tetrahydrofuran, 99.8%, Carl Roth, Germany) in a heated Schlenk-flask. First, 1 mmol PEG (1400 mg, 1400 g/mol molecular weight, Sigma-Aldrich, Germany) was dissolved in 90 mL of dry THF and cooled to −78 °C. At this temperature,

1.25 mL of N-butyl lithium (1.6 M solution in hexane, 2 mmol, Sigma-Aldrich, Germany) was added dropwise over 1 h and stirred for additional 30 min. Under continuous stirring, the reaction was slowly heated to room temperature and stirred for another 30 min. Then, 14 g of Krytox FSH (PFPE-carboxylic acid, 2 mmol, 7000 g/mol molecular weight, DuPont, Netherlands) was added dropwise over 30 min and stirred for 2 h. THF solvent with unreacted PEG was removed by a separatory funnel. After two THF washing steps, the product was dissolved in methanol (99.8%, Carl Roth GmbH, Germany) and dried with a rotary evaporator at 40 °C. The quality of the synthesized surfactant was analyzed by NMR and FT-IR measurements.

Droplet Production. For stable production of water-in-oil droplets,[27−29] a 5 mM solution of PFPE (7000 g/mol)-PEG (1400 g/mol)-PFPE (7000 g/mol) in HFE-7500 oil (3M, U.S.A.) was used as the oil phase. The aqueous phase consisted of PBS with 2 μM, 20 nM, or 2 nM Alexa Fluor 647 (C2-maleimide, A20347, Molecular Probes) as indicated. Different droplet production frequencies, between ∼2−20 kHz, were generated by adjusting the flow rates of the aqueous and oil phases ranging from 400 to 1000 μL/h and 800 to 3000 μL/h, respectively (Supplementary Table S1). All fluids were injected into the microfluidic device using 1 mL syringes (Omnifix-F, B. Braun Melsungen AG, Germany) connected by a cannula (Sterican, 0.4 × 20 mm, BL/LB, B. Braun) and PTFE-tubing (0.4 × 0.9 mm, Bola, Germany). For a fine flow-control, syringe pumps (Pump11Elite, Harvard Apparatus, U.S.A.) were used. High-speed camera (Phantom 7.2, Vision Research, U.S.A.) was used for a visual quality assessment of droplets production.

Encapsulation of Cells. CHO suspension cells were cultured in growth medium (EX-CELL ACF DHO Medium, Sigma-Aldrich, Germany) enriched with 4 mM solution of L-Glutamine (Gibco, ThermoFisher, U.S.A.). Prior to encapsulation, the cells were centrifuged for 5 min at 700 rpm and resuspended in PBS containing 8 μM Hoechst 33342 (Trihydrochloride, ThermoFisher, U.S.A.). Following an incubation of 10 min, the cells were washed three times by centrifugation and resuspension with PBS. Finally, the cells were suspended in PBS containing 2 μM Alexa Fluor 647 (C2-maleimide, A20347, Molecular Probes) to a concentration of 40 million cells per ml.

Microscopy. Fluorescence intensity measurements of flowing droplets were carried out on a LSM 880 confocal microscope (Carl Zeiss, Germany), using a C-Apochromat 40 × /1.2 W water-immersion objective (Carl Zeiss, Germany). Samples were excited with 405 and 633 nm laser lines, and fluorescence emission was detected within 419−615 nm and within 650−695 nm for the green and red detection channel, respectively. The pinhole was fully opened, to maximize photon collection and minimize optical sectioning. Photon count rate was detected and recorded at a sampling rate of 15 MHz.

Data Analysis. Autocorrelation curves of the acquired FCS data were calculated using the LSM software (ZEN, Carl Zeiss, Germany) in parallel with the data acquisition. For further analyses, the ConfoCor3 raw data files, listing time intervals between detected photons, were converted using a C++ program to ASCII files indicating the number of photons detected during each time bin (here 1 μs) along the measurement—hence obtaining $F_D(t)$ and $F_C(t)$. Where indicated, the single droplets were identified along $F_D(t)$ by segmentation, as described in the text. To segment encapsulated cells within each droplet, $F_C(t)$ fragments

corresponding to passing droplets were subjected to a modified one-dimensional watershed algorithm. The analyses of $F_D(t)$ and $F_C(t)$, and the autocorrelation of simulated $F_D(t)$ traces, were done with Matlab (Mathworks, U.S.A.).

Simulations. Simulations of intensity traces of flowing droplets were performed to systematically assess the derivation of droplets flow and content parameters from the autocorrelation curve. The input parameters for the simulation included the average fluorescence intensity level within a droplet (Fd) and in the gap between droplets (Fg), the average passing time of the droplets in the microfluidic channel (Ld), the average passing time of the gap between each two sequential droplets (Lg) and the variance of the droplet and gap passing times (noise, Dn). The intensity value in each time point within a droplet segment and within a gap segment was sampled from a Poisson distribution having a mean value of Fd and Fg, respectively. The time point at which a droplet segment ends, in respect to its start point, was sampled from a normal distribution having a mean value of Ld and a standard deviation of Dn. Similarly, the time point at which a gap segment ends, in respect to its start point, was sampled from a normal distribution having a mean value of Lg and a standard deviation of Dn. All simulations were done in Matlab (Mathworks, U.S.A.).

■ RESULTS AND DISCUSSION

Interpreting the Autocorrelation of Periodically Passing Objects. The autocorrelation function, $G(\tau)$, of the recorded fluorescence intensity fluctuation trace $F(t)$ can be written as $G(\tau) = \langle \delta F(t) \cdot \delta F(t + \tau) \rangle / \langle F(t) \rangle^2 + 1$, where $\delta F(t) = F(t) - \langle F(t) \rangle$. While the derivation of $G(\tau)$ from $F(t)$ is a straightforward calculation, the interpretation of $G(\tau)$ depends on the mechanisms underlying the fluorescence fluctuations. In the case of droplet flow, fluctuations along the intensity trace of the droplet marker, $F_D(t)$, are caused mainly by the constant flow of periodically passing droplets (Figure 1A and Figure S2). This periodicity in $F_D(t)$ is manifested by oscillations in $G_D(\tau)$ (Figure 1B).

We identified several important parameters concerning the droplets flow and content that can be derived from the autocorrelation curve $G_D(\tau)$ (Figure 1B):

(1) The τ value τ_{fp}, at which $G_D(\tau)$ reaches the first oscillation peak, indicates the average time period that is needed for a droplet and its subsequent gap to fully pass the observed volume. Hence, $1/\tau_{fp}$ equals the flow rate of the droplets (i.e., the number of droplets passing per time interval).

(2) In the case of homogeneous droplets and gaps, $G_D(\tau_{fp})$ should be equal to the amplitude of the autocorrelation curve, $G_D(0)$. Variation in droplets or gap sizes would cause damping of the $G_D(\tau)$ oscillations, allowing the quantification of irregularities in the flow of droplets, for example as $1 - G_D(\tau_{fp})/G_D(0)$.

(3) The autocorrelation amplitude, $G_D(0)$, equals to $\langle F_D(t)^2 \rangle / \langle F_D(t) \rangle^2$ (Supplementary Note S1). This implies that for homogeneously labeled droplets, $G_D(0) = P_D(1 - P_D)(\gamma - 1)^2/(1 + P_D(\gamma - 1))^2 + 1$, where $P_D = $ (mean droplet passing time)$/\tau_{fp}$ and γ is the ratio of droplets intensity over the background fluorescence intensity in the gaps between droplets (Supplementary Note S1). The partial derivative of $G_D(0)$ with respect to γ is positive, hence for a given P_D value, a higher
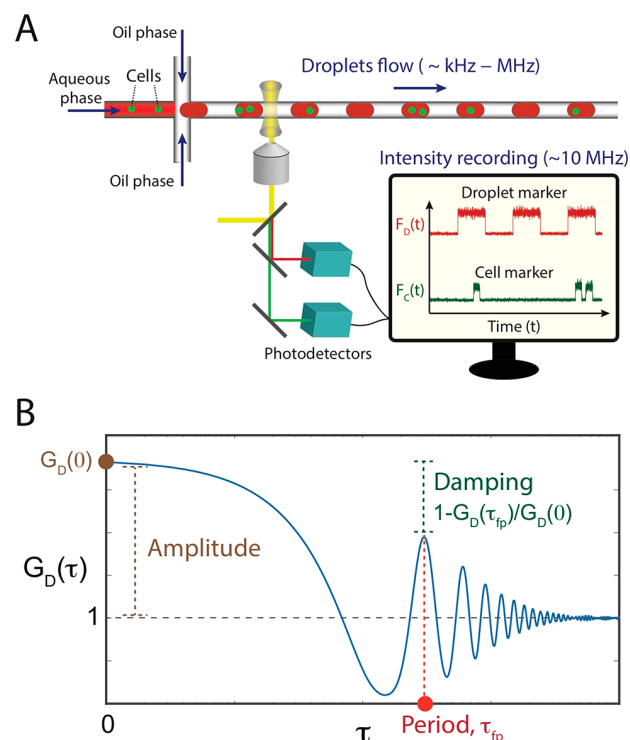

Figure 1. FCS-based monitoring of droplet flow and content in high-throughput microfluidics. (A) Schematic representation of a flow-focusing junction, where cell-containing droplets are generated, and of the FCS-based detection setup. Intensity fluctuations of a droplet marker, $F_D(t)$, and a cell marker, $F_C(t)$, are recorded at high sampling rates (15 MHz) at a spot along a droplet-carrying microchannel. (B) The autocorrelation curve of the droplet marker, $G_D(\tau)$, is calculated instantaneously. From this curve, the following parameters can be derived: (1) the period of $G_D(\tau)$ oscillations, τ_{fp} equals to 1/(droplet flow rate), (2) the extent of damping in $G_D(\tau)$ oscillations indicates the variability of droplets size or speed, (3) the amplitude of $G_D(\tau)$ can indicate changes in the (mean droplets fluorescence intensity)/(mean gaps fluorescence intensity) ratio.

autocorrelation amplitude implies a higher droplets intensity (Supplementary Note S1), given $\gamma > 1$. Thus, the autocorrelation amplitude provides a handle to monitor changes in droplets fluorescence intensity due to biological or chemical processes.

Simulation Assessments of Autocorrelation Responses to Droplet Parameters. We first assessed by simulations of droplet-marker intensity traces, $F_D(t)$, the effects of droplet flow and intensity on the autocorrelation curve $G_D(\tau)$ (Figure 2). The results show that droplet flow rates ranging from 20 Hz−5 MHz were accurately inferred from the $1/\tau_{fp}$ of the autocorrelation curve, given $F_D(t)$ with a temporal resolution of 0.1 μs (Figure 2, left column, upper row). Hence, autocorrelation can capture correctly the maximum theoretically feasible frequency, the Nyquist frequency, for a given sampling rate.

The large changes in droplet flow rates, up to ~2.5 MHz, did not affect the damping extent and the amplitude of $G_D(\tau)$- (Figure 2, left column). At 5 MHz, the damping extent of $G_D(\tau)$ decreased, reflecting under-sampling of the passing-time and intensity of each single droplet. Changing the standard deviation of the passing times of the droplets and gaps from 0 to 0.3 caused linearly proportional changes in the damping
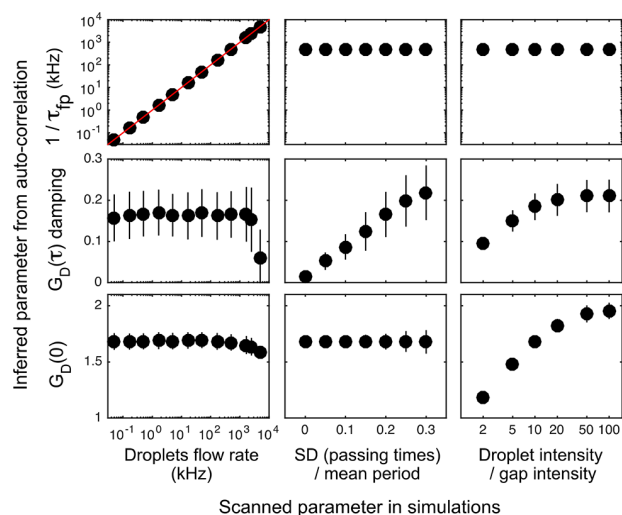
Figure 2. Simulation-based assessment of the effects of droplet flow parameters on the autocorrelation curve $G_D(\tau)$. Intensity fluctuation traces of flowing droplets, $F_D(t)$, were simulated as described. The default flow parameters were the following: intensity trace time resolution = 0.1 μs (corresponding to a sampling rate of 10 MHz), mean droplet passing time = 1 μs, mean gap passing time = 1 μs (resulting a flow rate of 500 kHz), standard deviation (SD) of droplet and gap passing time = 20% of the mean passing time, gap mean fluorescence intensity = 10 (a.u.), droplet mean fluorescence intensity = 100 (a.u.). The length of the simulated $F_D(t)$ spanned 5 passing droplets for the left and middle columns, and 15 passing droplets for the right column. Each column in the graph panel corresponds to a given simulation parameter that was altered. The ratio between the mean droplets intensity and mean gaps intensity was altered by changing the former one. Each row in the graph panel corresponds to a given parameter that was inferred from the autocorrelation curve $G_D(\tau)$. The damping of $G_D(\tau)$ was calculated as $1 - G_D(\tau_{fp})/G_D(0)$. Error bars indicate standard deviation (n = 300 simulation repeats).

intensity)/(mean gap intensity) ratios (Figure 3). The intensity of the droplets and gaps at each time bin was sampled from a
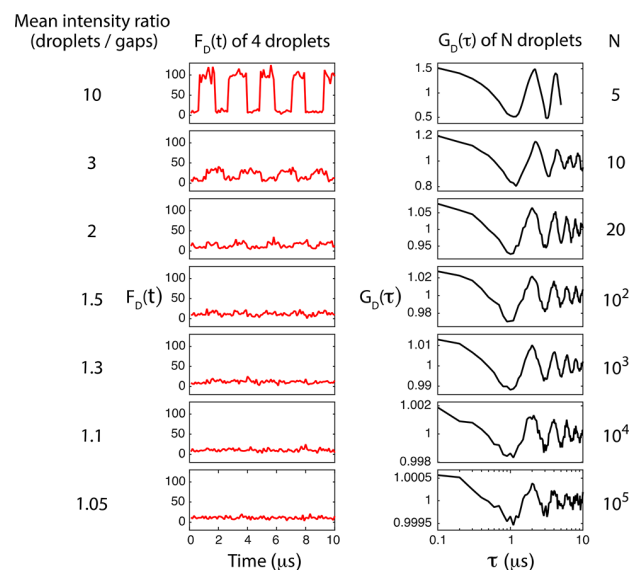

Figure 3. Autocorrelation captures the flow rates of droplets even with marginal fluorescence intensity. Intensity fluctuation traces of flowing droplets, $F_D(t)$, were simulated as described. The flow parameters were the following: intensity trace time resolution = 0.1 μs, mean droplet passing time = 1 μs, mean gap passing time = 1 μs (resulting a flow rate of 500 kHz), standard deviation of droplet and gap passing time = 20% of the mean passing time, mean gap fluorescence intensity = 10. The mean droplets fluorescence intensity was varied to achieve different ratios with the mean gap intensity, as indicated. The plots on the left show the simulated $F_D(t)$ for the first 10 μs, during which 4 droplets are fully passing. The plots on the right show the autocorrelation curves, $G_D(\tau)$, obtained from the corresponding $F_D(t)$ spanning the indicated number of passing droplets (N).

extent of $G_D(\tau)$, without changing $G_D(0)$ or $1/\tau_{fp}$ (Figure 2, middle column).

Changing the ratio of the droplets intensity over the background intensity in the gaps from 2 to 100 increased $G_D(0)$ (Figure 2, right column, bottom row). As expected, at high droplet/gap intensity ratio $G_D(0)$ converges to $1+(1 - P_D)/P_D$ (here, equals to 2), where P_D (here 0.5) equals (mean droplet passing time)/(mean droplet + gap passing time) (Supplementary Note S1). Increase of the droplet/gap intensity ratio also enhanced the damping extent of $G_D(\tau)$ but did not affect τ_{fp} (Figure 2, right column).

Conventionally, the monitoring of flowing droplets in microfluidics is performed in the time domain (i.e., by recognizing each droplet as an object along the recorded temporal intensity fluctuation trace).[16−19] Such recognition requires to have a sufficient signal-to-noise ratio of the labeled droplets to overcome stochastic fluctuations of intensity. Moreover, high droplet flow rates reduce the sampling points for each passing droplet, and hence reduce the statistical confidence in identifying and distinguishing the single droplets. In contrast to time-domain based analyses, autocorrelation captures and integrates the periodicity of a signal. Therefore, even if the fluorescence signal of the droplets is marginal, autocorrelation can be expected to capture their flow by integrating a sufficient number of droplets. We first assessed this expectation by simulating intensity traces of droplets flowing at 500 kHz rate with different (mean droplets

Poisson distribution around the mean droplets intensity and the mean gaps intensity, respectively. At droplet/gap intensity ratio ≤ 2, it is practically impossible to identify the single droplets along the intensify traces (Figure 3, left column). Remarkably, autocorrelation clearly detected the flow of droplets and accurately quantified its rate, even at droplet/gap intensity ratio of 1.05 (Figure 3, right column). At droplet/gap intensity ratio of 2, only 20 droplets were needed to be integrated by autocorrelation for a clear quantification of their flow rate. At the marginal droplet/gap intensity ratio of 1.05, the integration power of autocorrelation utilized 100 000 droplets passing during 0.2 s to clearly capture their flow rate.

To conclude, the simulation assessments indicate that the autocorrelation curve $G_D(\tau)$ can (1) quantify accurately fast droplet flow rates, up to the maximum theoretically possible for a given sampling rate, (2) provide a quantitative measure for changes in the variability of the droplets and gaps passing times, and (3) provide a quantitative measure for changes in the droplets' intensity/gap intensity ratio, for a given droplet-flow condition. Given a sufficient fluorescence intensity of droplets, it is enough to use short intensity traces, spanning the mean passing time of 5−10 droplets, to achieve accurately these quantifications. Additionally, the simulations show that even with a negligible droplets fluorescence intensity, the autocorrelation can accurately monitor and characterize their flow, by integrating the signal over a larger number of droplets.

Experimental Assessment of Droplet Monitoring by FCS. Following the assessment by simulations, we tested experimentally the effects of droplet flow conditions on the autocorrelation curve $G_D(\tau)$. First, we produced droplets containing 2 μM Alexa Fluor 647 at different rates (Figure 4A and Figure S3) and measured their flow rates by
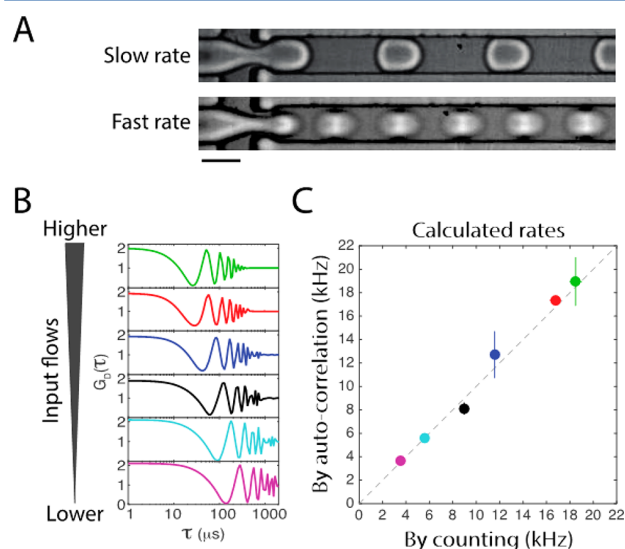

Figure 4. Accurate quantification of droplet flow rates by autocorrelation. Droplets were generated at different rates by modifying the input flow rates of the aqueous and oil phases, as indicated in Supplementary Table S1. (A) High-speed camera transmission images of droplets generated at the lowest (Slow rate) and highest (Fast rate) applied rates (Supplementary Table S1). Scale bar, 30 μm. (B) The autocorrelation, $G_D(\tau)$, curves obtained for different rates of droplet flow. (C) A scatter plot comparing the quantifications of droplet flow rates by autocorrelation and direct droplet counting. Dashed line indicates the line of equality. Error bars indicate the standard deviation ($n = 6$ and $n \geq 3$ for the horizontal and vertical axes, respectively). The color-code matches each data point in (C) with the corresponding example of autocorrelation curve in (B).

autocorrelation (Figure 4B). FCS data acquisition of the stream of droplets was performed at a spot adjacent to the flow-focusing junction (Figure 1A). Autocorrelation analysis of the recorded intensity traces shows that the values of τ_{fp} get smaller as the input flow rates increase, hence indicating a higher droplet flow rate (Figure 4B). As a quantitative control, short time-lapse movies (~300 ms) were recorded using a high-speed camera, and the number of passing droplets per time period was counted (Figure S3 and Table S1). The droplet flow rates obtained from direct counting matched well those obtained from autocorrelation analysis (Figure 4C). Hence, these results confirmed the capability of autocorrelation to monitor accurately droplet flow rates.

Next, we experimentally tested the effect of inhomogeneity in the droplet flow on the autocorrelation curve $G_D(\tau)$. By high-speed camera imaging, we noticed that cell encapsulation affects the speed of the encapsulating droplets, hence increases the variability of the distances between passing droplets (Figure 5A). Therefore, cell encapsulation provides an experimental system to induce droplet-flow inhomogeneity, which is relevant for many potential microfluidic applications. In order to generate flow variability, we added Hoechst-labeled cells into the input aqueous phase, leading to encapsulation of cells in the
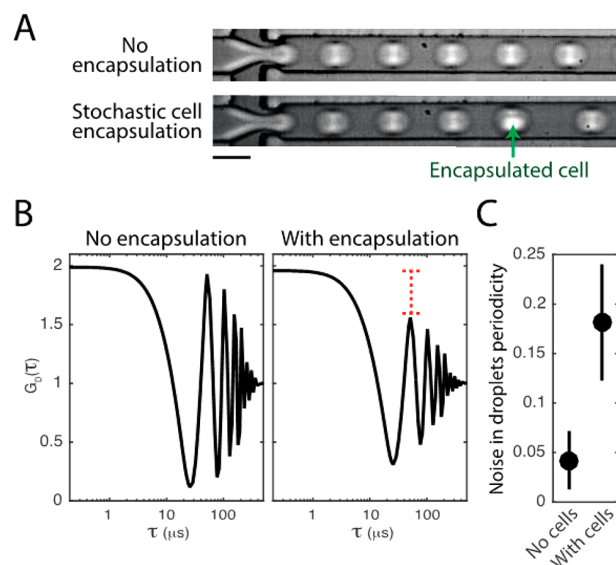

Figure 5. Quantifying the variability of droplet passing time by autocorrelation. $F_D(t)$ was recorded for droplets produced with or without cells encapsulation. (A) High-speed camera transmission images of droplets generated with or without stochastic encapsulation of cells. Scale bar, 30 μm. (B) Representative autocorrelation curves obtained with or without cells encapsulation. (C) A plot showing the mean $\pm$ standard deviation of the inferred level of periodicity noise, calculated as $1 - G_D(\tau_{fp})/G_D(0)$. Error bars indicate standard deviation ($n \geq 6$).

forming droplets (Figure 1A). At the applied droplet production rate (~20 kHz), cell encapsulation affected the speed of cell-containing droplets (Figure 5A). To study the effect of induced inhomogeneous droplet flow on $G_D(\tau)$ the density of cells was adjusted so that encapsulations were occurring stochastically. As predicted, the damping of $G_D(\tau)$ oscillations was found to be much stronger for the sessions of droplet production which included encapsulation of cells (Figure 5B,C).

In order to experimentally assess the effects of droplet/gap intensity ratios on $G_D(\tau)$, we produced droplets containing different concentrations of the fluorescent marker. As expected, the results show that for given flow conditions and excitation intensity, the autocorrelation amplitude $G_D(0)$ decreases as the droplets intensity decreases (Figure 6A). Remarkably, the autocorrelation provided an accurate measure of the droplet flow rates even if their fluorescence intensity is marginal (Figure 6A, 2 nM marker concentration). Moreover, autocorrelation captures the flow of droplets and its rate even if the droplets are unlabeled (Figure 6B). This sensitive detection is possible since autocorrelation averages negligible, periodic, changes of intensity levels generated as droplets are passing through the observed volume. The intensity changes are due to autofluorescence of the oil phase, which is marginal but still higher in comparison with the aqueous phase (Figure S4). Since averaging reduces the random noise, but not the mean fluorescence difference between droplets and gaps, autocorrelation increases the signal-to-noise ratio. Of note, autofluorescence of the oil phase is an important factor to account for, if its level is comparable to, or higher than, the fluorescence signal of the droplets. Particularly, if the fluorescence signal of the droplets is lower than the oil autofluorescence, $G_D(0)$ will be lower than that of droplets with no fluorescence signal.
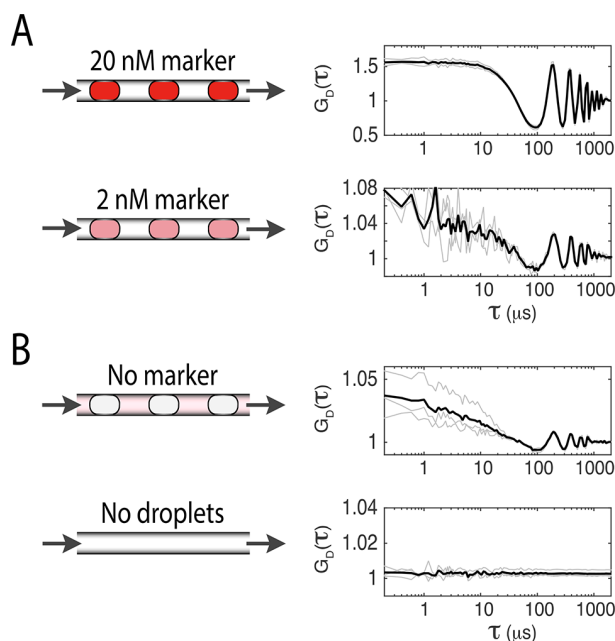
E

Figure 6. Effect of droplets relative fluorescence intensity on their autocorrelation curve. (A) Droplets were generated under the same flow conditions, with aqueous phase containing a fluorescent marker (Alexa 647) at 20 nM or 2 nM in PBS, as indicated. The autocorrelation curves $G_D(\tau)$ obtained for each measurement repeat of 10 s (thin lines) and their average (thick line, $n = 3$) are shown. (B) Autocorrelation curves and their averages ($n = 3$) of droplets containing PBS alone, or of flowing PBS without droplets formation (due to lack of oil-phase flow into the cross-junction). In (A) and (B) samples were excited solely with laser line 633 nm, and with power attenuator set to 0.3% power for (A) and to 30% power for (B). In the case of high laser power, a marginal autofluorescence of the oil phase can be detected, enabling to monitor flowing droplets containing no fluorescence marker. Thin and thick curves correspond to the measurement repeats and their mean, respectively.

Therefore, when dealing with marginal fluorescence signals it is important to measure the $G_D(0)$ of droplets containing no marker and calibrate accordingly.

Temporal Resolution of Droplet Monitoring by FCS. To provide a real-time feedback for rapid changes in a periodic flow of objects, the autocorrelation analysis should enable to derive information from short segments of the intensity trace $F_D(t)$. The simulation analysis indicated that given sufficient intensity, only few droplets are needed to be integrated to enable their flow-rate detection (Figure 3). To test this using experimental data, we applied multiresolution FCS (mrFCS)[7] analysis, scanning the recorded intensity fluctuation traces with different temporal integration levels. Toward this end, we partitioned $F_D(t)$ to short time periods (ranging from 200 to 2000 μs) and calculated $G_D(\tau)$ for each period along the trace. Analysis of a 500 μs period (5–10 droplets) was found to be sufficient for detecting an inhomogeneity in the droplet flow (Figure S5). Thus, by scanning $F_D(t)$ with a sliding window, and calculating $G_D(\tau)$ per each window, it is possible to monitor the cell-encapsulation frequency at a temporal resolution of 500 μs, corresponding to 5−10 passing droplets (Figure S5).

In addition to $G_D(\tau)$, the amplitude of the cell-marker autocorrelation, $G_C(\tau)$, can be calculated for each short time interval (Figure S5). In the absence of encapsulated cells the

amplitude of $G_C(\tau)$, $G_C(0)$, is low, due to uncorrelated intensity fluctuations and weakly labeled small debris. In the presence of one or more encapsulated cells $G_C(0)$ increases considerably, since the cells are few in number, relatively big and strongly labeled. Thus, $G_C(\tau)$ and $G_D(\tau)$ provide two independent indicators for cell encapsulation.

Identifying Objects within Flowing Droplets via FCS Data Acquisition. FCS relies on having fast sampling rates, typically >10 MHz, in order to capture accurately the residence time of diffusing particles in the confocal volume. This provides high spatial resolution for resolving signals of encapsulated cells or other objects within fast flowing droplets (Figure 1A and Figure S2). Segmentation of the droplets along $F_D(t)$ identifies the start and end of each droplet along the trace, hence enables analyzing its content along the corresponding part of the cell-marker intensity trace $F_C(t)$ (Figures S6 and S7). Thus, encapsulated cells within each flowing droplet can be detected and counted by segmenting them along the corresponding $F_C(t)$ fragment (Figure S8).

■ CONCLUSIONS

This study shows that FCS can be effectively applied for the study of periodically passing objects. To achieve this goal, we reconfigured the manner by which the autocorrelation is interpreted and analyzed. Moreover, we demonstrated that this approach converts FCS into a sensitive analytical tool for monitoring flowing droplets and their content in microfluidic devices. We showed that, in contrast to segmentation-based methods, autocorrelation can monitor and quantify ultrafast droplet flow rates accurately, even with very faint fluorescence signals. Additionally, FCS can monitor the heterogeneity among sequentially passing droplets at high temporal resolution and sensitivity. Therefore, this approach paves a way toward hitherto impossible feedback control for handling, processing, and manipulating of droplets and their content in various high-throughput microfluidic units.

Utilizing the power of FCS for the study of periodically passing objects can facilitate and trigger a variety of additional applications where microscale objects are spatially arranged in solution due to flow, gravity, acoustic waves, or electromagnetic fields. Additionally, this approach enables the use of FCS for detecting and analyzing immobilized nanoscale objects patterned on a sliding specimen. Such a combination would provide high-throughput molecular readouts for binding assays and other in vitro analytical applications.

■ ASSOCIATED CONTENT

Ⓢ Supporting Information

The Supporting Information is available free of charge on the ACS Publications website at DOI: 10.1021/acs.anal-chem.7b03108.

> Microfluidic device, importance of high sampling rate, generating droplets at different flow rates, marginal autofluorescence of the oil phase, monitoring cell encapsulations and droplets inhomogeneity at high temporal resolution, the droplet segmentation algorithm, segmentation and analysis of single droplets, detection of encapsulated cells in flowing droplets, input flow parameters of the aqueous and oil phases, interpretation of $G_D(\tau)$ amplitude (PDF)

■ AUTHOR INFORMATION

Corresponding Authors
*E-mail: eli.zamir@mpimf-heidelberg.mpg.de.
*E-mail: joachim.spatz@mpimf-heidelberg.mpg.de.

ORCID ⊙

Joachim P. Spatz: 0000-0003-3419-9807

Author Contributions
†(E.Z. and C.F.) These authors contributed equally.

Notes
The authors declare no competing financial interest.

■ REFERENCES

(1) Bacia, K.; Kim, S. A.; Schwille, P. *Nat. Methods* **2006**, *3*, 83−89.

(2) Machan, R.; Wohland, T. *FEBS Lett.* **2014**, *588*, 3571−3584.

(3) Magde, D.; Elson, E. L.; Webb, W. W. *Biopolymers* **1974**, *13*, 29−61.

(4) Magde, D.; Webb, W. W.; Elson, E. *Phys. Rev. Lett.* **1972**, *29*, 705−708.

(5) Elson, E. L. *Biophys. J.* **2011**, *101*, 2855−2870.

(6) Sigaut, L.; Villarruel, C.; Ponce, M. L.; Ponce Dawson, S. *Phys. Rev. E: Stat. Phys., Plasmas, Fluids, Relat. Interdiscip. Top.* **2017**, *95*, 062408.

(7) Zamir, E.; Lommerse, P. H.; Kinkhabwala, A.; Grecco, H. E.; Bastiaens, P. I. *Nat. Methods* **2010**, *7*, 295−298.

(8) Pal, N.; Dev Verma, S.; Singh, M. K.; Sen, S. *Anal. Chem.* **2011**, *83*, 7736−7744.

(9) Gosch, M.; Blom, H.; Holm, J.; Heino, T.; Rigler, R. *Anal. Chem.* **2000**, *72*, 3260−3265.

(10) Haustein, E.; Schwille, P. *Methods* **2003**, *29*, 153−166.

(11) Guo, M. T.; Rotem, A.; Heyman, J. A.; Weitz, D. A. *Lab Chip* **2012**, *12*, 2146−2155.

(12) Joanicot, M.; Ajdari, A. *Science* **2005**, *309*, 887−888.

(13) Prakash, M.; Gershenfeld, N. *Science* **2007**, *315*, 832−835.

(14) Teh, S. Y.; Lin, R.; Hung, L. H.; Lee, A. P. *Lab Chip* **2008**, *8*, 198−220.

(15) Shembekar, N.; Chaipan, C.; Utharala, R.; Merten, C. A. *Lab Chip* **2016**, *16*, 1314−1331.

(16) Huebner, A.; Srisa-Art, M.; Holt, D.; Abell, C.; Hollfelder, F.; deMello, A. J.; Edel, J. B. *Chem. Commun. (Cambridge, U. K.)* **2007**, 1218−1220.

(17) Lu, H.; Caen, O.; Vrignon, J.; Zonta, E.; El Harrak, Z.; Nizard, P.; Baret, J. C.; Taly, V. *Sci. Rep.* **2017**, *7*, 1366.

(18) Pekin, D.; Taly, V. *Methods Mol. Biol.* **2017**, *1547*, 143−164.

(19) Sciambi, A.; Abate, A. R. *Lab Chip* **2015**, *15*, 47−51.

(20) Whitesides, G. M. *Lab Chip* **2010**, *10*, 2317−2318.

(21) Niu, X.; deMello, A. J. *Biochem. Soc. Trans.* **2012**, *40*, 615−623.

(22) Duffy, D. C.; McDonald, J. C.; Schueller, O. J. A.; Whitesides, G. M. *Anal. Chem.* **1998**, *70*, 4974−4984.

(23) Hofmann, T. W.; Hanselmann, S. H.; Janiesch, J. W.; Rademacher, A.; Bohm, C. H. J. *Lab Chip* **2012**, *12*, 916−922.

(24) Lisensky, G. C.; Campbell, D. J.; Beckman, K. J.; Calderon, C. E.; Doolan, P. W.; Ottosen, R. M.; Ellis, A. B. *J. Chem. Educ.* **1999**, *76*, 537.

(25) Platzman, I.; Janiesch, J.-W.; Spatz, J. P. *J. Am. Chem. Soc.* **2013**, *135*, 3339−3342.

(26) Holtze, C.; Rowat, A. C.; Agresti, J. J.; Hutchison, J. B.; Angile, F. E.; Schmitz, C. H. J.; Koster, S.; Duan, H.; Humphry, K. J.; Scanga, R. A.; Johnson, J. S.; Pisignano, D.; Weitz, D. A. *Lab Chip* **2008**, *8*, 1632−1639.

(27) Anna, S. L.; Bontoux, N.; Stone, H. A. *Appl. Phys. Lett.* **2003**, *82*, 364−366.

(28) Christopher, G. F.; Anna, S. L. *J. Phys. D: Appl. Phys.* **2007**, *40*, R319.

(29) Thorsen, T.; Roberts, R. W.; Arnold, F. H.; Quake, S. R. *Phys. Rev. Lett.* **2001**, *86*, 4163−4166.

Supplementary Material

Reconceptualizing fluorescence correlation spectroscopy for monitoring and analyzing periodically passing objects

Eli Zamir[†,*], Christoph Frey[†], Marian Weiss, Silvia Antona, Johannes P. Frohnmayer, Jan-Willi Janiesch, Ilia Platzman and Joachim P. Spatz*

Department of Cellular Biophysics, Max Planck Institute for Medical Research, Jahnstraße 29, D-69120 Heidelberg, Germany

Department of Biophysical Chemistry, University of Heidelberg, Im Neuenheimer Feld 253, D-69120 Heidelberg, Germany
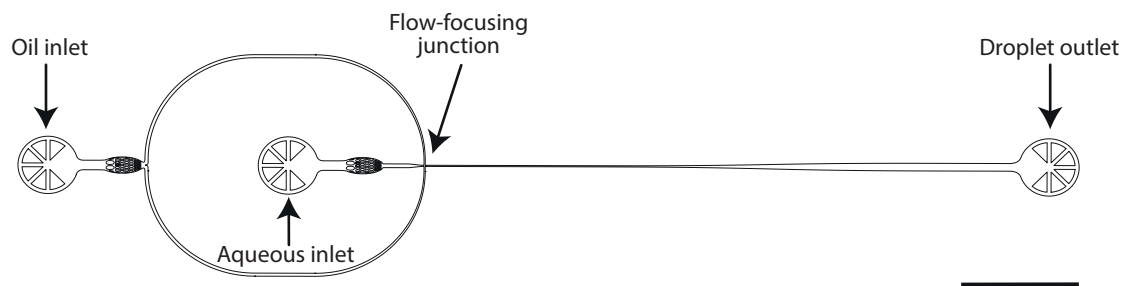
[†]Equal contribution
*Corresponding Authors:
eli.zamir@mpimf-heidelberg.mpg.de, joachim.spatz@mpimf-heidelberg.mpg.de
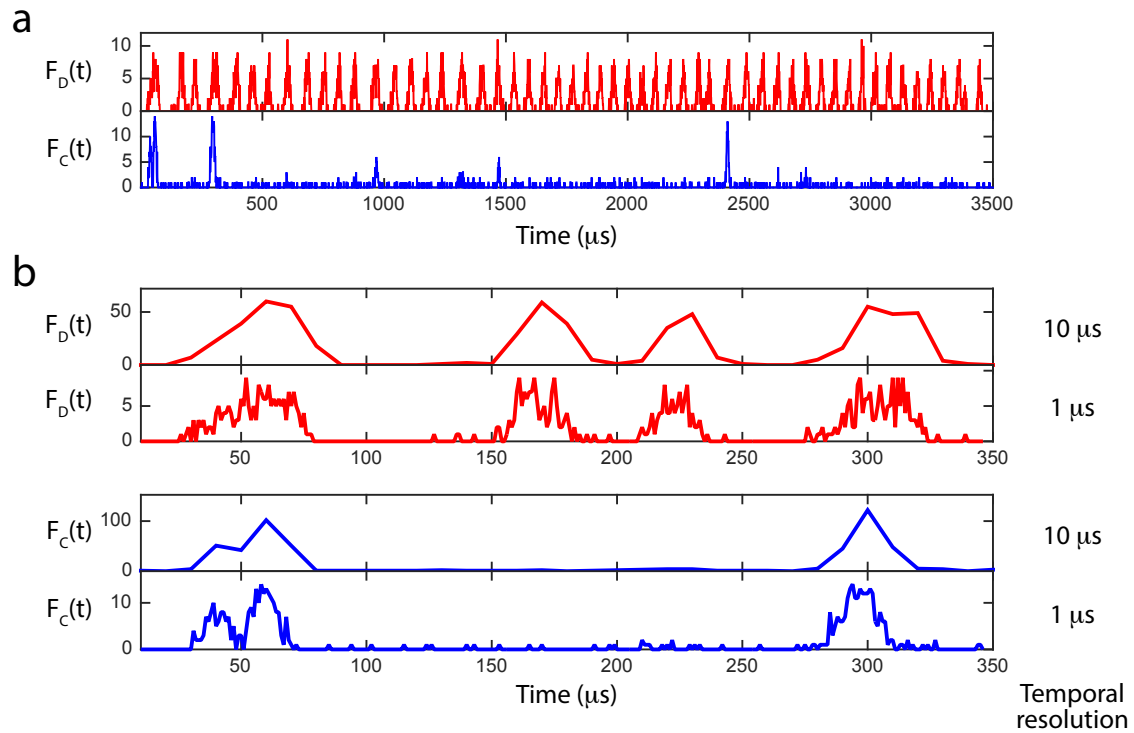
Table of Contents

SUPPLEMENTARY FIGURES

Supplementary Figure S1

Sketch of the microfluidic device used for the droplet production and cell encapsulation. Scale bar, 3 mm.

Supplementary Figure S2

The importance of high sampling rate for robust monitoring of fast-flowing droplets and their content. **(a)** An example of droplet-marker and cell-marker intensity traces recorded for droplets flowing at a rate of 17 kHz (for clarity, a 3.5 ms segment from these traces is shown). **(b)** Plots of $F_D(t)$ and $F_C(t)$ along the first 350 µs part of the recorded period shown in (a) binned to a temporal resolution of 10 µs or 1 µs.
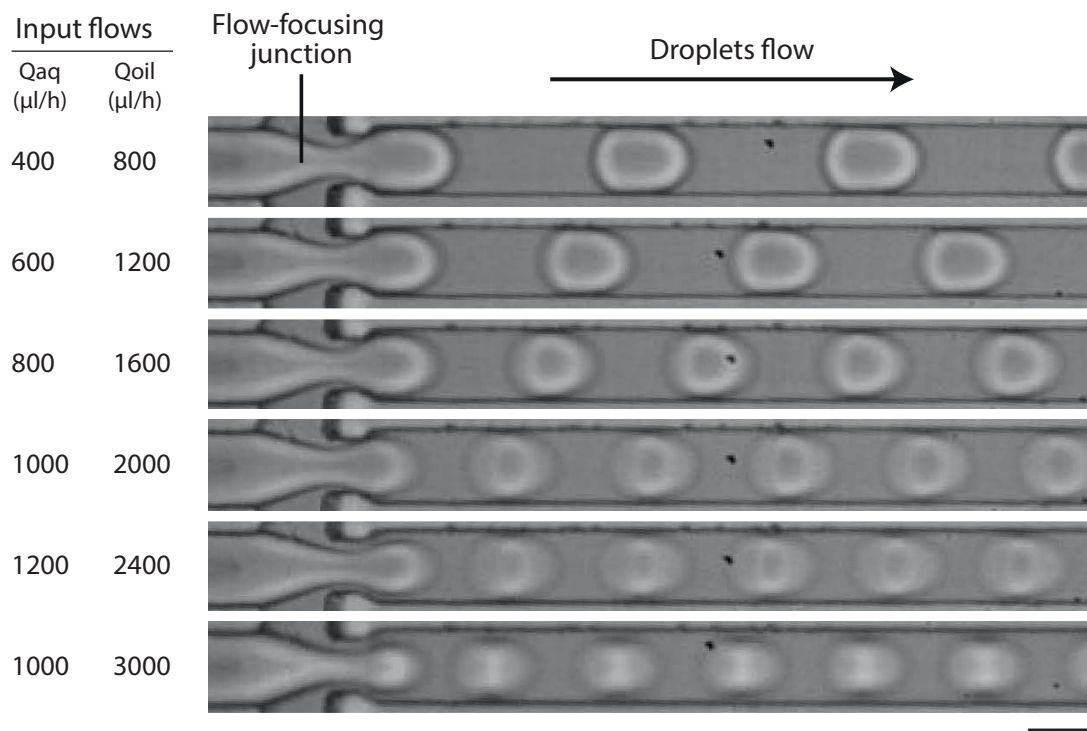
Supplementary Figure S3

Representative images of the flow-focusing junction in which the droplets are generated with different inlet flow rates for the aqueous and oil phases (Q_{aq} and Q_{oil}, respectively). The obtained droplets production rates for the different inlet flow rates are listed in Supplementary Table S1. Scale bar 30 μm.

a Transmission image

Oil phase
(HFE-7500)

Aqueous phase
(PBS)

b Fluorescence image

c Sum of 40 fluorescence images
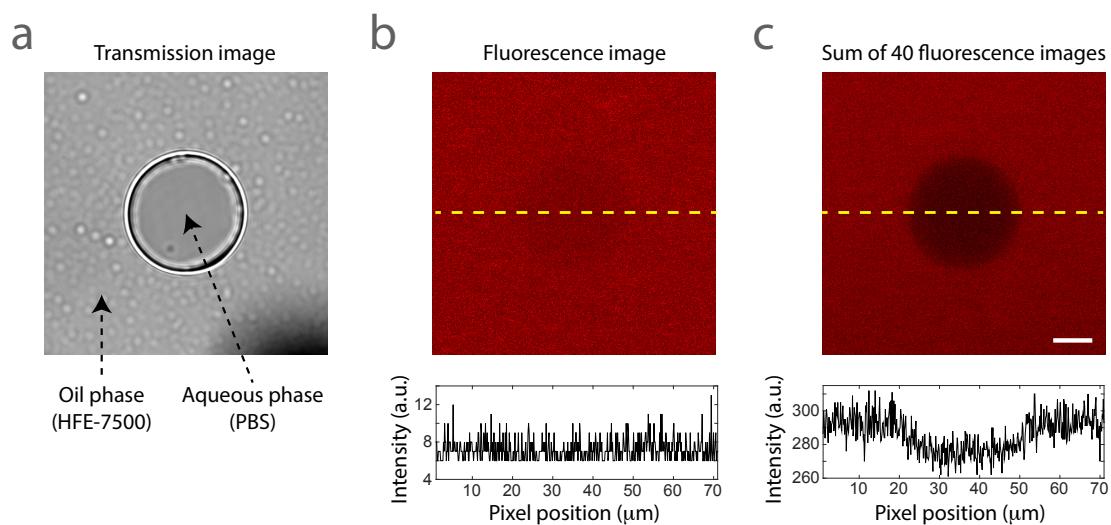
Supplementary Figure S4

Marginal auto-fluorescence of the oil phase. **(a)** A transmission image of a representative droplet containing PBS as the aqueous phase and embedded in HFE-7500 as the oil phase. **(b)** Top, a fluorescence image taken using excitation at 633 nm, with laser attenuator set to 50 % power, and detection range between 641-695 nm. Bottom, the profile of the fluorescence intensity along a sampled line, as indicated on the image (dashed line). **(c)** Top, an image summing 40 consecutive images of the same droplet, each of which taken as described in (b). Bottom, the corresponding fluorescence intensity profile. Scale bar 10 µm.
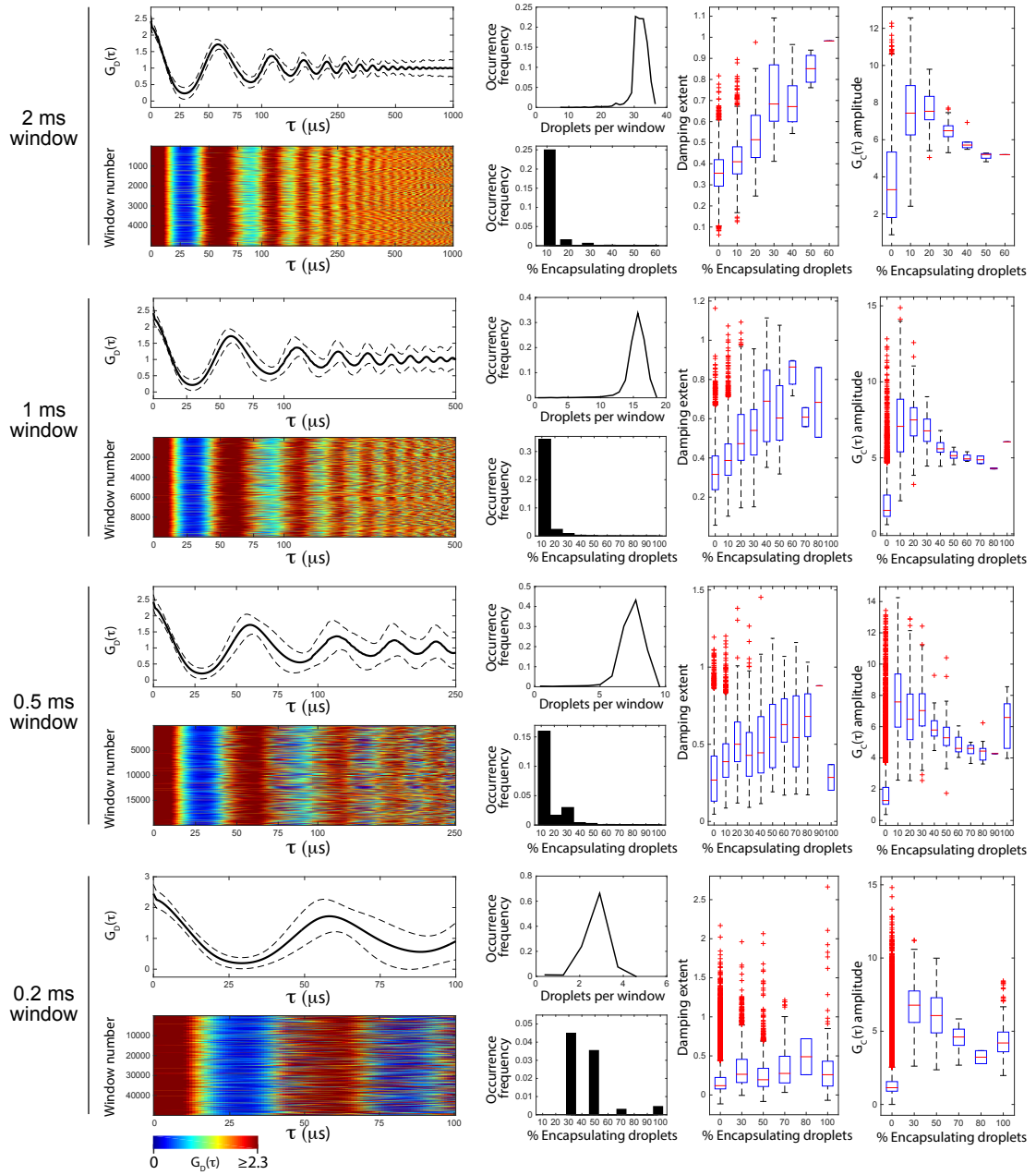
Supplementary Figure S5

Monitoring cell encapsulations and droplets inhomogeneity at high temporal resolution. Droplets were produced with cell encapsulation at droplets flow rate of 17 kHz. The recorded $F_D(t)$ was scanned with different window sizes, as indicated. For each window position $G_D(\tau)$ and $G_C(\tau)$ were calculated. Left column, plots showing the mean $G_D(\tau)$ (solid line) ± standard deviation (dashed lines) and heatmaps showing the $G_D(\tau)$ for each window position. Second column from left, distributions of droplets per window and of percentage encapsulating droplets. Third and fourth columns from left, boxplots of the damping extents of $G_D(\tau)$ and of $G_C(\tau)$ amplitudes as a function of percentage encapsulating droplets.

Start
t = 1

Initiate a gap mask — No — $F_D(t)$ in all next P_{thr} time bins > I_{thr} ? — Yes — Initiate a droplet mask

t = t + 1

Elongate gap mask by 1 time bin

Elongate droplet mask by 1 time bin

t = t + 1

$F_D(t)$ in all next P_{thr} time bins > I_{thr} ? — No

t = t + 1 — No

$F_D(t)$ in all next P_{thr} time bins < I_{thr} ? — No

Yes

Terminate the gap mask

End of $F_D(t)$ reached ?

No

Terminate the droplet mask

Yes

t = a time bin index number
$F_D(t)$ = Marker intensity trace
I_{thr} = Intensity threshold
P_{thr} = Persistency threshold
W_{thr} = Width threshold

Derived droplet masks

$F_D(t)$

t

Delete all droplet masks which are < W_{thr}

End

Supplementary Figure S6

A flowchart of the droplet segmentation algorithm. The algorithm scans the droplet-marker intensity trace, $F_D(t)$, which lists the total number of photons detected within each time bin (here 1 μs) along the recorded period. In addition to $F_D(t)$, the input parameters include: (i) I_{thr} − an intensity threshold to distinguish gap background intensity from droplet intensity levels, (ii) P_{thr} − a persistency threshold defining how many sequential time bins have to be above or below I_{thr} in order to initiate or terminate a droplet mask, respectively, (iii) W_{thr} − a width threshold, defining the minimal passing time below which an identified droplet mask can be assumed to be related to noise rather than to an actual droplet. The output of the algorithm is a binary mask indicating the periods along $F_D(t)$, that correspond to the individual droplets.
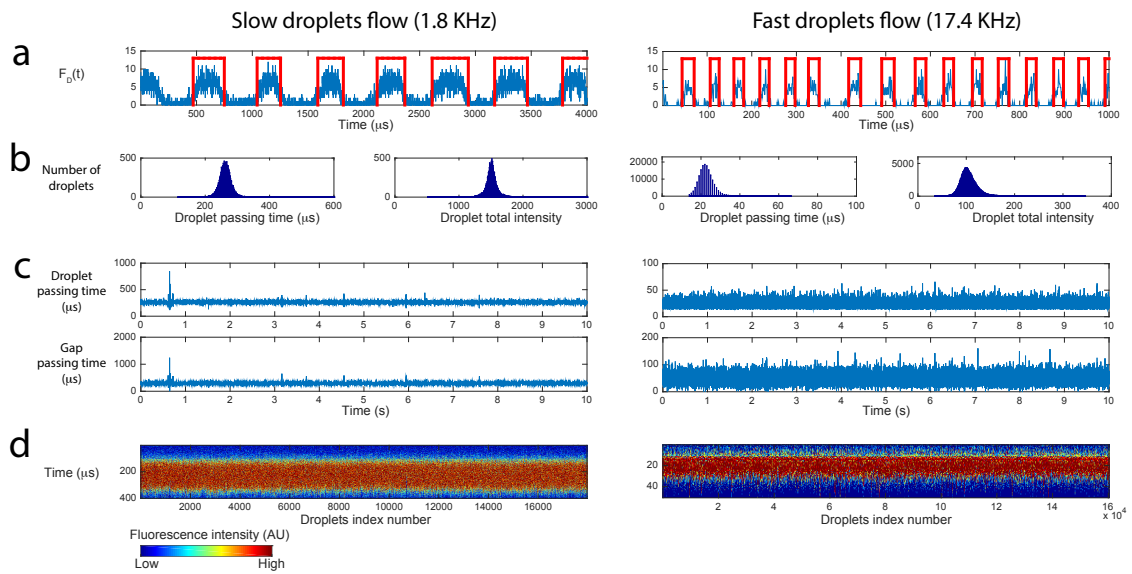
Supplementary Figure S7

Segmentation and analysis of single droplets. Droplets were produced for 10 seconds at rates of 1.8 kHz (left panel) and 17.4 kHz (right panel). For each production rate, the recorded $F_D(t)$ was subjected to the droplets-segmentation algorithm. **(a)** A fragment of $F_D(t)$ is shown (blue) overlaid with the obtained binary mask of the droplets segments (red). **(b)** histograms of the passing time and total intensity of the individual droplets. **(c)** The passing time of each droplet and of the gap between each two sequential droplets as a function of time along the droplet production session. **(d)** Heatmaps showing the intensity profile of each droplet.
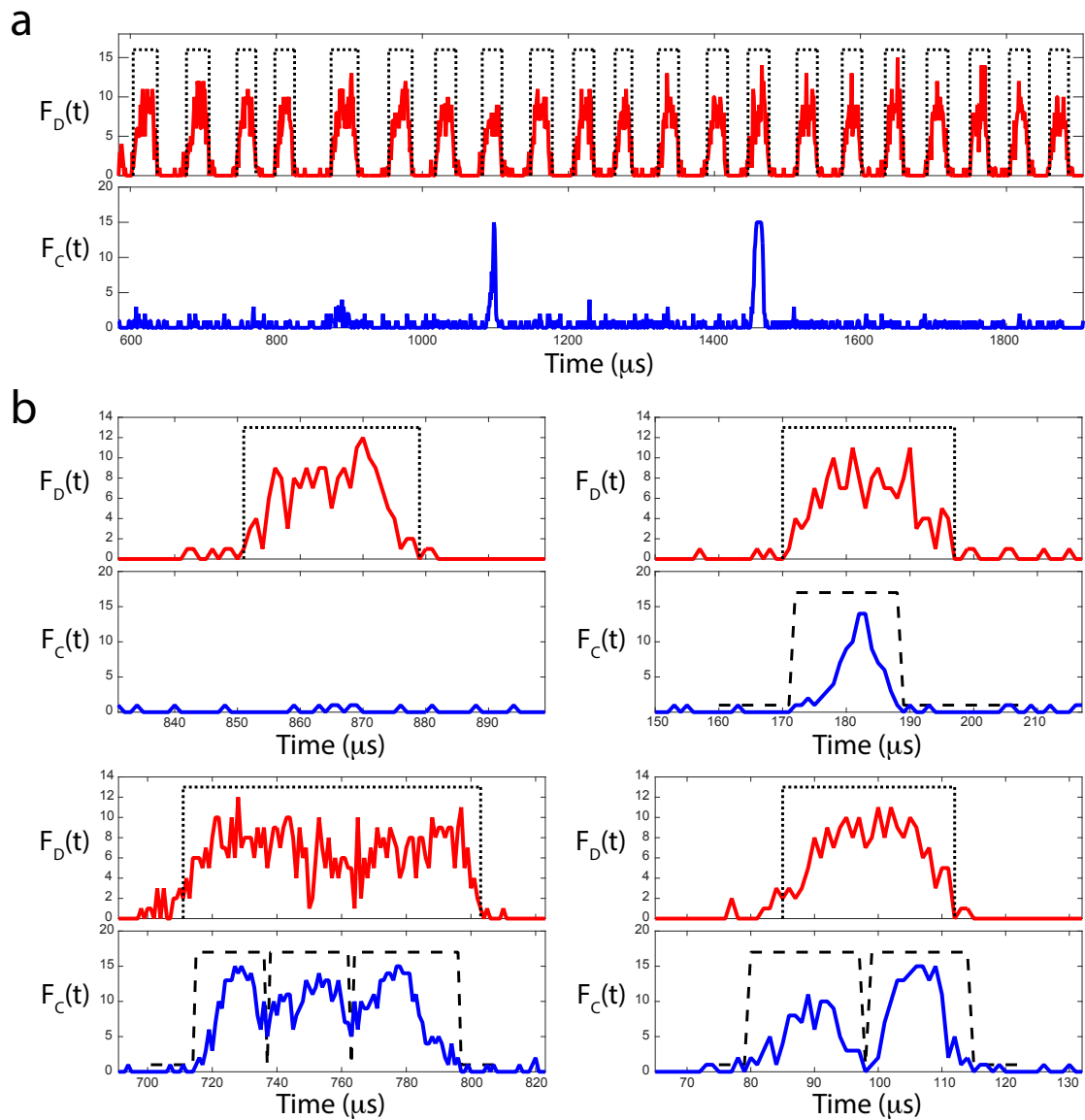
Supplementary Figure S8

Detection of encapsulated cells in the flowing droplets. Droplets were produced with cell encapsulation at droplet flow rate of 17 kHz. **(a)** An example of a short interval out of the recorded droplet-marker and cell-market intensity traces are shown. **(b)** Examples of droplets for which the watershed algorithm identified 0, 1, 2 and 3 cells (ordered clockwise from top-right). The dashed line in all plots indicates the masks of the droplets of the cells as generated by the respective segmentation algorithm.

SUPPLEMENTARY TABLES

| Input flow rates (µl/hr)		Obtained Droplets flow rate (kHz)
Qaq	**Qoil**	
400	800	3.52 ± 0.02
600	1200	5.59 ± 0.06
800	1600	8.97 ± 0.14
1000	2000	11.58 ± 0.05
1200	2400	16.75 ± 0.46
1000	3000	18.50 ± 0.50

Supplementary Table S1

Droplet production frequencies were determined by counting $20 - 32$ sequential droplets at the beginning, middle and end of two videos from each experiment. Mean frequencies values and their standard deviation are shown.

SUPPLEMENTARY NOTES

Supplementary Note S1: Interpretation of $G_D(\tau)$ amplitude

The amplitude of the auto-correlation curve of $F_D(t)$ at the origin ($\tau = 0$) can be calculated as:

$$G_D(0) = \frac{\langle(\delta F_D(t))^2\rangle}{\langle F_D(t)\rangle^2} + 1 = \frac{\langle(F_D(t) - \langle F_D(t)\rangle)^2\rangle}{\langle F_D(t)\rangle^2} + 1 =$$

$$= \frac{variance(F_D(t))}{\langle F_D(t)\rangle^2} + 1 = \frac{\langle F_D(t)^2\rangle - \langle F_D(t)\rangle^2}{\langle F_D(t)\rangle^2} + 1 = \frac{\langle F_D(t)^2\rangle}{\langle F_D(t)\rangle^2} \; . \tag{1}$$
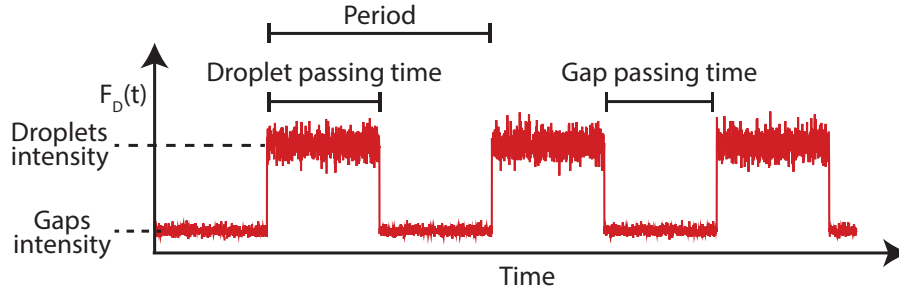
For a flow of droplets that are homogenously labeled with intensity I_D, the fraction P_D of the time at which $F_D(t)$ equals I_D is

$$P_D = \frac{droplet\; passing\; time}{droplet + gap\; passing\; time} \tag{2}$$

and the fraction of time at which $F_D(t)$ equals the gap intensity, I_G, is $1 - P_D$. Accordingly, the mean of the trace is

$$\langle F_D(t)\rangle = I_D P_D + I_G(1 - P_D) \; . \tag{3}$$

Combining equations (1) and (3) gives

$$G_D(0) = \frac{\langle F_D(t)^2\rangle}{\langle F_D(t)\rangle^2} = \frac{P_D I_D^2 + (1 - P_D)I_G^2}{(I_D P_D + I_G(1 - P_D))^2} \; . \tag{4}$$

By defining the intensity in the droplets as its fold increase in respect to the background intensity in the gaps, $I_D = \gamma \cdot I_G$, we get:

$$G_D(0) = \frac{P_D(1-P_D)(\gamma-1)^2}{\left(1+P_D(\gamma-1)\right)^2} + 1 \quad . \tag{5}$$

The derivative of this $G_D(0)$ in respect to γ is

$$\partial_\gamma G_D(0) = \frac{2(\gamma-1)(1-P_D)P_D}{(1+(\gamma-1)P_D)^3} \quad . \tag{6}$$

By definition $0 < P_D < 1$. Therefore, given $\gamma > 1$, Equation 6 implies $\partial_\gamma G_D(0) > 0$, meaning that for a given P_D, the amplitude of the auto-correlation curve of $F_D(t)$ increases as the ratio between the droplets intensity and the background intensity increases. This increase is monotonous but not linear. If $\gamma = 1$ (i.e. the droplets intensity is as the gaps intensity) then $G_D(0)=1$, while for $\gamma \rightarrow \infty$, $G_D(0)$ converges to $(1-P_D)/P_D+1$. Accordingly, flow conditions with lower P_D's enable a higher dynamic range for detecting changes in γ. The figure below plots $G_D(0)$ as a function of γ for different values of P_D, calculated based on Equation 5.
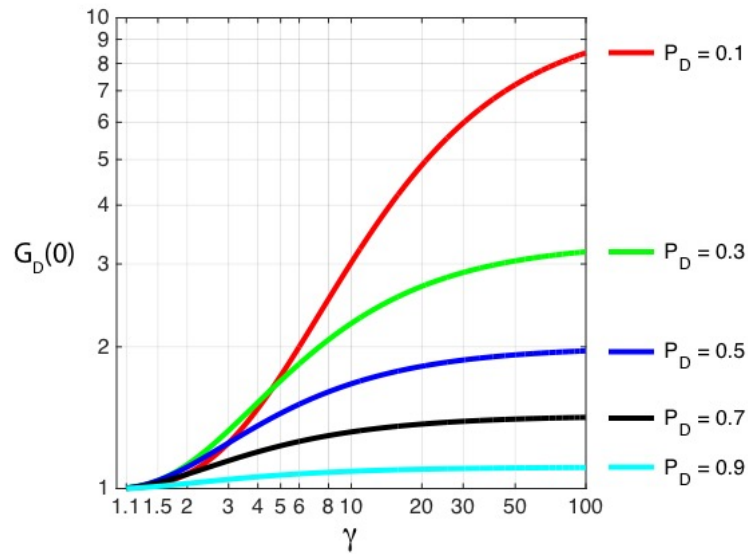
CHAPTER 3

Discussion and Outlook

3.1 Discussion

The question 'What is Life' asked at the beginning of this thesis is nowadays tackled by researchers originating from a variety of different core disciplines, such as Physics, Mathematics, Chemistry or Material Science [118]. The applications and combinations of different methodological approaches and techniques towards Biology resulted in the development of new research areas such as *System Biology* or *Synthetic Biology*. From these, *bottom-up synthetic biology* strives for an experimental reconstruction of a living cell or even a living organism, using engineering principles. The ultimate goal is to combine either already existing molecular building units from a living cell or equivalent synthetically produced components to a minimal system that is able to perform fundamental tasks associated with a living system. Towards this end, the generation of compartments for a controlled encapsulation and combination of these building units has become a remarkable challenge. On the one hand such compartments should be bio-compatible as well as mechanically and chemically stable. Bottom-up synthetic biology approaches on the other hand require a sequential and controllable loading of these compartments with bio-molecules under different buffer conditions. So far, these two contradictory requirements have not been met in a satisfying way.

This discussion points out the contributions of the thesis to new developments in bottom-up synthetic biology, especially the formation of manipulatable compartments with tuneable properties for a controlled assembly of biomolecules. The use of microfluidic water-in-oil droplets as compartments and the associated microfluidic manipulation tools are critically discussed. Furthermore, the newly-developed dsGUV compartment system and the demonstrated applications and analysis methods are evaluated in regards to future applications. Finally, this discussion gives an outlook to next possible research questions.

3.1.1 Characterization of Microfluidic Droplets as Compartments

Every cell needs a shell in order to separate the interior processes from the outside. In the past, most bottom-up synthetic cell approaches were based on lipid bilayer vesicles or polymersomes as compartments [119]. This is intuitively understandable, since living cells represent a water-in-water system, where interior and exterior are separated by a biomembrane. However, the utilized compartments so far showed a limited stability and even more importantly, technologies which allow for the precise and efficient delivery of different biological components (see Section 1.2) into the compartments were still missing. Therefore, in this thesis, the use of microfluidic water-in-oil droplets (see Section 1.4.2) as compartments for a bottom-up synthetic cell approaches was investigated.

In a first step, the physical and chemical key factors for stable droplet production and the reliable encapsulation of fluorescent dyes and bio-molecules into the droplets were investigated. It was shown, that the stability of microfluidic water-in-oil drop- lets depends on the physical properties of the surfactants (see Section 1.4.3). Surfactants with triblock geometry have two PFPE-tails and can thus form a denser PFPE layer at the outside of the droplet's periphery in comparison to diblock surfactants. This provides a better shield against coalescence of the droplets. Similar observations have been made by other groups [120, 121]. Furthermore, the concentration of the surfactants influences the stability of the droplets. Surfactant concentrations below 1 mM led to coalescence of the droplets, which is in good agreement with previous studies [86, 121]. For concentrations above 10 mM the creation of small daughter-droplets was observed, which can be attributed to a shift

from dripping mode to tipstreaming mode (see [122]). These effects have now been experimentally assessed and have to be considered in future droplet-based microfluidic applications, where the creation of stable and uniform droplets as compartments is desired.

Following these investigations, the retention ability of different fluorescent dyes in microfluidic droplets was analyzed for various surfactant types, surfactant concentrations and buffer conditions. Fluorescent dyes are crucial for many biochemical and biomedical applications, since they allow the visualization and localization of labeled biomolecules. Thus, different dyes covering the whole visible spectrum and therefore allowing for multicolor acquisitions were selected. It was shown, that the retention of these dyes for given buffer conditions depends mainly on their hydrophilicity. By calculating the distribution coefficient LogD, which is a measurement for the hydrophilicity, the probable retention of the corresponding fluorophore can be estimated. However, the LogD value can not be considered as an exclusive criterion for the retention ability of the dyes, since it could be shown that also other factors such as the molecular weight and the three-dimensional structure of the dyes influence the retention.

Additionally, the choice of surfactant types and concentrations has a strong influence on the retention of the dyes. Surfactants with diblock geometry showed the best retention ability for the fluorescent dyes. This can be explained with a denser hydrophilic PEG layer at the inner periphery of the droplets in comparison to triblock surfactants [89]. Furthermore, surfactants with longer PEG and PFPE tails showed better retention ability than short ones. This observation can be explained with a higher energetic barrier the dyes have to pass in order to dissipate into the oil phase. Similar results for silicone-based polymeric surfactants were found in [123].

Finally, the inevitability of choosing adjusted fluorescent dyes for the labeling of biomolecules was demonstrated with the bio-molecule tubulin (see Section 1.2.2). The amphiphilic nature of tubulin in addition to the 'wrong' choice of labeling dyes or surfactant types led to a release of the corresponding microtubules out of the droplets into the oil phase. In contrast, stable retention was achieved for adjusted surfactant types or adjusted fluorescent dyes.

The results presented here allow for the following statements, which should be considered in future applications based on microfluidic droplets:

- The mechanical stability of microfluidic water-in-oil droplets depends mainly on the stabilizing surfactant type and the surfactant concentration.

- The key factors for stable retention of fluorophores inside droplet-compartments depend on the physical and chemical structure of the dye, the buffer conditions, as well as the surfactant type and concentration. A screening of the different conditions allows for the creation of 'look-up tables' for the choice of appropriate dyes under specific conditions for future applications.

- Advanced retention of labeled (bio-) molecules inside microfluidic droplets can be achieved by proper adjustment of the identified key factors, e.g by changing the labeling dye or the surfactant type.

3.1.2 Microtubule Self-organization inside Microfluidic Droplets

After optimizing the conditions for a stable creation of microfluidic droplets, the next step was to investigate how these droplets can serve as compartments for the encapsulation of bio-molecules under controlled conditions. Towards this end, the polymerization and self-assembly of tubulin into microtubule structures (see Section 1.2.2) inside microfluidic droplets was investigated. First experiments focused on optimizing the conditions for a reproducible polymerization of tubulin inside microfluidic droplets (see Appendix A).

It was demonstrated, that the transfer from unconfined bulk conditions to compartments with volumes in the range of living cells needs the adjustment of the utilized biochemical components and concentrations. After optimizing these conditions, microtubule self-assembly and the organization into different arrangements was observed. It is worth mentioning here, that the microtubule polymerization and organization was achieved without any stabilizing agent such as taxol or glycerol, which was necessary in previous experiments [124]. In principle, this allows to study the dynamic behavior of microtubules.

Furthermore, it could be demonstrated that growing microtubules can deform and elongate their compartment by aligning into parallel bundles. This behavior remarkably resemble the mitotic spindle formation in living cells during mitosis (see Section 1.2.2). In my research, this formation was observed for an increased tubulin concentration inside the droplets and without the involvement of any motor proteins. Similar observations have been made by other groups for microtubules encapsulated into lipid vesicles [125, 126]. However, the exact mechanism behind the formation process could not be explained, since the experiments were only to a limited extent reproducible and the interactions of tubulin with the surfactant layer dominated in most of the cases (see Appendix A.1). Nevertheless, future studies might allow for the controlled creation of these arrangements and could thus mimic cellular division by an induced droplet division.

During all the experiments mentioned above, the interactions of tubulin with the surfactant layer at the periphery of the droplets dramatically limited the use of microfluidic droplets as optimal compartments (see Appendix A.1). Therefore, long-term observations of microtubule organization and dynamic processes, which would involve the use of motor proteins could not be investigated. In order to overcome this problem, two approaches were taken. The first one involved the introduction of an additional lipid bilayer at the droplet's inner periphery with the ultimate goal to prevent interactions of tubulin with the surfactant layer. This approach is demonstrated in Publication 3.

The second one addressed the surfactants and the surrounding oil. During experimental work in my research it became clear, that the purification of the synthesized surfactants was insufficient, thus leaving a small portion of unreacted Krytox (perfluoropolyether, PFPE) in the surrounding oil-surfactant mix in the continuous phase. This led to an acidification of the aqueous phase inside the droplets and thus to the observed depolymerization of the microtubule structures over time (see Appendix A.1). Based on these findings, co-worker Michael Juniper investigated the polymerization of microtubules in microfluidic droplets surrounded by HFE7500 oil (3M, USA) and 1.8 % RAN-008 fluorosurfactants (RAN Biotechnologies, USA), which are commercially available and have no traces of Krytox. Under these conditions no interactions of tubulin with the surfactant layer were observed and a dynamic, reversible arrangement of microtubules in combination with motor proteins was achieved. The results are published in Publication 2.

In this context, the use of microfluidic technology allowed for a controlled creation of monodisperse compartments with a well-defined size. Under these conditions, the self-organization of microtubules into aster-like structure, mediated by the minus-end-directed motor protein *Xenopus laevis* kinesin-14 (XCTK2), was studied. The process of aster formation was found to be dependent on the motor protein concentration as well as on the chemical conditions of the boundary, i.e. the surfactant concentration. For optimized conditions, robust aster formation was detected in hundreds of droplets. These findings demonstrate one major advantage of microfluidic droplets as compartments, having identical and controlled conditions in a high number of samples. This allows for statistically significant observations and statements of the behavior of a minimal synthetic system.

Theoretical models [127] predict the formation of microtubule asters and vortices in the presence of motor proteins such as kinesin or dynein for unconfined conditions. The system developed here could be a suitable tool to experimentally study these results under controlled conditions for compartments with different sizes and to investigate biological pattern formation for a minimal system with reduced complexity.

Summarizing the above, the following conclusions for microfluidic water-in-oil droplets as compartments for bottom-up synthetic cell approaches can be drawn:

- Microfluidic droplets do not provide entirely sealed and chemically inert compartments, instead the physical and chemical properties of the surrounding oil and the surfactants in particular have to be considered.

- After optimizing the external conditions, microfluidic droplets can serve as monodisperse compartments in a large quantity, showing uniform chemical conditions and thus allowing for highly-reproducible experiments.

- The precise control over the biochemical micro-environment inside the compartments allows for omitting artificial stabilizing agents and thus enables the investigation of dynamic and reversible self-organization processes of tubulin and associated motor proteins.

- Even though the synthetic system described and developed here is very much reduced in complexity, it already exhibits attributes of living cells, notably parallel microtubule organization and relating elongation of the microfluidic droplets.

3.1.3 Droplet-stabilized Giant Unilamellar Vesicle (dsGUVs)

So far, the use of microfluidic droplets as compartments for studying the self-organi- zation of proteins was demonstrated by the example of tubulin polymerization into micro-tubule structures. In this system the microfluidic droplets serve as a stable and manip-ulatable, three-dimensional confinement. However, the main limitation to realistically mimic a living cell is the missing bio-membrane and the continuous oil phase around the compartments. In order to overcome this problem, a fundamental new approach was taken, namely the formation of an enclosed lipid bilayer at the inner periphery of the droplets. This system was termed *droplet-stabilized Giant Unilamellar Vesicle* (dsGUVs) and is presented in Publication 3.

Since this system represents a new type of compartments for bottom-up synthetic cell approaches, the properties were characterized thoroughly. The investigation of the exact nature of the created lipid arrangement was of particular importance. In a first step, the formation mechanism of dsGUVs was investigated. It could be shown, that the transfer from encapsulated lipid vesicles to an enclosed lipid bilayer at the periphery depends on an optimized ion concentration of the interior aqueous phase. These findings are in good agreement with previous studies on two-dimensional supported lipid bilayer systems (see Section 1.3.2), where it could be shown that ions are necessary to promote the adhe-sion between approaching vesicles and the supporting substrate [79, 128]. This leads to the rupture of the vesicles and a subsequent fusion of the lipid patches, resulting finally in a continuous lipid bilayer. In order to visualize the formation process in real time, GUVs were formed by electroformation and were encapsulated into microfluidic droplets. This allowed a quantification of the formation process. Additionally, the formation process out of SUVs was analyzed by fluorescence intensity measurements of flowing droplets in a microfluidic device shortly after droplet production (see Appendix A.4). The formation times are in good agreement with theoretical considerations based on the mean diffusion time of the vesicles inside the droplets. Knowing the temporal formation process of ds-GUV is crucial for future applications, where an intact lipid bilayer has to be established prior to other processes such as e.g. the polymerization of biomolecules inside the ds-GUVs.

Furthermore, the physical properties of the created dsGUV system were analyzed. Flu-orescence intensity measurements of dsGUVs and corresponding GUVs formed by elec-troformation were performed and compared. The results indicate the formation of a continuous, unilamellar lipid bilayer for adjusted lipid concentrations. Another inves-tigation was the formation of a phase-separated dsGUV-system (see Appendix A.2 and Section 1.2.1). However, the creation of phase-separated dsGUVs was not achieved in this work, most probably due to perturbations from the supporting surfactant layer. On the other hand, the occasional observation of defects inside dsGUVs might indicate the lipid-bilayer like structure of the system (see Appendix A.2). Additionally, the mobility of the lipids forming the dsGUVs was investigated by FRAP measurements. It could be shown, that the diffusion coefficient of the lipids inside dsGUVs is slightly reduced com-pared to free-standing GUVs, but in the same order of magnitude. This reduction can be explained by perturbations of the supporting surfactant layer of the droplets, as it was also observed for two-dimensional supported lipid bilayer systems [129, 130].

In order to definitively reveal the nature of the created system, different approaches were developed and realized to release the assembled lipid bilayer compartments from the stabilizing surfactant-oil phase into an aqueous environment (see Appendix A.3). All

these approaches are based on bringing the dsGUVs in close contact with the continuous aqueous phase and on subsequently breaking the stabilizing oil-surfactant layer without destroying the lipid bilayer (see Figure A.8). This could be demonstrated in a "Bulk Release" approach in an Eppendorf tube. In order to better understand and analyze the release process, another approach was taken, using a flow chamber to bring dsGUVs and the continuous aqueous phase together. This allowed the direct observation of the release process. Furthermore, by labeling the aqueous phase inside the droplets, the continuous aqueous phase as well as the oil phase with different fluorophores (using the results from Publication 1) it could be shown that the content inside the droplets was conserved and that there was no exchange during the release process. Finally, in order to integrate the release process into a microfluidic droplet pipeline and therefore to aim for a real Lab-on-Chip application, different microfluidic release devices were designed and tested (see Section A.3). It could be shown, that adjusted microfluidic geometries allow for a remarkable deceleration of the droplets before they come into contact with the continuous aqueous phase (see Figure A.11). This enabled a gentle transition and a reduction of the shear forces acting on the lipid bilayer. The release of the lipid compartments from the stabilizing oil phase into an aqueous environment and their subsequent analysis indicate strongly the unilamellar lipid bilayer structure of the dsGUV system. Furthermore it represents a new technique to create monodisperse GUVs in a controlled way.

However, in recent years, the controlled high-throughput formation of monodisperse GUVs using other microfluidic methods such as pulse jets, droplet shooting or layer-by-layer lipid assembly was achieved [76–78]. In order to point out the superior properties of the system developed here, the ability of a sequentially loading with bio-molecules was demonstrated. Towards this end, microfluidic pico-injection technology (see Section 1.4.4) was adopted for the precise delivery of bio-molecules into dsGUVs. A first demonstration was the injection of his-tagged GFP into dsGUVs, functionalized with NTA(Ni) complexes. The functionalized lipid bilayer at the droplet's inner interface presents anchoring points for the injected his-tagged GFP bio-molecules. Indeed, it could be observed, that the GFP binds to the lipid bilayer, indicating that both the lipid bilayer as well as the bio-molecules are functionally not affected by the pico-injection process. Furthermore, the mobility of the GFP molecules in the lipid bilayer was analyzed by FRAP measurements. The resulting diffusion coefficient is in good agreement with previous studies on SLB and indicates a successful binding of GFP to the lipid bilayer.

Following the success of applying pico-injection technology to dsGUVs, the incorporation of transmembrane proteins into the lipid bilayer was investigated. Therefore, the transmembrane protein F_0F_1-ATPase (see Section 1.2.2) was reconstituted into proteoliposomes and injected into preformed dsGUVs via pico-injection. A successful fusion of the ATPsynthase-containing proteoliposomes with the lipid bilayer was observed by correlated fluorescence signals. Furthermore, the mobility of the incorporated ATPase was analyzed by FRAP measurements and found to be in good agreement with previous studies in pure GUV systems. Additionally the functionality of the incorporated transmembrane proteins was investigated. Towards this end, a transmembrane pH gradient between the interior of the dsGUVs and the surrounding oil phase was applied by introducing acidic molecules via the oil phase. It could be demonstrated, that the energizing force of the pH gradient is sufficiently enough to drive the ATPase to synthesize ATP inside the dsGUVs. However, the total synthesized ATP amount is much lower than it would be expected from theoretical calculations. This can be mainly attributed to the missing transmembrane electric potential gradient (see Section 1.2.2). Furthermore, the procedure to detect ATP is currently unsufficient, since the long time delay between ATP

synthesis and ATP detection leads to the hydrolysis of ATP and therefore to a lower measurable concentration. To overcome this problem, the direct observation of ATP inside the dsGUV would be desirable. Therefore, an optical setup for the sensible detection of bioluminescence, corresponding to synthesized ATP still has to be established in future applications. Nevertheless, the principal functionality of the reconstituted ATPsynthase was shown, demonstrating the successful reconstitution of a rather complex transmembrane protein, composed of various subunit with specific functions, into the dsGUV system.

Additionally it was demonstrated, that the pico-injection technology enables the loading of dsGUVs with cytoskeleton proteins, such as tubulin. This is of particular importance, since a direct mixing approach, where tubulin and lipids were introduced into the droplets at the same time, did not result in the formation of a continuous lipid bilayer. Additionally it was shown, that interactions of the microtubules with the surrounding surfactant layer (see Appendix A.1) could be minimized in the case of dsGUVs. These findings pave the road towards a sequentially assembly of a synthetic cytoskeleton, allowing to study the self-organization with reduced complexity under controlled conditions.

Summarizing the above, the combination of droplet-based microfluidic manipulation methods and biologically relevant membrane properties allows to overcome limitations of traditional compartments in synthetic cell biology. The sequential loading with different molecules, proteins and buffer conditions enables combinations, that would not occur for a direct mixing of all at once. The enhanced mechanical and chemical stability of the compartments pave the road for a bottom-up assembly of different bio-molecules as it was exemplary demonstrated for the cytoskeleton protein tubulin and the transmembrane protein ATPsynthase.

The high-throughput microfluidic production methods allow for the creation of up to 10^3 compartments per second. Due to the sequential, controllable and adjustable loading methods developed in this thesis, different compositions and concentrations of the molecular components of the synthetic cells can be achieved, which will enable the screening and analysis of vast numbers of synthetic cells having different compositions within short times. Additionally, the possibility of releasing the assembled lipid compartments into an aqueous environment opens the door for investigations of the assembled protocells under physiologically relevant conditions.

The characteristics of the new compartment type and applications for bottom-up synthetic cell approaches developed in this thesis can be summarized as follows:

- The newly-developed dsGUV compartments combine the advantages of biologically relevant membrane properties and microfluidic manipulation methods such as a sequential loading by pico-injection technology.

- The created lipid structure is a three-dimensional, intact and continuous lipid bilayer with full lipid mobility supported by the surfactant interface of the droplets.

- The applications of microfluidic manipulation tools towards dsGUVs were successfully demonstrated, in particular the use of pico-injection technology to sequentially load dsGUVs with various bio-molecules.

- The preserved functionality of selected transmembrane and cytoskeleton proteins was demonstrated, paving the road towards more sophisticated minimal synthetic cells.

- The release of the assembled lipid compartments into an aqueous environment opens the door for investigations of the assembled protocells under physiologically relevant conditions.

3.1.4 FCS for Analyzing Periodically Passing Droplets

The analysis of the formation process of dsGUVs out of fluorescently labeled SUVs was performed using the point-spot excitation of a confocal microscope (see Appendix A.4 and Figure A.12, a). The confocal volume of the excitation spot was chosen to be in the middle of a microfluidic channel, shortly after the droplet production unit and at distinct positions in the subsequent channel. The velocity of the droplets and the known distance between the production unit and the selected spots allowed to calculate the time after droplet production and thus enabled an estimation of the temporal lipid bilayer formation process. Directly after the droplet production unit, the fluorescently labeled SUV are assumed to be homogeneously distributed inside the microfluidic droplets, resulting in a stepwise intensity function over time for passing droplets. After a sufficiently long time, the SUVs diffuse to the periphery of the droplet, where they rupture and fuse to form a lipid bilayer. This results in the formation of two intensity peaks per passing droplets. While analyzing the fluorescence intensity traces of the periodically passing droplets, the idea to perform FCS measurements using microfluidic droplets arose (see Publication 4).

Traditionally, FCS is based on fluorescence intensity fluctuations of labeled molecules due to stochastic Brownian motion. In case of periodically passing droplets, the fluorescence intensity fluctuations can be caused by fluorescent dyes, encapsulated into the droplets. The fluorescence of monodispersed droplets, flowing equally spaced in the microfluidic channels results in a square-wave intensity function over time. The corresponding auto-correlation function has characteristic properties, which allow to draw conclusions for the flow of the droplets:

1. The period of the oscillations of the auto-correlation function is the inverse flow rate of the droplets.

2. The damping of the auto-correlation function is related to irregularities in the flow of the droplets.

3. The initial amplitude of the auto-correlation function correlates to the fluorescence intensity inside the droplets.

The method developed within this work overcomes fundamental limitations of microfluidic droplet flow monitoring: Conventionally, the investigation of the flow of microfluidic droplets is performed by recording the intensity trace over time and by subsequently analyzing the trace by object recognition criteria. This procedure is on the one hand depended on individual segmentation algorithms but also on an appropriate fluorescence intensity inside the droplets. The use of FCS and the analysis of the auto-correlation function allows for a precise detection of the flow properties mentioned above for low fluorescence intensity. Additionally it could be shown, that a small number of droplets is already enough to derive the auto-correlation function. Even for very low fluorescence signals, e.g. for a droplet to gap intensity ratio of 1.05, a total amount of 100 000 droplets was sufficient enough to derive the auto-correlation function. For a typical flow rate of 500 kHz, this corresponds to a recording time of 0.2 sec.
The advantage of producing vast numbers of droplet-based synthetic cells within short times by microfluidics calls for adequate analysis tools. The method developed here is

a first demonstration of such a new analysis tool for monitoring the flow of microfluidic droplets. In future microfluidic droplet-based synthetic cell applications this method could possibly be used for monitoring the distribution and interactions of fluorescently labeled (bio-) molecules inside the droplets.

To conclude, the application of FCS towards microfluidic droplets allows for the following investigations:

- FCS can be adopted to serve as a sensitive analysis tool towards periodically passing microfluidic droplets, allowing for a fast detection of the flow-rates, the variability and the fluorescently labeled content of the droplets.

- The fast calculation of the auto-correlation function allows to monitor vast numbers of droplets, making statistically significant statements possible in future microfluidic droplet-based synthetic cell applications.

3.2   Conclusion and Outlook

The results I achieved in my research can be considered as a meaningful contribution for the experimental realization of bottom-up synthetic cells in the research field of synthetic biology. The general use of microfluidic droplets to serve as compartments for the assembly of bio-molecules was demonstrated. However I observed, that the droplets cannot be considered as completely sealed containers. Instead the partitioning of fluorophores or even bio-molecules into the surrounding oil phase (Publication 1) as well as interactions of the encapsulated bio-molecules with the stabilizing surfactant layer (Appendix A.1) were observed. In my research I could demonstrate, that these limitations can be overcome by adjusting the physical and chemical properties of the surfactants (Publication 1 and Publication 2). Therefore, in future droplet-based applications, the properties of the encapsulated components and the surfactants have to be considered and possible interactions with the surfactant layer should be carefully monitored.

Driven by these results, a lipid bilayer was integrated inside the microfluidic droplets in order to mimic the cellular bio-membrane and thus to extend and to improve the droplet-based synthetic cell model system. In doing so, the results from Publication 1 and Publication 2 were included, especially by choosing adjusted fluorescent dyes for the labeling of the lipids and the bio-molecules. The developed system can bridge the gap between a functional bio-membrane, being essentially for most synthetic cell models and microfluidic droplet-based manipulation tools, especially pico-injection technology. The results I achieved with the newly-developed dsGUV system are at an early stage of this research direction. However, the successful reconstitution of the cytoskeleton protein tubulin inside dsGUV and the functional incorporation of the transmembrane protein ATPsynthase already indicate the potential of the dsGUV system. Thanks to the ability of a sequential loading of these compartments by pico-injection technology, combinations of different bio-molecules can be assembled, which would not assemble in a direct mixing approach. This might enable the synthetic reconstruction of independent functional units. One example would be a controllable ATP-generating unit being composed of ATPsynthase and bacteriorhodopsin. The latter is a protein that acts as a proton pump upon light illumination, thus creating a pH gradient, which in turn could be used by the ATPsynthase to generate ATP. Such a unit could therefore be used to generate ATP locally and on demand via an external light illumination. The ultimate goal would be the combination of several of these functional units into an independent and controlled system that mimics certain attributes or properties of a living cell. One example would be the combination of the

ATP-generating unit with a synthetic mitotic spindle. Upon external light illumination, ATP would be produced, providing the energy for molecular motor proteins to align microtubules and thus to initiate droplet division.

Furthermore, I achieved the release of the assembles lipid systems from the stabilizing droplet shell into an aqueous environment. For these experiments, the results from Publication 1 were used again to find suitably fluorophores in order to label and visualize the different phases. These findings show a great potential for future synthetic cell applications, since the behavior of the assembled synthetic cell can be investigated in a physiological relevant environment after the release. This might enable to study the interactions of synthetic cells with each other or with different substrates.

Up till now, the full potential of microfluidic droplet production and manipulation methods was not exploited. The production of monodispersed compartments with identical chemical conditions in the kHz range enables the creation of thousands of droplet-based synthetic cells per second. In combination with the reduced complexity of a minimal synthetic cell, this allows for reproducible and statistically significant experiments as in the case of microtubule aster formation (Publication 2). In future experiment these advantages can be further exhausted. Multiple pico-injectors in a row could be used to create synthetic cells with adjusted and controlled concentration gradient of different bio-molecules. This would allow to investigate the behavior of minimal synthetic cells for different compositions and might enable to draw conclusions to the interactions of the components. As an example, droplets with different tubulin and motor protein concentration could be produced and the resulting microtubule arrangements might provide new insight into the interactions.

The possibility to create minimal synthetic cells in the kHz range also requires for the development of new methods to monitor and analyses the production process. In this context, Fluorescence Correlation Spectroscopy (FCS) was applied towards microfluidic droplets, flowing periodically in a microfluidic channel (Publication 4). So far, the working principle of analyzing the auto-correlation function was demonstrated by fluorophores encapsulated in microfluidic droplets. However, this method offers great potential in monitoring also the production of microfluidic drop- let-based synthetic cells, especially for the control of different concentration gradients as described in the section above. Other future application might include the analysis of protein-protein interactions or protein interaction with the lipid bilayer of dsGUVs by the use of fluorescence cross - correlation.

All in all, the results and methods achieved in this work show new paths towards the creation of minimal synthetic cells and therefore might provide one small piece of the puzzle towards an answer to the original question 'What is Life?'

CHAPTER 4

Summary

The question 'What is life?' is one of the questions that have always stirred and challenged humanity since the beginnings. Scientific explanatory approaches culminated in the creation of a whole new scientific field, *Biology* (bios-logia), the 'study of life', with the aim to understand all facets of living organisms and the processes involved. In the beginning, these studies were limited to direct descriptions and observations by eye. However, the development of new technologies in other research fields, such as e.g. microscopy techniques in optical Physics, allowed for an improved observation of living organisms, resulting nowadays in the studies of single molecular building units and their functions. Nevertheless, the pure observation of these processes so far has not led to a complete understanding of life. This is mainly due to the large number of players involved in living organisms, but also due to the highly dynamic processes and the manifold pathways and interplays. Consequently, interdisciplinary approaches arose to tackle these problems. In this context, different methods and techniques from other disciplines such as Physics, Mathematics, Chemistry or Engineering were applied, adopted and combined towards a better understanding of the functional properties of living organisms. One branch of this new research field is '**Synthetic Biology**'.

Synthetic biology is characterized by not being limited to the observation and description of the components of a living organism, instead it aims for a precise manipulation and the application of engineering principles towards living organisms. The intended goal is the creation of a minimal synthetic cell to understand the basic processes necessary for life. In this context, the bottom-up approach aims for a controlled assembly of molecular building blocks into functional units and eventually to an independent, self-reliant system. In doing so, the compartment for the controlled assembly of the building blocks plays a crucial role.

In this thesis, I focused on the investigation of new, cell-sized compartments for a sequential bottom-up assembly of minimal synthetic cells. In a first step, I studied the applicability of microfluidic water-in-oil droplets stabilized by copolymer surfactants towards such compartments. In doing so, key factors for stable droplet production were identified. In order to evaluate the retention ability of microfluidic droplets, different fluorescent dyes were encapsulated into the droplets. It turned out, that not only the physical and chemical properties of the dyes can influence the retention ability, but also the buffer composition inside the droplets as well as the physical properties of the surfactants and their concentrations in the oil phase. The importance of these results was demonstrated by labeling encapsulated bio-molecules with 'wrong' combinations, which resulted in a dissipation into the oil phase. In contrast, for optimized conditions, stable retention of the labeled bio-molecules was achieved. Therefore, the outcomes of this research provided crucial information for a reliable and stable encapsulation of bio-molecules.

Driven by these results, microfluidic droplets were used as compartments for the investigation of microtubule self-organization under confined and well-controlled conditions. Different arrangements of microtubule networks were identified and an elongation of the droplets for high tubulin concentration was observed. However, the reproducibility of the experiments was limited because of strong interactions of tubulin with the copolymer surfactants I used during my research. In order to overcome this issue, two approaches were investigated. The first one comprised the addition of a lipid bilayer at the inner interface of the droplets with the aim to shield the microtubule structures from the surrounding surfactant layer. I could show, that the integration of such a shielding lipid bilayer indeed minimized the interactions and led to an enhanced stability of the system.

The second approach tackled the surfactants themselves, by replacing the TRI7000 surfactant with a commercial one. This led to the reproducible and reversible formation of microtubule asters, mediated by the motor protein kinesin.

So far, microfluidic water-in-oil droplets stabilized by copolymer surfactants were used as compartments. Even though these droplets provided stable and manipulatable compartments, the missing bio-membrane as well as the surrounding oil phase limited their utilization as optimal compartments for synthetic cell approaches. Therefore, in a fundamental new approach, a novel compartment system was invented: The formation of a lipid bilayer at the inner periphery of microfluidic droplets, so-called: *droplet-stabilized giant unilamellar vesicles* (dsGUVs). Since dsGUVs represented a novel kind of compartment systems, the underlying properties were characterized extensively. In a first step, I could demonstrate that the formation process of dsGUVs depends on the presence of divalent ions such as $MgCl_2$. The formation process was further analyzed by encapsulating differently-sized vesicles into the droplets, allowing to observe the formation process for different time scales.

Different analysis methods revealed that the lipid structure is indeed an enclosed, continuous lipid bilayer supported by the surfactant interface of the microfluidic droplets. Furthermore, dsGUVs are accessible to different analytic methods. As an example, FRAP measurements revealed the dynamic behavior of the lipid bilayer, similar to free-standing equivalents. In order to ultimately explore the properties of the created system, I developed different approaches to release the assembled lipid compartments from the stabilizing surfactant shell into an aqueous environment. Towards this end, I demonstrated the successful 'bulk release' in an Eppendorf tube as well as in an observation chamber. The latter allowed to observe the release process in real time and to evaluate the stability of the lipid compartments and the retention ability of encapsulated fluorophores during the release process. Finally, I designed and tested different microfluidic devices to allow for a fully automated release process with the ultimate goal to create future droplet-based synthetic cells on a single device (lab-on-chip application).

The superior features of the developed system in comparison to other microfluidic GUV production methods were demonstrated by applying microfluidic droplet manipulation tools towards dsGUVs. In particular, the successful loading of dsGUVs with different biomolecules using 'pico-injection' technology was achieved. It could be exemplary shown, that both the loading with cytoskeleton proteins as well as transmembrane proteins was possible, remarkably without reducing their functionality. In this context I could demonstrate the successful polymerization of tubulin within dsGUVs, as well as the incorporation of ATPsynthase into the lipid bilayer of dsGUVs. For the latter, I could additionally demonstrate full functionality after the incorporation, which means that I could detect ATP synthesized by ATPsynthase inside energized dsGUVs.

The production of dsGUV-based synthetic cells in the kHz regime by microfluidics requires adequate analysis tools, which can match the high production rates. Therefore, while performing the analysis of the dsGUV formation process, the idea to perform Fluorescence Correlation Spectroscopy (FCS) measurements on microfluidic droplets was born. Towards this end, the fluorescence intensity fluctuations of fluorophores inside microfluidic droplets, passing periodically through a channel, were measured and analyzed. The resulting auto-correlation function allows for a fast determination of the flowrates, the variability and the fluorescently labeled content of the rapidly passing droplets. This enables to monitor and analyze the formation process of microfluidic droplet-based synthetic cells in the kHz regime.

The results and methods achieved and developed in this thesis might pave the road towards a new level of development in bottom-up synthetic cell biology. The results of the experiments, especially related to dsGUVs, demonstrate the basic functionality of the developed system and the applicability towards a real bottom-up synthetic cell assembly. Future applications might exploit the full potential of the generation and the manipulation of these compartments by high-throughput microfluidic technology. This might lead to the construction of more complex minimal synthetic cells in an engineering-like manner, allowing to mimic, study and better understand fundamental processes of life.

APPENDIX A

Additional Data and Methods

The following sections provide additional data and methods, which were not or only partially documented in the Publications.

A.1   Microtubule Polymerization in Microfluidic Droplets

Publication 2 was based on preliminary experiments, which I performed in the context of my research. The following section provides an overview of these results.

In living cells, the internal structure depends on the cytoskeleton, which consists mainly of actin filaments, intermediate filaments and microtubules. In combination with associated motor proteins the latter create a highly dynamic network, which is altered to specific cellular tasks and functions (see Section 1.2.2). The molecular mechanism behind the adaptability of the microtubule network is still only poorly understood. Beside various biochemical components, which can influence the formation of microtubule networks, the confined space and the boundary conditions play a similar role. Since microtubules are rather rigid structures, they can either deform the confinement or are bent themselves, depending on the stiffness and the geometry of the compartments.

In this context, I studied the polymerization of tubulin into microtubule structures in confined microfluidic water-in-oil droplets of controlled and adjustable size. Based on these results, the influence of motor proteins (mCherry-labelled *Xenopus laevis* kinesin-14, XCTK2) on the microtubule networks was analyzed and the results were published in Publication 2.

Microtubule polymerization inside microfluidic droplets

In order to produce microtubule networks and to observe self-organization of microtubules inside microfluidic water-in-oil droplets, the polymerization of tubulin into microtubules has to be controlled and should be triggered only after droplet production and encapsulation. Therefore, droplets containing the protein solution with all polymerization agents were produced at a temperature of 4°C, at which polymerization is suppressed. For the production, a standard microfluidic droplet production device with one aqueous channel was used. The size of the droplets was controlled by adjusting the ratio of aqueous- to oil-phase and in the case of droplets with a diameter > 75 μm a device with an adopted geometry was used. This allowed for the control of droplet sizes in a range of roughly 10-150 μm in diameter, which mimics the size of somatic metazoan cells [131]. In order to observe the self-assembly process of tubulin into microtubules, the produced droplets with the encapsulated, fluorescently labeled tubulin solution were transferred to an observation chamber and observed with a confocal microscope at 34°C. The temperature shift triggered the polymerization of tubulin, thus allowing for the observation of the microtubule self-organization over time (see Figure A.2).

In a first step, the biochemical conditions for *in vitro* polymerization of tubulin inside confined droplets were investigated and adopted from bulk experiments.
Figure A.1, a) shows microfluidic droplets with encapsulated tubulin labeled with ATTO-488 45 min after the transfer to 34°C. In this case, the biochemical conditions were the same as in bulk experiments with a tubulin concentration of $14.5 \mu M$, a GTP concentration of 1.5 mM and the stabilizing agent taxol at $3 \mu M$. In case of corresponding bulk experiments, tubulin polymerized into microtubules for the given conditions, however in droplets no polymerization was observed. Therefore, in an attempt to increase the efficiency of tubulin polymerization, the concentration of tubulin and GTP was increased to $20 \mu M$ and 3 mM, respectively. This led to a visible nucleation of microtubules within the
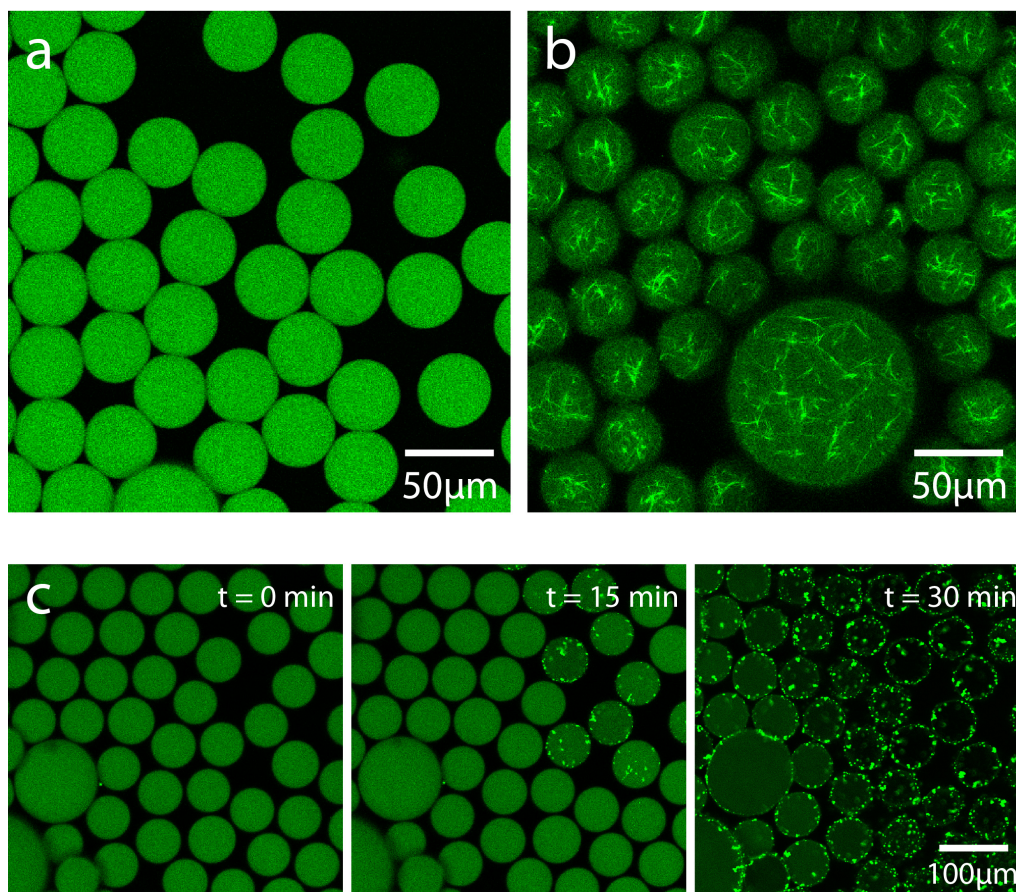
Figure A.1 – Representative fluorescence images of tubulin labeled with ATTO 488 and encapsulated into microfluidic droplets after transfer to 34°C. a) For low tubulin concentration, no polymerization is observed after 45 min. b) Increased tubulin and GTP concentration led to microtubule aggregates. c) Time series of tubulin aggregation after omitting taxol.

droplets, as shown in Figure A.1, b). However, the microtubules formed thick aggregates and clustered together. In order to overcome this problem and to move to physiologically more relevant conditions, the use of taxol was omitted. A representative time series is shown in Figure A.1, c). In this case, tubulin formed aggregates, which however did not polymerize into microtubules and which interacted strongly with the droplets' periphery. This behavior was prevented by additionally omitting the oxygen scavenger system, i.e. the omission of glucose oxidase, catalase and β-casein. These conditions led to a reproducible polymerization of tubulin into microtubules inside microfluidic water-in-oil droplets.

Importantly, the final polymerization was even possible without any additional stabilizer, such as taxol or glycerol, which have been used in most other studies to allow for microtubule polymerization. This enabled to mimic cellular processes much better, since the dynamic behavior of tubulin is conserved.

After adopting the biochemical conditions for tubulin polymerization inside microfluidic droplets, the polymerization of microtubules triggered by a temperature increase was observed over time. Figure A.2 shows different time series of fluorescently labeled tubulin inside microfluidic droplets. At t = 0 min, the droplets were transferred to the heat chamber. Therefore, tubulin is not polymerized and thus distributed equally inside the
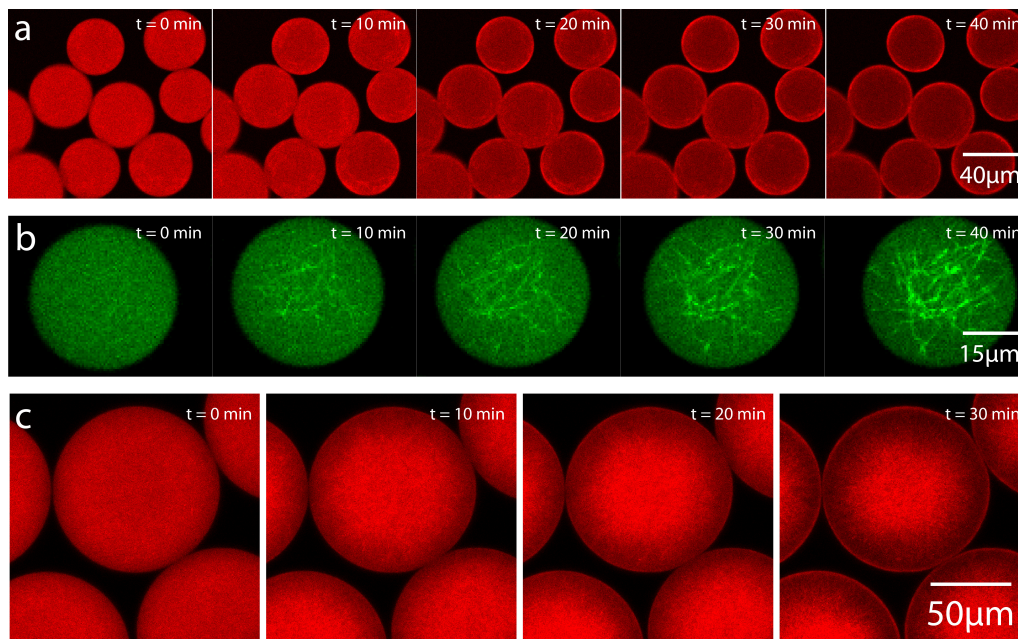
Figure A.2 – Fluorescence images of tubulin polymerization inside microfluidic droplets. Red color indicates labeling with Alexa 647, green color labeling with ATTO 488 dyes. a) represents the formation process of cortical structures and b) the formation of aster-like structures in droplets with a diameter of 40 μm. c) shows the formation process of aster-like structures in droplets with a diameter of 150 μm.

droplets. As the temperature is increased, polymerization of tubulin into microtubules is initiated and filaments start to grow. These filaments move around freely until the microtubule network is to dense and motion comes to halt. After roughly 30-40 min the microtubule self-assembly process is completed.

Following the formation process, the influence of the droplet size on the microtubule self-organization was analyzed. Therefore, in a first step, droplets with a diameter of $d \approx 40\mu m$ were produced.
Figure A.3, a) and b) show the equatorial confocal plane of typical arrangements for the microtubule networks. Mainly four configurations were observed, namely a 'centered' arrangement, a 'ring-like' arrangement, a 'wide cortical' arrangement and a 'narrow cortical' arrangement (see Figure A.3, b). The most frequently occurring arrangement of microtubule networks inside microfluidic droplets with 40 μm diameter was a cortical arrangement (see Figure A.3, a) Note: Similar observations have been made earlier for microtubule organization in confined lipid-monolayered droplets [124]. However, the findings in [124] were performed with stabilizing agents (both taxol and glycerol) and without the control of the droplet size.

In a second step, the microtubule organization for droplets with a diameter of $d \approx 150\mu m$ was analyzed. The majority of the droplets showed a aster-like microtubule arrangement with individual microtubules growing from the droplet's center to its periphery (see A.3, c). Only in minor cases (<10%) an even distribution of microtubules inside the droplets was observed (see A.3, d).
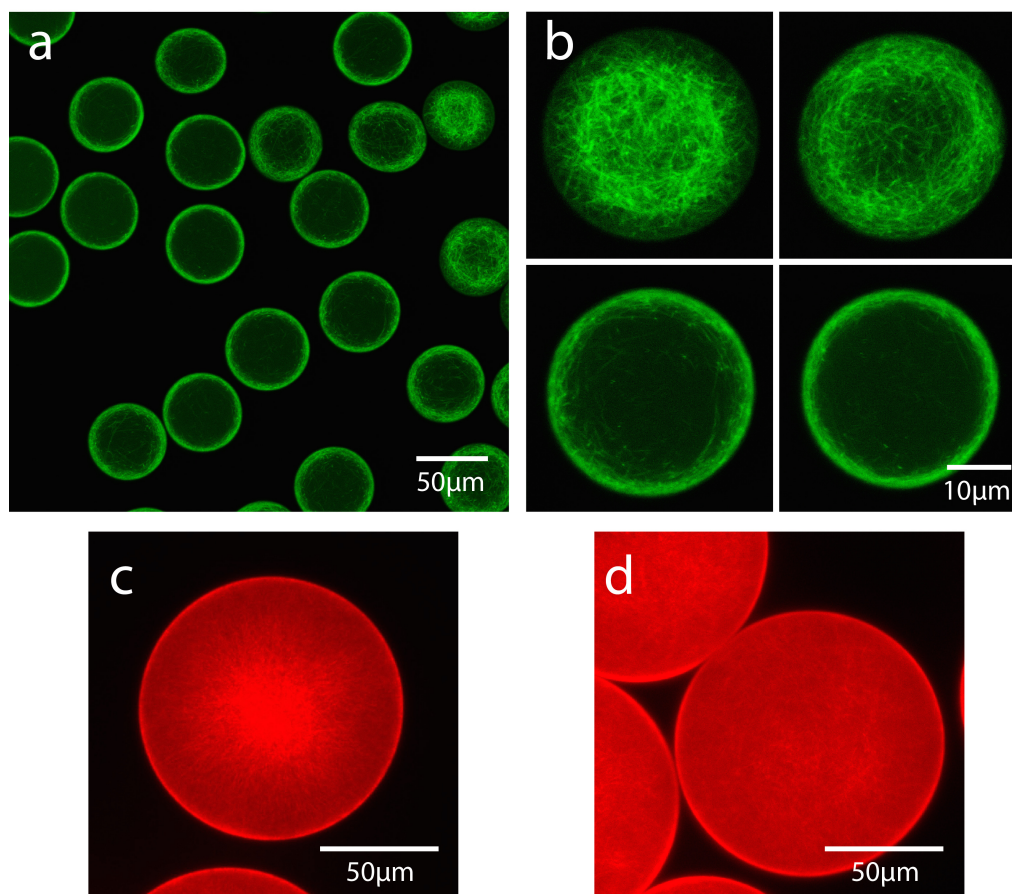
Figure A.3 – Fluorescence images of microtubule arrangements inside microfluidic droplets. a) Overview for droplets with a diameter of 40 μm. b) Different microtubule arrangements identified for 40 μm droplets. c) and d) Microtubule arrangements for 150 μm droplets.

Elongation of microfluidic droplets by growing microtubules

The dynamic nature of microtubules in living cells allows for the adaptation of the cellular cytoskeleton to perform different tasks and functions. During cellular division, the microtubule network has the ability to deform the whole cell into two polar halves by mitotic spindle assembly. This finding has been demonstrated *in vitro* for lipid bilayer compartments [125, 126]. In this study, the ability of microtubules to deform water-in-oil droplets was demonstrated.

Figure A.4 a) shows fluorescence and corresponding brighfield images of microfluidic droplets with encapsulated microtubules after polymerization. In contrast to the previous section, a lower surfactant concentration for droplet stabilization was used and the tubulin concentration was increased to 50 μM. It can be observed, that tubulin accumulates mainly at the periphery and occasionally forms single or multiple microtubule poles, as indicated by bright spots in the fluorescence image. At these points, the droplet's periphery is curved and deformed. In case of two opposite poles, this behavior leads to an elongation of the droplet into a 'rugbyball'-like shape, which can be observed both in fluorescence and in brightfield images. Figure A.4, b) represents a closer look at one of the elongated droplets with one pole. The projection of a stack scan in z-direction (right image) indicates, that the microtubules arrange in a radial geometry from the pole at the droplet interface, thus aligning in parallel bundles between the pole and the opposite side of the droplet. This formation enables a deformation and elongation of the droplet. Most
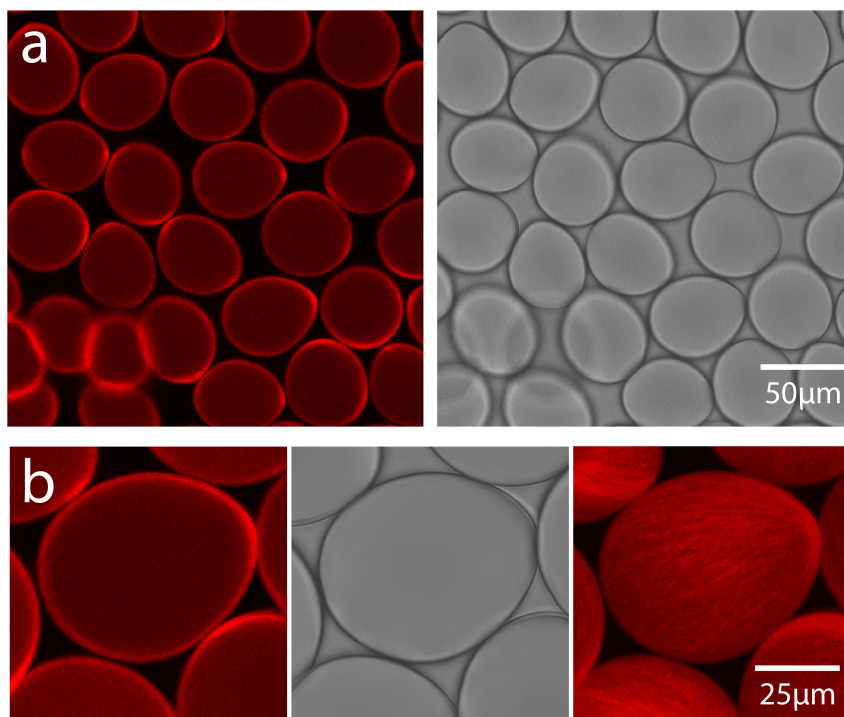
Figure A.4 – a): Representative fluorescence and corresponding bright-field image of microfluidic droplets, being deformed by growing micro-tubules. b): Detailed representation of a deformed droplet with corresponding brightfield image. Right image shows the two-dimensional projection of a z-stack, indicating a parallel arrangement of the microtubules.

probably the enhanced tubulin concentration leads to a higher polymerization-force, acting on the oil-water interface and ultimately leading to the observed deformations.

Interaction of microtubules with surfactants

Even though the results from the previous sections were promising, the use of microfluidic water-in-oil droplets as compartments to study microtubule self - organization in confinements was limited. This can be mainly traced back to long-term observations, which are demonstrated in Figure A.5.

For most microtubule experiments performed in water-in-oil droplets, the microtubule structures depolymerized shortly after the final arrangement and interacted strongly with the surfactant layer. This led to a complete destruction of both the microtubules and the droplets. As it can be seen in the brightfield channel of Figure A.5 b), the surfactant layer at the oil-water interface shows concavities and deformations. In case of droplets with a diameter > 100 μm (see Figure A.5, c)), small fluorescent dots appeared, which can be attributed to depolymerized and destroyed microtubules. Additionally, the droplets' boundaries became less stiff, leading to a deformation into a hexagonal pattern of squeezed droplets. Interestingly, this geometrical deformation was stable, even when the droplets were isolated (see Figure A.5, d)).

In order to investigate the origin of this behavior, the interactions of polymerized microtubules and the oil/surfactant phase were investigated in bulk conditions. Towards this end, a flow chamber was constructed, allowing to introduce FC-40 oil with 2.5mM TRI7000 surfactants from one side and tubulin in polymerization buffer from the other side. Figure A.6 shows the temporal development and interactions at the boundary layer.
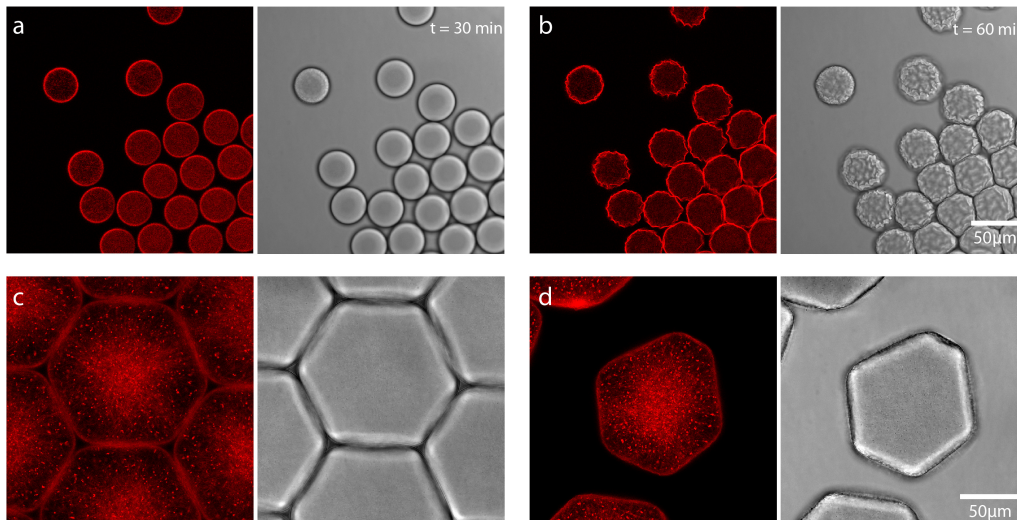
Figure A.5 – a) shows fluorescence and corresponding brightfield image of microfluidic droplets with encapsulated microtubules shortly after complete microtubule polymerization. b) shows the same droplets as in a), after 60 minutes observation time. c) shows droplets with a diameter of roughly 100 μm, 45 minutes after production. The deformation of the droplets into a hexagonal pattern stays intact even after isolating the droplets from the bulk arrangement, as demonstrated in d).

As it can be observed, the microtubules interact strongly with the oil/surfactant layer, resulting in a depolymerization of microtubules close to the boundary as well as a deformation of the boundary itself. The breakage of intact microtubule structures might be explained by the influence of labeling dyes and irradiation of excitation light, as it was demonstrated in [132]. Under light illumination, the labeling fluorescent dyes can create reactive oxygen species such as singlet oxygen, which can cause damage to bio-molecules like microtubules. Therefore, the intact microtubules can break and depolymerize. The amphipotential behavior of tubulin might lead to interactions with the surfactant layer and thus to an aggregation at the boundary layer.
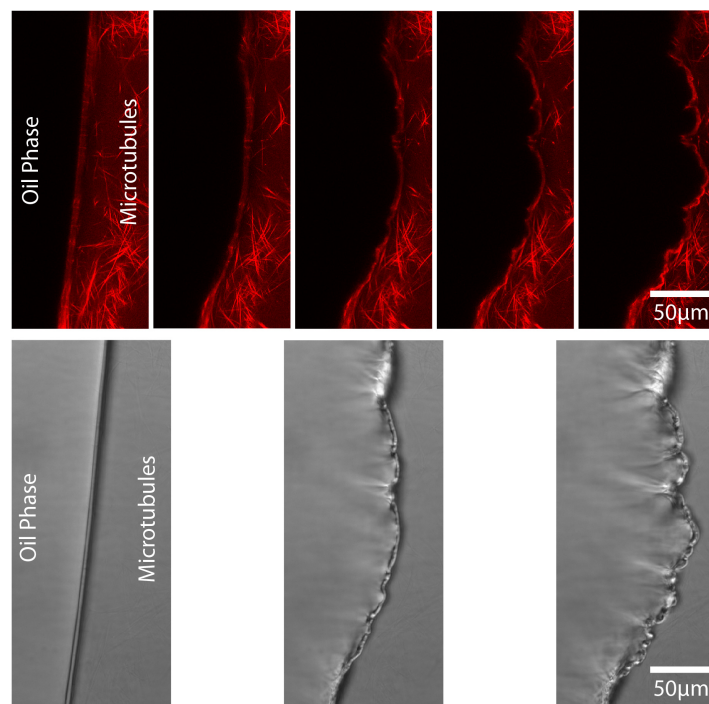
Figure A.6 – Time lapse series of micrutubules interacting with the oil/surfactant layer. Fluorescently labeled microtubules are shown in red, whereas the oil/surfactant phase is unlabeled. A deformation of the boundary layer can be observed over time. Lower panel shows the corresponding brightfield images. Time between the fluorescence images: 5 min.

A.2 Phase Separation and Lipid Defects

This part provides additional data, which was obtained in order to characterize the lipid bilayer-like structure of the dsGUVs system. Towards this end, the creation of dsGUVs showing lipid phase separation behavior was investigated. For an increased temperature, lipids undergo a transition from the liquid-phase to the gel-phase. The transition temperature T_T depends on the physical properties of the lipids, like e.g. the length of the hydrophobic tails and the packing density (See Section 1.2.1). A lipid bilayer, consisting of a mixture of lipids with different T_T, shows macroscopic domains of coexisting liquid- and gel-phases. The formation of these domains is considered to be an indicator for an unilamellar lipid bilayer-like structure. Therefore, this part aimed for the creation of dsGUVs, showing lipid phase separation behavior.

The formation of phase-separated GUVs was performed at temperatures higher than the maximum T_T of the lipids. In this state all lipid species are in the liquid-phase. When the vesicles were cooled down, lipids with a high T_T were transferred to the gel phase, whereas lipids with low T_T remained in the liquid-phase. This phase separation was visualized with fluorescently labeled lipids, which only partition into one specific phase [128].

Figure A.7 a) shows phase-separated GUVs formed by electroformation as described above and encapsulated into microfluidic droplets, as indicated by a dashed circle line. The macroscopic domains of the different phases, one labeled with a fluorescent dye, the other unlabeled, are clearly visible. To achieve the formation of dsGUVs an optimized solution of MgCl$_2$ was subsequently injected into these droplets by pico-injection technology to a final concentration of 10 mM. However, as it can be observed in Figure A.7,
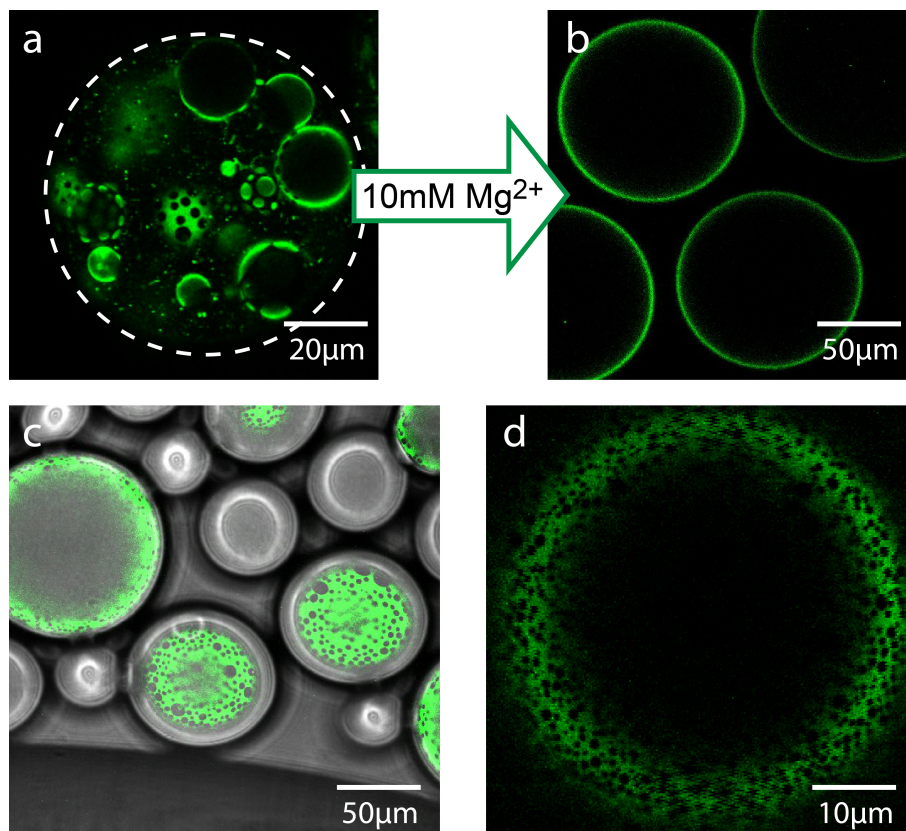
Figure A.7 – a) shows fluorescence image of phase-separated GUVs encapsulated inside a microfluidic droplet, as indicated by a white circle. After addition of ions via picoinjection, the GUVs fuse to the periphery, however the phase separation is not conserved, as demonstrated in b). c) and d) show the appearance of lipid bilayer defects in dsGUVs, as indicated by black holes in the fluorescently labeled lipid layer.

b), the resulting dsGUVs showed no phase separation. Perturbations from the dynamic droplet interface like friction or attractive forces could be an explanation for this observation, as it was found for SLB [59]. Furthermore, the formation of dsGUVs at high temperatures above the maximum T_T by transferring the whole droplet production setup into an oven and a subsequent cooling did likewise not result in a phase-separation of the lipids. Summarizing these findings, the issue of phase separation in the dsGUV membranes remains an open question for further studies.

Even though the phase separation in dsGUVs membranes was not successful, another observation might indicate the lipid bilayer-like structure of the dsGUVs. Occasionally, dsGUVs formed by only one lipid species, showed the appearance of black 'holes' or better 'defects', as it can be seen in Figure A.7, c) and d). This phenomenon has been reported in literature before for SLB systems [133] and can be attributed to mobile regions devoid of any lipids. Even though the exact conditions and the formation process of these defects remained unclear, it strongly supports the lipid bilayer-like structure of the dsGUVs, since a multilayer would not lead to completely dark regions.

A.3   Release of dsGUVs

This part provides more detailed information on methods, which I developed in order to release the assembled lipid bilayer compartments from their stabilizing surfactant shell into an aqueous environment (see Publication 3). The general underlying principle is sketched in Figure A.8.
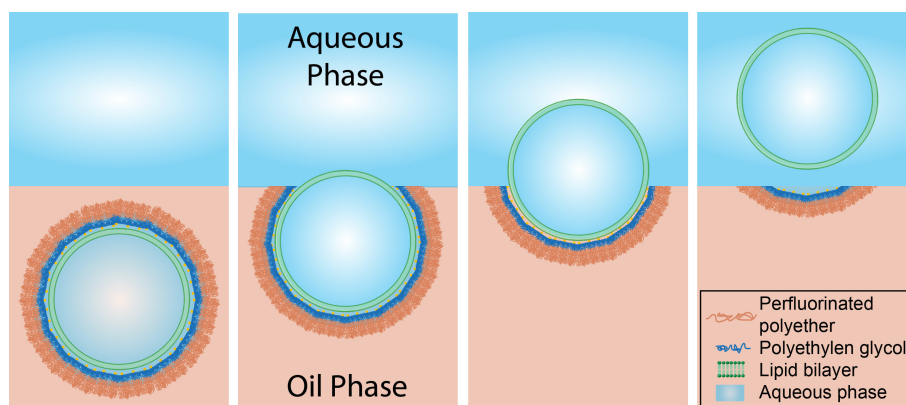

Figure A.8 – Schematic representation of dsGUV release into an aqueous environment. dsGUVs have to come into close contact with the continuous aqueous phase. Subsequently, the separating oil-surfactant layer has to be broken without damaging the lipid bilayer. This leads to a release of the GUV into the continuous aqueous phase.

The release of dsGUVs into an aqueous environments provides better analytic access for the characterization of the assembled lipid system and is also crucial for future applications, where protocells are first assembled by microfluidic technology and finally released. The latter will allow the investigation of protocell-protocell interactions and protocell-environment interactions and obviously mimics living cells much better than the dsGUV system. In the following sections, several approaches and their realizations for dsGUV release into an aqueous phase are presented. The crucial factor for all approaches is to bring the dsGUVs in the oil phase into close contact with a continuous aqueous phase. After destabilizing the surfactant layer the GUV might be released into the connected aqueous phase. In doing so, shear stress on the lipid bilayer has to be avoided in order to preserve the fragile GUV structure.

Bulk Release Approach

One possibility to bring the droplet in the oil phase close to a continuous aqueous environment was achieved with a bulk release approach. In this case, thousands of dsGUVs were produced and transferred to an Eppendorf tube. After addition of a sufficient amount of the continuous aqueous phase, droplets were align at the oil-water interface, being still separated by a remaining oil-surfactant layer. In order to remove the latter, destabilizing surfactants were added and the droplets' interior including the lipid bilayer was released into the continuous aqueous phase.

In order to investigate the potential of this approach, in a first step free-standing GUVs were formed by electroformation and subsequently encapsulated into microfluidic droplets in MilliQ water (see Figure A.9, a). Following this process, the bulk release approach was applied to recover the encapsulated GUVs into a continuous aqueous phase. As it

can be seen in Figure A.9, b), the released GUVs stayed intact and showed roughly the same size distribution as the encapsulated GUVs prior to the release process.
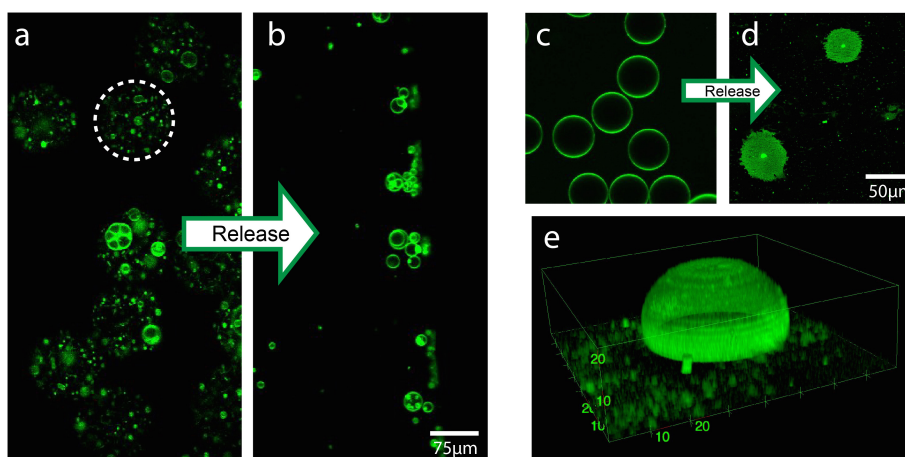

Figure A.9 – Bulk release approaches. a) shows fluorescently labeled GUVs formed by electroformation and encapsulated into microfluidic droplets as indicated by the white circle. After the bulk release process, GUVs with similar size distribution as in a) can be observed in the continuous aqueous phase, b). The same approach was applied to fluorescently labeled dsGUVs, depicted in c). After the release process, lipid patches on the cover-slip of the observation chamber can be observed, as demonstrated in d). e) shows a three-dimensional representation of the released GUVs, indicating a semi-fusion with the cover-slip.

Driven by these results, the release of dsGUVs into a continuous aqueous phase was studied. Figure A.9, c) shows dsGUVs surrounded by a continuous oil phase. After applying the bulk release method, the continuous aqueous phase containing the released GUVs was transferred to an observation chamber and the resulting lipid formations were observed, as exemplary shown in Figure A.9, d) and e). It can be seen that the released GUVs settled down to the bottom of the observation chamber and ruptured into membrane patterns due to interactions with the glass slide. However, the size of the membrane patterns resembles the original size of the dsGUVs, indicating a successful release process. Frequently, three-dimensional structure as in Figure A.9, e) (three-dimensional representation of a z-stack) were observed, showing a semi-fusion of the released GUVs with the glass slide.

These results demonstrate a successful release of GUVs from their supporting surfactant layer. After the realization of the bulk release concept achieved here, co-worker Lucia Benk optimized the conditions for the bulk release method by screening different lipid compositions and by functionalizing the glass slides of the observation chambers in order to reduce GUV rupture.

In order to directly visualize the release process, another bulk release approach was investigated by using an open flow-cell chamber for the observation. The results are presented in Publication 3, Supplementary Figure 6. This method also enabled to monitor molecular exchange between the internal and the external aqueous phase by dissolving adjusted fluorescent dyes, based on the results from Publication 1. During the release process, no molecular exchange of the fluorophores between the two phasese was observable, indicating the successful release of intact lipid compartments.

Microfluidic Release Approach

In addition to the bulk release methods, microfluidic devices for a controllable release of GUVs from the stabilizing surfactant layer were developed. The motivation for a microfluidic release device was on the one hand to better observe the release process. On the other hand such a device could be implemented as a part of a synthetic cell production pipeline, or in other words as a part of a lab-on-chip device, allowing for the generation of dsGUVs, their manipulation and analysis and finally the release of the assembles protocells into an aqueous environment with one single device. A first prototype of such an microfluidic release device is shown in Figure A.10.
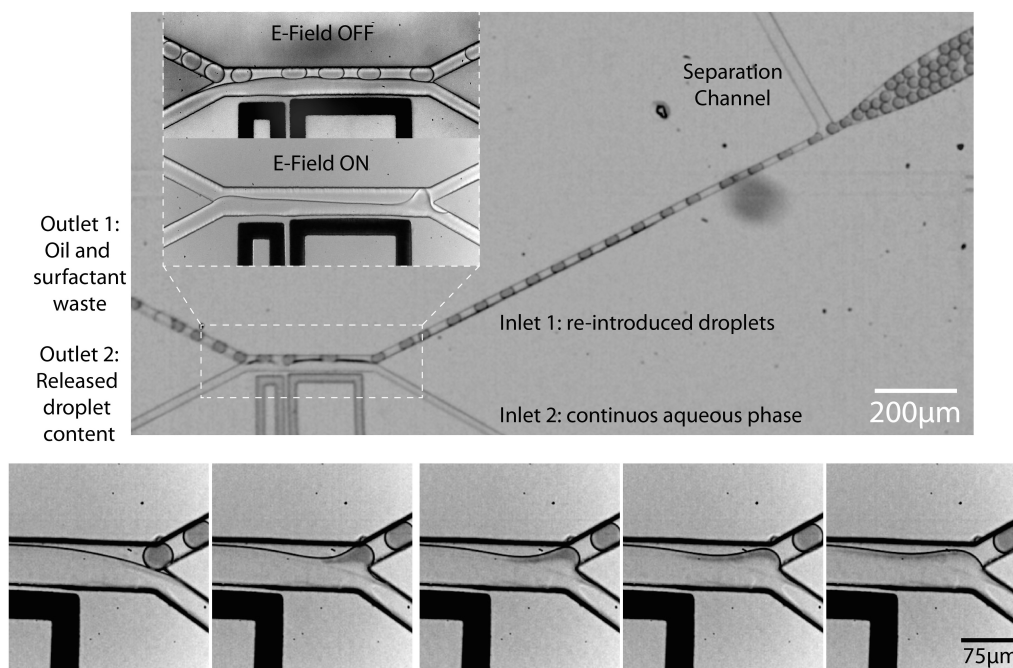

Figure A.10 – This Figure shows the first design for the automated release of the content of microfluidic droplets. Produced droplets are reintroduced into the device and separated by an additional oil channel. The latter also serves to introduce destabilizing surfactants. In the fusion unit, droplets flow parallel to the continuous aqueous phase. By applying an electrical AC field, fusion is achieved, as indicated by the inserts. The lower panel shows a time series of the fusion process in more detail. The content of the droplets is visualized by black ink. Time between the images: 0.5 ms.

The two inlet channels allow for a parallel flow of droplets in the oil phase and the continuous aqueous phase. Due to the low Reynolds Numbers in microfluidic devices and the resulting laminar flow, the steam lines of the two phases do not mix (see Section 1.4). Therefore, two outlet channels allow for a separation of the continuous oil phase and the continuous aqueous phase. As shown in Figure A.10, the surfactant-stabilized droplets do not fuse with the attached aqueous phase. However, fusion can be induced by electrical fields, imposed by the microelectrodes. Similar like in the case of pico-injection, these electrical fields induce electroporation of the stabilizing surfactant layer, thus enabling the fusion of the aqueous content of the droplets with the continuous aqueous phase (see inlet in Figure A.10). However, in the case of dsGUVs, the lipid bilayer is also subject to the electroporation and thus the created lipid bilayer structure would be destroyed by the electrical fields.

In an attempt to omit the use of strong electrical fields, a destabilizing surfactant as in the case of bulk release was introduced. This was done by the separation channel, actually allowing for the separation of the reintroduced droplets (see Figure A.10). The subsequent channel length was adjusted to be long enough to allow for an exchange of stabilizing surfactant with the destabilizing one. Droplets reaching the fusion unit directly merged with the continuous aqueous phase. This process is illustrated in the time series in Figure A.10, where the droplets inner aqueous phase is labeled with dark ink. However, the shear forces on the released content of the droplets are very strong, leading to a dissolving of the content. Consequently, these forces would be to high to allow for a successful release of GUVs form the stabilizing surfactant layer as in the case of dsGUVs.

In order to overcome this problem, a new device was designed with the aim to apply as little forces as possible to the released GUVs. Figure A.11 shows the microfluidic release device, which I designed during my research.
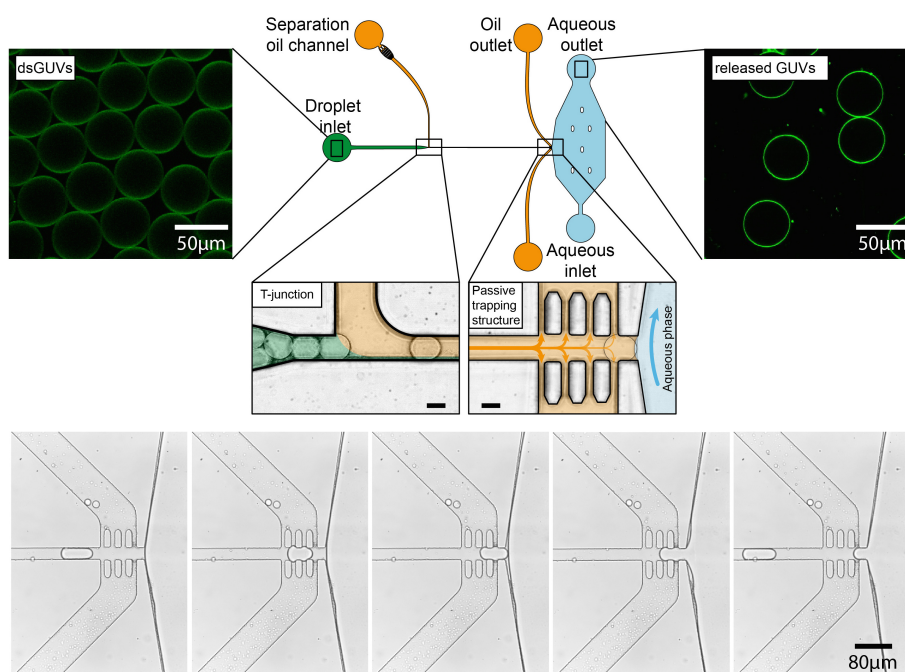

Figure A.11 – Final design for the automated release of GUVs using a microfluidic device. dsGUVs are reintroduced and separated by a T-junction. The separation channel also allows for the introduction of destabilizing surfactants. In the fusion-unit, droplets are decelerated due to passive trapping structures. These structures additionally serve as outlets for the oil phase. This enables a gentle transition of the dsGUV with the continuous aqueous phase, thus making the release of GUVs possible. The lower panel shows a time series of the deceleration process of the droplets. Time between the images: 1.0 ms

The first part of the device consists of a channel for the reintroduction of droplets and a second, rectangular-connected oil channel. The latter serves two functions. Firstly, the additional oil separates the droplets in a way that they sequentially flow spatially separated by consistent and uniform distances. Secondly, the oil in the separation channel contains destabilizing surfactants. Thus, the stabilizing surfactant of the droplets is replaced by the short destabilizing one inside the subsequent channel section.

The second part of the device is the actual release unit. The passive trapping structures again fulfill two purposes. Firstly, they allow the flow of the oil phase out into the connected oil outlet channels. Secondly, they decelerate the approaching droplets before they come into contact with the continuous aqueous phase, which is connected to the end of the trapping structures. This allows a smooth and gentle transition of single dsGUVs into the aqueous phase.

The time series in Figure A.11 (lower panel) shows a droplet approaching the passive trapping structure. After entering the rows of pillars, excessive oil is pushed into the oil outlet channels, resulting in a pressure drop in the main channel. Therefore, the droplet is decelerated until it comes to halt shortly before the oil-water interface. The subsequent droplet arriving in the main channel gives the ultimate push to induce fusion of the droplet with the continuous aqueous phase, allowing a gentle release of the droplet's content. This release process can be performed at rates up to 300 droplets per second.

In the context of this thesis, I designed and produced the microfluidic release device and performed first experiments with microfluidic droplets. Based on these achievements, co-worker Johannes Frohnmayer improved the handling of the device and demonstrated successful release of dsGUVs into the continuous aqueous phase.

A.4   Formation Process of dsGUVs

In an attempt to understand the properties of dsGUVs, the formation mechanism was studied in detail. Towards this end, lipid vesicles with different sizes were encapsulated into microfluidic droplets under ionic conditions of 10 mM $MgCl_2$. As it was shown in Publication 3, the time for a complete formation of dsGUVs, t_c depends on the size of the vesicles and the corresponding mean diffusion time. In case of encapsulated GUVs, t_c is in the order of minutes, whereas in the case of SUVs, t_c is in the order of seconds. In most cases, dsGUVs were produced using SUVs, since for this situation the total lipid concentration inside the droplets could be controlled precisely. The knowledge of the dsGUV formation time is of particular interest for the design of microfluidic devices consisting of several manipulation units. As an example, it would be desirable to form complete dsGUV before using the pico-injection unit. Towards this goal, fluorescence intensity analysis of flowing microfluidic droplets was performed.

The optical setup, which was implemented into a LSM 880 microscope (Zeiss, Oberkochen, Germany), is schematically shown in Figure A.12, a).
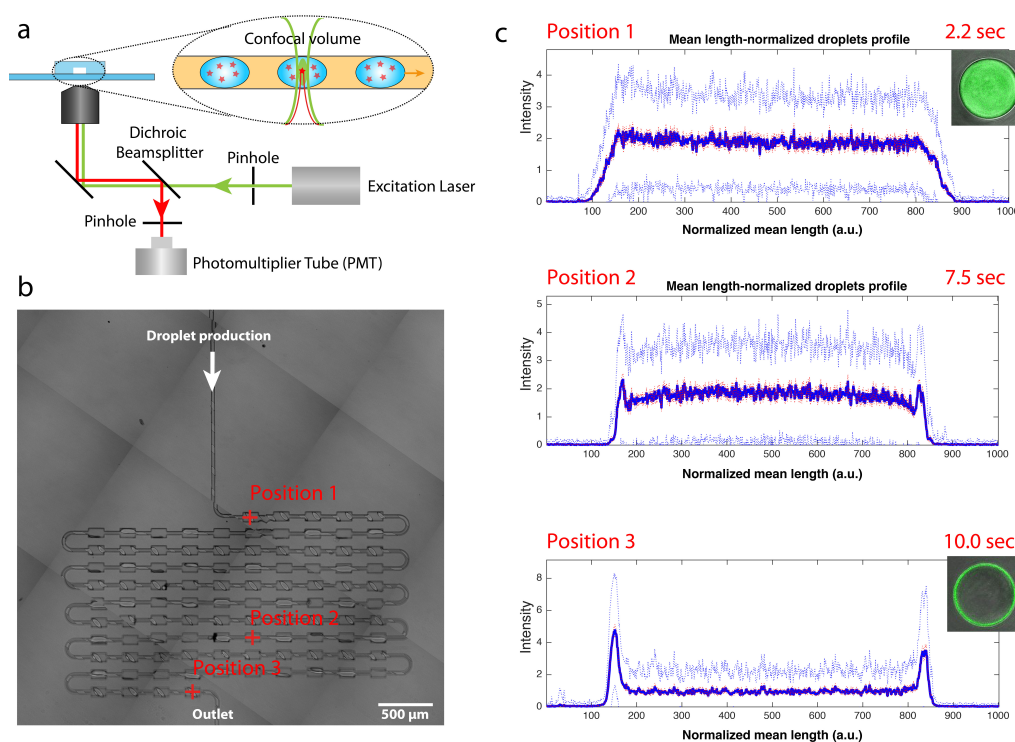

Figure A.12 – a) shows a schematic representation of the fluorescence detection setup. The two pinholes allow for a defined confocal detection volume. b) shows the microfluidic device for the detection of the dsGUV formation process. Fluorescence intensity traces were measured at the indicated positions. c) shows the average fluorescence intensity (a.u.) and corresponding standard derivation of labeled lipids in 120 by-passing, length-normalized droplets at different positions. The corresponding time after creation is indicated in the Figure. The inserts show the fluorescence intensity distribution inside droplets before and after the introduction of $MgCl_2$.

The two pinholes serve to provide a defined confocal excitation volume inside a microfluidic channel. Such a spot-like excitation of fluorescent dyes allows for a fast detection of

the emission signals in the MHz-range, using a PMT.

In order to evaluate the formation process of dsGUVs, droplets with encapsulated SUVs, labeled with ATTO-488 in 10 mM $MgCl_2$ were produced. The device, shown in Figure A.12, b) enables the observation of the droplets for different distances after the production, as indicated in the figure. With the velocity of the droplets, known by observations with a high-speed camera at 10Mhz, the corresponding time after production could be evaluated, as indicated in c). The fluorescence intensity traces at the different positions were recorded for 120 droplets in each case. Following acquisition, the traces of single droplets in the intensity profiles were identified and the lengths of the droplets were normalized. Figure A.12, c) shows the resulting mean intensity values for the three different positions. The transformation from a homogeneous fluorescence distribution (corresponding to homogeneously distributed SUVs) to two distinguishable intensity peaks after roughly 10 seconds (corresponding to an established lipid bilayer at the droplets periphery) can be observed. This value is in good agreement with theoretical considerations, see Publication 3, Supplementary Note 2 and allows for an estimation of the lengths and geometry of microfluidic devices to achieve full dsGUV formation.

In the context of this observations, the idea arose to use fluorescence correlation spectroscopy (FCS) for periodically passing droplets. It turned out, that the resulting autocorrelation curve can be used to draw precise conclusions to the droplet production frequency, to irregularities in the flow of the droplets as well as to the fluorescence intensity inside the droplets. These results are presented in Publication 4.

APPENDIX B

Permissions

PERMISSION/LICENSE IS GRANTED FOR YOUR ORDER AT NO CHARGE

npg

nature
publishing
group

Title: Sequential bottom-up assembly
of mechanically stabilized
synthetic cells by microfluidics

Author: Marian Weiss, Johannes Patrick
Frohnmayer, Lucia Theresa
Benk, Barbara Haller, Jan-Willi
Janiesch et al.

Publication: Nature Materials

Publisher: Nature Publishing Group

Date: Oct 16, 2017

Author Request

If you are the author of this content (or his/her designated agent) please read the following. If you are not the author of this content, please click the Back button and select an alternative Requestor Type to obtain a quick price or to place an order.

Ownership of copyright in the article remains with the Authors, and provided that, when reproducing the Contribution or extracts from it, the Authors acknowledge first and reference publication in the Journal, the Authors retain the following non-exclusive rights:

a) To reproduce the Contribution in whole or in part in any printed volume (book or thesis) of which they are the author(s).

b) They and any academic institution where they work at the time may reproduce the Contribution for the purpose of course teaching.

c) To reuse figures or tables created by them and contained in the Contribution in other works created by them.

d) To post a copy of the Contribution as accepted for publication after peer review (in Word or Text format) on the Author's own web site, or the Author's institutional repository, or the Author's funding body's archive, six months after publication of the printed or online edition of the Journal, provided that they also link to the Journal article on NPG's web site (eg through the DOI).

NPG encourages the self-archiving of the accepted version of your manuscript in your funding agency's or institution's repository, six months after publication. This policy complements the recently announced policies of the US National Institutes of Health, Wellcome Trust and other research funding bodies around the world. NPG recognises the efforts of funding bodies to increase access to the research they fund, and we strongly encourage authors to participate in such efforts.

Authors wishing to use the published version of their article for promotional use or on a web site must request in the normal way.

If you require further assistance please read NPG's online author reuse guidelines.

For full paper portion: Authors of original research papers published by NPG are encouraged to submit the author's version of the accepted, peer-reviewed manuscript to their relevant funding body's archive, for release six months after publication. In addition, authors are encouraged to archive their version of the manuscript in their institution's repositories (as well as their personal Web sites), also six months after original publication.

ACS Publications
Most Trusted. Most Cited. Most Read.

Search   Citation   Subject   Advanced Search

Enter search text / DOI   Anywhere   Search

Subscriber access provided by MPI FUR INTELLIGENTE SYSTEME

Authors & Reviewers | Librarians & Account Managers | ACS Members | Alerts | About Us | ACS & Open Access

Standard *ACS AuthorsChoice/Editors' Choice* Usage Agreement

This ACS article is provided to You under the terms of this Standard *ACS AuthorChoice/Editors' Choice* usage agreement between You and the American Chemical Society ("ACS"), a federally-chartered nonprofit located at 1155 16th Street NW, Washington DC 20036. Your access and use of this ACS article means that you have accepted and agreed to the Terms and Conditions of this Agreement. ACS and You are collectively referred to in this Agreement as "the Parties").

1. SCOPE OF GRANT

ACS grants You non-exclusive and nontransferable permission to access and use this ACS article subject to the terms and conditions set forth in this Agreement.

2. PERMITTED USES

a. For non-commercial research and education purposes only, You may access, download, copy, display and redistribute articles as well as adapt, translate, text and data mine content contained in articles, subject to the following conditions:

i. The authors' moral right to the integrity of their work under the Berne Convention (Article 6bis) is not compromised.

ii. Where content in the article is identified as belonging to a third party, it is your responsibility to ensure that any reuse complies with copyright policies of the owner.

iii. Copyright notices or the display of unique Digital Object Identifiers (DOI's), ACS or journal logos, bibliographic (e.g. authors, journal, article title, volume, issue, page numbers) or other references to ACS journal titles, web links, and any other journal-specific "branding" or notices that are included in the article or that are provided by the ACS with instructions that such should accompany its display, should not be removed or tampered with in any way. The display of *ACS AuthorChoice* or *ACS Editors' Choice* articles on non-ACS websites must be accompanied by prominently displayed links to the definitive published versions of those articles on the ACS website.

iv. Any adaptations for non-commercial purposes must prominently link to the definitive published version on the ACS website and prominently display the statement: "This is an unofficial adaptation of an article that appeared in an ACS publication. ACS has not endorsed the content of this adaptation or the context of its use."

v. Any translations for non-commercial purposes, for which a prior translation agreement with ACS has not been established, must prominently link to the definitive published version on the ACS website and prominently display the statement: "This is an unofficial translation of an article that appeared in an ACS publication. ACS has not endorsed the content of this translation or the context of its use."

b. Each time You distribute this ACS article or an adaptation, ACS offers to the recipient a license to this ACS article on the same terms and conditions as the license granted to You under this License.

c. For permission to use ACS copyrighted articles beyond that permitted here, visit:
http://pubs.acs.org/copyright/permissions.html

3. PROHIBITED USES

a. Use of this ACS article for commercial purposes is prohibited. Examples of such prohibited commercial purposes include but are not limited to:

i. Copying or downloading of articles, or linking to such postings, for further distribution, sale or licensing, for a fee;

ii. Copying, downloading or posting by a site or service that incorporates advertising with such content;

iii. The inclusion or incorporation of article content in other works or services (other than normal quotations with an appropriate citation) that is then available for sale or licensing, for a fee;

iv. Use of articles or article content (other than normal quotations with appropriate citation) by a for-profit organizations for promotional purposes, whether for a fee or otherwise;

AMERICAN PHYSICAL SOCIETY LICENSE
TERMS AND CONDITIONS

Nov 03, 2017

This Agreement between Max -- Marian Weiss ("You") and American Physical Society ("American Physical Society") consists of your license details and the terms and conditions provided by American Physical Society and Copyright Clearance Center.

License Number	4212960730836
License date	Oct 20, 2017
Licensed Content Publisher	American Physical Society
Licensed Content Publication	Physical Review Letters
Licensed Content Title	Decompressing Emulsion Droplets Favors Coalescence
Licensed Content Author	Nicolas Bremond, Abdou R. Thiam, and Jérôme Bibette
Licensed Content Date	Jan 15, 2008
Licensed Content Volume	100
I would like to...	Thesis/Dissertation
Requestor type	Student
Format	Print, Electronic
Portion	chart/graph/table/figure
Number of charts/graphs/tables/figures	1
Portion description	Figure 3
Rights for	Main product
Duration of use	Life of Current Edition
Creation of copies for the disabled	no
With minor editing privileges	no
For distribution to	Worldwide
In the following language(s)	Original language of publication
With incidental promotional use	no
The lifetime unit quantity of new product	0 to 499
The requesting person/organization is:	Marian Weiss
Order reference number	
Title of your thesis / dissertation	Microfluidic Approaches for Sequential Bottom-up Assembly of Mechanically Stabilized Cell-Like Proteoliposomes
Expected completion date	Jan 2018
Expected size (number of pages)	200
Requestor Location	Max-Planck Institute for Medical Research Jahnstraße 29

ROYAL SOCIETY OF CHEMISTRY LICENSE TERMS AND CONDITIONS

Nov 03, 2017

This Agreement between Max -- Marian Weiss ("You") and Royal Society of Chemistry ("Royal Society of Chemistry") consists of your license details and the terms and conditions provided by Royal Society of Chemistry and Copyright Clearance Center.

License Number	4212961210668
License date	Oct 20, 2017
Licensed Content Publisher	Royal Society of Chemistry
Licensed Content Publication	Lab on a Chip
Licensed Content Title	Pillar-induced droplet merging in microfluidic circuits
Licensed Content Author	Xize Niu,Shelly Gulati,Joshua B. Edel,Andrew J. deMello
Licensed Content Date	Oct 8, 2008
Licensed Content Volume	8
Licensed Content Issue	11
Type of Use	Thesis/Dissertation
Requestor type	academic/educational
Portion	figures/tables/images
Number of figures/tables/images	1
Format	print and electronic
Distribution quantity	100
Will you be translating?	no
Order reference number	
Title of the thesis/dissertation	Microfluidic Approaches for Sequential Bottom-up Assembly of Mechanically Stabilized Cell-Like Proteoliposomes
Expected completion date	Jan 2018
Estimated size	200
Requestor Location	Max-Planck Institute for Medical Research Jahnstraße 29
	Heidelberg, 69120 Germany Attn: Max-Planck Institute for Medical Research
Billing Type	Invoice
Billing Address	Max-Planck Institute for Medical Research Jahnstraße 29
	Heidelberg, Germany 69120 Attn: Max-Planck Institute for Medical Research
Total	**0.00 EUR**

NATURE PUBLISHING GROUP LICENSE
TERMS AND CONDITIONS

Nov 03, 2017

This Agreement between Max -- Marian Weiss ("You") and Nature Publishing Group ("Nature Publishing Group") consists of your license details and the terms and conditions provided by Nature Publishing Group and Copyright Clearance Center.

License Number	4202990038996
License date	Oct 06, 2017
Licensed Content Publisher	Nature Publishing Group
Licensed Content Publication	Nature
Licensed Content Title	Molecular motors: What makes ATP synthase spin?
Licensed Content Author	Paul D. Boyer
Licensed Content Date	Nov 18, 1999
Licensed Content Volume	402
Licensed Content Issue	6759
Type of Use	reuse in a dissertation / thesis
Requestor type	academic/educational
Format	print and electronic
Portion	figures/tables/illustrations
Number of figures/tables/illustrations	2
Figures	Figure 1 and 2
Author of this NPG article	no
Your reference number	
Title of your thesis / dissertation	Microfluidic Approaches for Sequential Bottom-up Assembly of Mechanically Stabilized Cell-Like Proteoliposomes
Expected completion date	Jan 2018
Estimated size (number of pages)	200
Requestor Location	Max-Planck Institute for Medical Research Jahnstraße 29
	Heidelberg, 69120 Germany Attn: Max-Planck Institute for Medical Research
Billing Type	Invoice
Billing Address	Max-Planck Institute for Medical Research Jahnstraße 29
	Heidelberg, Germany 69120 Attn: Max-Planck Institute for Medical Research

NATURE PUBLISHING GROUP LICENSE
TERMS AND CONDITIONS

Nov 03, 2017

This Agreement between Max -- Marian Weiss ("You") and Nature Publishing Group ("Nature Publishing Group") consists of your license details and the terms and conditions provided by Nature Publishing Group and Copyright Clearance Center.

License Number	4202940966413
License date	Oct 06, 2017
Licensed Content Publisher	Nature Publishing Group
Licensed Content Publication	Nature Cell Biology
Licensed Content Title	A unified vision of the building blocks of life
Licensed Content Author	Jamey D. Marth
Licensed Content Date	Sep 1, 2008
Licensed Content Volume	10
Licensed Content Issue	9
Type of Use	reuse in a dissertation / thesis
Requestor type	academic/educational
Format	print and electronic
Portion	figures/tables/illustrations
Number of figures/tables/illustrations	1
High-res required	no
Figures	Figure 1
Author of this NPG article	no
Your reference number	
Title of your thesis / dissertation	Microfluidic Approaches for Sequential Bottom-up Assembly of Mechanically Stabilized Cell-Like Proteoliposomes
Expected completion date	Jan 2018
Estimated size (number of pages)	200
Requestor Location	Max-Planck Institute for Medical Research Jahnstraße 29
	Heidelberg, 69120 Germany Attn: Max-Planck Institute for Medical Research
Billing Type	Invoice
Billing Address	Max-Planck Institute for Medical Research Jahnstraße 29
	Heidelberg, Germany 69120

NATURE PUBLISHING GROUP LICENSE
TERMS AND CONDITIONS

This Agreement between Max -- Marian Weiss ("You") and Nature Publishing Group ("Nature Publishing Group") consists of your license details and the terms and conditions provided by Nature Publishing Group and Copyright Clearance Center.

License Number	4202970878313
License date	Oct 06, 2017
Licensed Content Publisher	Nature Publishing Group
Licensed Content Publication	Nature Reviews Molecular Cell Biology
Licensed Content Title	Tracking the ends: a dynamic protein network controls the fate of microtubule tips
Licensed Content Author	Anna AkhmanovaandMichel O. Steinmetz
Licensed Content Date	Apr 1, 2008
Licensed Content Volume	9
Licensed Content Issue	4
Type of Use	reuse in a dissertation / thesis
Requestor type	academic/educational
Format	print and electronic
Portion	figures/tables/illustrations
Number of figures/tables/illustrations	1
High-res required	no
Figures	Figure 1
Author of this NPG article	no
Your reference number	
Title of your thesis / dissertation	Microfluidic Approaches for Sequential Bottom-up Assembly of Mechanically Stabilized Cell-Like Proteoliposomes
Expected completion date	Jan 2018
Estimated size (number of pages)	200
Requestor Location	Max-Planck Institute for Medical Research Jahnstraße 29
	Heidelberg, 69120 Germany Attn: Max-Planck Institute for Medical Research
Billing Type	Invoice
Billing Address	Max-Planck Institute for Medical Research Jahnstraße 29
	Heidelberg, Germany 69120

This Agreement between Max -- Marian Weiss ("You") and Nature Publishing Group ("Nature Publishing Group") consists of your license details and the terms and conditions provided by Nature Publishing Group and Copyright Clearance Center.

License Number	4221531035129
License date	Nov 03, 2017
Licensed Content Publisher	Nature Publishing Group
Licensed Content Publication	Nature
Licensed Content Title	Structure of the αβ tubulin dimer by electron crystallography
Licensed Content Author	Eva Nogales, Sharon G. Wolf, Kenneth H. Downing
Licensed Content Date	Jan 8, 1998
Licensed Content Volume	391
Licensed Content Issue	6663
Type of Use	reuse in a dissertation / thesis
Requestor type	academic/educational
Format	print and electronic
Portion	figures/tables/illustrations
Number of figures/tables/illustrations	2
Figures	Figure 3 Figure 4
Author of this NPG article	no
Your reference number	
Title of your thesis / dissertation	Microfluidic Approaches for Sequential Bottom-up Assembly of Mechanically Stabilized Cell-Like Proteoliposomes
Expected completion date	Jan 2018
Estimated size (number of pages)	200
Requestor Location	Max-Planck Institute for Medical Research Jahnstraße 29
	Heidelberg, 69120 Germany Attn: Max-Planck Institute for Medical Research
Billing Type	Invoice
Billing Address	Max-Planck Institute for Medical Research Jahnstraße 29

Bibliography

[1] Harald Huber et al. "A new phylum of Archaea represented by a nanosized hyperthermophilic symbiont". In: *Nature* 417.6884 (2002), pp. 63–67.

[2] Anthony R. Ambrose, Stephen C. Sillett, and Todd E. Dawson. "Effects of tree height on branch hydraulics, leaf structure and gas exchange in California redwoods". In: *Plant, Cell & Environment* 32.7 (2009), pp. 743–757.

[3] Richard K. Grosberg and Richard R. Strathmann. "The Evolution of Multicellularity: A Minor Major Transition?" In: *Annual Review of Ecology, Evolution, and Systematics* 38.1 (2007), pp. 621–654.

[4] R. Macelroy. "Some comments on the evolution of extremophiles". In: *Biosystems* 6.1 (1974), pp. 74–75.

[5] Pabulo Henrique Rampelotto. "Extremophiles and Extreme Environments". In: *Life : Open Access Journal* 3.3 (2013), pp. 482–485.

[6] Chris P McKay. "What Is Life — and How Do We Search for It in Other Worlds?" In: *PLoS Biology* 2.9 (2004), e302.

[7] Richard Parry. "Empedocles". In: *The Stanford Encyclopedia of Philosophy*. Metaphysics Research Lab, Stanford University, 2016.

[8] Aristotle. *De anima*. Critical edition. Leiden, E.J. Brill, 1994., 1994.

[9] Sophie Roux and Daniel Garber. *The mechanization of natural philosophy*. Springer, 2013.

[10] Erwin Bauer. "Vitalismus und Mechanismus - Die Grundprinzipien der rein Naturwissenschaftlichen Biologie und ihre Anwendungen in der Physiologie". In: Springer Berlin Heidelberg, 1920, pp. 6–9.

[11] Marc Kirschner, John Gerhart, and Tim Mitchison. "Molecular Vitalism". In: *Cell* 100.1 (2017), pp. 79–88.

[12] Erwin Schrödinger. *What is life? The Physical Aspect of the Living Cell*. Cambridge University Press, 2001, p. 184.

[13] Daniel E. Koshland. "The Seven Pillars of Life". In: *Science* 295.5563 (2002), 2215 LP –2216.

[14] Jamey D. Marth. "A unified vision of the building blocks of life". In: *Nat Cell Biol* 10.9 (2008), p. 1015.

[15] Harvey F. Lodish. *Molecular cell biology*. W.H. Freeman, 2000, p. 36.

[16] Bruce Alberts et al. *Molecular biology of the cell*. Garland Science, 2002.

[17] Tharwat Tadros. "Critical Micelle Concentration BT - Encyclopedia of Colloid and Interface Science". In: Springer Berlin Heidelberg, 2013, pp. 209–210.

[18] Derek Marsh. *Handbook of Lipid Bilayers*, p. 1145.

[19] Michael F. Brown. "Curvature Forces in Membrane Lipid – Protein Interactions". In: *Biochemistry* 51.49 (2012), pp. 9782–9795.

[20] Hein Sprong, Peter van der Sluijs, and Gerrit van Meer. "How proteins move lipids and lipids move proteins". In: *Nat Rev Mol Cell Biol* 2.7 (2001), pp. 504–513.

[21] Malinda Salim et al. "Amphiphilic designer nano-carriers for controlled release: from drug delivery to diagnostics". In: *MedChemComm* 5.11 (2014), p. 1602.

[22] Pierre-Alain Monnard and David W. Deamer. "Membrane self-assembly processes: Steps toward the first cellular life". In: *The Anatomical Record* 268.3 (2002), pp. 196–207.

[23]   Jeremy M. Berg, John L. Tymoczko, and Lubert Stryer. "Lipids and Many Membrane Proteins Diffuse Rapidly in the Plane of the Membrane". In: *Biochemistry. 5th edition.* (2002).

[24]   Michael O. Eze. "Phase transitions in phospholipid bilayers: Lateral phase separations play vital roles in biomembranes". In: *Biochemical Education* 19.4 (1991), pp. 204–208.

[25]   Rumiana Koynova and Martin Caffrey. "Phases and phase transitions of the sphingolipids". In: *Biochimica et Biophysica Acta (BBA)* 1255.3 (1995), pp. 213–236.

[26]   Gora M'Baye et al. "Liquid Ordered and Gel Phases of Lipid Bilayers: Fluorescent Probes Reveal Close Fluidity but Different Hydration". In: *Biophysical Journal* 95.3 (2008), pp. 1217–1225.

[27]   Frederick A. Heberle and Gerald W. Feigenson. "Phase Separation in Lipid Membranes". In: *Cold Spring Harbor Perspectives in Biology* 3.4 (2011), a004630.

[28]   John Gribbin. *In search of the big bang : quantum physics and cosmology.* Bantam Books, 1986, p. 413.

[29]   Eva Nogales, Sharon G. Wolf, and Kenneth H. Downing. "Structure of the [alpha][beta] tubulin dimer by electron crystallography". In: *Nature* 391.6663 (1998), pp. 199–203.

[30]   Susanne Moelbert, Eldon Emberly, and Chao Tang. "Correlation between sequence hydrophobicity and surface-exposure pattern of database proteins". In: *Protein Science : A Publication of the Protein Society* 13.3 (2004), pp. 752–762.

[31]   Peggy Findeisen et al. "Six Subgroups and Extensive Recent Duplications Characterize the Evolution of the Eukaryotic Tubulin Protein Family". In: *Genome Biology and Evolution* 6.9 (2014), pp. 2274–2288.

[32]   Anna Akhmanova and Michel O. Steinmetz. "Tracking the ends: a dynamic protein network controls the fate of microtubule tips". In: *Nat Rev Mol Cell Biol* 9.4 (2008), pp. 309–322.

[33]   Marcel E. Janson, Mathilde E. de Dood, and Marileen Dogterom. "Dynamic instability of microtubules is regulated by force". In: *The Journal of Cell Biology* 161.6 (2003), pp. 1029–1034.

[34]   Tim Mitchison and Marc Kirschner. "Dynamic instability of microtubule growth". In: *Nature* 312.5991 (1984), pp. 237–242.

[35]   Jingchao Wu and Anna Akhmanova. "Microtubule-Organizing Centers". In: *Annual Review of Cell and Developmental Biology* 33.1 (2017), pp. 51–75.

[36]   H. V. Goodson, S. J. Kang, and S. A. Endow. "Molecular phylogeny of the kinesin family of microtubule motor proteins". In: *Journal of Cell Science* 107.7 (1994), 1875 LP –1884.

[37]   Anthony J. Roberts et al. "Functions and mechanics of dynein motor proteins". In: *Nat Rev Mol Cell Biol* 14.11 (2013), pp. 713–726.

[38]   Susan L. Kline-Smith and Claire E Walczak. "Mitotic Spindle Assembly and Chromosome Segregation: Refocusing on Microtubule Dynamics". In: *Molecular Cell* 15.3 (2004), pp. 317–327.

[39]   J. H. Hayden, S. S. Bowser, and C. L. Rieder. "Kinetochores capture astral microtubules during chromosome attachment to the mitotic spindle: direct visualization in live newt lung cells." In: *The Journal of Cell Biology* 111.3 (1990), pp. 1039 –1045.

[40]   Marc Kirschner and Tim Mitchison. "Beyond self-assembly: From microtubules to morphogenesis". In: *Cell* 45.3 (1986), pp. 329 –342.

[41]   C. L. Rieder and S. P. Alexander. "Kinetochores are transported poleward along a single astral microtubule during chromosome attachment to the spindle in newt lung cells." In: *The Journal of Cell Biology* 110.1 (1990), pp. 81 –95.

[42]   Rebecca Heald et al. "Self-organization of microtubules into bipolar spindles around artificial chromosomes in Xenopus egg extracts". In: *Nature* 382.6590 (1996), pp. 420 –425.

[43]   Christoph von Ballmoos, Alexander Wiedenmann, and Peter Dimroth. "Essentials for ATP Synthesis by F1F0 ATP Synthases". In: *Annual Review of Biochemistry* 78.1 (2009), pp. 649–672.

[44]   Wolfgang Junge and Nathan Nelson. "ATP Synthase". In: *Annual Review of Biochemistry* 84.1 (2015), pp. 631–657.

[45]   Peter Mitchell. "Coupling of Phosphorylation to Electron and Hydrogen Transfer by a Chemi-Osmotic type of Mechanism". In: *Nature* 191.4784 (1961), pp. 144–148.

[46]   Paul D. Boyer. "Molecular motors: What makes ATP synthase spin?" In: *Nature* 402.6759 (1999), pp. 247–249.

[47]   Daichi Okuno, Ryota Iino, and Hiroyuki Noji. "Rotation and structure of FoF1-ATP synthase". In: *The Journal of Biochemistry* 149.6 (2011), pp. 655–664.

[48]   D. Ewen Cameron, Caleb J. Bashor, and James J. Collins. "A brief history of synthetic biology". In: *Nat Rev Micro* 12.5 (2014), pp. 381–390.

[49]   Steven A. Benner and A. Michael Sismour. "Synthetic biology". In: *Nat Rev Genet* 6.7 (2005), pp. 533–543.

[50]   Daniel G. Gibson et al. "Creation of a Bacterial Cell Controlled by a Chemically Synthesized Genome". In: *Science* 329.5987 (2010), 52 LP –56.

[51]   Dae-Kyun Ro et al. "Production of the antimalarial drug precursor artemisinic acid in engineered yeast". In: *Nature* 440.7086 (2006), pp. 940–943.

[52]   C. J. Paddon et al. "High-level semi-synthetic production of the potent antimalarial artemisinin". In: *Nature* 496.7446 (2013), pp. 528–532.

[53]   Petra Schwille. "Jump-starting life? Fundamental aspects of synthetic biology". In: *The Journal of Cell Biology* 210.5 (2015), 687 LP –690.

[54]   Michael L. Simpson. "Cell-free synthetic biology: a bottom-up approach to discovery by design". In: *Molecular Systems Biology* 2 (2006), p. 69.

[55]   Ralf P. Richter, Rémi Bérat, and Alain R. Brisson. "Formation of Solid-Supported Lipid Bilayers:- An Integrated View". In: *Langmuir* 22.8 (2006), pp. 3497–3505.

[56]   Erich Sackmann. "Supported Membranes: Scientific and Practical Applications". In: *Science* 271.5245 (1996), 43 LP –48.

[57]   Ralf Richter, Anneke Mukhopadhyay, and Alain Brisson. "Pathways of lipid vesicle deposition on solid surfaces: a combined QCM-D and AFM study." In: *Biophysical journal* 85.5 (2003), pp. 3035–47.

[58]   Paul S. Cremer and Steven G. Boxer. "Formation and Spreading of Lipid Bilayers on Planar Glass Supports". In: *The Journal of Physical Chemistry B* 103.13 (1999), pp. 2554–2559.

[59]   Gregory J. Hardy, Rahul Nayak, and Stefan Zauscher. "Model cell membranes: Techniques to form complex biomimetic supported lipid bilayers via vesicle fusion". In: *Current opinion in colloid & interface science* 18.5 (2013), pp. 448–458.

[60] J. Simon Attwood, Youngjik Choi, and Zoya Leonenko. *Preparation of DOPC and DPPC Supported Planar Lipid Bilayers for Atomic Force Microscopy and Atomic Force Spectroscopy*. 2013.

[61] Markus Axmann, Gerhard J. Schütz, and Johannes B. Huppa. "Single Molecule Fluorescence Microscopy on Planar Supported Bilayers". In: *Journal of Visualized Experiments : JoVE* 104 (2015), p. 53158.

[62] Hudson Pace et al. "Preserved Transmembrane Protein Mobility in Polymer- Supported Lipid Bilayers Derived from Cell Membranes". In: *Analytical Chemistry* 87.18 (2015), pp. 9194–9203.

[63] P. Bao et al. "Controlling transmembrane protein concentration and orientation in supported lipid bilayers". In: *Chemical Communications* 53.30 (2017), pp. 4250–4253.

[64] Ryugo Tero. "Substrate Effects on the Formation Process, Structure and Physicochemical Properties of Supported Lipid Bilayers". In: *Materials* 5.12 (2012), pp. 2658–2680.

[65] Yee-Hung M. Chan and Steven G. Boxer. "Model Membrane Systems and Their Applications". In: *Current opinion in chemical biology* 11.6 (2007), pp. 581–587.

[66] Christine Schmitt et al. "Compartmentalization and Transport in Synthetic Vesicles". In: *Frontiers in Bioengineering and Biotechnology* 4 (2016), p. 19.

[67] C. I. McPhee et al. "Measuring the Lamellarity of Giant Lipid Vesicles with Differential Interference Contrast Microscopy". In: *Biophysical Journal* 105.6 (2013), pp. 1414–1420.

[68] B. J. Frisken, C. Asman, and P. J. Patty. "Studies of Vesicle Extrusion". In: *Langmuir* 16.3 (2000), pp. 928–933.

[69] P. Mueller, T. F. Chien, and B. Rudy. "Formation and properties of cell-size lipid bilayer vesicles." In: *Biophysical Journal* 44.3 (1983), pp. 375–381.

[70] Olga Wesołowska et al. "Giant unilamellar vesicles - a perfect tool to visualize phase separation and lipid rafts in model systems." In: *Acta biochimica Polonica* 56.1 (2009), pp. 33–9.

[71] Peter Walde et al. "Giant Vesicles: Preparations and Applications". In: *ChemBioChem* 11.7 (2010), pp. 848–865.

[72] John P. Reeves and Robert M. Dowben. "Formation and properties of thin-walled phospholipid vesicles". In: *Journal of Cellular Physiology* 73.1 (1969), pp. 49–60.

[73] M. I. Angelova et al. "Preparation of giant vesicles by external AC electric fields. Kinetics and applications". In: ed. by C Helm, M Lösche, and H Möhwald. Darmstadt: Steinkopff, 1992, pp. 127–131.

[74] Daniel J. Estes and Michael Mayer. "Giant liposomes in physiological buffer using electroformation in a flow chamber". In: *Biochimica et Biophysica Acta (BBA) - Biomembranes* 1712.2 (2005), pp. 152–160.

[75] David L. Richmond et al. "Forming giant vesicles with controlled membrane composition, asymmetry, and contents". In: *Proceedings of the National Academy of Sciences* 108.23 (2011), pp. 9431–9436.

[76] Yung-Chieh Tan et al. "Controlled Microfluidic Encapsulation of Cells, Proteins, and Microbeads in Lipid Vesicles". In: *Journal of the American Chemical Society* 128.17 (2006), pp. 5656–5658.

[77] Ho Cheung Shum et al. "Double Emulsion Templated Monodisperse Phospholipid Vesicles". In: *Langmuir* 24.15 (2008). PMID: 18613709, pp. 7651–7653.

[78] Jeanne C. Stachowiak et al. "Unilamellar vesicle formation and encapsulation by microfluidic jetting". In: *Proceedings of the National Academy of Sciences* 105.12 (2008), pp. 4697–4702.

[79] Bastien Seantier and Bengt Kasemo. "Influence of Mono- And Divalent Ions on the Formation of Supported Phospholipid Bilayers via Vesicle Adsorption". In: *Langmuir* 25.10 (2009), pp. 5767–5772.

[80] Taiki Shigematsu, Kenichiro Koshiyama, and Shigeo Wada. "Effects of Stretching Speed on Mechanical Rupture of Phospholipid/Cholesterol Bilayers: Molecular Dynamics Simulation". In: *Scientific Reports* 5 (2015), p. 15369.

[81] Jonathan R. Howse et al. "Templated formation of giant polymer vesicles with controlled size distributions". In: *Nat Mater* 8.6 (2009), pp. 507–511.

[82] Dennis E Discher and Adi Eisenberg. "Polymer Vesicles". In: *Science* 297.5583 (2002), 967 LP –973.

[83] Bohdana M. Discher et al. "Polymersomes: Tough Vesicles Made from Diblock Copolymers". In: *Science* 284.5417 (1999), pp. 1143 –1146.

[84] Alexandra Graff et al. "Virus-assisted loading of polymer nanocontainer". In: *Proceedings of the National Academy of Sciences* 99.8 (2002), pp. 5064–5068.

[85] Ludwig Klermund, Sarah T Poschenrieder, and Kathrin Castiglione. "Simple surface functionalization of polymersomes using non-antibacterial peptide anchors". In: *Journal of Nanobiotechnology* 14 (2016), p. 48.

[86] Jean-Christophe Baret. "Surfactants in droplet-based microfluidics". In: *Lab on a Chip* 12.3 (2012), pp. 422–433.

[87] Shelley L. Anna, Nathalie Bontoux, and Howard A. Stone. "Formation of dispersions using "flow focusing" in microchannels". In: *Applied Physics Letters* 82.3 (2003), pp. 364–366.

[88] Makito Miyazaki, Masataka Chiba, and Shin'ichi Ishiwata. "Preparation of cell-sized water-in-oil droplets for in vitro reconstitution of biological processes in cellular compartments". In: *Nature Publishing Group* (2015).

[89] C. Holtze et al. "Biocompatible surfactants for water-in-fluorocarbon emulsions". In: *Lab on a Chip* 8.10 (2008), pp. 1632–1639.

[90] Ilia Platzman, Jan-Willi Janiesch, and Joachim Pius Spatz. "Synthesis of nanostructured and biofunctionalized water-in-oil droplets as tools for homing T cells". In: *Journal of the American Chemical Society* 135.9 (2013), pp. 3339–3342.

[91] Adam R Abate et al. "High-throughput injection with microfluidics using picoinjectors". In: *Proceedings of the National Academy of Sciences* 107.45 (2010), pp. 19163–19166.

[92] John A. Rogers and Ralph G. Nuzzo. "Recent progress in soft lithography". In: *Materials Today* 8.2 (2005), pp. 50–56.

[93] George M Whitesides. "The origins and the future of microfluidics". In: *Nature* 442.7101 (2006), pp. 368–373.

[94] Andrew J. DeMello and Robert C. R. Wootton. "Miniaturization: Chemistry at the crossroads". In: *Nat Chem* 1.1 (2009), pp. 28–29.

[95] Daniel Mark et al. "Microfluidic lab-on-a-chip platforms: requirements, characteristics and applications". In: *Chemical Society Reviews* 39.3 (2010), p. 1153.

[96] George Gabriel Strokes. *On the effect of the internal friction of fluids on the motion of pendulums*. 1851.

[97] O. Reynolds. "An Experimental Investigation of the Circumstances Which Determine Whether the Motion of Water Shall Be Direct or Sinuous, and of the Law of Resistance in Parallel Channels." In: *Proceedings of the Royal Society of London* 35.224-226 (1883), pp. 84–99.

[98] Joshua Lederberg. "A Simple Method for Isolating Individual Microbes". In: *Journal of Bacteriology* 68.2 (1954), pp. 258–259.

[99] Carsten Cramer, Peter Fischer, and Erich J. Windhab. "Drop formation in a coflowing ambient fluid". In: *Chemical Engineering Science* 59.15 (2004), pp. 3045–3058.

[100] Tsevi Beatus, Roy H Bar-Ziv, and Tsvi Tlusty. "The physics of 2D microfluidic droplet ensembles". In: *Physics Reports* 516.3 (2012), pp. 103–145.

[101] J. R. Burns and C. Ramshaw. "The intensification of rapid reactions in multiphase systems using slug flow in capillaries". In: *Lab on a Chip* 1.1 (2001), pp. 10–15.

[102] Virginie Mengeaud, Jacques Josserand, and Hubert H Girault. "Mixing Processes in a Zigzag Microchannel:- Finite Element Simulations and Optical Study". In: *Analytical Chemistry* 74.16 (2002), pp. 4279–4286.

[103] Pingan Zhu and Liqiu Wang. "Passive and active droplet generation with microfluidics: a review". In: *Lab on a Chip* 17.online (2017), pp. 34–75.

[104] Todd Thorsen et al. "Dynamic Pattern Formation in a Vesicle-Generating Microfluidic Device". In: *Physical Review Letters* 86.18 (2001), pp. 4163–4166.

[105] Johannes P. Frohnmayer et al. "The Giant Vesicle Book". In: CRC Taylor & Francis, 2017. Chap. Droplet-Supported Giant Vesicles as Cell-Like Compartments for Synthetic Biology.

[106] Andrew S Utada et al. "Dripping to jetting transitions in coflowing liquid streams". In: *Physical Review Letters* 99.9 (2007), p. 94502.

[107] F. Sarrazin et al. "Mixing characterization inside microdroplets engineered on a microcoalescer". In: *Chemical Engineering Science* 62.4 (2007), pp. 1042–1048.

[108] Ansgar Huebner et al. "Static microdroplet arrays: a microfluidic device for droplet trapping, incubation and release for enzymatic and cell-based assays". In: *Lab on a Chip* 9.5 (2009), pp. 692–698.

[109] Nicolas Bremond, Abdou R Thiam, and Jérôme Bibette. "Decompressing Emulsion Droplets Favors Coalescence". In: *Physical Review Letters* 100.2 (2008), p. 24501.

[110] Xize Niu et al. "Pillar-induced droplet merging in microfluidic circuits". In: *Lab on a Chip* 8.11 (2008), pp. 1837–1841.

[111] Venkatachalam Chokkalingam et al. "Optimized droplet-based microfluidics for sol-gel reactions". In: *Lab on a Chip* 10.13 (2010), pp. 1700–1705.

[112] J. M. Koehler et al. "Digital reaction technology by micro segmented flow — components, concepts and applications". In: *Chemical Engineering Journal* 101.1 (2004), pp. 201–216.

[113] Wei-Heong Tan and Shoji Takeuchi. "Timing controllable electrofusion device for aqueous droplet-based microreactors". In: *Lab on a Chip* 6.6 (2006), pp. 757–763.

[114] Max Chabert, Kevin D. Dorfman, and Jean-Louis Viovy. "Droplet fusion by alternating current (AC) field electrocoalescence in microchannels". In: *Electrophoresis* 26.19 (2005), pp. 3706–3715.

[115] Jan-Willi Janiesch et al. "Key Factors for Stable Retention of Fluorophores and Labeled Biomolecules in Droplet-Based Microfluidics". In: *Analytical Chemistry* 87.4 (2015), pp. 2063–2067.

[116] Marian Weiss et al. "Sequential bottom-up assembly of mechanically stabilized synthetic cells by microfluidics". In: *Nat Mater* advance on (2017).

[117] Eli Zamir et al. "Reconceptualizing fluorescence correlation spectroscopy for monitoring and analyzing periodically passing objects". In: *Analytical Chemistry* (2017).

[118] Frank J. Bruggeman and Hans V. Westerhoff. "The nature of systems biology". In: *Trends in Microbiology* 15.1 (2007), pp. 45–50.

[119] Chiara Martino and Andrew J DeMello. "Droplet-based microfluidics for artificial cell generation: a brief review." In: *Interface focus* 6.4 (2016), p. 20160011.

[120] Aaron P. Debon, Robert C. R. Wootton, and Katherine S. Elvira. "Droplet confinement and leakage: Causes, underlying effects, and amelioration strategies". In: *Biomicrofluidics* 9.2 (2015), p. 24119.

[121] Jean-Christophe Baret et al. "Kinetic Aspects of Emulsion Stabilization by Surfactants: A Microfluidic Analysis". In: *Langmuir* 25.11 (2009), pp. 6088–6093.

[122] Shelley L Anna and Hans C Mayer. "Microscale tipstreaming in a microfluidic flow focusing device". In: *Physics of Fluids* 18.12 (2006), p. 121512.

[123] Fabienne Courtois et al. "Controlling the Retention of Small Molecules in Emulsion Microdroplets for Use in Cell-Based Assays". In: *Analytical Chemistry* 81.8 (2009), pp. 3008–3016.

[124] Hella Baumann and Thomas Surrey. "Motor-mediated Cortical versus Astral Microtubule Organization in Lipid-monolayered Droplets". In: *Journal of Biological Chemistry* 289.32 (2014), pp. 22524–22535.

[125] Michael Elbaum, Deborah Kuchnir Fygenson, and Albert Libchaber. "Buckling Microtubules in Vesicles". In: *Physical Review Letters* 76.21 (1996), pp. 4078–4081.

[126] Deborah Kuchnir Fygenson, John F Marko, and Albert Libchaber. "Mechanics of Microtubule-Based Membrane Extension". In: *Physical Review Letters* 79.22 (1997), pp. 4497–4500.

[127] Igor S. Aranson and Lev S. Tsimring. "Pattern formation of microtubules and motors: Inelastic interaction of polar rods". In: *Physical Review E* 71.5 (2005), p. 50901.

[128] Tripta Bhatia et al. "Fluid domain patterns in free-standing membranes captured on a solid support". In: *Biochimica et Biophysica Acta (BBA) - Biomembranes* 1838.10 (2014), pp. 2503–2510.

[129] Radek Macháň and Martin Hof. "Lipid diffusion in planar membranes investigated by fluorescence correlation spectroscopy". In: *Biochimica et Biophysica Acta - Biomembranes* 1798.7 (2010), pp. 1377–1391.

[130] Magdalena Przybylo et al. "Lipid Diffusion in Giant Unilamellar Vesicles Is More than 2 Times Faster than in Supported Phospholipid Bilayers under Identical Conditions". In: 6 (2006), pp. 9096–9099.

[131] Andrew D. Griffiths and Dan S. Tawfik. "Miniaturising the laboratory in emulsion droplets". In: *Trends in Biotechnology* 24.9 (2006), pp. 395 –402.

[132] Honglian Guo et al. "Mechanism and Dynamics of Breakage of Fluorescent Microtubules". In: *Biophysical Journal* 90.6 (2006), pp. 2093–2098.

[133] L. K. Tamm and H. M. McConnell. "Supported phospholipid bilayers." In: *Biophysical Journal* 47.1 (1985), pp. 105–113.

Acknowledgments

First and foremost, I would like to thank my advisor Prof. Joachim Spatz for giving me the opportunity to work on such an exciting research topic, that has always fascinated me. During my PhD, I could always rely on his support and he opened the doors for new research directions and interesting cooperations. I am very thankful for both the freedom and the guidance I was given during research.

I want to thank Prof. Rainer Fink for accepting to review my thesis. I also want to deeply thank him for putting me on the path towards interdisciplinary research by his exciting lectures in Biophysics during my undergraduated education.

I would particularly like to thank Ilia Platzman for the supervision of my research. He was literally available day and night as a competent contact person and provided good advice in every situation, both scientific and personal. I enjoyed the many discussions we had from which I have learned a lot about scientific work. Also, I will always remember the fun time we spend on conferences and elsewhere.

I also want to thank my cooperation partners from other labs, especially Jonathon Hannabus, Michael Juniper and Thomas Surrey for their help and supply with tubulin as well as Thomas Heitkamp and Michael Boersch for their help and supply with ATPsynthase.

The microfluidic group started to grow a lot during my research. I want to thank all the members for the productive collaborations, the supportive environment, the good atmosphere and the fun time during and after work. It was great working and spending time with you! Especially I want to thank Jan-Willi Janiesch and Johannes Frohnmayer for the good collaborations, which allowed to achieve many results much faster than alone.

It was a pleasure to work in the inspiring environment of the Spatz department, both in Heidelberg and Stuttgart. I appreciate having you not only as colleagues but as good friends.

I want to thank all members of the Conduction Band for the great time we had during our studies. I am very curious where the wind will take us in the future.

Ein ganz besonderer Dank geht an meine Familie, vor allem an meine Eltern. Sie haben mich schon als Kind für die 'Naturforschung' begeistert, mich auf meinem Weg immer unterstützt und motiviert und mir dadurch vieles ermöglicht. Vielen Dank!

Finally, I want to thank my wonderful wife Sanam and our son Jona for their endless support. Sanam, you motivated me in the discussions we had and you always gave me strength and confidence, when I needed it. Thank you so much for that.